Development of swept, confocally-aligned planar excitation (SCAPE) microscopy for high-speed, volumetric imaging of biological tissue

---

Venkatakaushik Voleti

Submitted in partial fulfillment of the
requirements for the degree of
Doctor of Philosophy
in the Graduate School of Arts and Sciences

Columbia University

2019

ABSTRACT

Development of swept, confocally-aligned planar excitation (SCAPE) microscopy for high-speed, volumetric imaging of biological tissue

Venkatakaushik Voleti

With the wide-spread adoption of exogenous fluorescent indicators – and more recently genetically encoded fluorescent proteins – over the past two decades, there exists a diverse chemical toolkit with which to probe biological systems. Individual cell types and sub-cellular compartments can be targeted in an increasingly wide range of model organisms. However, imaging these samples is often an exercise in balancing the needs of any given experiment against the constraints of the chosen imaging technology. For example, a volume of brain tissue is host to neurons, glia, vascular compartments and red blood cells that all occupy discrete locations in 3D space, but must work together to support healthy organ function. Single-cell activity on the order of milliseconds can trigger downstream processes that unfold over the course of multiple seconds or even minutes. The development of a technique capable of providing depth-resolved, volumetric imaging with scalable spatiotemporal resolution is crucial to developing a proper understanding of such biological systems.

Bottlenecks in the throughput of existing technologies stem from a combination of inefficient illumination and volume acquisition strategies, and insufficient sensor read-out speeds. Light sheet microscopy is a promising solution, but individual designs tend to be highly specialized to specific types of samples and do not easily adapt to a wide range of experimental settings. In this thesis, I detail my work in developing swept, confocally-aligned planar excitation

(SCAPE) microscopy from a first-generation prototype into a versatile, easy-to-reproduce, easy-to-use system for high-speed, 3D imaging.

The first chapter introduces the challenges of designing optical systems capable of high-speed, volumetric imaging. An introduction to design choices faced in the construction of fluorescence microscopes, and current approaches to 3D imaging are discussed. **The second chapter** describes the progression from the 1st to 2nd generation SCAPE system. Improvements made through ray-tracing models and an enhanced optomechanical design are described, and results from this system in a number of model organisms are presented. **The third chapter** presents results from a range of biological applications to which SCAPE microscopy has been applied. Work in imaging the zebrafish heart to demonstrate the system's improved imaging speed, the *C. elegans* to show the system's resolution, and finally a number of examples of large field-of-view and high-resolution structural imaging are all described. Finally, **the fourth chapter** concludes with an overview of the work that lies ahead to both further develop of SCAPE microscopy, as well as to bring the existing system's strengths to bear in a wider range of environments.

Table of Contents

List of Figures

List of Tables

Acknowledgements

This thesis was a labor of love that owes its completion to a community of wonderful individuals from whom I was privileged to learn. I hope it may serve to provide guidance to some of the students who come after me, as the work of those who came before have served to ease my way.

First, I would like to thank my thesis advisor, Dr. Elizabeth Hillman. The design of SCAPE microscopy was influenced by my work with many different research labs, numerous demonstrations of the technology at various imaging courses and conferences, as well as interactions with a number of industrial partners. I would not have had any of these experiences without Dr. Hillman’s hard work and the countless opportunities it has provided me and my colleagues.

Researchers both within and outside Columbia University provided advice, materials and data analysis. My committee members, Drs. Andreas Hielscher, Christine Hendon, Samuel Sia and Ioannis Kymissis provided guidance and feedback to the completion of this work. Dr. Kimara Targoff, Caitlin Ford, Carmen de Sena Tomas and Vanessa George provided zebrafish embryos for cardiac imaging. Dr. Koutarou Kimura and Dr. Chentao Wen performed the cell tracking for the purpose of extracting calcium signals from cardiomyocyte nuclei within the zebrafish heart. Dr. Ed Boyden and Danielle Cosio, Dr. Andrew Leifer and Dr. Francesco Randi, and Dr. Saul Kato and Raymond Dunn all provided *C. elegans* samples for imaging. Further *C. elegans strains* were provided by the Caenorhabditis Elegans Genetics Center (funded by the NIH Office of Research Infrastructure Program No. P40OD010440). Dr. Tian Zheng, Sihan Huang, Owen Gerard provided advice on Trackpy and cell tracking in the C. Elegans. Dr. Ning Tian and Brent Young provided mouse retinal flat-mounted samples. Dr. Pavel Osten and Arun Narasimhan provided the mCUBIC cleared mouse brain sample. Drs. Randy Bruno, Clay Lacefield and Sam Benezra provided virally transfected mice expressing GCaMPX in the apical dendrites of Layer 5 cortical neurons. Drs. Claire Wyart, Michael Orger, David Schoppik, Jeremy Ullmann and David Reutens all provided zebrafish embryos expressing panneuronal calcium indicators for whole-brain or whole-circuit imaging. I would also like to thank Dr. David Schoppik and his lab for kindly supplying me with chocolate and Thai food each time we worked together. Drs. Wes Grueber, Rebecca Vaadia, Cesar Mendes and Richard Mann provided us with transgenic Drosophila larva. Dr. Luke Hammond and Darcy Paterka provided advice and training on the confocal and confocal

spinning disk microscope for photobleaching studies. Each lab which provided live samples also supplied valuable advice regarding best imaging and husbandry practices. Phillippe Clemenceau and Johan Herz at Axiom Optics for demonstrated and provided support for the HICAM Fluo camera. Bradley Witover from Morrell Instruments generously loaned us cameras, objective lenses and optomechanics over the period of 6-7 years. Thorlabs and Coherent also loaned us various components over the years.

I would further like to thank my colleagues in Dr. Hillman's research group. Dr. Matthew Bouchard laid down the foundational work for SCAPE microscopy, taught me during my first year and provided valuable guidance thereafter. Kripa Patel developed the large field-of-view applications with SCAPE microscopy shown in Chapter 3 and contributed to the design of SCAPE's user interface, optical layout and data-processing pipeline. Dr. Wenze Li supports the computational workstations and a great many collaborations with SCAPE microscopy, was one of my earliest collaborators and assisted in a number of experiments shown in this thesis. Citlali Perez-Campos made valuable contributions to the dissemination of SCAPE microscopy and assisted in a number of experiments shown in this work. Srinidhi Bharadwaj assisted in the cell tracking and analysis of the zebrafish heart and whole-body crawling C. elegans shown in Chapter 4. I would also like to thank the following people for serving as sounding boards for my ideas, teachers and confidantes: Dr. P. Thilanka Galwaduge, Dr. Mohammed Shaik, Dr. Sharon Kim, Dr. Ying Ma, Teresa Zhao, Hang Yu, Nic Thibodeaux, Grace Lee, Mary-Kate Montgomery, John Mavroudes, Carla Kim, Jacob Portes, Richard Yan and Malte Casper. My conversations with my colleagues through the years ranged from hilariously absurd to deeply insightful, and I cherish the friendships that have developed over the years.

Finally, I would like to thank my family. My parents have always believed in me. This work would not have been possible without their encouragement and tireless support. My brother embodies the values of hard work and perseverance and has served as a source of inspiration throughout my life. And lastly, my fiancée, Veena Sridhar, who kindly allowed me to go on endlessly about microscopy for seven years and transported suitcases full of home-cooked food across the country. I'm incredibly fortunate to have found someone so patient to accompany me on this journey.

Funding Sources

Funding for the work shown in this text was provided by National Institutes of Health (NINDS) R21NS053684, R01NS076628, R01NS063226, National Institutes of Health BRAIN initiative grants 5U01NS09429, UF1NS108213 (EMCH) and U19NS104649 (Costa) and R01HL13143801A1 (KT), the National Science Foundation (graduate fellowship Patel, IGERT funding to Voleti and CAREER CBET-0954796 to Hillman), the Simons Foundation Collaboration on the Global Brain (542951), Department of Defense MURI W911NF-12-1-0594, the Kavli Institute for Brain Science and the Columbia-Coulter Translational Research Partnership and Coulter Foundation (to Hillman).

Chapter 1 – Introduction

Biological systems are incredibly complex. A cubic centimeter of brain tissue consists of a complex network of tightly packed neurons each with their own morphologies, excitability, connectivity and genetic profiles. These characteristics can change as a function of stimulus, development and disease. Perturbations to biological tissue (such as thrombosis) that occur on the order of seconds can unleash complex signaling cascades that have long lasting effects days or even years after the initial event. Imaging these processes is crucial to developing a better understanding of the mechanisms behind them. Such an understanding can help us find optimal points of intervention to stave off disease through newly designed therapeutics, or even enhance biological function for our own ends.

While tools such as the X-ray, ultrasound and MRI have been clinically game-changing and are widely used to facilitate non-invasive visualization of biological function, these modalities lack both the resolution and mechanisms of contrast to probe behavior at the cellular level. Here, optical microscopy can serve as an essential tool for investigation. Its primary goal is to permit the visualization of micro-structures within tissue not immediately apparent to the naked eye. However, in addition to structural imaging, functional imaging – i.e. the study of how a system changes over time in response to or on the absence of stimulus – is also crucial. Optical microscopy offers a wide variety of contrast mechanisms such as absorption, phase contrast and polarization that can all be used at the cellular level. Most notably, the usage of fluorescence has become increasingly ubiquitous over the past two decades in concurrence with the development of sophisticated genetic techniques to localize that fluorescence to specific, subcellular targets.

However, one of the key challenges of optical microscopy is that these two goals – structural and functional imaging – are often at odds with one another. Imaging fine structures requires sampling those structures finely; imaging fast processes involves acquiring data faster than the processes themselves. And understanding activity distributed in 3D space clearly must involve sampling that 3D space in its entirety. Broadly speaking, the trade-offs one must make when balancing the ability to acquire high-quality structural data or high-quality functional data using a 3D optical system are a result of inadequate data rates and the sample's own intolerance to external perturbation.

3D microscopy techniques are generally limited to low volumetric speeds for reasons more thoroughly discussed later this section. As a result, many high-speed systems are highly specialized to a given application and resist modification that might make them more accessible to the larger research community. Within this thesis, I will describe my work in developing **S**wept, **C**onfocally **A**ligned **P**lanar **E**xcitation (SCAPE) microscopy, a high-speed, 3D fluorescence imaging technology, that can be used on a wide variety of model organisms to address key applications in the field of neuroscience and cardiology.

Within the first chapter, I provide the requisite background needed to understand the development of SCAPE microscopy. A brief introduction to fluorescence is provided followed by an explanation of basic optical principles that play a role in future design choices. I then discuss previous approaches to high-speed, scanning 3D microscopy, their benefits and their drawbacks with particular attention placed on light-sheet based illumination strategies.

In the second chapter, I will describe my work in developing SCAPE microscopy. Throughout the course of this work, I placed great emphasis on the system's versatility as well as its potential for dissemination which motivated a large number of design choices described herein. I discuss my work on the initial implementation of the system (SCAPE1.0) and then the drawbacks of such an architecture. I developed a new design with a simpler geometry based on confocal microscopy. The new system retained the data rates of SCAPE1.0 but significantly improved the system's performance along a number of metrics. As a result of high demand, I was simultaneously developing and supporting three systems within the lab and there was a need for standardization of performance across systems. I developed successive generations of custom opto-mechanical alignment techniques and performance metrics. These initial systems facilitated four collaborations between our lab and other groups at Columbia University, requiring 3D calcium imaging within the larval and adult Drosophila, in vivo mouse brain and olfactory sensory neurons. Examples from some of these model organisms, as well as from the zebrafish central nervous system that resulted from shorter one-to-two week collaborations are presented to highlight the next-generation system's capabilities.

In the third chapter, I highlight key biological applications that served as a driving force behind further optimization of the system's speed and resolution: the zebrafish heart and the C. elegans. The zebrafish heart is a commonly used model organism in regenerative medicine and developmental biology, however direct 4D measurements of the sample are complicated by the fact that the system is consistently in motion (beating 2-4 times per second). I describe the standard approaches to 4D imaging of this sample, with an emphasis on the light-sheet based techniques that have been developed over the past decade for the imaging of blood flow and calcium activity. The limitations of current approaches led me to incorporate a high-speed, next-generation camera in order to develop a version of SCAPE microscopy that can perform depth-resolved 3D imaging at hundreds of volumes per second. This represents over an order of magnitude improvement in acquisition speed. The C. elegans is a commonly used model organism in the field of neuroscience and is the only animal with a fully characterized connectome. I describe previous approaches to whole-brain imaging of this sample using light sheet microscopy, spinning disk confocal microscopy and other modalities. Due to the much smaller size of the C. elegans, pursuing this application required me to develop a version of SCAPE with sub-micron to near-micron resolution. By further incorporating the high-speed camera used for zebrafish heart imaging, I was able to image the entire body of a C. elegans at rates fast enough to perform cell tracking with enough detail to resolve cellular nuclei and fine dendritic processes. Additional applications of high-resolution structural imaging – including those in cleared tissues and retinal flat mounts - that arise as a natural consequence of this improved resolution are then presented.

The final chapter concludes with thoughts on the potential for future development of SCAPE, alternative implementations of the technology and the challenges facing the field of high-speed, volumetric microscopy as a whole.

Fluorescence in Biological Imaging

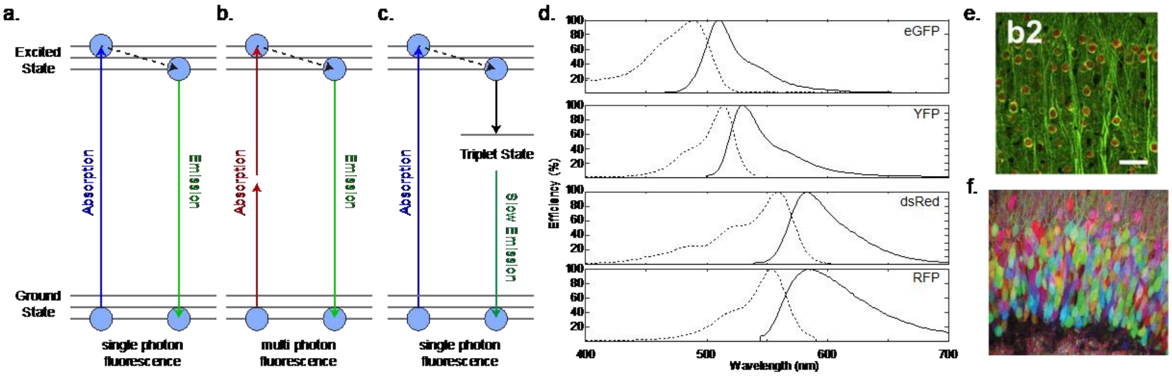

Figure 1.1: *Explanation of fluorescence*
a. *Energy level transitions of electrons transitioning from the ground to excited states and back. Linear or single-photon absorption occurs when a high energy photon (blue) is absorbed by an electron, non-radiatively emits energy and releases a lower energy photon (green)* ***b.*** *Multi-photon absorption occurs when an electron absorbs two or more low energy photons (red), non-radiatively emits energy and then releases a higher energy photon (green).* ***c.*** *Excited electrons can also transition into a triplet states before decaying back down to the ground state, which can take 1000's of times longer that simple fluorescence emission* ***d.*** *Excitation (dashed) and emission (solid) spectra for commonly used fluorophores spanning the visible range of light* ***e.*** *Mouse brain slice expressing GFP in layer 2/3 and layer 5 neurons of the cortex taken from ((Chen, Cichon et al. 2012))* ***f.*** *Dentate gyrus of Thy1-Brainbow1.0 mouse brain expressing combinations of CFP, YFP and RFP*

Fluorescence is a biophysical phenomenon by which a fluorophore (molecule or atom) absorbs a photon containing a specific amount of energy and then emits a lower energy photon at some later time. In its simplest form, linear fluorescence occurs when an electron within a fluorophore absorbs a single photon that causes it to transition from its ground or lowest energy state into a higher energy state (**Figure 1.1**a). The energy potential difference between these two states corresponds to the wavelength, λ, of the photon absorbed:

$$\lambda = hc/E$$

In which h is Planck's constant, c is the speed of light and E is the energy bandgap. The electron releases energy through a non-radiative processes while in its excited state and then falls back to the ground level emitting another photon in doing so. Multi-photon absorption processes involve the absorption of two-photons simultaneously (**Figure 1.1**b). Alternatively, excited electrons can also transition into triplet states, significantly delaying the emission of a photon from the electron (**Figure 1.1**c).

Due to the non-radiative energy loss prior to photon emission, the wavelength of the emitted photon will be longer than that of the absorbed photon. The excitation and emission spectra of a given fluorophore correspond to the probability that light of a particular wavelength will be absorbed or emitted by the fluorophore (**Figure 1.1**d). This wavelength shift between the excitation and emission spectra is known as the Stokes shift. Fluorescent microscopes reliant on linear fluorescence use low-wavelength excitation sources and selectively filter wavelengths corresponding to the fluorophore's emission band into optical paths directed towards the detector.

Fluorescent molecules come in a range of colors and following the rapid proliferation of GFP (green fluorescent protein) through the research community, the past two decades have seen a combination of genetic and chemical engineering that have allowed us to target virtually any transgene with a host of multi-colored fluorescent proteins (FPs). Targeting of FP expression to specific transgenes can be accomplished acutely in individual animals through bulk injection of plasmids into tissue followed by electroporation, or through the use of viral vectors. Alternatively, it is also possible to create stable lines of transgenic animals through techniques such as embryonic stem cell-mediated gene transfer. Such techniques have led to the creation of a host of model organisms with libraries of fluorescently labeled transgenes, as well as libraries of the plasmids themselves. In addition to targeted expression of FP's, many naturally occurring molecules found in tissues are also fluorescent. Examples include collagen found in structured lattices within connective, fibrous tissues such as tendons and ligaments, lipofuscin which is deposited in organs such as the brain and liver in response to aging and injury, and flavin proteins which are crucial to metabolic processes in cellular respiration. Together, these endogenous sources contribute to a background signal known as autofluorescence.

The color and mere presence of FP’s are the most commonly used form of contrast in fluorescence microscopy (**Figure 1.1**e). However, buried within the process of linear fluorescence are a plethora of other contrast mechanisms capable of providing detailed information about tissue structure and function. For example, different FP’s can take different amounts of time to emit fluorescence after the initial absorption event. This distribution of emission times is called fluorescence lifetime and can help disambiguate the presence of fluorophores with similar emission spectra. Most FP’s have fluorescence lifetimes between 2.3-3.5 ns. As a reference, GFP has a lifetime of 2.8 ns, though recent work has created variants as low as 0.8 ns (Mamontova, Solovyev et al. 2018). Similarly, hyperspectral imaging uses the absorption or emission spectra of FP’s as uniquely identifying fingerprints (Radosevich, Bouchard et al. 2008, Grosberg, Radosevich et al. 2011). By sweeping a narrow band light source through a range of wavelengths spanning the excitation spectra of a number of spectrally overlapping FP’s, it is possible to unmix the amount of each individual fluorescent protein at every position within the image. Furthermore, ratio-metric imaging can be used to distinguish the boundaries between tightly packed adjacent tissues that express different fluorophores to varying degrees. For example, **Figure 1.1**f shows how combinatorial expression of 4 proteins allows clear disambiguation of adjacent cells using a technique called Brainbow. Over the past twenty years, the development of fluorescent proteins has extended the emission spectrum into redder areas of the visible and near infrared spectrum (Rodriguez, Campbell et al. 2017). In this thesis, we use SCAPE to image red fluorescent proteins such as dsRed, mCherry, tdTomato and tagRFP for ratiometric functional imaging.

Functional fluorescent proteins are targeted FP's that change their signal in response to an environmental perturbation. GCaMP is a calcium-sensitive fluorescent indicator that fuses circularly permuted GFP to calmodulin, a calcium binding messenger protein, and M13, a myosin light chain kinase. In order to emit fluorescence, it must be simultaneously excited by wavelengths within its excitation spectra (usually 488 nm) as well as in the presence of unbound calcium. Upon binding to calcium, the conformational structure of the protein temporarily shifts resulting in emission of photons between 480-590 nm, with a peak at approximately 510-520 nm. GCaMP has been widely adopted in neuroscience where increases in intracellular calcium levels following an action potential are used as a proxy measure of neuronal firing (Chen, Cichon et al. 2012). It has since spread to other research areas such as the study of the cardiac (Tallini, Ohkura et al. 2006, Weber, Scherf et al. 2017) and vascular (Tallini, Brekke et al. 2007) activity. Since its initial invention in 2001, development of successive generations of GCaMP have produced variants with improved dynamic range, signal-to-background ratio (SBR), responsivity and binding kinetics. The version of GCaMP expressed in an organism can limit the types of processes one can study. For example, slow rise or decay time kinetics can affect the ability to resolve high-frequency calcium dynamics, as one calcium spike merges into another. Alternatively, other variants such as GCaMP6s with low background significantly improve the SBR but provide little information about the location of inactive cells. FP selection plays an important role in determining optimal parameters for an imaging study or, as I describe later in this chapter, in the design or limitations of imaging systems. The examples in this work focus on applications in neuroscience and the cardiovascular system, and primarily use GCaMP6 variants as metrics of cellular activity. In addition to GCaMP, recent years have also seen the development of proteins sensitive to voltage (Xu, Zou et al. 2017), neurotransmitters and neuromodulators (Wang, Jing et al. 2018), glucose (Hu, Wei et al. 2018), pH (Martynov, Pakhomov et al. 2018) and other metabolic processes (Bilan and Belousov 2016).

Working with fluorescent proteins, however, comes with a number of caveats that must be taken into consideration. Live cell and live animal imaging require that the method chosen be non-destructive to the sample over the duration of the experiment. While fluorescent proteins are excellent sources of targeted contrast for the reasons described above, one of the key challenges is collecting enough photons from FP's to achieve sufficiently high signal on the detector. This is challenging for a number of reasons. Unlike stains or dyes used in histopathology, FP's are expressed by utilizing the cells native transcriptional and translational mechanisms. FP's might be attached to molecules that are natively expressed by the cell itself. As a result, the concentration of fluorophores within a given area might be too low to generate sufficient signal when excited. Artificially boosting the signal by driving increased production of the FP could alter cellular processes dependent on the machinery that the FP was designed to investigate. In extreme cases, the presence of the fluorophores themselves might be cytotoxic and negatively affect the behavior of the organism in question.

In addition to issues relating to FP expression and concentration, fluorophores only convert a fraction of absorbed photons into emitted fluorescence (a ratio known as quantum yield): $QY = (emitted\ photons) \div (absorbed\ photons)$. Improving the quantum yield of FP's is an active area of research, and imaging studies generally try to use high quantum yield FP's in order to maximize detected signal. Fluorophores also contain triplet states into which photons can transition into when in the excited state. Electrons can remain in these triplet states for orders of magnitude longer than in the excited state, thereby destroying the ability of the molecule to generate fluorescence. Energy or electron transfer can then occur from this triplet state into molecular oxygen, creating reactive oxygen species that are capable of degrading fluorophores (and by extension, SNR) over time in a process called photobleaching. These reactive oxygen species can also damage cells in a process known as phototoxicity.

While the exact mechanisms of action behind photobleaching and phototoxicity are still poorly understood, they are important considerations when choosing imaging parameters. Signal drop-off due to photobleaching parameters typically take the shape of a two- part decaying exponential function, with the exact time constants of the exponentials varying as a function of laser exposure and fluorophore used. Recent work suggests that photobleaching rates are non-linearly related to the intensity of illuminating light, with higher light levels causing supra-linear increases in fluorescence decay (Cranfill, Sell et al. 2016). The way in which imaging systems with different illumination paradigms trade off their ability to image rapidly with higher rates of photobleaching will be discussed in future sections.

Optical Microscopy and the Design of Imaging Systems

This section will introduce terminology and certain design fundamentals of optical microscopy (specifically fluorescence microscopy) that will serve as a reasonable base of knowledge for chapters to come. This section is not meant to be an authoritative guide to imaging systems. For an excellent mathematical description of the physics of optics, see “Optics” by Eugene Hecht, “Fundamentals of Photonics” by B.E.A Saleh and M.C. Teich and “Principles of Optics” by Max Born and Emil Wolf. For step-by-step tutorial to lens design, see “Modern Lens Design” by Warren J. Smith and “Introduction to Lens Design: With Practical Zemax Examples” by Joseph M. Geary. Finally, for an exhaustive work on the nuances of experimental protocols pertaining to fluorescence microscopy, imaging system design and processing of biological images, I refer readers to “The Handbook of Confocal Microscopy” by James Pawley.

Lenses

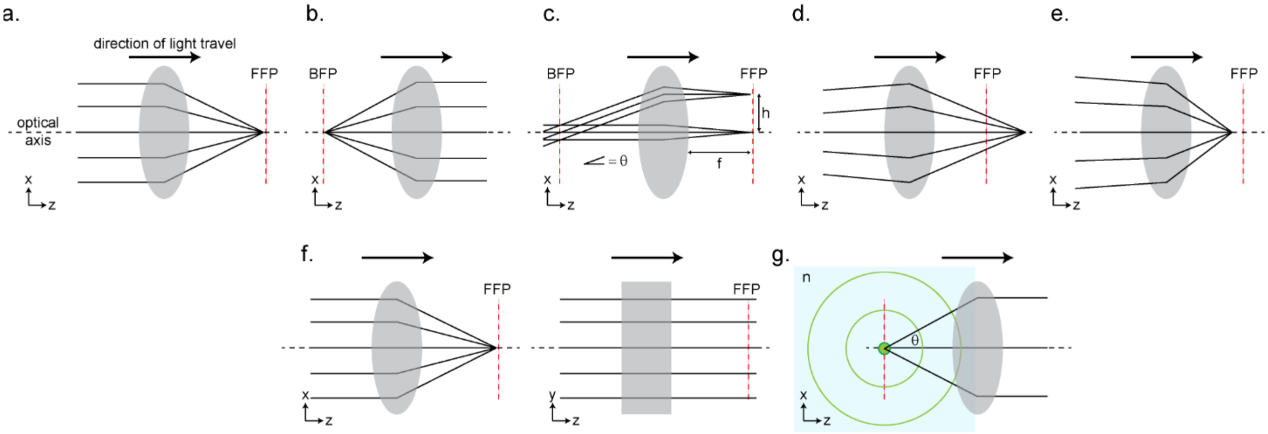

Figure 1.2: *Basic lens properties*
a. *Collimated rays passing through a lens focus at the lens’ front focal plane (FFP)* ***b.*** *Rays emanating from a point at the back focal plane (BFP) of a lens emerge collimated* ***c.*** *Collimated rays traveling at an angle focus at the focal plane above the optical axis* ***d.*** *Divergent rays entering a lens focus beyond the focal plane* ***e.*** *Convergent rays entering a lens focus before the focal plane* ***g.*** *Non-rotationally symmetric lenses such as cylindrical lenses only focus light along a single dimension* ***g.*** *Numerical aperture of a lens is determined by the half angle of its cone of collection (θ) and the refractive index (n) of the immersion medium*

First, consider an optical system containing a single lens collecting light from a light source (**Figure 1.2**a). The simplest light source is one in which all rays are travelling parallel to one another; these rays are called “collimated.” The optical axis of a system is the imaginary line passing through the center of curvature of a lens or lens sequence. Collimated rays passing through a lens aperture focus at the lens’ focal plane. The reverse is also true; light originating from a point on the lens’ focal plane and passing through the lens will exit the lens collimated (**Figure 1.2**b). The focal length, f, of a simple lens is the distance from the lens surface to the focal plane and in simple, thin lenses is inversely related to the curvature of the lens. For the purpose of this example, let us assume that we have a thin lens with an equivalent front and back focal length. If collimated rays traveling parallel to the optical axis pass through the lens, they will focus at the intersection of the optical axis and the focal plane. If the collimated rays pass through the lens traveling at some angle, θ, relative to the optical axis, they will converge at the focal plane at some height, h, above the optical axis (**Figure 1.2**c) in which:

$$h = ftan(\theta).$$

Again, this equation can be used in reverse. A ray passing through a point on the focal plane of a lens at some height, h, will exit the lens traveling at an angle, θ, relative to the optical axis. Simply put, this equation speaks to a relationship between the front and back focal plane of a lens. The location of a light ray at the back focal plane (BFP) of a lens will determine the angle at which that ray hits the front focal plane (FFP) of the lens; the angle at which that light ray intersects the BFP will determine the position that the ray will intersect the FFP. Light rays that are converging or diverging while entering the lens will focus away from the focal plane (**Figure 1.2**de).

Finally, most lens surfaces are ground to spherical shapes due to considerations relating to ease of manufacturing and so are radially symmetric about the optical axis. In this case, the "height" of a ray can be replaced by the radial distance of that ray from the optical axis. However, in future sections, we will see that light sheet microscopes (and by extension, SCAPE) use cylindrical lenses which may only be curved along a single axis (**Figure 1.2**f). As a result, light is only focused along this particular axis and optical systems containing such radially asymmetric elements must be thought of independently along each of these axes.

An important consideration in optical system design is collection efficiency. Let us assume a simple point emitter, like a fluorophore, placed along the optical axis at the focal plane of a lens (**Figure 1.2**g). The emitter is radiating light in a spherical wave outward in all directions. Because of the lens' finite aperture size, it is only able to collect light from within a limited conical range of these angles. The maximum angular range determines the lens' collection efficiency and when describing microscope objective lenses, is described by the lens' numerical aperture (NA):

$$NA = nsin(\theta)$$

Here, n is the immersion medium of the substance between the sample and lens and θ is the ½ angle of the cone collected by the lens. As the aperture diameter (D) increases and the focal length (f) decreases, the lens is able to collect larger cone angles. Another way to describe light collection efficiency is through the F-number (F/#) or "speed":

$$F/\# = \frac{1}{2NA} \cong \frac{f}{D} \; when\; \theta \leq 15°$$

The F/# is more commonly used to describe lenses used in photography or machine vision applications. The radial flux of the system is inversely proportional to the square of the F/#:

$$Flux \propto \frac{1}{(F/\#)^2} = 4NA^2$$

If we were to consider two microscope objective lenses with two different numerical apertures (NA_1 = 0.75 and NA_2 = 0.0.5), the first objective lens would have 2.25x the light collection efficiency of the second: $Ratio = \; (4 * 0.75^2)/(4 * 0.5^2) = 2.25$

Resolution

Numerical aperture is an important consideration when discussing a lens' resolution. While thus far, we have focused on properties of lenses that allow us to treat light like pencil beams or rays, light can also be treated as a wave in which the pencil beams are defined as the vectors of light propagation normal to the light's wavefronts. A planar wave traveling along the z-direction would contain periodic, flat wavefronts and we can draw a number of rays indicating the direction of light travel. Due to diffraction, a planar wave passing through a circular aperture such as a lens will converge onto the focal plane and different points on the wavefront will constructively and destructively interfere with one another. The resulting electric field creates an intensity distribution near the focal plane known as the 3D point-spread-function. The cross section of the point spread function at the lens' focal plane is described by a circularly symmetric first order Bessel function which contains a large central lobe, followed by side-lobes organized in concentric rings around the primary side lobe. The distance from the lobe's peak to its first minima is defined as the in-plane or lateral resolution limit as specified by the Rayleigh criterion:

$$r_{lateral} = 0.61\frac{\lambda}{NA} = 0.61\frac{\lambda}{n\sin\theta}$$

The minimum resolvable distance between two points situated on the optical axis, or the axial resolution, is defined as:

$$r_{axial} = \frac{2\lambda n}{NA^2} = \frac{2\lambda n}{(n\sin\theta)^2}$$

Note here that in comparison to camera or photography systems in which resolution is specified as the number of pixels on the camera (which would ideally be large), the resolution of a microscopy system is the minimum resolvable distance between two point emitters (which should be as small as possible). To improve resolution, one may either lower the wavelength of light used (though this places limits in terms of absorption, toxicity and scattering within tissue), increase the refractive index of the immersion medium, or increase the angular collection range of the lens.

Optical Trains/Relays

Optical systems consist of multiple lenses following one another in order to relay an image of the sample to the sensor with some degree of magnification. There are three types of magnification: lateral, angular and axial.

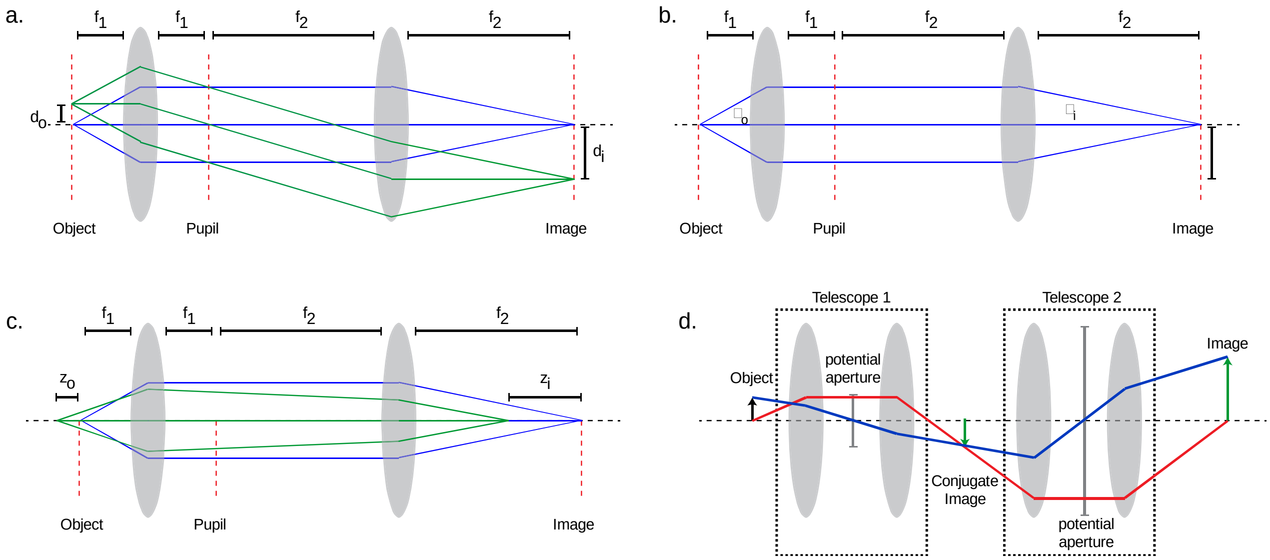

Figure 1.3: *Fundamentals of optical trains*
a. *2-lens telescope mapping a 2 objects from one plane to another with a lateral magnification between them* ***b.*** *Telescope mapping an object from object space to image space with an angular magnification between them* ***c.*** *Telescope mapping 2 objects laying along the optical axis onto 2 locations surrounding the image with an axial magnification* ***d.*** *Optical relay consisting of 2 telescopes mapping an object onto a conjugate image before mapping it to the image plane. Marginal ray is shown in red and chief ray is shown in blue.*

Consider the basic telescope consisting of two lenses (L_1, and L_2), with different focal lengths (f_1 and f_2) and angular collection cone angles (Θ_1 and Θ_2) where all parts of the imaging system are in air. There are two objects resting on the focal plane of L_1 that are mapped to the focal plane of L_2 where we find a camera sensor (**Figure 1.3**a). The distance between those two objects is d_o whereas the distance between the *images* of the two objects is d_i. The lateral magnification of a system is defined as the ratio between these two distances and in this configuration, is equivalent to the ratio between the two focal lengths:

$$M_{lateral} = \frac{d_i}{d_o} = \frac{f_2}{f_1}$$

The lateral magnification is inversely related to the angular magnification (**Figure 1.3**b):

$$M_{angular} = \frac{\theta_i}{\theta_o} = \frac{d_o}{d_i} = \frac{f_1}{f_2}$$

This relationship also provides a mathematical description as to why it is not possible to simply increase your magnification in order to increase the resolution (i.e. NA) of your system. As the lateral magnification of your system increases, the numerical aperture of the cone of light responsible for creating the final image decreases. In order to increase resolution, one must increase the actual frequency content of light collected by system.

Finally, consider two objects lying at varying distances from the focal plane of L_1 along the optical axis (**Figure 1.3**c). The telescope will map them to positions along the optical axis surrounding the focal plane of L_2. If the distance between the points is d_o and the distance between the *image* of the two points is d_i, then the axial magnification will be the ratio of these two distances:

$$M_{axial} = \frac{d_i}{d_o} = M_{lateral}^2 = \left(\frac{f_2}{f_1}\right)^2$$

Note that in comparison to lateral magnification, axial magnification is non-linear. If we link together a series of telescopes (as we soon will with SCAPE), one can multiply their individual lateral magnifications to determine the overall magnification of the system ($M_{total} = M_1 M_2$).

In addition to the front and back focal planes, there are a number of important surfaces and rays to that are useful when designing optical systems (see **Figure 1.3**d) These surfaces are:

1. **Conjugate image planes:** These planes are all of the locations that an optical system will create an image of the object. The sensor will always be an image plane but many optical systems will utilize lens relays with other “conjugate” image planes between the object and sensor.

2. **Field stop position:** This stop is the element within the optical train that limits the system's field of view. In high-magnification systems, the camera sensor's size determines the maximum field of view over which it is possible to collect information and acts as the de-facto field stop. Alternatively, SCAPE microscopy also uses physical apertures placed at conjugate image planes for alignment, testing or imaging purposes.

3. **Entrance and exit pupil planes:** These planes describe the system's light gathering ability and are images of an aperture stop as viewed from the entrance or exit ports of the system. Apertures throughout each telescope can make their contribution to defining the entrance and exit pupil planes. In **Figure 1.3**d, note how the aperture in the 1st telescope defines the size of the system's pupil whereas the aperture in the 2nd telescope plays no role. It is possible to get an intuitive sense of the shape of one's pupil by imaging a defocused point source. In microscopy, pupils tend to be circular so point objects look like circles. In photography, polygonal apertures are used which define the shape of the pupil (Google "hexagonal bokeh" for examples). Entrance and exit pupil boundaries in SCAPE are actually a combination of a number of apertures stops found within the system acting in tandem, so the utilized pupil will not be circular.

4. **Marginal Ray:** The marginal ray passes through the center of the object or field of view and intersects the edge of the system pupil.

5. **Chief Ray:** The chief ray is a ray that travels from the center of the system's primary aperture stop to the furthest off axis point within the object or image.

When describing an optical system, it is useful to start within a paraxial approximation of the system utilizing "thin" or "ideal" lenses, in which each lens is described only by its focal length and pupil diameter.

Aberrations and Issues

When moving from thin lens approximations to using real lenses, control of aberrations will play a critical role in system performance. The key lens aberrations discussed are chromatic aberration, spherical aberration, coma, astigmatism and field curvature.

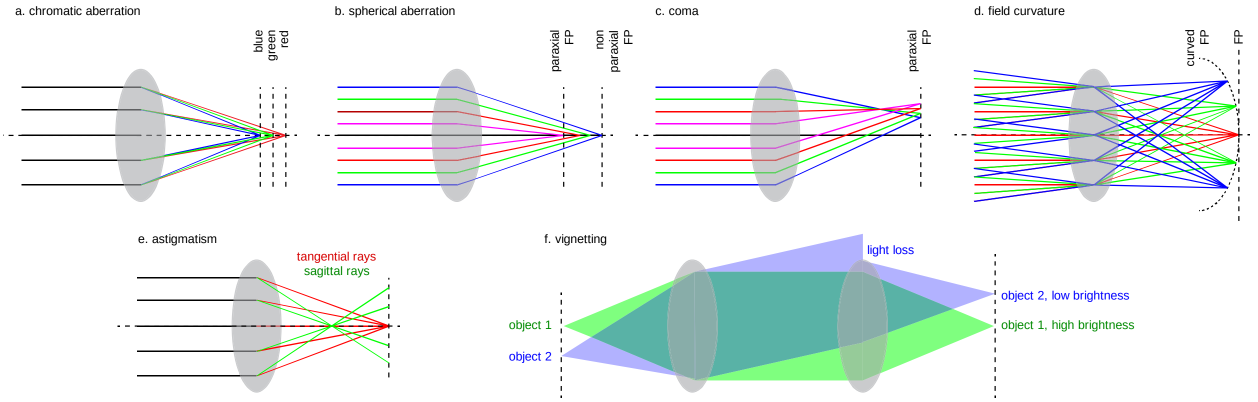

Figure 1.4: *Common lens aberrations*
a. *Chromatic aberrations (colors represent different wavelengths of light)* ***b.*** *Spherical aberration (colors represent distance of ray from optical axis)* ***c.*** *Coma (colors represent distance of ray from optical axis)* ***d.*** *Field curvature (colors represent off-axis points)* ***e.*** *Astigmatism (colors represent rays propagating along different planes) in which rays focus at the focal plane the tangential plane but not along the sagittal plane* ***f.*** *Vignetting due to un-even light losses over the field of view*

Chromatic aberration arises from the fact that the refractive indices of various glasses used in the manufacturing of lenses vary as a function of wavelength. As a result, a given lens will have different effective focal lengths for different wavelengths of light (**Figure 1.4**a). Achromatic lenses are a compound design that combine two separate lenses made of flint glass (high refractive index and dispersion) and crown glass (low refractive index, low dispersion) in order to bring two different wavelengths to a common focus. Apochromatic lenses are more expensive, but are designed to bring three wavelengths to a common focus. Most of the lenses used in SCAPE – and other benchtop microscopes – are achromatic lenses. A system with poorly corrected chromatic aberrations will only be able to generate a properly focused point-spread function over a narrow band of wavelengths, and will therefore have a blurrier polychromatic point spread function. Single-photon fluorescence microscopes can use excitation wavelengths as low as 405 nm and collect fluorescence to 680 nm and must therefore be corrected over the entire visible range.

Spherical aberrations arise when rays passing close to the optical axis (paraxial rays) through the lens focus at a different focal plane than rays passing further from the optical axis (marginal rays) (**Figure 1.4**b). Lenses in which marginal rays focus closer to the lens surface than paraxial rays are said to have positive spherical aberration, whereas lenses in which marginal rays focus farther than paraxial rays have negative spherical aberration. These aberrations arise primarily on lenses with high numerical apertures (i.e. high lens curvatures to achieve short focal lengths and large entrance pupil diameters). The effect of spherical aberration is to decrease the axial resolution of a system by axially elongating its point spread function and deteriorate in-plane contrast.

Coma is a phenomenon analogous to spherical aberration arising at points within the image that do not lie along the optical axis of a system. It occurs when rays passing through different portions of the lens pupil intersect the image plane at different transverse heights (**Figure 1.4**c).

Field curvature occurs when collimated rays entering a lens at different angles do not focus at the same distance from the lens surface, giving rise to a "curved" focal plane (**Figure 1.4**d). The effect of such an aberration will be a steady decrease in image contrast from the center to the edges of the image. Alternatively, adjusting the system in order to bring the edges of the image into focus will blur the center of the image, creating a ring of best focus.

Astigmatism occurs when an optical system is radially asymmetric and contains multiple focal lengths along each transverse axis (**Figure 1.4**e). As a result, light focusing along – for example – the horizontal dimension will not focus to the same plane as light focusing along the vertical dimension, requiring the user to choose a plane of best focus. The effect of this aberration on an image will therefore be a loss of contrast along one dimension.

Finally, in addition to the lens aberrations just described, optical systems may also suffer from a phenomenon known as vignetting, which describes a steady decrease in image intensity from the center to the edge of the image (**Figure 1.4**f). Such a phenomenon arises when aperture stops within the system are positioned so as to occlude light rays generated from points at the image periphery than those generated at the image center. In fluorescence systems, this phenomenon can arise through uneven illumination patterns (light exciting fluorescence at the periphery is of lower intensity than light generating florescence in the center) or through uneven detection throughput (equivalent amounts of fluorescence generated at image periphery and center result in different signal levels at the detector). The location of pupils within the system plays an important role in determining the degree of vignetting experienced.

Objective Lenses

Microscope objective lenses are complex, multi-lens assemblies designed to provide a high level of aberration correction over a given field of view. Because of the considerable amount of work involved in their design, the internal lens prescriptions of these lenses are kept secret. For a given lens, manufacturers typically provide the magnification, numerical aperture, working distance, required immersion medium and field number. They also contain a short code describing the types of aberration corrected by the design (eg: “Plan” refers to a correction for field curvature, while “Apo” refers to a correction for chromatic aberrations) (Chandler and Roberson 2009).

The sample lies at the front focal plane of an objective lens. Most microscope objective lenses used for confocal or multi-photon microscopy are “infinity-corrected” which is to say that objects at the front focal plane produces collimated rays exiting the objective lens. The back focal plane of infinity corrected objective lenses are located within the objective lens itself. Because light exiting the objective does not focus at an image plane, infinity corrected lenses must be focused onto a sensor with a tube lens. The magnification specified on the objective lens is actually the ratio between the tube and objective lens' focal lengths (f_T and f_o respectively):

$$M = \frac{f_T}{f_O}$$

Objective lens manufacturers generally design objective lenses for tube lens of a standard focal length. Nikon, Mitutoyo, Thorlabs and Leica objective lenses are designed for tube lengths with a focal length of 200 mm. A 20x Nikon objective lens will therefore have a focal length of 200/20 = 10 mm. In comparison, Zeiss' tube lenses have a focal length of 165 mm and Olympus' tube lenses have a focal length of 180 mm. (Note that these values apply to microscope objectives. Objectives designed for wide-field or dissection scopes may have different tube lengths). The back pupil diameter (BPD) of an objective lens is given by:

$$BPD = 2 * NA * f_o = 2 * n * sin(\theta) * f_0$$

Furthermore, certain lens manufacturers such as Leica and Zeiss perform aberration corrections outside of the primary objective lenses, in conjunction with other optical components within the lens relay. Lenses from these manufacturers will be more difficult to substitute directly into and out of an existing design.

Fluorescence Microscopes

The optical layout of fluorescent microscopes can be separated into detection and excitation subsystems. The role of the excitation subsystem is to introduce light emitting the appropriate wavelength to the sample. The role of the detection subsystem is to collect the generated fluorescence and map it to a detector. Because fluorescence emission is isotropic, the excitation and detection subsystems may share optical components between them or be entirely de-coupled. This is in contrast to – for example – phase contrast or darkfield imaging systems in which the illumination and detection optics must achieve Köhler illumination in order to achieve the best performance (Chandler and Roberson 2009).

Widefield fluorescence microscopes bulk-illuminate the entire sample and map fluorescence back to the detector. These systems use lamps or LEDs which generate a broadband excitation spectrum, using interchangeable dichroic/excitation/emission filters to disambiguate signals from specific fluorophores. Unfortunately, while conventional wide-field microscopes can achieve resolutions on the order of 200-300 nm, they do not intrinsically provide optical sectioning – i.e. the ability to discriminate features at one depth plane from another. As a result, they are primarily suited to imaging flat, thin samples such as cells in culture or slide preparations. Thick samples imaged under widefield microscopes need to be fixed and sectioned into thin slices, which precludes attempts at imaging these tissues behaving organisms. Computationally intensive techniques such as deconvolution microscopy attempt to provide depth sectioning in widefield images by inferring the point spread function of the optical system and algorithmically reconstructing a 3D volume.

Existing approaches to functional, volumetric imaging

The Gold Standard

The most commonly used techniques for imaging fluorescence in thick biological samples are laser scanning confocal microscopy (LSCM) and multi-photon microscopy (MPM). These techniques use an objective lens to focus a laser beam of a given wavelength into a diffraction limited spot at the lens' focal plane. Fluorescence generated by this laser beam –

either via single-photon or multi-photon excitation processes – are then collected by the same objective lens and relayed onto a detector. Because confocal microscopy relies on a single-photon absorption process, laser excitation generates fluorescence both above and below plane being imaged. As a result, fluorescence must be de-scanned onto a point-detector. Optical sectioning is achieved via a pinhole placed before the detector that occludes fluorescence generated from above and below the focal plane. A pinhole with a smaller diameter can improve lateral resolution by up to a factor of $\sqrt{2}$ as well as achieve better background rejection, but will also significantly decrease the amount of SNR collected from the image.

In comparison, MPM relies on the simultaneous absorption of at least two photons by a single fluorophore in order to transition an electron from its ground to higher-energy state. Multi-photon absorption events are only achieved at areas of high photon densities, which are created through a combination of temporal compression using pulsed laser sources with high peak energies and low pulse widths (~100-150 fs), and high-NA lenses that are capable of generating tight focuses at the lens' focal plane.

With both techniques, an image is formed by sequentially scanning that spot throughout each pixel within the desired field of view (Pawley 1995). On standard commercially available confocal and two-photon systems, scanning of the beam through the focal plane (i.e. the XY plane) is achieved using two galvanometric mirrors that deflect an incoming laser beam along the orthogonal axes. Translating the focus of the beam along the third dimension (Z) is achieved either by translating the objective lens through a range of depths with a piezo-electric motor, or by translating the sample itself along this axis with a motorized stage.

Because the laser beam needs to sequentially visit each voxel of interest, point-scanning systems are bottlenecked by the maximum achievable speed of individual components (e.g.

galvo mirrors, piezo-scanners, stages, etc) and the amount of signal collected from the sample (Ji, Freeman et al. 2016). For example, imaging a field of view of 500 μm x 500 μm x 200 μm at modest rate of 10 volumes per second with an isotropic sampling density of 1 μm requires a sampling rate of 500,000,000 pixels/second. Two-photon microscopy techniques use pulsed laser sources that compress the photon density into an ~100-150 fs time period in order to achieve the requisite high photon-densities. The standard repetition rate of these pulsed lasers is 80 MHz (over 6 times slower than the required pixel rate). Even for confocal microscopy which does not require pulsed laser sources, image scanning is performed via two orthogonally-scanning galvo-mirrors translating the beam along a fast and slow axes respectively. The faster scanner would need to achieve a line rate of 500*200 = 100 kHz (close to an order of magnitude faster than high-speed resonant scanners available today) in order to achieve the imaging speeds high-lighted above. Scanning along the axial dimension (Z) is even further complicated by the need to account for the inertia of moving heavy lenses or sample rigs. Finally, even if a technical solution to each of these image-scanning bottlenecks is found, single-photon excitation processes are ultimately limited by the fluorescent lifetimes of available fluorophores (0.1 – 10 ns); the exposure time of a scanner operating at a 500 MHz pixel rate is 2 ns (Berezin and Achilefu 2010).

Parallelized Illumination Schemes

Over the past decade, a number of techniques have emerged that alter the excitation optics and scan patterns of conventional point-scanning modalities in order to address this limitation. Random-access-pattern scanning, for example, reduces the total number of voxels that need to be acquired by the system by only imaging pre-selected regions of interest within the sample (Grewe, Langer et al. 2010, Nadella, Ros et al. 2016). While this approach can permit sub-cellular imaging at kilohertz rates, it also relies *a priori* information and is therefore susceptible to motion artefacts in living samples. Furthermore, one may also miss important regions of interest during pre-selection especially with the development of low-background fluorescent calcium indicators such as GCaMP6 (Grewe, Langer et al. 2010, Chen, Wardill et al. 2013). Other methods create multiple foci in the sample (Watson, Nikolenko et al. 2009) or temporally multiplex laser pulses to image from multiple brain regions simultaneously (Cheng, Goncalves et al. 2011). Such multiplexing significantly increases the complexity of the imaging system. Furthermore, minimum pixel dwell times of approximately 0.1-1.0 µs per pixel (1.0–10 MHz) are required to achieve adequate SNR in most experiments (Ji, Freeman et al. 2016). Single point-scanning techniques, therefore, are presently an untenable solution for high-speed volumetric imaging of large volumes of tissue.

In order to reach the rates needed to – for example – image calcium activity in neuronal tissue (>5-10 Hz), optical imaging technologies have opted to sacrifice the high levels of sectioning achieved by single point-scanning methodologies in order to excite larger areas of tissue simultaneously. Spinning disk confocal microscopy, for example, simultaneously excites thousands of points within the sample and images the generated fluorescence onto a high-speed camera. Here, the acquisition time for a single plane is dictated by the camera frame rate. Similarly, line-scanning (or swept-field) confocal microscopes excite fluorescence over a line within the focal plane instead of just at a single point, de-scanning the fluorescence onto a line-detector. The overall acquisition speed of a line-scanning confocal microscope is dictated by the sampling rate of the line detector. In both of these systems, 3D imaging is again achieved via piezo-scanning the objective lens. While these systems are capable of providing diffraction limited resolution in thin samples, they suffer from two main drawbacks when applied to volumetric imaging. The first is that cross-talk between multiple points decreases contrast when imaging deeper within scattering tissue. The second is that these systems all excite fluorescence above and below the focal plane, and rely on occluding apertures in order to block unwanted fluorescence. As a result, when acquiring a volume with N depth planes, each plane is illuminated N times while only being imaged once. Remember that individual fluorescent molecules only emit a finite number of photons before entering a permanent dark state. The illumination paradigms of all confocal microscopes (single-point, spinning disk, line-scanning) needlessly waste this photon budget while risking damage to samples that are sensitive to high levels of laser light (eg. C. Elegans embryos, Schmidtea mediterranea, etc). See (Hillman, Voleti et al. 2018) for a more thorough discussion about the effects of scanning and illumination strategies on sample photobleaching.

Certain multi-photon techniques use axially extended beams to simultaneously image multiple depths at once (Lu, Sun et al. 2017) or use stereoscopic illumination strategies in order to infer depth information from 2D projections of the sample (Song, Charles et al. 2017). However, like random access pattern scanning approaches, these techniques assume that the sample has a degree of sparsity. Imaging of 3D activity along biological structures that exist along a continuum is therefore going to be challenging for these techniques.

Single Shot Volumetric Imaging Techniques

The examples discussed previously have used increasingly faster scanners or beamlet parallelization in order to improve imaging speed. In contrast, single-shot volumetric imaging techniques illuminate the entire sample and reconstruct an entire volume of data from a single camera frame. As a result, the volumetric acquisition speed is equivalent to the camera frame rate, and is not reliant on the inertial limitations of mechanical scanners. In principle, this is accomplished by introducing some optical element into the system that alters spatial intensity distribution of light on the sensor as a function of the object's position within the sample.

For example, light field microscopy places a lenslet array between the camera sensor and tube lens in order to acquire an extra dimension of information about the sample (Broxton, Grosenick et al. 2013, Prevedel, Yoon et al. 2014, Cong, Wang et al. 2017). Whereas conventional imaging systems only relay spatial information (i.e. *where* a feature is within the field of view), the lenslet array serves to project a mixture of spatial and angular information on the camera (i.e. *where* a feature is within the sample and the *direction* that the light takes when exiting the sample and impinging upon the sensor). However, it is important to note that the volume must be reconstructed from the raw data via computationally-intensive algorithms which can take hours to days in order to run. For example, the most recent implementation of a modified light-field microscope by (Cong, Wang et al. 2017) required 4 minutes to reconstruct a single 3D volume using a custom deconvolution algorithm with GPU-acceleration. The resolution achieved by this reconstruction is also dependent on the algorithms and structures being imaged. These reconstruction algorithms and the resolution of existing camera sensors are the key bottlenecks to such light-field techniques.

Light Sheet Microscopy

The first demonstration of light sheet-based illumination strategies was by Siedentopf and Zigmondy who develop the technique named Ultramicroscopy to analyze nanoparticles in glass and, later, in colloidal solutions (Siedentopf and Zsigmondy 1902). These particles did not absorb significant quantities of light and were only capable of being imaged through darkfield microscopy. By imaging the at an angle orthogonal to the direction of illumination, it became possible to reduce the amount of un-reflected illumination contributing to the image and visualize the particles with high levels of contrast.

The de-coupling of the excitation and detection subsystems introduced by the ultramicroscope did not make its way into biological research until the increased adoption of fluorescent indicators in the early 1990's and 2000's (Voie, Burns et al. 1993, Huisken, Swoger et al. 2004). Conventional light sheet fluorescence microscopes (LSFMs) consist of two orthogonally aligned optical trains: one which generates a sheet of laser light within the sample, and another which images fluorescence generated by this sheet onto a detector using a well corrected microscope objective. Because fluorescence is only generated at the focal plane of the objective lens, light sheet illumination is inherently depth-sectioning. A 3D volume is then formed by physically translating or rotating the sample through the co-aligned light sheet, or by translating the sheet through the sample and tracking its motion with the detection telescope. As a result of this volume acquisition strategy, biological tissue can be imaged in toto without an implicit need for sample sparsity.

By parallelizing the acquisition of every pixel within a single plane, sheet-based illumination strategies can achieve pixel-rates that are orders of magnitude higher than point-scanning methodologies over the same fields of view while using exposure times that are orders of magnitude longer than conventional point-scanning techniques (1-100 ms vs 1-10 µs). Lower laser irradiance densities can therefore be used to illuminate the sample. As a result, light sheet microscopes can not only image the sample at higher frame rates than point-scanning methodologies with nearly equivalent SNR, but also subject delicate samples to lower levels of photobleaching and phototoxicity (Hillman, Voleti et al. 2018).

However, the orthogonality requirement of conventional LSFMs means that sample geometries are highly restrictive, often requiring embedding or specialized sample mounting procedures to enable proper illumination, immersion and repositioning of the sample (Schmied and Tomancak 2016). As a result, early implementations of light-sheet microscopy have either focused on imaging small, cylindrical samples that can be embedded in agarose, or large volumes of cleared tissue through which laser excitation can deeply penetrate. Examples of such implementations are shown in **Figure 1.5**. Switching between different samples or experimental preparations in these systems would require one to use completely different light sheet systems. Furthermore, 3D imaging in many of these systems involved moving the sample through a stationary light sheet requiring seconds to minutes in order to acquire a single volume. Functional imaging with early light-sheet microscopes focused on long-term developmental imaging, or restricted high-speed functional experiments to single plane acquisitions (Holekamp, Turaga et al. 2008, Keller, Schmidt et al. 2008, Tomer, Khairy et al. 2011). More recent systems translate the sheet through a stationary sample using galvo-scanning and track the motion of the sheet by piezo-scanning the detection objective achieving volume rates on the order of 1-5 Hz, however even these systems are ultimately limited by the inertia of large, heavy objective lenses (Ahrens, Orger et al. 2013, Lemon, Pulver et al. 2015).

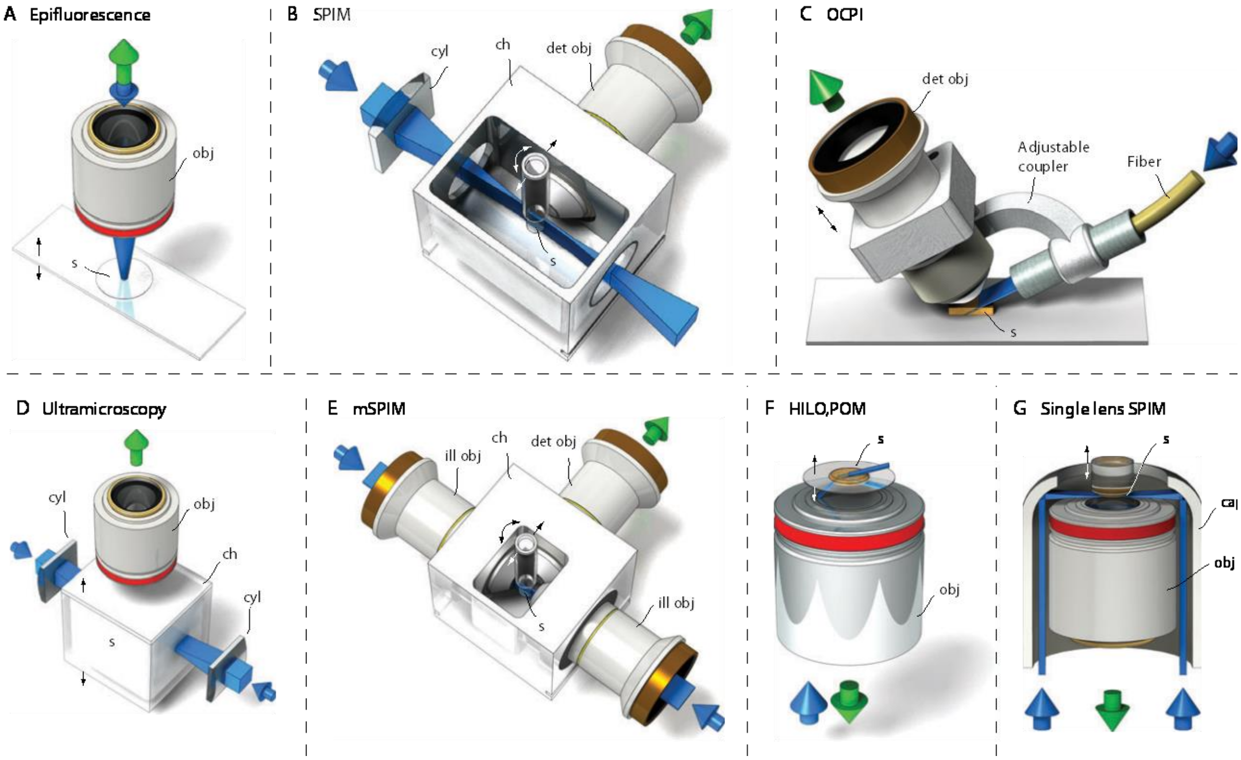

Figure 1.5: *Different variants of light sheet microscope geometries*
These systems accommodate a number of different sample geometries. Blue arrows represent incoming laser excitation (conventionally ~488 nm to excite GFP-based fluorophores) and green arrows represent collected fluorescence. Figure adapted from (Huisken and Stainier 2009)

There exist a wide range of applications that could benefit from the low phototoxicity and high throughput of light-sheet imaging. Understanding the influence of cellular processes on organ/organism-wide behavior requires increasingly sophisticated experimental setups. For example, additional equipment such as cameras can monitor animal position, health and reactions to stimuli in real-time; a number of research groups have made a great deal of progress in this direction in recent years (Robie, Seagraves et al. 2017, Thouvenin and Wyart 2017). As the scope and complexity of these experiments steadily increase to involve not only monitoring biological systems - but the real time manipulation of the same – imaging systems need to be capable of sharing the area surrounding the sample with other instrumentation such as electrodes, VR rigs, stimuli, behavioral tasks and more. However, many of the systems shown in **Figure 1.5** would be unable to image something as commonplace as a piece of tissue resting on a microscope slide.

Microscopy techniques such as point-scanning or bright-field microscopy perform all of their imaging through a single objective lens, and in so doing afford the experimentalist a great deal more flexibility in this regard. Over the past decade, a small subfamily of imaging techniques has formed which utilize light sheet illumination strategies while both illuminating and imaging the sample through the same objective lens. I have attached a review of these techniques at the end of this thesis (see Appendix F) cataloging the members of this family, their general design principles and the applications they have thus far addressed. SCAPE is one among that family.

Chapter 2 - Development of Swept Confocally Aligned Planar Excitation Microscopy

During my graduate work, I developed SCAPE microscopy in several stages iterating over at least 6 separate physical systems constructed over a 5-year period. The work presented within this chapter describes the lifetime of that development. I take the reader through major optical engineering and system parameter questions that were addressed between the first generation of SCAPE (SCAPE1) to the second (SCAPE2) which allowed the latter to become a workhorse system within our lab. Some examples in the zebrafish brain, drosophila and mouse brain resulting from this work are presented.

First Generation SCAPE Microscopy (SCAPE1.0)

Swept, confocally-aligned planar excitation microscopy is a high-speed fluorescence imaging technique capable of acquiring 3-dimensional images of large fields of view (~0.5 – 1 mm) at rates exceeding 20 volumes/second. By inserting a beam of laser light off-axis onto the back aperture of a high-NA objective lens, an angled sheet of laser excitation is produced within the sample. Fluorescence generated by this sheet within the sample is then collected by the same objective lens and then relayed onto a conjugate image plane, which is then imaged onto a camera chip. SCAPE merges the excitation and detection pathways of the system through a single objective lens, providing the benefits of sheet-based illumination strategies discussed in the previous section while maintaining an *en face* imaging geometry similar to confocal or two-photon microscopy. This innovation addresses the access problem faced by most light-sheet

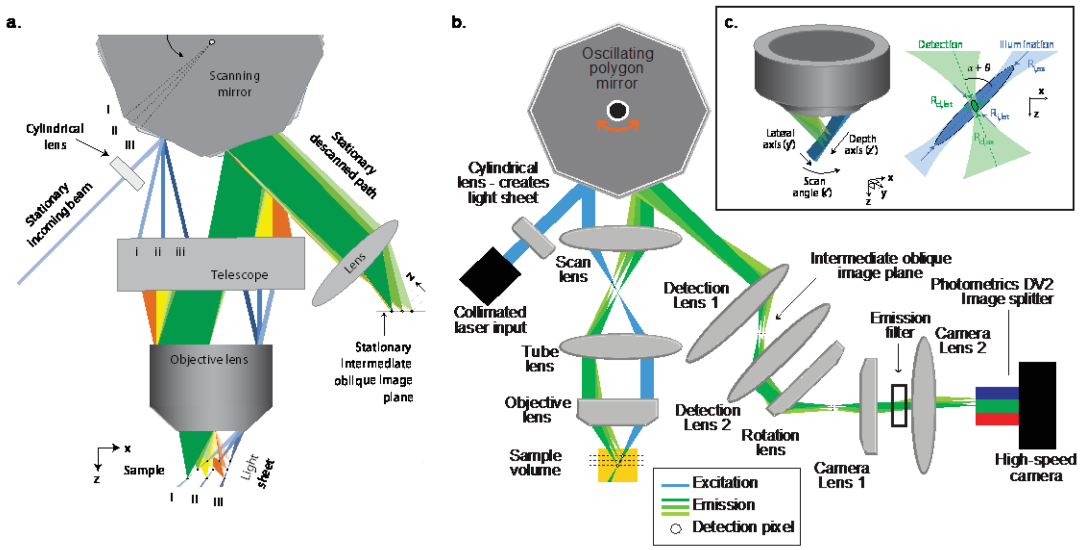

***Figure 2.1**: Explanation of SCAPE1*
***a.** Scanning a laser beam off facets of a polygonal mirror scans the beam within the sample. An adjacent facet of the mirror de-scans fluorescence onto a conjugate image plane **b.** Full system schematic of SCAPE1 consisting of three telescopes. The scan telescope (scan lens, tube lens, objective lens) and detection telescope (detection lens 1, 2 and rotation lens) work together to create a conjugate image of the light sheet within the sample. An obliquely aligned camera telescope maps this conjugate image plane onto a camera sensor **c.** (Left) Close up of the imaging geometry defining the axis of the coordinate space. The y-axis travels laterally along the length of the sheet, the z'-axis travels along the propagation direction of the sheet, and the x'-axis is the axis along which the sheet sweeps through the sample (Right) Orientation between the light sheet shown in blue and the cone of detection shown in green defines the overall point spread function of the system.*

microscopes and provides a workspace surrounding the primary objective lens that allows for far more versatile experimental design.

In its initial implementation, volumetric imaging on SCAPE1 was achieved by bi-directionally scanning laser light off of one facet of a 12-sided polygonal mirror, which in turn swept the angled light sheet through the sample (Bouchard, Voleti et al. 2015). Fluorescence generated by the sheet traveled back through the same optical path and was then de-scanned off of the adjacent facet of the polygonal mirror (**Figure 2.1**). Because the same polygonal mirror both scanned excitation and de-scanned the generated fluorescence, any fluorescent intermediate image planes generated after the polygonal mirror would be stationary. In SCAPE1, the scan telescope (scan lens, tube lens, objective lens) and detection telescope (detection lens 1, 2 and rotation lens) had identical magnifications. The scan lens and detection lens 1 were 1'' diameter, 50 mm focal length achromatic lenses (*Thorlabs, AC254-050-A*), while the tube lens and detection lens 2 were 2’’ diameter, 100 mm focal length achromatic lenses (*Thorlabs, AC508-100-A*). The objective lens and relay lens were an Olympus 20x/1.0NA water immersion and Olympus 20x/0.75NA dry lens respectively. A conjugate image of the angled light sheet was then mapped using an obliquely aligned camera consisting – at minimum – of an objective lens (Olympus 10x/0.30NA) and tube lens (*Thorlabs, AC254-075-A*) onto the camera (**Figure 2.1**b).

By synchronizing the acquisition of the camera to the polygonal mirror’s motion, sequential frames capture planes in an oblique X-Z dimension (see **Figure 2.1**c for the imaging geometry). Reconstruction of a fully depth-resolved volume is achieved simply by reshaping the sequence of frames collected in the proper order. Because frames are acquired both on the forward and backwards sweep of the scanner, the volume rate of the system is equivalent to twice the line-rate of the scanner. If the galvo scans at 10 Hz, the volume rate of the system is 20 volumes/sec.

SCAPE1 used the Andor Zyla 5.5, a high-speed, high-sensitivity scientific CMOS (sCMOS) camera for its acquisitions. The sheet dimension that encodes depth into the sample (Z) corresponds to rows on the camera while the length of the sheet (Y) corresponds to columns. Commercially available sCMOS cameras achieve their high frame-rates via a rolling shutter coupled with an “overlap read-out” exposure. What this means is that each frame acquisition begins by exposing the rows in the center of the camera chip, followed by the rows adjacent and so on until the outer-most rows have finished exposing. Acquiring fewer rows or depths on the camera allows one to acquire at higher frame rates. Therefore, the camera frame rate, the field of view over which the polygonal mirror scans and the sampling density along that field of view determine the achievable volumetric imaging speed of the system:

$$Volume\ Rate = \frac{Camera\ Frame\ Rate\ (fps)}{Scan\ FOV,\ X\ (\mu m)} * Scan\ Step\ Size, X\ (\mu m)$$

Second Generation SCAPE Microscopy (SCAPE2)

The first generation SCAPE system published by (Bouchard, Voleti et al. 2015) served as a proof-of-principle for the potential applications of light-sheet based illumination strategies to imaging challenges facing the neuroscience community. Its en-face geometry allowed access to a wider variety of samples of samples than conventional light sheet microscopes, while the confocal scanning-descanning paradigm elegantly addressed bottle-necks in volumetric imaging speed faced by systems reliant on piezo-scanning or sample translation.

However, a number of key issues needed to be addressed in order to turn SCAPE into a workhorse system for daily use within the lab:

1. Optimize the scanning and de-scanning volume acquisition paradigm for SCAPE
2. Improve the light sheet parameters within the sample
3. Improve system uniformity over the field of view
4. Improve light collection efficiency
5. Create metrics for system characterization
6. Create a formalized alignment protocol

In this chapter, I will describe my work in addressing each of these issues and present the resulting systems. Note that this work actually spanned the construction of two separate designs systems. I will use the term SCAPE2 when referring to them collectively, SCAPE2a when referring to the first system and SCAPE2b when referring to the second, more advanced system.

Volume Acquisition via Confocal Scanning/Descanning

One of the key ideas driving SCAPE microscopy is that confocal scanning and de-scanning can be extended beyond simple point-by-point imaging. Previous implementations of confocal scanning and de-scanning paradigms that image areas larger than a single point at a time do exist, but are regardless invested in fluorescence generated at the focal plane of the primary objective lens. For example, both swept-field confocal microscopy or confocal theta line-scanning microscopy excite and scan a line of fluorescence across the objective lens' focal plane, subsequently de-scanning the resultant fluorescence onto a line-detector (Dwyer, DiMarzio et al. 2006, Dwyer, DiMarzio et al. 2007). Laminar optical tomography excites and scans a point of laser excitation across the lens' focal plane, and de-scans a linear field of view surrounding that point onto a linear or planar detector. This linear/planar detection provides information about diffuse backscattering and absorption events within tissue that then facilitates reconstruction of structures across a range of depths into the sample (Hillman, Boas et al. 2004, Burgess, Bouchard et al. 2008).

However, in order to truly benefit from light-sheet illumination strategies, SCAPE needed to collect fluorescence from planes above and below the focal plane, as well as the focal plane of the lens itself. The design for the scan-engine of SCAPE1.0 was modeled closely on that of line-scanning, confocal-theta microscopy (Dwyer, DiMarzio et al. 2006, Dwyer, DiMarzio et al. 2007, Bouchard 2014). Here, one facet of a polygonal mirror surface is used to scan the excitation laser beam through the sample while an adjacent facet de-scans the fluorescence generated by the sample onto a stationary conjugate image plane. As a result, the reflective surface did not lie on scanner's axis of rotation. Only a fraction of the primary objective lens' back pupil was utilized for imaging and two separate fractions of the back pupil were utilized for excitation and detection respectively.

Scanning with a Polygonal Mirror

I created two system models of SCAPE1.0 using Optalix-PRO, an optical design software, in order to validate whether the polygon-based scan engine was capable of scanning and de-scanning a sheet that spanned an extended z-range within the sample. Note that this initial validation occurred on models describing SCAPE1.0 and the results were published in the supplementary methods of (Bouchard, Voleti et al. 2015). The two models described the system's excitation and detection paths respectively shared the polygonal scanner and scan telescope (i.e. the primary scan (S1), tube (T1) and objective (O1) lenses). **Figure 2.2**a,d combine the excitation and detection models into a joint schematic.

The excitation path consisted of a 488/532/635 nm laser passing through a 3-part cylindrical lens telescope (CL1, CL2 and CL3), reflecting off of the left-hand facet of the polygonal mirror, entering the scan telescope and passing through the primary objective lens (O1) into the sample. The polygonal mirror was rotated through a range of angles about its axis of rotation to simulate scanning the laser beam through the sample. The excitation model outputted ray-tracing information containing the lateral position, x_i, of the laser at the objective lens' focal plane and sheet angles, α_i, for the central ray within the sample at each of the polygonal angles, θ_i. **Figure 2.2**b shows the central ray of the laser beam scanning over a 5 mm range in x. The angle of sheet, α, depicted through color. The focal plane of the objective lens rests at $z = 0$ mm and the optical axis of the scan telescope lies at $x = 0$ mm.

The detection path modeled fluorescence emitted from a point source within the sample traveling back through the scan telescope (S1, T1 and O1), reflecting off of the opposing facet of the polygonal mirror, entering the detection telescope (consisting of secondary scan (S1), tube (T2) and objective (O2) lenses) and creating a conjugate image of the emitter near the focal plane of the secondary objective lens (O2). The fluorescence was modeled using the same laser lines in the excitation path, which broadly sampled the emission spectra of green and red fluorophores and the location of the conjugate image was determined by minimizing the spot size of the point emitter.

The distance between S1 and T1, S2 and T2, and CL1 and CL2 were set to the sum of the focal lengths of each lens pair. If the resting position of the polygonal mirror existed at $\theta_i = 0^\circ$, then the scan telescope was positioned such that its optical axis lay directly on the line connecting the scanner's rotational center to one of the polygon's vertices. The cylindrical lens and detection telescopes were positioned such that they were perpendicular to the polygonal mirror's facets. When using a 12-sided polygonal mirror, the 3 telescopes are oriented 30 degrees from one another.

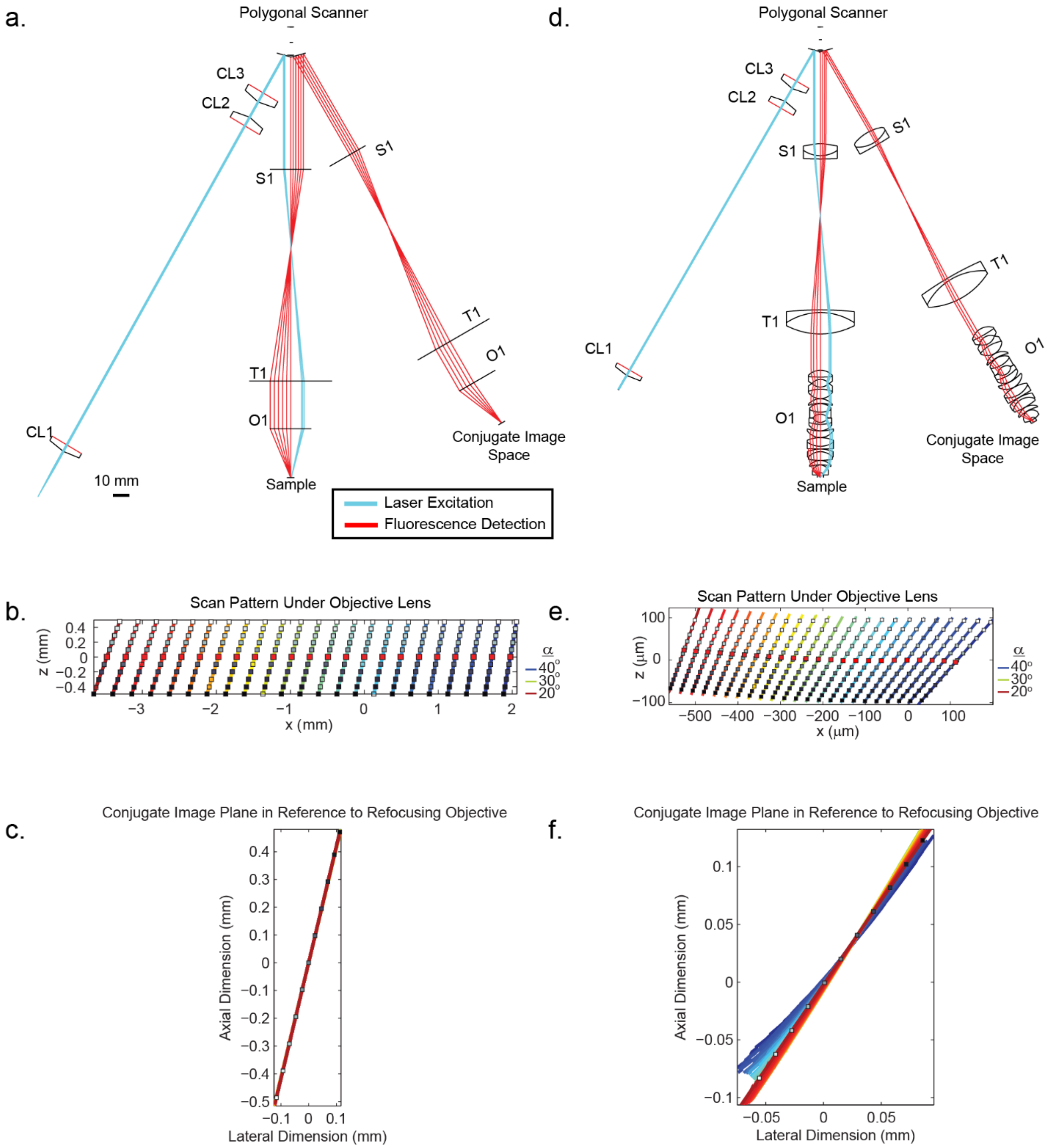

***Figure 2.2:** Scanning and de-scanning with a polygonal mirror in SCAPE1.0.*

*The excitation pathway consisting of a low-numerical aperture laser beam is shown in blue while the detection pathway is shown in red **a.** Layout of optical pathway containing the ideal or thin lenses used in SCAPE1.0. **b.** Simulation of the scan pattern made by the light sheet within the sample **c.** Points remapped from the light sheet shown in (b) into the conjugate image space referenced in (a) **d-f.** The same model as shown in (a-c) except that the thin lenses are replaced with the achromats specified in Appendix E. Figure is adapted from (Bouchard, Voleti et al. 2015)*

The excitation and detection models were coupled together using a custom macros written in Optalix-PRO and Matlab. The excitation model iterated over a range of polygonal rotation angles, θ_i, and extracted the position, x_i, of the sheet at each of these angles at various depths, z_i, within the sample spanning +/- 500 µm around the focal plane of the objective lens. The grey dots in **Figure 2.2**b correspond to equidistant points along the extent of the sheet whereas the red dots correspond to the z-plane at which the sheet achieved its best focus for a particular polygon position. The set of locations, x_i and z_i, and their corresponding polygon angles, θ_i, were fed into the detection model and corresponding positions of best focus found within the conjugate image space. The rotation of these angles within the excitation model, and subsequent usage of the same angles within the detection model is, in practice, equivalent simulating confocal scanning and de-scanning with SCAPE. **Figure 2.2**c shows to the remapped positions of all points, x_i and z_i, into the conjugate image space. As can be seen, the lateral or “x” positions of the sheet at any polygonal rotation angle (shown in **Figure 2.2**b) are all mapped to the same lateral position within the conjugate image space. This re-mapping is valid over the full range of depths investigated, proving that confocal scanning and de-scanning is achieved a) over complete volumes, b) using a polygonal scanner, and c) while the excitation and detection paths utilize different fractions of the objective lens’ back pupil.

I repeated this modeling replacing the thin lenses shown in **Figure 2.2**a with the real achromatic lenses used to construct the SCAPE1.0 system in (Bouchard, Voleti et al. 2015). The lenses used for this system are found in Appendix E. The primary objective lens was an Olympus XLUMPlanFl N 20x/1.0NA with a working distance of 2 mm and a back focal diameter of 18 mm (Kasahara 2002). The scan telescope was set to a magnification of 2x. The relative locations of the polygonal mirror and cylindrical lens telescope was adjusted in order to position the laser beam at the edge of the primary objective lens' back aperture. The detection telescope was replicated to match the scan telescope exactly. The distance between each of the scan lenses (S1, S2) and the objective lenses (O1, O2) were adjusted such that the polygonal mirror scanned onto the back aperture of the objective lens using the following equation (Tsai, Nishimura et al. 2002):

$$d_1 = \frac{f_1^2}{f_2} + f_1 - d_3\left(\frac{f_1}{f_2}\right)^2$$

In which f_1 and f_2 were the focal lengths of the scan (S_1, S_2) and tube (T_1, T_2) lenses, d_1 is the distance from the scan lens to the scanning face of the polygonal scanner, and d_3 is the distance between the tube lens and objective lens back aperture. Here it is assumed that the distance between the scan and tube lenses is equal to the sum of their focal lengths. This equation effectively maps the scanner onto the back focal plane of the objective lens. As can be seen in **Figure 2.2**e, rotating the polygonal scanner still translates the sheet through the sample, with the sheet angle, α, steadily changing as a function of scan position. De-scanning points along the sheet as described previously also results in a relatively stationary de-scanned plane (**Figure 2.2**f). This model further validates that the confocal scanning and de-scanning imaging paradigm is valid over the conditions previously described, even when using real lenses.

However, there are a number of caveats that need to be addressed here. The first is that in addition to sheet angle variation over the scan range, the location of the sheet's best focus – as indicated by the red dots in **Figure 2.2**e – is far less variable when using thin lenses (**Figure 2.2**b). This is indicative of the presence of field curvature within the scanning system. Secondly, the re-mapping of scanned points into conjugate image space degrades as a function of distance from the focal plane which is indicative of distortion within the optical system. Finally, the magnification of the scan telescope from the polygon to the back aperture of the primary objective lens was set to be 2x in order to translate a narrower angular rotation of the polygon into a proportionally larger scan range within the sample. As a result of this 2x magnification, the back aperture of the Olympus 20x/1.0NA lens was mapping back onto the galvo mirror as a 9 mm pupil. Half of this pupil was lost to the polygonal facet facing the cylindrical lens.

Moving from a Polygon to Planar Mirror

The move from polygonal scanning to planar mirror scanning was in large part motivated by practical difficulties in system construction. SCAPE1.0 consisted of 3 co-aligned optical telescopes that radiated outwards from the rotational axis of the 12-sided polygonal scanner. Each of these telescopes needed to point precisely at the scanner's center of rotation and be offset by 30 degrees from one another in order to be co-aligned to one another. Not only did this significantly complicate the alignment of the system, but it unnecessarily placed limitations on the size of optomechanical components placed closest to the scanner. For example, the scan lens and detection lens 1 in **Figure 2.2**a could not be placed closer to the scanner or be replaced with 2'' diameter lenses because they would collide with one another. Furthermore, the usable height of the polygonal mirror facet was only ~9.4 mm. As a result, the height of the 9 mm image of the primary objective lens' back pupil needed to be very precisely aligned to the height of the mirror, further complicating system construction.

In order to simplify system design, SCAPE2's scan engine was based more closely on that of a standard confocal microscope (**Figure 2.3**a). The multi-faceted polygonal mirror was replaced by a single planar front-facing mirror with a 14 mm face. This allowed the scan and detection telescopes to be oriented at 90 degrees from one another. The excitation and detection paths were separated by a dichroic mirror, though were technically also at 90 degrees from the other telescopes. This new orientation allowed for each telescope to be designed independently of the other two without needing to account for spatial limitations between optical components.

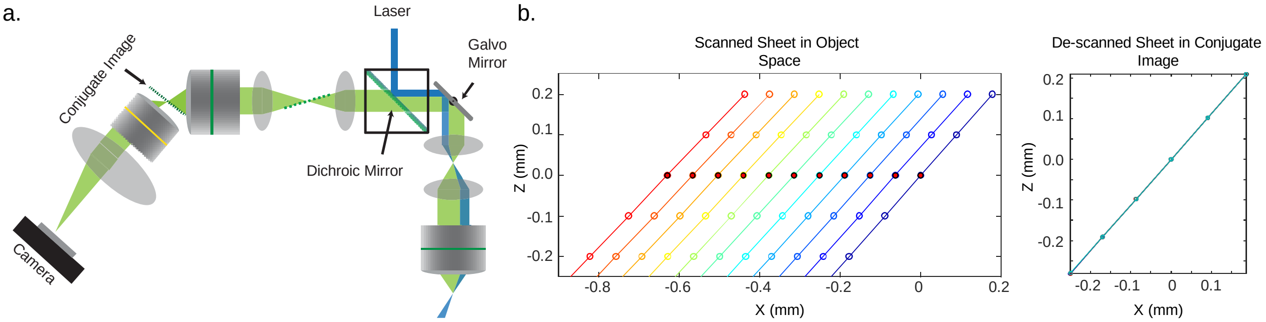

Figure 2.3: *Scanning and de-scanning with a planar mirror in SCAPE2*
a. *Schematic of SCAPE2 built with galvo mirror and dichroic mirror based on confocal microscopy* ***b.*** *Theoretical model of sheet being scanned in the object and de-scanned in the conjugate image space, modeled with Optalix-PRO*

Furthermore, the polygonal mirror was heavy and could only be scanned at a maximum line rate of 100 Hz, though in practice this line rate was limited to 10-20 Hz. In comparison, the planar mirror could be easily be scanned at line rates upwards of 1 kHz, opening up the possibility of performing volumetric imaging 10-100x faster faster than SCAPE1.0.

The excitation and detection models in Optalix-PRO were re-created for the orthogonally-aligned, planar-mirror based geometry using thin lenses. Results confirmed that confocal scanning and de-scanning would also work when using planar mirrors (**Figure 2.3**b).

Improving Scan Uniformity

As can be seen in **Figure 2.2**e, the scan angle of the light sheet changes as a function of its position within the sample. This is a major problem when trying to do quantitative analysis of any kind as it implies that the sampling density along the X direction changes over the field of view, and does so in a way that varies with the depth plane being imaged. This can result in erroneous results when attempting to measure the distance between two samples, or even distort the signal emitted by a continuous structures such as dendrites or cell bodies.

I hypothesized that this effect was due to the under-utilization of the primary objective lens' back pupil plane. For objective lenses, the back pupil plane and the back focal plane are equivalent, and are location within the objective lens itself at a location separate from the lens' back aperture. Scanning telescopes (consisting of a scanner, scan lens, tube lens and objective lens) in confocal and two-photon microscopy generally tend to map the scanner onto the back aperture of the objective lens, which was the strategy followed by SCAPE1.0.

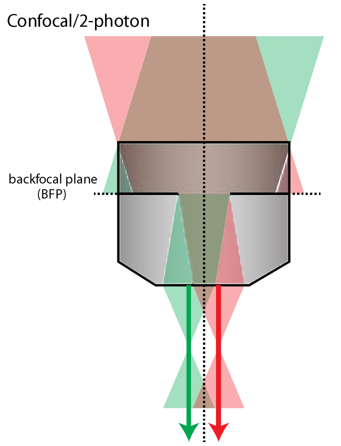

Figure 2.4: *Telecentric imaging Overfilling and scanning on the back aperture of the objective lens with confocal and two-photon microscopy. Colors represent different scan angles. Note how the chief ray (shown as an arrow) propagates through the center on the back focal plane in both cases.*

Confocal and two-photon microscopes can be constructed this way because both techniques increase the size of the laser beam in order to overfill the back apertures of the objective lens. This is done in order to minimize vignetting while scanning over the field of view. Confocal microscopes can overfill the back aperture by as much as a factor of 2x in order to accommodate the magnifications of different objective lenses that are all used on the same system. The back pupil diameters of various objective lenses are dependent on the lens' focal length and numerical apertures. Therefore, one can presume that there are stops within the lens that limit the back pupil diameter of the lens to a specified value. By overfilling the back aperture of the objective lens, one presumably fills the back focal plane with light as well, and so this configuration implies an equivalency between scanning on the back focal plane and back aperture of the objective lens. By scanning on the back focal plane of the objective lens, the cone of light generated by the confocal or two-photon microscope's scan engine travels parallel to the optical axis at every point in the scan, a phenomenon known as object space telecentricity (**Figure 2.4**)

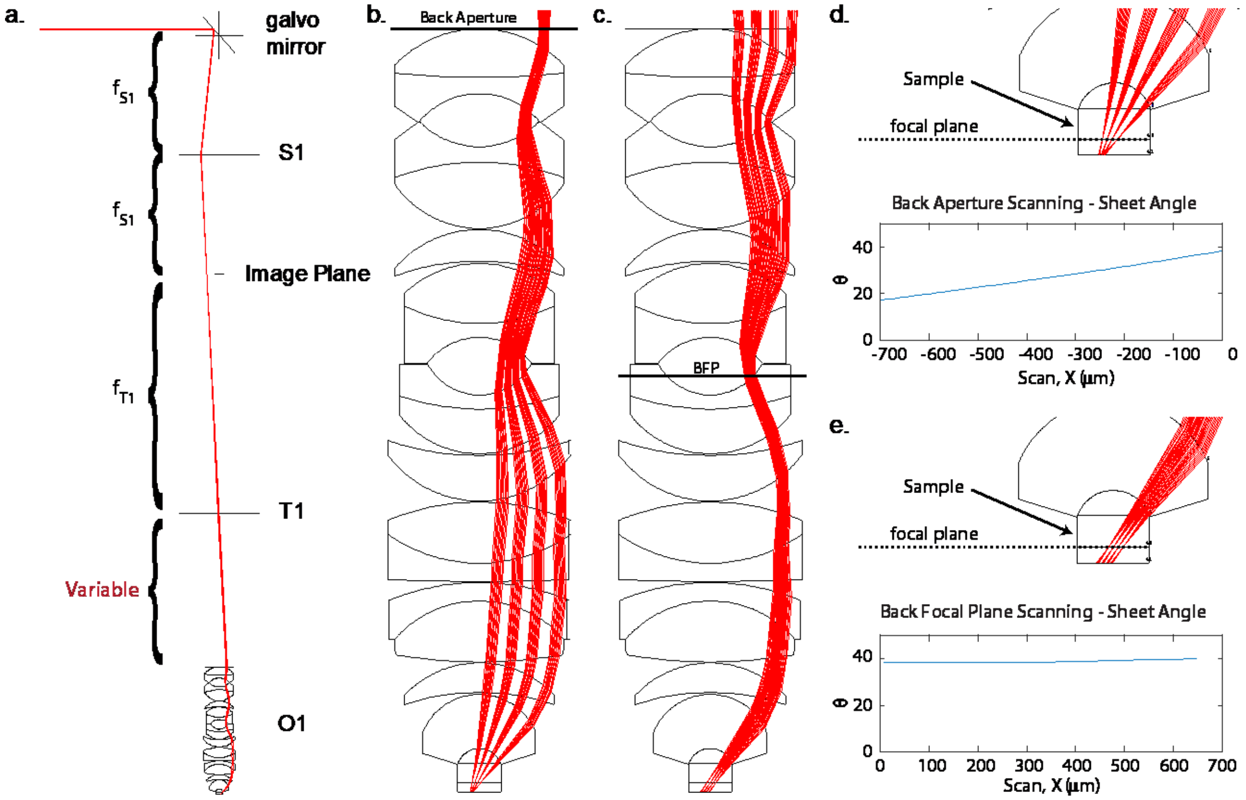

***Figure 2.5:** Determining the location of the galvo scanner's conjugate image*
***a.** Schematic of entire model of the scan lens telescope (Scan Lens, S1: 75 mm; Tube lens, T1: 150 mm, Objective Lens, O1: Olympus 20x/0.95NA W) **c.** Schematic of objective lens in model wherein the galvo mirror is mapped to the back aperture (marked by a flat plane) at the back of the objective lens. The red rays indicate the laser beam along the XZ dimension at four mirror angles **c.** Schematic of objective lens in model wherein the galvo mirror is mapped to the back focal plane of the objective lens **d.** Close up of the objective lens near the sample showing the effect of the laser beam scanning on the back aperture. Graph shows how the sheet angle with respect to the optical axis of the objective lens varying (Θ) as a function of the sheet's position within the sample along the X dimension **e.** Close up of sample with the galvo scanning along the back focal plane and plot of sheet angle remaining relatively stationary over a 600 µm scan range.*

In SCAPE, however, because the light sheet does *not* overfill the back aperture of the objective lens, scanning onto the back aperture will result in the laser beam utilizing different regions of the lens' back focal plane at each position in the scan. The back pupil diameter equation can be re-organized into the following equation relating the offset of the beam from the optical axis at the back focal plane, dx_{BFP}, to the angle of the beam within the sample, α:

$$\alpha = \sin^{-1}\left(\frac{\mathrm{dx}_{BFP}}{2f_o n}\right)$$

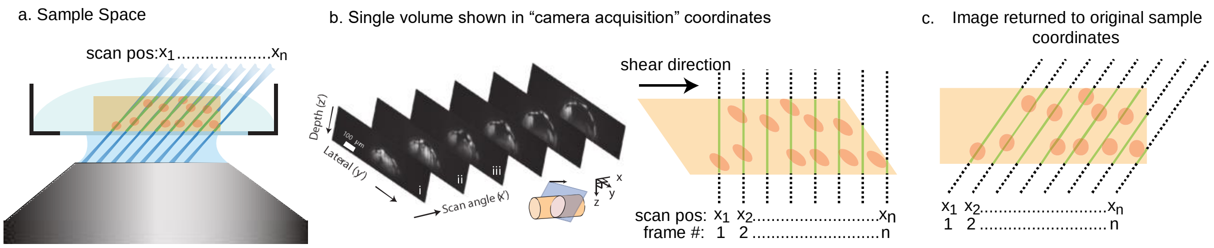

Figure 2.6: *Acquisition of a volume with SCAPE microscopy*
a. *Galvo scanning through an arbitrary sample results in oblique sections acquired through the sample. Each section is captured on a camera frame* ***b.*** *The camera outputs this data in its own coordinate space, not taking into account the angle of the light sheet. This causes a smearing of features along the XZ dimension that can result in errors in downstream image processing algorithms* ***c.*** *When scanning on the back focal plane, a shear transform along the XZ plane is all that is necessary to remap the data from "camera acquisition" coordinates back into sample coordinates. Triangles represent zero-padded areas at the edge of the scan.*

To test this hypothesis, I modeled two separate cases. One in which the scanning mirror was mapped onto the back aperture, and another in which it was mapped to the back focal plane of the Olympus 20x/1.0NA lens. A range of scanner angular positions were simulated. The distance from the scanner's axis of rotation to the scan lens was set equivalent to the scan lens' focal length. The distance between the scan and tube lenses was set to the sum of their focal lengths. The distance from the tube lens to the objective lens was variable (**Figure 2.5**a).

By setting the distance from the tube lens, T1, to the back aperture of the lens equivalent to the focal plane of the tube lens, f_{T1}, the mirror scans onto the back aperture of the objective lens (**Figure 2.5**b). In this case, I find that the angle of the light sheet with respect to the optical axis of the objective lens, Θ, changes over the course of a 600 µm scan range (**Figure 2.5**d).

The back focal plane of the Olympus 20x/0.95 NA lens was determined by directing collimated light into the front aperture of the lens (nearest to the sample) and calculating the focal point of convergence of rays exiting the back aperture. By setting distance from the tube lens, T1, to the back focal plane (BFP) of the objective lens as equivalent to the focal plane of the tube lens, f_{T1}, we map the scanner onto the BFP of the lens (**Figure 2.5**c). In this case, the sheet angle remains relatively constant over the course of the scan, addressing a major source of non-uniformity over the field of view (**Figure 2.5**e).

A further benefit to mapping the scanner onto the primary objective's back focal plane is the ease with which the data could be transformed back into its original coordinates. Recall that rows along the camera chip correspond to depth within the sample. Because SCAPE1.0 scanned on the back aperture of the system, the same row corresponded to different depths as the sheet scanned through the objective lens. Re-mapping this non-uniform scan field back into the standard cartesian space would require in-depth knowledge about the scan pattern, and a computationally intensive transformation function. The data presented in (Bouchard, Voleti et al. 2015) was therefore represented in "camera acquisition coordinates" i.e. the x-coordinate simply represented the index of the frame captured within a single volume. In next-generation SCAPE systems, volumes are acquired by scanning on the back focal plane and can be transformed back into "sample coordinate space" by simply shearing the volume along the X dimension (**Figure 2.6**). The degree of shear is determined by a single measurement of the sheet angle within the sample and the retransformation into "sample space" is now implemented as part of a pre-processing pipeline as an affine transform within the XZ plane. Note that this de-skewing more faithfully represents the structure of the sample being imaged, but may result in an unnecessary increase in data size due to zero-padding at the edges of the field of view. De-skewing may not be strictly necessary for all data analysis applications.

Optimizing the Lens Train

I created an optical model of the entire scan telescope including the galvo mirror, scan lens, tube lens and objective lens to assess how the location of the sheet waist changes as a function of scan angle. Ideally, the sheet waist should remain locked at the objective focal plane regardless of the scan angle. By using a 9 mm thin lens approximation to model the 20x/1.0NA

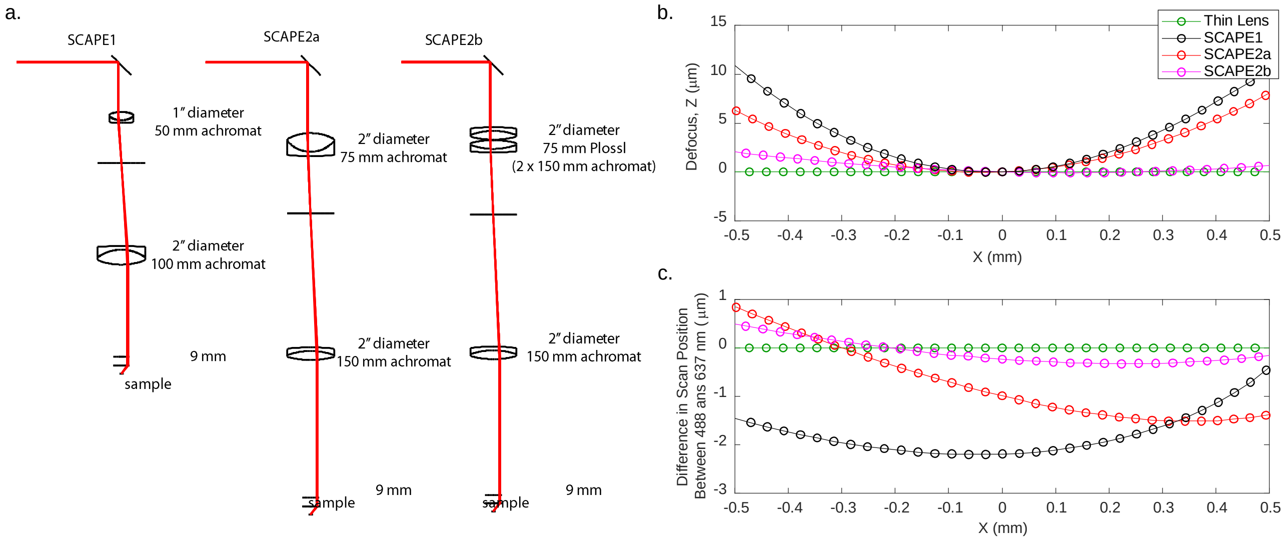

***Figure 2.7**: Modeling the performance of the scan telescope*
***a.** Schematics of scan telescope models for SCAPE1, SCAPE2a and SCAPE2b **b.** Field curvature of a 488 nm laser beam as a function of scan position within the sample over a +/- 500 µm scan range **c**. Chromatic aberrations of visible laser lines as a function of scan angle evaluated as difference in scan position between 488 nm and 637 nm over a +/- 500 µm scan range.*

objective lens, I was able to simulate the contributions to field curvature and chromatic aberrations arising specifically from the scan and tube lens. Note that a thin lens approximation is more valid for objective lenses made by specific manufacturers such as Olympus and Nikon which perform aberration corrections entirely within the objective lens body.

I modeled 3 laser lines (488, 561 and 637 nm) over a range of galvo scan angles using the scan and tube lenses of SCAPE1, SCAPE2a and SCAPE2b (**Figure 2.7**a). SCAPE1.0 originally contained a 50 mm scan lens and 100 mm tube lens (Thorlabs, *AC254-050-A* and *AC508-100-A* respectively). I optimized the scan telescope by replacing the scan lens and tube lenses with a 75 mm achromat (*Edmund Optics, 49-292-INK*) and 150 mm achromat (*Edmund Optics, 49-285-INK)* for SCAPE2a. Note that simply by using the planar mirror configuration we were able to use a 2'' diameter scan lens, which would not have been possible given the limited space near the polygonal scanner. In SCAPE2b, I replaced the 75 mm achromatic scan lens with a 75 mm

Plössl lens, a commonly used and easy to implement multi-lens configuration consisting of two 150 mm achromat lenses (*Edmund Optics*, *49-285-INK*) placed adjacent to one another (Negrean and Mansvelder 2014).

The SCAPE1 configuration showed more than a 10 µm defocus over a +/- 500 µm scan range at 488 nm (**Figure 2.7**b). In comparison, the SCAPE2b configuration brought this level of field curvature down to ~ 6 µm, while the addition of the Plössl lens further reduced field curvature to ~ 2 µm. I also evaluated the chromatic aberrations expected of different laser lines (**Figure 2.7**c) which shows the difference between the focal positions (in the X-dimension) of sheets made with 488 nm and 637 nm laser lines. In comparison to SCAPE1 and SCAPE2a, SCAPE2b – variants of which are now implemented with a combination of 488, 561 and 637 nm lasers – shows less than a 0.5 µm separation between these two laser lines over the entire scan range. Note that this assumes perfect alignment of the lasers as they enter the scan telescope which may not necessarily be the case if the laser lines are combined via free-space alignment.

Optimizing the Scan Waveform

Finally, the last source of scan non-uniformity stemmed not from the optical arrangement of the scan telescope, but through an interaction between the scan waveform and the rolling-shutter acquisition scheme of the sCMOS camera (Andor Zyla 5.5). SCAPE's hardware control software uses a primary/secondary configuration in which the camera outputs a TTL pulse at the start of each exposure. The rising edge of this pulse is used to trigger the next output position of the scanner. Because the two rows closest to the center of the camera (i.e. the two central z-planes) would always acquire first for any acquired frame, these rows were always acquired as the scanner was arriving at its requested position. As a result, the desynchronization between odd and even time points at these two z- planes was relatively minor. However, the top and bottom rows within the camera frame would begin their exposures later than the middle rows, allowed the scanner time to move to a slightly different x-position. In SCAPE1.0, the polygonal mirror was scanned using a bi-directional, triangle wave which – when coupled with the camera's rolling shutter – resulted in a spatially-variant desynchronization between the forward and backwards sweeps (i.e. the odd and even time points) of the scan. In SCAPE2, the significantly faster response time of the planar mirror galvo scanner allowed for us to switch to a saw-tooth scan pattern that only acquired volumes while sweeping the galvo mirror in a single direction.

Designing the Excitation Subsystem in SCAPE

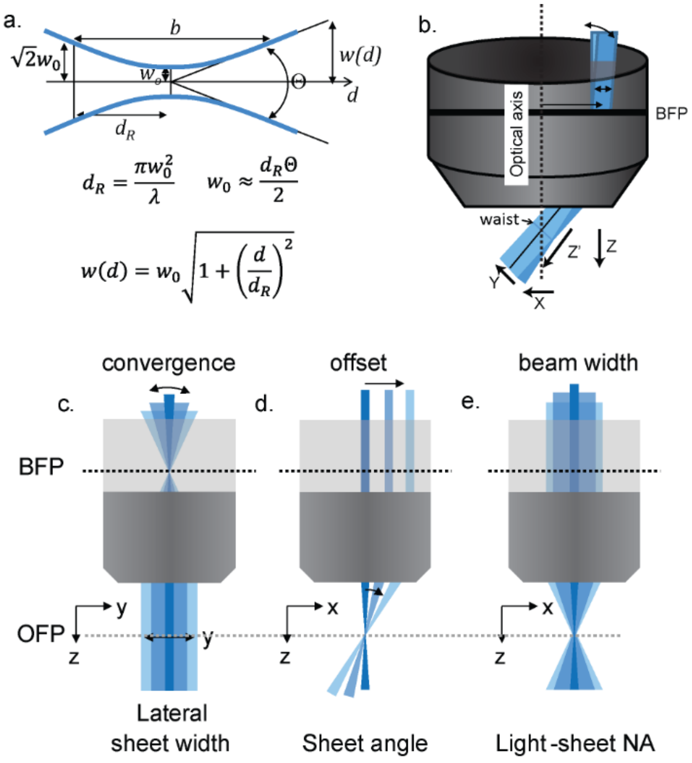

Figure 2.8: *Engineering the sheet parameters of SCAPE* ***a.*** *Gaussian properties that apply to the formation of light sheets. Equations show an inverse relationship between the sheet waist thickness and its depth of field* ***b.*** *Coordinate system and geometry of SCAPE* ***c-e.*** *Illustrations of how the shape and directionality of the beam entering the objective lens affect the sheet profile within the sample. The convergence of the light sheet at the back focal plane along the YZ dimension determines the length of the sheet in the Y-dimension and determines the Y-dimension field of view. The offset on the back focal plane along the XZ plane determines the angle of the sheet within the sample. The fraction of the beam back focal plane occupied by the beam width in the XZ plane determines the divergence angle of the Gaussian beam in the sample.*

Laser sources used for fluorescence microscopy are generally engineered to output a beam that follows Gaussian optics (**Figure 2.8**a). These beams have a gaussian intensity distribution along any of its transverse cross-sections. When focused by a lens, there exists an inverse relationship between the minimum beam radius at the beam waist, w_o, and the Rayleigh range, d_R, which is the distance from the beam waist that the beam radius remains within $\sqrt{2}$ or w_o. The beam waist thickness is equal to ½ of the w_o and the beam's depth of focus is equivalent to ½ of the Rayleigh range. These parameters are also related to the wavelength of light being focused.

In designing the excitation pathway that creates the sheet, the three main system parameters under consideration are the lateral extent of the sheet profile along the Y dimension, the sheet angle within the sample with respect to the optical axis, and the thickness of the sheet waist at the focal plane (**Figure 2.8**c-e). Note that because a light-sheet is created by unidirectionally focusing a beam of light using one or more cylindrical lenses, the excitation optics must be designed by taking each of the two dimensions of the sheet into account separately.

Controlling Lateral Field of View

The lateral extent of the sheet will determine the field of view of the system in the Y dimension. This parameter will be determined by the amount of convergence that the beam makes when focusing on the back focal plane of the objective (**Figure 2.8**c). Alternatively, one can think of the lateral field of view within the system as determined by the magnification along the y-dimension from the laser to the sample.

In SCAPE1, the laser beam passed through a vertically aligned cylindrical lens telescope consisting of two cylindrical lenses (f_{CL1} = 50 mm, Thorlabs, LJ1695RM-A; f_{CL2} = 250 mm, Thorlabs, LJ1267RM). A third cylindrical lens (f_{CL3} = 50 mm, Thorlabs, LJ1695RM-A) was used to focus the light sheet along the y-dimension onto the galvo mirror. The sheet then passed through the scan telescope consisting of a scan lens, tube lens and objective lens (f_{scan} = 50 mm, Thorlabs, AC254-050-A; f_{tube} = 100 mm, Thorlabs, AC508-100-A; f_{obj} = 9 mm lens, Olympus 20x/1.0NA). Together, the magnification of the system along the y-dimension is calculated as:

$$M_{y-dim} = \frac{f_{obj}}{f_{tube}}\frac{f_{scan}}{f_{CL3}}\frac{f_{CL2}}{f_{CL1}} = \frac{9 * 50 * 250}{100 * 50 * 50} = 0.45$$

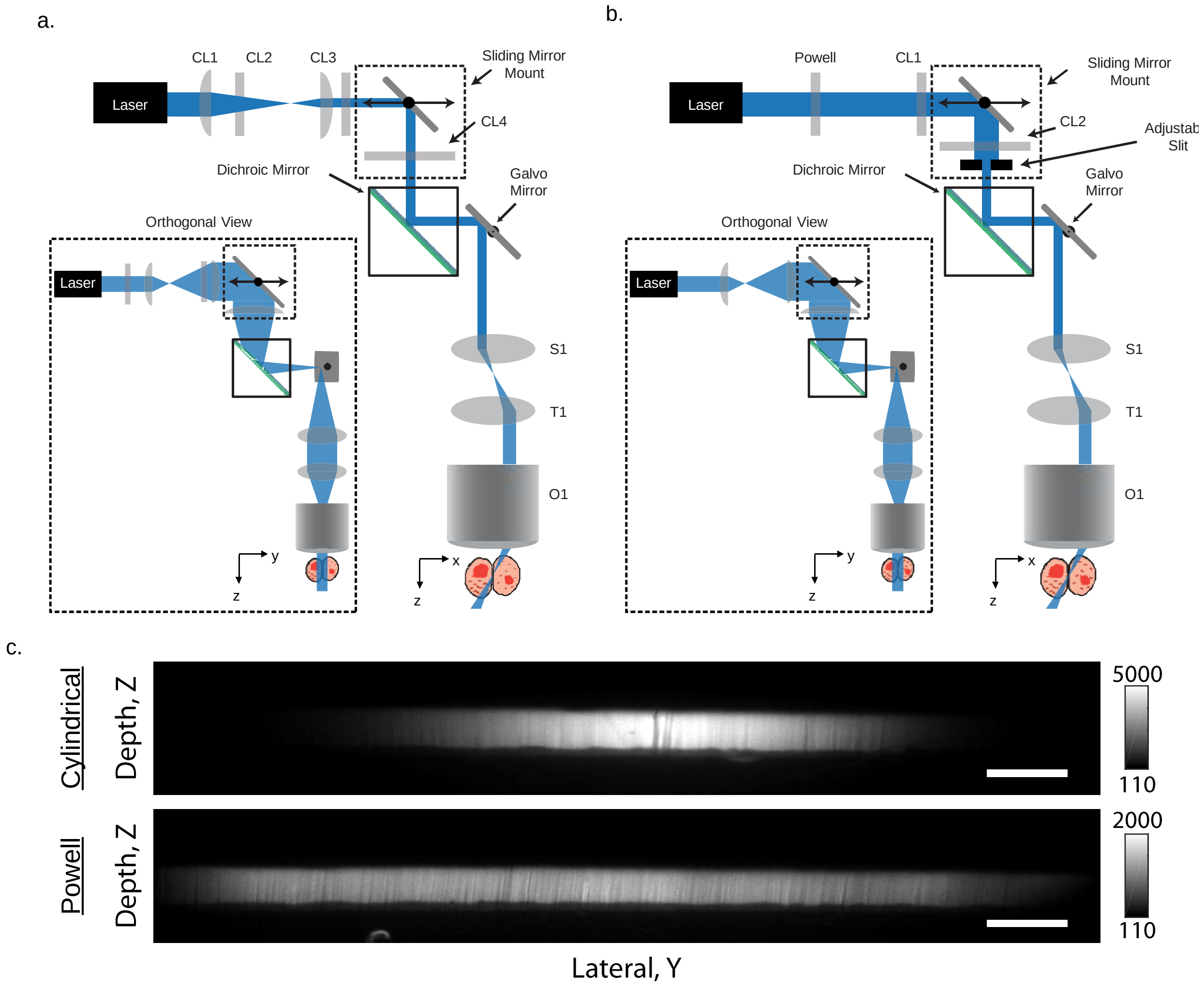

Figure 2.9: *Improving the system field of view in Y and illumination uniformity*
a. *Lens train of SCAPE2a* ***b.*** *Lens train of SCAPE2b* ***c.*** *Comparison of system FOV uniformity and lateral field of view when using a Cylindrical vs Powell lens as the first lens in the beam shaping optical train. Scale bar is 100 µm*

For SCAPE2a, the I altered the design of the system in order to achieve a larger magnification from the laser to the sample (**Figure 2.9**a):

$$M_{y-dim} = \frac{f_{obj}}{f_{tube}} \frac{f_{scan}}{f_{CL3}} \frac{f_{CL2}}{f_{CL1}} = \frac{9 * 75 * 250}{150 * 75 * 20} = 0.75$$

However, note, that because the beam profile exiting the laser is Gaussian, the illumination profile of the sheet within the sample will also be Gaussian decaying in brightness towards the edge of the sample.

For SCAPE2b, I replaced the first of the vertically aligned cylindrical lenses within the beam-shaping optical path with a Powell lens (Laser Line Generating Lens with 30° fan angle, N-BK7, Thorlabs, PL0130) (**Figure 2.9**b). A Powell lens is an aspheric lens that consists of one hyperbolic surface and one flat surface and introduces a controlled spherical aberration into the beam path in order to re-distribute energy from the center of the beam towards its periphery. This effectively converts the profile of the sheet along the Y dimension from a Gaussian into a flat-top profile. The vertically expanding beam created by the Powell lens is then collimated by a cylindrical lens, before being focused onto the galvo along the y-dimension by a second cylindrical lens (f_{CL1} = 50 mm , Thorlabs, LJ1695RM-A; f_{CL2} = 75 mm, Thorlabs, LJ1703RM-A). This simple change dramatically improved the illumination uniformity of the system (**Figure 2.9**c).

Controlling Sheet Angle

The sheet angle will determine the range of depths within the sample, Z, that the sheet thickness will remain within the depth of focus and therefore "sufficiently" thin. The initial system required 3 telescopes precisely aligned to one another and the offset of the cylindrical lens telescope on the polygonal mirror facet determined the angle of the sheet. From the equation for back pupil diameter ($BPD = 2*NA*f_o$), we find that achieving control of the sheet angle to within 2 degrees required controlling the offset of the beam on the back focal plane to within ~0.5 mm accuracy. The magnification of the scan telescope was 2x, which meant that we needed to control the accuracy of the cylindrical lens telescope's position to within 250 µm – impossible to achieve by hand. In the previous section describe how the scanner must map onto the back focal plane in order for the sheet to maintain a constant angle over the course of the scan. Following this result, the offset of the beam on the galvo mirror solely determined the sheet angle within the sample. I implemented a controlled, sliding mirror mount prior to the dichroic mirror (**Figure 2.10**a) that was de-coupled from the majority of the cylindrical lenses. This allowed us to reliably translate the beam on the back aperture of the objective lens in increments of 0.001’’.

Controlling Sheet Width

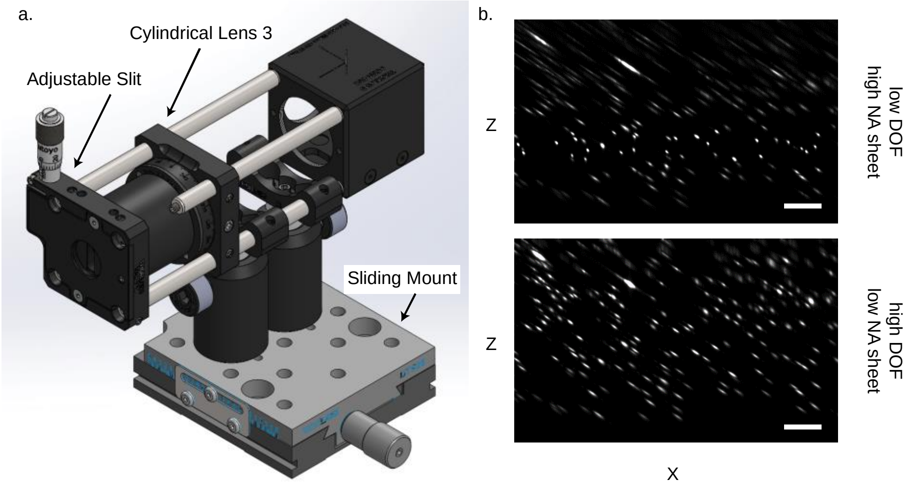

Figure 2.10: *Sheet angle and depth of field control*
a. *Controlled sliding stage used to control sheet that adjusts the position of the turning mirror, third cylindrical lens and adjustable slit used to control the light sheet’s numerical aperture* ***b.*** *3d phantom made of 200nm beads was imaged using the full sheet aperture (high-NA) and 1/3 of the sheet aperture (low-NA) altering the sheet’s depth of field from ~50 to 200 µm. The sheet aperture was altered by opening and closing the slit. Scale bar - ~50 µm.*

The x-dimension of the sheet dictates the waist thickness, its angle with respect to the vertical and its scan position. In conventional light sheet microscopes, the Rayleigh range dictates the lateral (XY) field of view over which the sheet provides adequate sectioning within the sample. In SCAPE microscopy, however, because the sheet penetrates from the surface into the sample, the Rayleigh range dictates the depth range (Z) over which the sheet provides uniform sectioning. It will be thinnest near the focal plane of the objective lens and diverge steadily above and below the focal plane. The waist thickness will be determined by the fraction of the back focal plane of the objective lens taken up by a collimated beam entering the objective lens **Figure 2.8**e). The width of the beam on the back aperture is a function of the initial beam width exiting the laser and the magnification, M_x, of subsequent telescopes that act along the X-dimension. In the initial SCAPE1.0 system, none of the cylindrical lenses acted along the X-dimension and so the M_x was equivalent to the magnification of the scan telescope (2x).

In SCAPE2a, we used a cylindrical lens telescope (CL1/CL3) in order to demagnify the beam in the x-dimension prior to entering the dichroic in order to achieve a larger depth of field within the sample, which allowed us to control the degree to which we under-filled the back aperture of O1 and achieve a depth range within the sample of ~200-300 µm. This depth range was sufficient to image relatively large samples such as the larval zebrafish brain. However, by optically hard-coding the sheet's depth of focus (and by extension, its waist thickness) into our system, we precluded ourselves from using narrower sheet widths to image samples between 20-100 µm thick that do not need a system with such a large depth range. SCAPE2b removes CL1 and CL3 and instead incorporates a cage-mounted adjustable slit (VA100C, Thorlabs) into the beam path prior to the dichroic mirror. This adjustable slit is the only optical component prior to the scan telescope that works along the sheet width dimension, providing greater homogeneity to the sheet's depth sectioning capabilities (**Figure 2.10**b).

Power Control

I made a number of modifications to the system in order to improve the experience of end-users using the system. SCAPE2a used a 488 nm, 30 mW DPSS laser (Melles Griotte, 85-BDD-030-115) which was incapable of high-speed modulation. Power control came via a 6-level neutral density filter wheel controlled via a custom Matlab GUI. A polarizer on a rotating mount was used for many experiments in order to afford tighter control of laser power. For SCAPE2b, I replaced our DPSS laser with a diode laser (Coherent Obis LX, 488 nm, 150 nm) capable of modulating its laser power at rates up to 500 kHz. These lasers are currently controlled via a TTL-modulated digital shutter and serial communications interface. In addition, I replaced the 6-level filter wheel with an upgraded 12-level filter wheel (FW212CNEB, Thorlabs) for increased versatility during experiments. This change permitted us to minimize laser exposure while we position our sample within the field of view and optimize image acquisition parameters at the beginning of an experiment.

Designing the Detection Subsystems in SCAPE

The task of improving the detection subsystem of SCAPE can be compartmentalized into improving the mapping from the object to the conjugate image space, and then from the conjugate image space to the sensor. Together, these two sub-systems determine the effective numerical aperture of the system and by extension, its resolution and light collection efficiency.

Correcting In-Plane Distortion

Recall how a change in sheet angle as a function in scan manifests itself as a depth-dependent magnification change along the X-dimension, wherein features at the top of the object are sampled more coarsely in X whereas features at the bottom of the object are sampled more finely. A similar phenomenon was occurred along the Y-dimension, with different z-planes within the sample mapping onto the sensor with different levels of magnification. Because we assume that the system's voxel sizes do not change over the field of view, these distortions will lead to inaccurate measurements of sample structure and brightness.

The effective magnification of the system, M_{system}, is a product of the magnification from the sample to the conjugate image space ($M_{S\text{-}CI}$) and from the conjugate image space to the sensor (i.e. the magnification of the camera telescope, M_{camera}). I considered a range of causes for this deformation and hypothesized that this effect was most likely due to improper mapping of the sample into conjugate image space. In much the same way that mapping the galvo onto the back pupil plane of the primary objective (O1) solved issues relating to scan inhomogeneity, it was likely that mapping the pupil planes of the two objectives (O1, O2) onto one another could create uniform in-plane magnification. Previous work by (Corbett, Burton et al. 2014) demonstrated the importance of proper pupil mapping for telecentric imaging of points across multiple depths in a scanning 2-photon microscope. The microscope in this work utilizes remote focusing to refocus the depth plane of a point-scanned two-photon microscopy system. The paper details the need for uniform magnification at each individual depth plane across the scanned field of view.

In SCAPE1.0, the scan telescope and the detection telescope were almost identical. The scan telescope contained a 50 mm scan lens, 100 mm tube and a 9 mm objective lens (Olympus 20x/1.0NA water immersion). The detection telescope also contained a 50 mm scan lens, 100 mm tube lens and 9 mm objective lens (Olympus 20x/0.75 NA air immersion). As a result, the magnification from the sample to the conjugate image space ($M_{S\text{-}CI}$) is equal to 1. The camera telescope consisted of a 20 mm objective lens (Olympus 10x/0.30NA air immersion) and a 75 mm tube lens, making M_{camera} and M_{system} equal to 3.75. For an Andor Zyla with 6.5 µm pixels, the effective in-plane sampling density would be ~ 1.73 and 1.39 µm in the Y and Z planes respectively.

Let us consider, for example, the case of the zebrafish brain imaged with SCAPE1.0 The sample takes up ~ +/-140 µm along the Z dimension and +/- 460 µm along the lateral dimension. If we had two cells located on the focal plane of the objective lens at the center and edge of the field of view respectively (460 µm apart), they would be situated ~265.4 pixels apart on the sensor (460 µm/1.73 µm). If we moved the sample upwards by 140 µm, we would want the two cells to remain 265-267 pixels apart from one another, indicating that $M_{S\text{-}CI}$ would need to remain between 0.996-1.004 (a change in magnification of +/- 0.4%) over an axial range of +/- 140 µm.

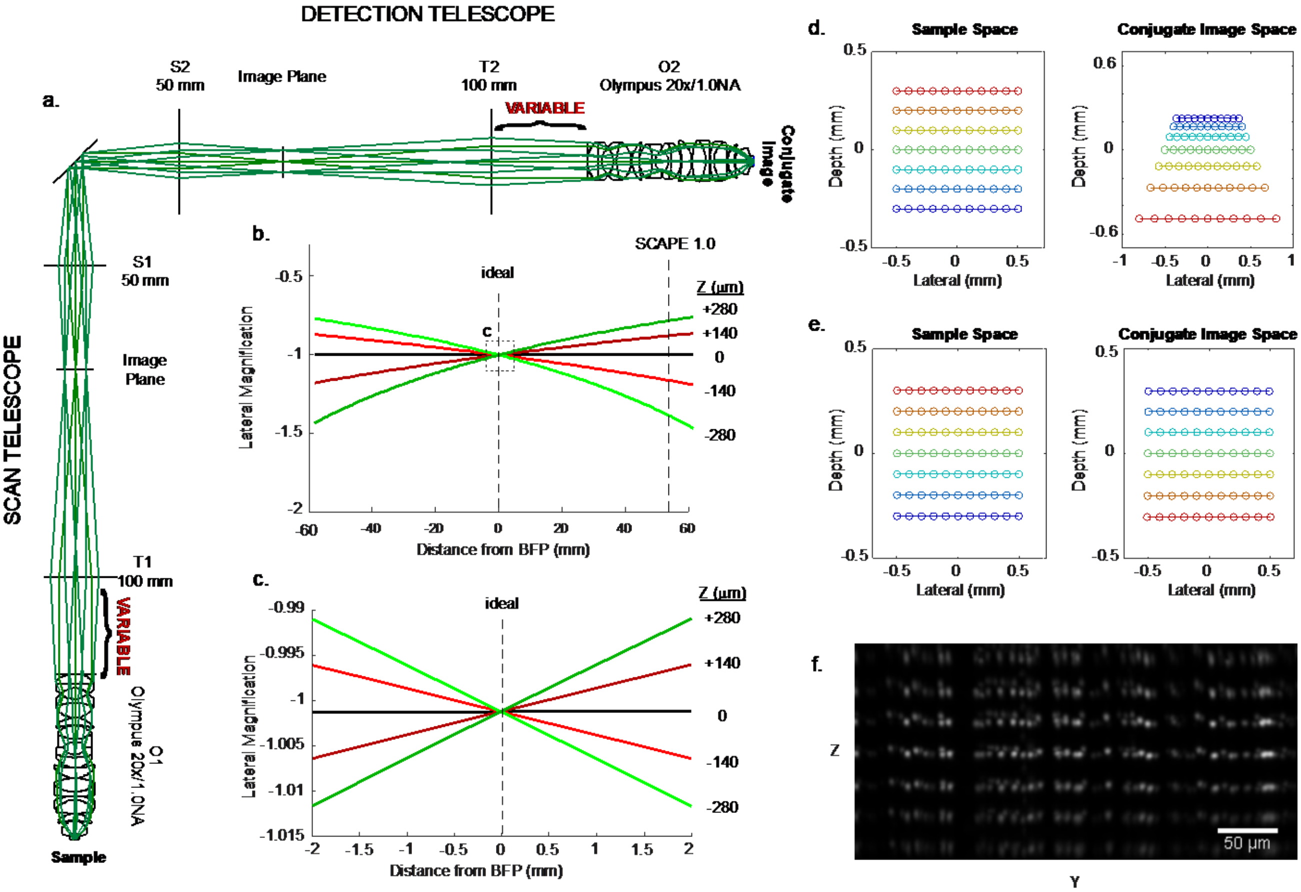

Figure 2.11: *Modeling in-plane distortions in SCAPE1*
a. *Model containing the optical path of SCAPE1 taken by fluorescence traveling from the sample under the primary objective lens (O1) to the conjugate image space under the secondary objective lens (O2). The distance between the tube lens to the objective lens back aperture in each telescope are set equal to one another and varied* ***b.*** *Magnification of the system for points mapped from above, below and at the focal plane of the primary objective lens plotted as a function of distance between the tube lens and objective lens. The zero position corresponds to when the focal planes of the tube lenses map onto the back focal plane of the objective lens* ***c.*** *Zoom in to the inset drawn in (b)* ***d.*** *Mapping of points distributed across multiple depths in sample space (left) into conjugate image space (right) when the tube lens' focal planes lie on the objective lens back apertures* ***e.*** *Mapping of points distributed across multiple depths in sample space (left) into conjugate image space (right) when the tube lens' focal planes lie on the objective lens back focal planes* ***f.*** *Data acquired on SCAPE2 in which the distance between the tube lens' focal planes map onto the back focal planes of the objective lenses show negligible differences in in-plane magnification across different depths.*

I created a model of the optical relay from the sample to the conjugate image plane using lenses nearly identical to SCAPE1 (**Figure 2.11**a). The scan and tube lenses (50 mm and 100 mm respectively) were modeled as thin lenses and the galvo scanner was modeled as a flat 45° mirror. The objective lenses were modeled as Olympus 20x/0.95NA water immersion lenses seen in previous models. The distance from the mirrors to the scan lenses (S1, S2) was set equivalent to the focal length of the scan lens. The distance between the scan and tube lenses (S1/T1 and S2/T2) in each telescope was set to the sum of their focal lengths. The distance between the tube lenses and objective lenses were set to be equivalent to one another and were the primary variable altered during the model. Because objective lenses are infinity corrected, altering this distance solely affects the mapping of the two objective pupils onto the galvo and one another. **Figure 2.11**b shows how the magnification of features at above and below the focal plane of the objective lens changes as a function of pupil mismatch. The line indicating "SCAPE1.0" is a scenario in which the back apertures of the two objective lenses map onto one another; note how different z-planes have different magnifications. The depicted "ideal" scenario is found when the curves all intersect, representing uniform magnification at each depth plane. This scenario occurs when the back focal planes (or pupil planes) of the objective lenses map onto one another. One can also think about this as creating an optical system which is telecentric both at the sample *and* in conjugate image space, resulting in parallel chief rays in both locations. **Figure 2.11**c is an inset zooming in on the region surrounding the "ideal" scenario showing how the magnification of the system over an axial range of +/- 280 µm can remain uniform to within 0.5%, even if the focal planes are misaligned by ~ 1 mm on each objective lens. Because of difficulty in obtaining accurate lens prescriptions for objective lens models, the lenses in this simulation are not ultimately what will be incorporated into the SCAPE2 layout. It was nevertheless useful to show that the tolerance for axial misalignment was on the order of millimeters instead of microns. A set of 11 field points spanning +/- 500 µm at 7 depth planes spanning +/- 300 µm were mapped from the sample to the conjugate image plane when the back apertures are mapped to one another (**Figure 2.11**d), and when the back focal planes map onto one another (**Figure 2.11**e) further validating the advantage of the latter configuration. **Figure 2.11**f shows a "virtual structured sample" created by taking multiple stacks of the same beads slide across multiple depths (obtained by following the procedures in 0: Depth Calibration). The image was acquired on a SCAPE system in which the back focal planes were properly aligned and shows uniform magnification in the Y-dimension over a range of depths.

Note here that while this optical model simulates the mapping of a 3D volume from object space into conjugate image space, SCAPE only maps fluorescence generated by the angled light sheet within the sample onto an angled conjugate image plane. When improperly aligned, the non-linear magnification changes can create an image of the light sheet that is curved along the XZ dimension.

Trade-offs between Light Collection Efficiency v. Image Quality

The previous section described the condition necessary for creating an optical system in which multiple depth planes within the sample were all mapped to the conjugate image space with uniform magnification. However, note that this refers to *lateral* magnification which describes how the distance between points lying within the *same z-plane* changes as the image propagates through the system. The axial magnification, M_A, describes how distances between points lying along *different* z-planes change and is proportional to the square of the lateral magnification, M_L, of an optical system:

$$M_A = \frac{n_1}{n_o} M_L^2$$

where n_o and n_1 are the refractive indices at the sample and conjugate image space respectively. Because SCAPE creates an image of an oblique light sheet, both the lateral and axial magnifications play a role in determining the angle of this sheet in conjugate image space. For example, let us assume that both the sample and conjugate image space are in air ($n_o = n_1 = 1$) and the lateral magnification of the system is 1.0x. A light sheet in the sample created at 35˚ with respect to the optical axis of the first objective lens ($\Theta_s = 35˚$) will be remapped as a sheet at 35˚ with respect to the optical axis of the second objective lens (O2), ($\Theta_{CI} = 35˚$). Because this virtual sheet is re-imaged onto the sensor via an obliquely aligned camera telescope, the angle of the conjugate image determines the angle of the camera telescope and by extension, the light collection efficiency between the second and third objective lenses (**Figure 2.12**).

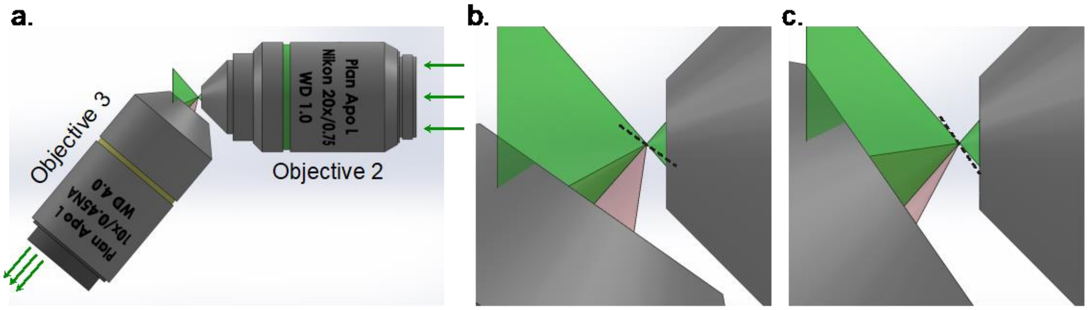

Figure 2.12: *Interface between objective 2 (O2) and objective 3 (O3)*
a. *Fluorescence enters the back aperture of O3 and exits the front and is collected by O3 (at an oblique angle). Green cone defined by the angular collection range of O2 (asin(NA_{O2})). Red cone is the angular collection range of O3 (asin(NA_{O2})). The overlap between these two cones is the collection efficiency* ***b.*** *Overlap of O2/O3 collection cones when $\theta_{CI} = 35˚$* ***b.*** *Overlap of O2/O3 collection cones when $\theta_{CI} = 55˚$*

If Θ_{CI} is high, then the camera telescope will be aligned less obliquely resulting in greater light collection. It would be possible to create a mapping from the object to the conjugate image space with a lower lateral magnification which would effectively increase Θ_{CI}:

$$\theta_{CI} = \tan^{-1}\left(\frac{M_L \sin\theta_s}{M_a \cos\theta_s}\right)$$

In the example provided before, if we were to instead use an axial magnification of 0.5x, a light sheet where $\Theta_s = 35^\circ$ would be remapped as a sheet in which $\Theta_s = 55^\circ$, utilizing a larger fraction of the camera telescope objective's (O3) numerical aperture. The light collection efficiency therefore is a function of the sheet angle within the sample, the magnification from the sample to the objective lens and the angular collection efficiencies of the second and third objective lens. This is exactly the trade-off outlined by (Dunsby 2008) on oblique plane microscopy. If the second objective lens is air-immersion with a numerical aperture of 0.75, then its angular range will be 48°. If we were to collect, for example, some portion of this angular range with the third objective lens, α_{CI}, that would correspond to a certain angular range collected by the primary objective lens at the sample, α_s. The effective numerical aperture of the entire system is then dictated by:

$$NA_{eff} = n_0 \sin(\alpha_s)$$

The relationship between α_s and α_{CI} brings us to our second source of light loss: pupil mismatch. Note how the lateral magnification from the sample to the conjugate image space is the given by:

$$M_L = \frac{f_{O2} f_{S2} f_{T1}}{f_{O1} f_{S1} f_{T2}}$$

Wherein "f" refers to the focal lengths of the lenses described by the subscripts (O1, O2, etc) and the she subscripts reference the lens components in **Figure 2.11**. However, the magnification of the back pupil diameter of O1:

$$M_{BPD} = \frac{f_{S1} f_{T2}}{f_{T1} f_{S2}}$$

In SCAPE1.0, O1 was an Olympus 20x/1.0NA water immersion objective with a back pupil diameter (BPD) of 18 mm, O2 was an Olympus 20x/0.75NA dry objective with a BPD of

13.5 mm (recall that $BPD = 2n_i f_o \sin\theta$) whereas the scan and detection telescopes had equal magnifications. Therefore, while the angular apertures and focal lengths of O1 and O2 were equivalent ($f_{O1, O2}$ = 9 mm, $\Theta_{O1, O2}$ = 48˚), the back pupil diameters were different due to the refractive index mismatches between the two objectives (n_1 = 1.33, n_2 = 1.0). Because M_{BPD} = M_L = 1, an 18 mm pupil was mapped onto a 13.5 mm pupil reducing the effective numerical aperture of O1 from 1.0 to 0.564. Collecting the full numerical aperture of O2 (α_{CI} = +/- 48˚) would therefore only be collecting a cone angle of α_S = +/- 34˚ in the sample, decreasing collection efficiency. The relationship between these two angles is given by:

$$\sin\alpha_S = \frac{M_L n_1 \sin\alpha_{CI}}{n_0}$$

However, because of this index of refraction mismatch, the reduced axial magnification (M_A = 0.75) changed the sheet angle from Θ_s = 35˚ to Θ_{CI} = 43˚, which in turn would improve the transmission from objective 2 to objective 3. As a result, we have these competing effects: using an axial magnification < 1 would rotate the sheet angle improving collection efficiency at the O2/O3 interface, but would also decrease the angular collection range at the primary objective lens. We could theoretically select a higher numerical aperture lens as O2 that would counteract the effect of this pupil mismatch. However, there are a few issues with this approach. Lenses with higher numerical apertures also tend to have larger magnifications and proportionally smaller fields of view, making the system far less versatile. Furthermore, arbitrarily changing the lateral and axial magnifications comes at a cost of image quality.

Thus far, we have only spoken about angular collection efficiency without considering any system aberrations that might be introduced. In 1858, Maxwell detailed a set of rules for the design of an optical instrument (i.e. series of lenses) which state that mapping a set of 3D points from object to image space without astigmatism, curvature or distortion is possible (Maxwell 1858). The condition that must be true for un-aberrated (or stigmatic) mapping of points that lie on one plane (normal to the optical axis) to another is known as the sine condition:

$$M_L = \frac{y_{CI}}{y_S} = \frac{n_0 \sin \gamma_0}{n_1 \sin \gamma_1}$$

And the condition that must be true for un-aberrated mapping of points that lie along the optical axis is known as the Hershel condition:

$$M_A = \frac{z_{CI}}{z_S} = \frac{n_0 \sin\left({}^{\gamma_0}/_{2}\right)}{n_1 \sin\left({}^{\gamma_1}/_{2}\right)}$$

Wherein M_L and M_A corresponds to the lateral and axial magnifications of a system, y_o and y_1 correspond to lateral positions of individual points in the sample and conjugate image space respectively, z_o and z_1 correspond to the axial positions of points in the sample and image space, n_o and n_1 are the refractive indices in the sample and conjugate image space, and γ_0 and γ_1 are the angles of a single ray starting at y_o and ending at y_1 (Born and Wolf 1970). It can be seen that the only way in which to achieve simultaneous, un-aberrated mapping of points both within a single plane and along an optical axis (i.e. throughout all of 3D space) is if the angles, γ_0 and γ_1, were equal to one another and $M_L = M_A = n_0/n_1$. If an optical system were to follow the sine condition, γ_0 and γ_1 were not equal to one another, one would expect z_{CI} to steadily change as a function of γ_0. This is the definition of a spherical aberration.

(Botcherby, Juškaitis et al. 2007) described a technique called remote focusing which uses this principle in order to create a perfect 3D mapping from one space to another using high-NA objective lenses. Our scan and detection telescopes are an optical relay that served the same function as those of a “perfect, 3D imaging system” as described by (Botcherby, Juškaitis et al.

2007, Botcherby, Juškaitis et al. 2008). By mapping the pupils of high-NA objective lenses onto one another, the two objective lenses effectively serve to negate the spherical aberration induced by the imaging of off-axis points using lenses that follow the sine condition.

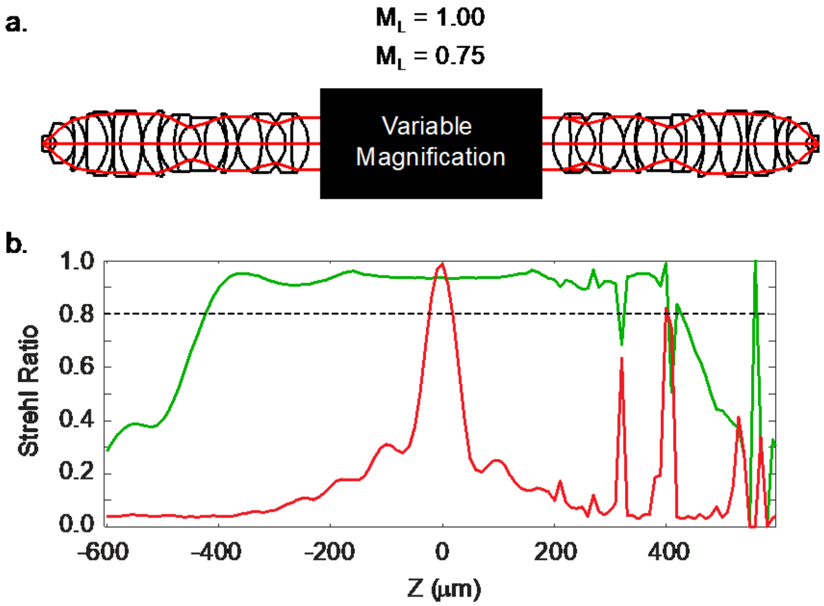

Figure 2.13: *Modeling relationship between image quality and magnification*
a. *Layout of optical model of lens train from the sample to the conjugate image plane. The variable magnification telescope modeled T1, S1, S2 and T2 from SCAPE2b as 2''-diameter achromats from Thorlabs. The lens for T2 was switched to alter magnification of the system* ***d.*** *Field points within the sample along the optical axis were mapped into conjugate image space at 2 magnifications. Dashed line indicates the cutoff for minimum acceptable Strehl ratio, a standard metric of image quality. The spurious sharp peaks between Z = 300-500 µm are due to ray tracing errors in the model.* $M_L = 1$ *(green),* $M_L = 0.75$ *(red).*

I created an Optalix model to determine the effects of non-unitary magnification on the range of depths that can be properly focused. I imaged the back pupils of two Olympus 20x/1.0NA objective lenses and implemented a variable magnification telescope between them (**Figure 2.13**). I mapped points along the optical axis at the sample into the conjugate image space and calculated the calculated the Strehl ratio as a function of defocus (**Figure 2.13**). I found, however, that this choice trades off the resolution achieved at features away from the focal plane of O1 and O2. Our model found that implementing isotropic lateral and axial the magnification (i.e. $M_L = M_A = n_o/n_1$) from the sample to conjugate image space improved the system’s depth range by an order of magnitude, from 50 µm to approximately 500 µm.

While the angle of the plane in conjugate image space was steeper as a result of this choice, I remedied the loss in light throughput by replacing O2 with a Nikon 10x/0.45NA objective. O2 was changed from an Olympus 20x/0.75NA to a Nikon 20x/0.75NA to accommodate this change.

Designing the Camera Telescope

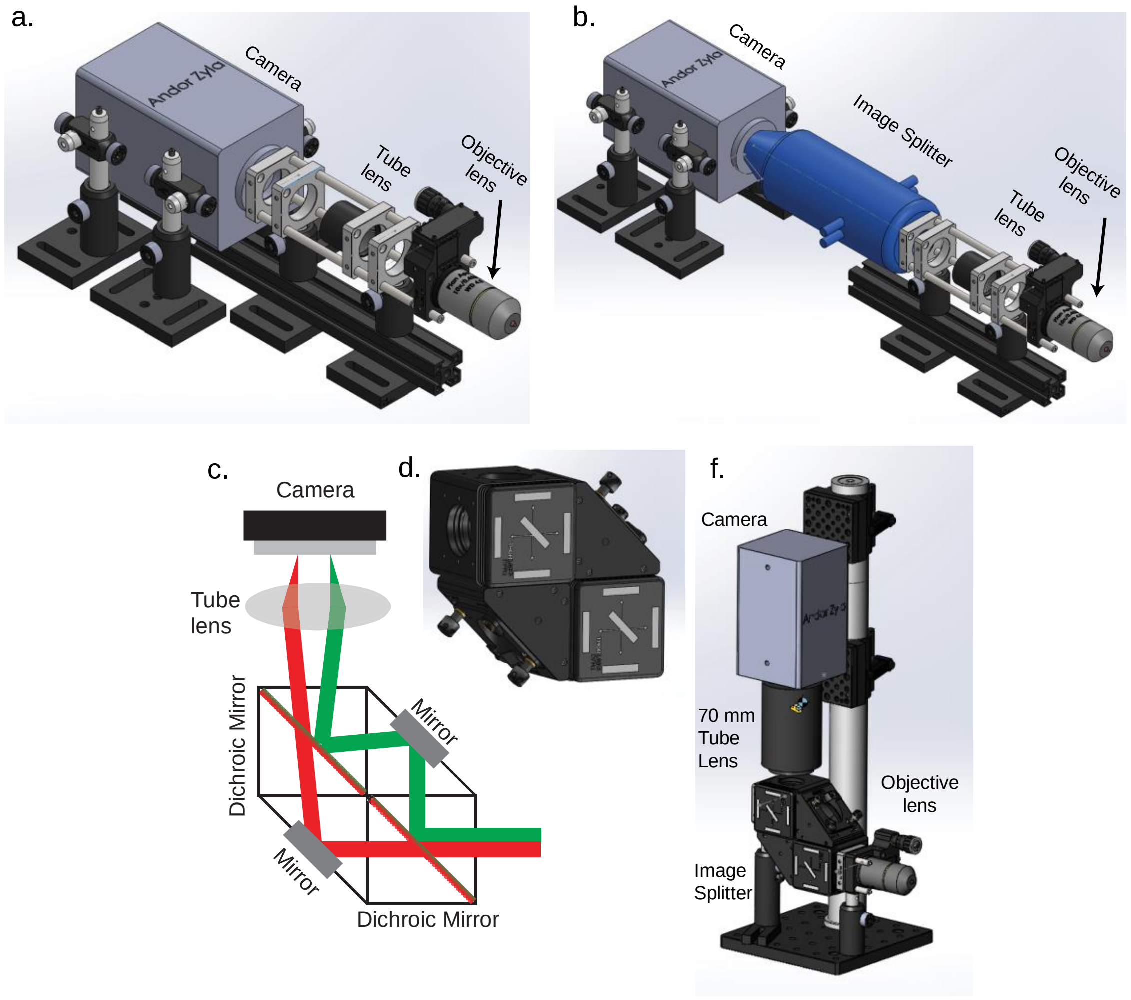

Figure 2.14: *Camera telescope designs*
a. *Camera telescope for single-color imaging with SCAPE2a* ***b.*** *Camera telescope for dual-color imaging with SCAPE2a* ***c.*** *Schematic of custom image splitter showing how multiple channels are mapped to separate parts of the same camera chip* ***d.*** *Picture of image splitter built from Thorlabs components* ***e.*** *Camera telescope of SCAPE2b which decouples the objective and image splitter from the camera and tube lens*

The SCAPE2a camera telescope consisted of an optical rail upon which were mounted the tube lens, camera and objective lens unit (**Figure 2.14**a). Multi-color imaging on SCAPE2 entailed using a commercially available image splitter (DV2, Photometrics) which included an attachment containing a custom filter-set (**Figure 2.14**b). Changing the dichroic on this filter-set in order to alter the cut-off frequency of the image splitter would have required us to purchase an additional attachment from the company. We generally took the DV2 into and out of the system when wanting to switch between single-color to dual-color mode in order to retain the system's light collection efficiency. While this procedure could be performed quickly, it required the expertise of someone familiar with aligning the system and was not something we could ask of typical end users. I used a number of commercially available optics including the W-View Gemini from Hamamatsu and the Optosplit from Cairn Optics. Both of these solutions were designed as add-ons to wide-field microscopes with standard microscope frames. In addition to requiring custom alignment procedures, they were over 1 foot in length. In SCAPE2b, we replaced the commercial image splitter with a custom unit developed in our lab consisting of opto-mechanics purchased from Thorlabs (**Figure 2.14**cd). This new custom image splitter can accept arbitrary filter sets purchased from any of the major vendors as well as be converted smoothly from multi-color to bypass mode by simply removing the filter cubes from their mounts.

Finally, from an early stage of development, variable magnification was a key feature that was requested by most potential collaborators. Recall from the first chapter that the effective magnification of a standard microscope – from the image to the sensor – is the ratio between the focal lengths of the tube lens (f_T) and the objective lens (f_O). Conventional light microscopes implement magnification changes by fixing the tube lens – generally embedded within the trinocular containing the microscope eyepieces – and use a nosepiece to switch the objective lens near the sample. A given widefield microscope contains a rotating set of parfocal lenses (i.e. lenses that share a common distance from the sample focal plane to the objective lens shoulder) with a range of focal lengths. Note that microscope manufacturers standardize their tube lens' focal lengths to specific lengths. Thorlabs, Mitutoyo, Nikon and Leica microscopes use 200 mm tube lenses. Zeiss uses 165 mm tube lenses and Olympus uses 180 mm tube lenses. Because higher magnification lenses generally provided greater resolution, I was asked whether changing the primary objective lens nearest the sample to a higher-magnification, higher-numerical aperture lens would radically improve system performance.

Such an approach could potentially work, albeit with an incredibly restrictive trade-off. As described in previous sections, SCAPE can be thought of as an instrument that maps the totality of a 3D volume within the sample to another 3D volume at some distant conjugate image space. The basic conditions for non-aberrated mapping of such a 3D volume is that the magnification from the sample to the conjugate image plane needs to be equivalent to the ratio between the refractive indices of the immersion media found at the sample and at the conjugate image plane ($M = n_1/n_2$, typically is usually close to 1). As a result, the bulk of the magnification from the sample to the sensor is provided by the camera telescope. This means that one can alter the magnification by changing either the objective lens or the tube lens within this telescope ($M = f_{tube}/f_{objective}$). However, the third objective lens not only dictates the overall light collection efficiency of the system but must also be optomechanically compatible with the second objective lens. As a result, it would be simpler to implement changes to system magnification by altering the tube lens. The initial tube lens used on SCAPE1 and SCAPE2a was a 75 mm achromat (*Thorlabs, AC254-075-A*) which needed to be manually aligned to the camera sensor in order to focus the conjugate image onto the camera. Furthermore, the entire camera telescope was constructed as a single component that would need to be disassembled, precluding on-the-fly modification. Therefore, we split the camera telescope into two disjoined parts that could be altered independently of one another (**Figure 2.14**e). The first unit consists the third objective lens and image splitter. The second unit consists of the tube lens and camera. This division allows us to alter the tube lens without risking a major misalignment of the camera telescope with respect to the rest of the system.

I used Optalix-PRO to assess the image quality of a range of achromats or other simplified lens designs. We further replaced the tube lens with a set of custom optics with a focal length of 70 mm (*Morrell Instrument Company Inc., MXA20714 and MQD42070*) that screwed into the camera's adapter. Changing the magnification of the system is now a simple matter of unscrewing the tube lens from the camera and screwing in a replacement, avoiding a tedious alignment process.

More recently, we have also tested out various zoom lenses used for photography and machine vision applications in the camera tube lens position. These substitutes allow users to set the tube lens' focal length to a non-discrete value between 70 – 200 mm. However, when using these lenses, it is important to develop calibration metrics for any given tube lens focal length.

Hardware/Software Control

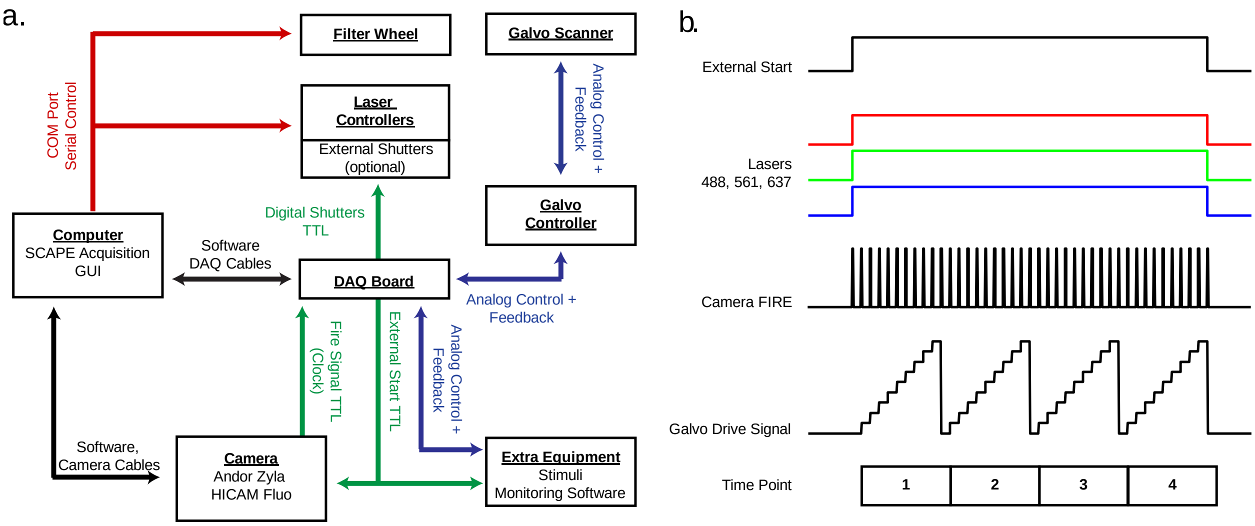

***Figure 2.15**: SCAPE DAQ control and data acquisition paradigm*
***a.** Schematic showing all control system connections between computer and hardware components of SCAPE. Software control connections are in black. Serial port communications are in red. Digital input/output to and from the DAQ board are in green. Analog input/output signals to and from the DAQ board are in blue **b.** Sequence of signals sent to and from the DAQ board following the initiation of a trial*

The control software for SCAPE consists of a custom data acquisition GUI written in MATLAB which interfaces with the filter wheel, lasers, Andor Zyla and National Instruments DAQ board (**Figure 2.15**a).We use a mixture of software and hardware control in order to synchronize the frame-by-frame acquisition of the camera to the motion of the scanning galvo mirror.

The amount of laser power entering the system is controlled by the GUI via Serial COM ports that communicate with the filter wheel and up to three laser controllers. The camera is controlled through its own native software (Andor SOLIS). A set of scripts written in the SOLIS macro language interface between the camera and the Matlab acquisition GUI, updating requested camera parameters such as the save file directory, file name, camera ROI, frame rate, camera binning and acquisition time.

The National Instruments DAQ board (*NI USB-6363*) provides TTL output channels that control the laser shutters. It also contains a TTL output that connects to the EXTERNAL START port of the Andor Zyla and serves as a start trigger for the entire acquisition. A TTL input channel connects to the FIRE port of the Andor Zyla and serves as an external clock. The DAQ board also contains an analog output channel that controls the voltage applied to the galvo controller, as well as an arbitrary number of high-speed analog input channels to log feedback from the galvo controller or any additional equipment (such as stimuli) that are specific to a given experiment.

Figure 2.15b shows the signals passing through at the digital and analog channels of the DAQ board after the initiation of a scan. At the start of an acquisition, the DAQ board sends an external start trigger to the camera by setting a TTL channel from low to high. The same signal also triggers the DAQ's input channels and any external stimuli that might be connected to the system. The external start pulse signals the camera to begin acquiring frames at the requested ROI and camera frame rate, outputting a FIRE signal – a brief TTL pulse at the start of each frame. At the rising edge of each TTL pulse from the fire signal, the DAQ board sends a voltage to the galvo controller updating the galvo mirror's deflection angle and by extension, the position of the sheet within the sample along the X-direction. A camera frame is acquired at each position and streamed to disk through a 10-tap camera link interface. A time point consists of a single period of the sawtooth waveform outputted to the galvo controller.

Computational Workstation

The high-speed sCMOS cameras used for SCAPE microscopy require workstations that can handle high read and write speeds. Capable of generating between 200-600 MB per second (or between 1-2 TB of data per hour), the hardware we were using to stream this data to disk was insufficient for prolonged acquisitions (> 1 minute). The data acquisition computer was upgraded with a better CPU (2xIntel Xeon E5-2630 v3, 8 cores, 2.4 GHz, 20xPCIe lanes), 192 GB of

RAM (8x16GB DDR3-2133), a high end graphics card (Nvidia GeForce GTX980) and 10 gigabit ethernet connectivity (Intel X540-T2, 2x10 Gb ethernet port, RJ45 interface). A 2 TB solid state SSD hard drive connected via a PCIe slot was added to provide 1.5 GB/s read/write capabilities. Another 35 TB RAID5 HDD volume (Areca ARC-1882IX-12) can be added to sustain 0.7GB/s read/write operations and provide more permanent storage functionality. For more information on designing a high-speed workstation for SCAPE microscopy, please refer to the thesis work of Dr. Wenze Li.

Creating System Characterization Metrics

Alongside the initial development of SCAPE, I built multiple replicas of the same system to support collaborations between the Hillman lab and other groups. In order to create benchmarks of performance, I created protocols for evaluating various system parameters. 0 includes techniques on how to calibrate the system along each of its 3 axes and measure the sheet angle within the sample. Metrics on how measure the system's in-plane field of view, the system's resolution, compare excitation and detection light throughput and characterize depth-dependent distortions of field can be found in Appendix B.

Standardization of Protocol for Alignment and Maintenance of SCAPE

Proper alignment of the system is crucial to achieving sufficient resolution over the entire field of view. One of the primary challenges to alignment was insufficient knowledge about the objective lenses we were using. Objective lens manufacturers rarely provide the location of the back focal planes within the objective lens, measurements of light throughput at specific wavelengths or the degree to which one can expect the resolution to fluctuate as a function of distance away from the center of the field of view. Objective lens designs such as those used to model the Olympus 20x obtained through patents can serve as a useful testbed for potential design ideas but usually contain obsolete or inaccurate lens parameters, rarely containing the location of internal stops or lens diameters and never truly achieve the performance of the actual objective lens. This makes it difficult to model, for example, the variations in laser power delivered to the sample one could expect as a function of the galvo scan angle.

I developed a standardized protocol for aligning galvo/dichroic-based SCAPE systems during the construction of SCAPE2a and b (see Appendix D for details on the protocol). These alignment/calibration protocols are constantly being updated as we alter the system design, as new users/designers gain experience and insight into system construction, and as new tools become commercially available to characterize system performance. It is important to note that the initial alignment of SCAPE2a took almost 6-7 months. Alignment of the following system, SCAPE2b, took almost 4-5 months. The newest versions of SCAPE that I have built at various conferences (CSHL Imaging Course and the EMBO Light Sheet Microscopy course), as well as at other sites of collaboration (NYU, Alexandria Center) have taken between 3-7 days, with the tail-end of that period spent refining image quality. At the time of this works' writing, there are currently four systems nearly identical to SCAPE2b within the Hillman lab that have been constructed by 3 different users using a version of the protocol outlined in Appendix D. Two other systems that follow the general principles of pupil mapping, sheet creation within the sample and oblique detection that I've outlined within this chapter are also under development.

2nd Generation SCAPE

System Descriptions

SCAPE2a and SCAPE2b are built according to the optical design principles highlighted in previous sections using the alignment protocols detailed in Appendix C. Schematics of both systems highlighting their similarities and differences are found in **Figure 2.16** above. Tables detailing the lenses chosen for both systems are found in Appendix E.

SCAPE2a (**Figure 2.16**ab) separated the excitation and detection pathways via a long-pass dichroic mirror (FF495-Di03-25x36, Semrock). The key non-lens components of the system consisted of a 488 nm DPSS laser (85-BDD-050-002, Melles Griot), a large beam-diameter galvanometric mirror (GVS211, Thorlabs) and a high-speed sCMOS camera (Zyla 5.5, Andor). The beam shaping optics were chosen to de-magnify the sheet in the "horizontal" dimension (i.e. the dimension controlling the light sheet's numerical aperture) by a factor of two, as well as magnify the beam in the vertical dimension to achieve a lateral field of view (Y) of ~ 1 mm. The primary and secondary objective lenses (O1 and O2) were chosen to be an Olympus 20x/1.0NA water immersion lens and a Nikon 20x/0.75NA air immersion lens respectively. The third objective lens was selected to be the Nikon 10x/0.45NA air immersion lens. The achromatic

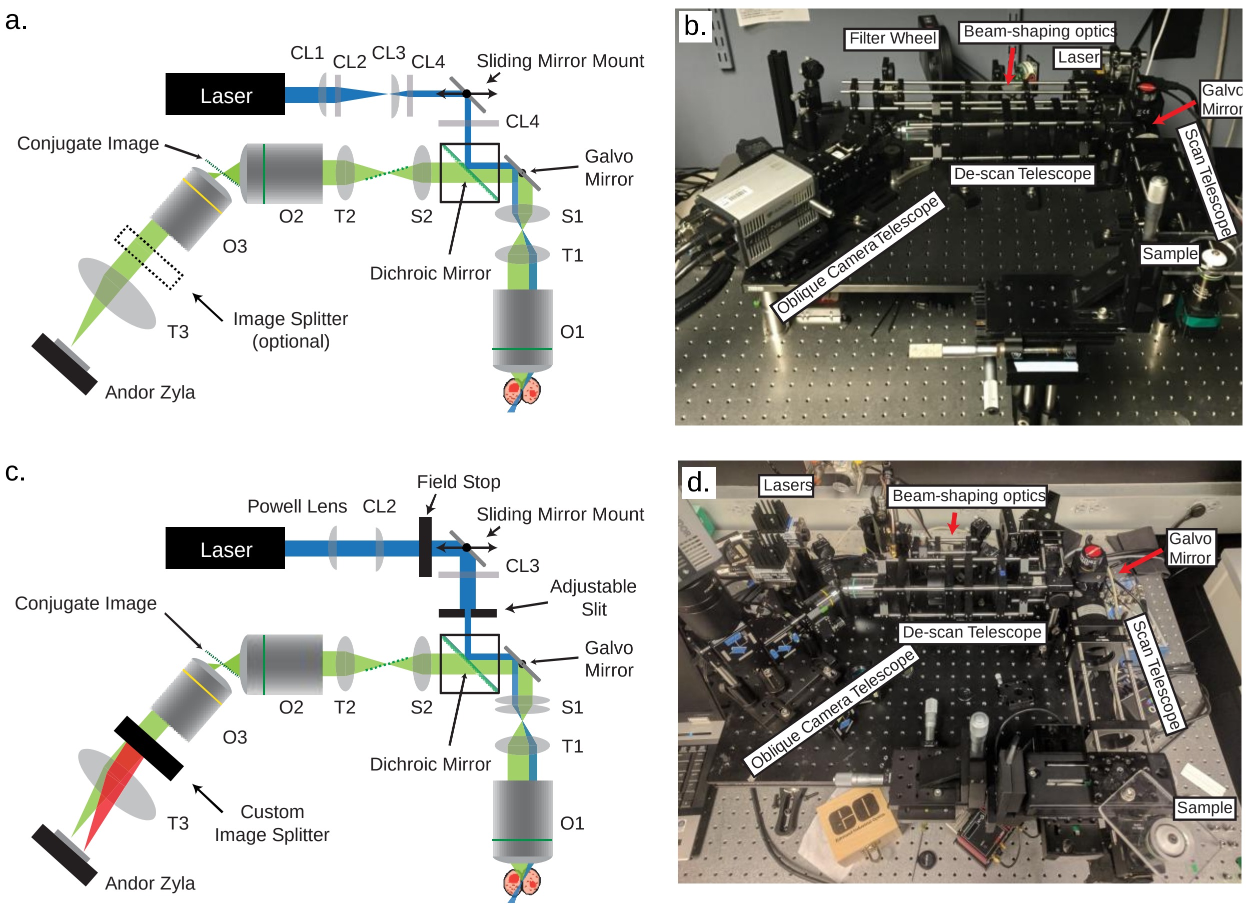

Figure 2.16: *Final designs and layouts of SCAPE2a/b*
a. *Schematic of SCAPE2a. The system is designed in long-pass configuration around a dichroic and galvo mirror. Note the re-organization of the four telescopes. The scan telescope consists of a scan lens (S1), tube lens (T1) and the first objective lens (O1). The de-scan telescope consists of a scan lens (S2), tube lens (T2) and the second objective lens (O2). The camera telescope consists of the third objective lens (O3), a camera tube lens (T3), an optional image splitter and the camera. Finally, the beam shaping optics consist of a series of cylindrical lenses (CL1…4) and a sliding mirror mount. The blue lines represent the excitation pathway from the laser to the sample. The green lines represent the detection pathway of the fluorescence from the sample to the camera* ***b.*** *Photo of SCAPE2a in which the system is set up in an inverted configuration to image samples from the bottom and in single-color mode* ***c.*** *Schematic of SCAPE2b. The key differences from the schematic presented in (a) are a simplified cylindrical lens telescope (containing a Powell lens and adjustable slit), a Plössl type scan lens, and a custom image splitter mounted on a vertically aligned camera telescope* ***d.*** *Photo of a later variant of SCAPE2b containing multiple laser lines (488nm/637 nm) set up in an inverted configuration.*

lenses within the scan and de-scan telescopes were chosen to ensure that the magnification from the sample to the conjugate image plane between O2 and O3 was 1.33 (i.e. M = n1/n2). There was no in-built image splitter for SCAPE2a and the camera telescope needed to be continuously re-aligned in order to switch between dual-color and single-color imaging.

SCAPE2b (**Figure 2.16**cd) was developed in order to incorporate degrees of freedom into the system that could be easily manipulated by the user without interfering significantly with system function. These degrees of freedom significantly improved the system's versatility and was motivated in part by three factors:

1. The need for a more stream-lined solution for multi-channel (excitation and emission) imaging
2. The difficulties of switching system magnification between experiments
3. The desire to alter system depth of field and sectioning capabilities to accommodate samples of variable thickness

As a result, the camera telescope of SCAPE2b incorporated a custom-designed image splitter, and was built with the camera telescope and tube lens pointing upwards. I also included an adjustable slit and field stop for better control of the light sheet parameters. SCAPE2b also incorporated the powell and plossl lenses for improved sheet and scan uniformity.

The SCAPE2a design, which served as a temporary workhorse to bridge the gap between SCAPE1.0 and SCAPE2b, was eventually upgraded to the SCAPE2b design. SCAPE2b continues to serve as a base design for SCAPE systems within our lab, fielding collaborations from at least 5 different laboratories both within and outside of Columbia University. Data from three of those collaborations are presented in the next section. I've helped construct the system to advanced imaging workshops and conferences both in the United States and Europe, and efforts to support its dissemination to over 10 labs worldwide are ongoing.

Performance Metrics

As can be seen in **Figure 2.17**a, SCAPE2b has a reasonably uniform field of view over an approximately 900 x 900 x 300 μm (X, Y, Z) field of view. The vignetting at the edges of the

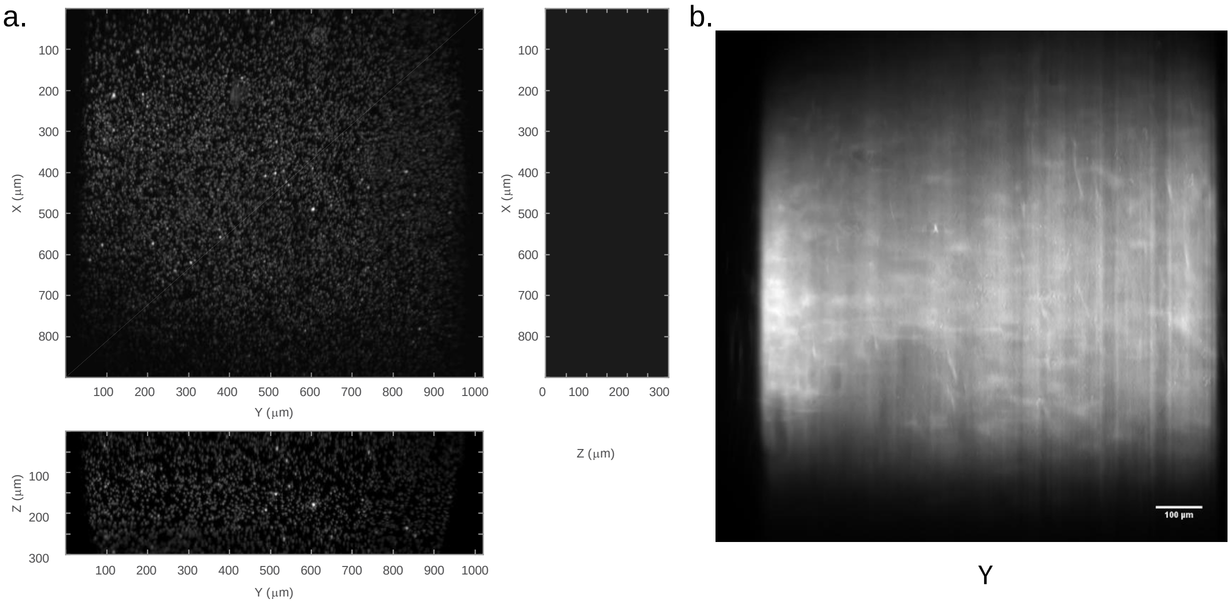

Figure 2.17: *Field of view characterization of SCAPE2b*
a. *1 µm beads distributed through an agar phantom over a field of view of 900 x 900 x 300 µm* ***b.*** *Image of a flat piece of fluorescent tape placed at the focal plane illustrate the uniform distribution of intensities over most of the field of view*

scan field of view (**Figure 2.17**b) are a function of throughput, with excitation throughput decreasing to zero at one edge of the scan field and the detection throughput decreasing at the other. The fall-off in intensity as a function of depth is dependent on the Gaussian properties of the light sheet.

To measure the system's maximum optical resolution, I opened the slit and replaced the camera tube lens with a 200 mm focal length lens from Thorlabs (*Thorlabs, TTL200*) and imaged 200 nm beads using the procedure detailed in Appendix B. At a magnification of 13.33x, I found that the maximum optical resolution of SCAPE2b was 1.2 x 0.86 x 1.95 µm (X, Y, Z) (**Figure 2.18**ab). These values were calculated as the average FWHMs of cross-sections taken along each of the 3 dimensions of the 10 beads found at the beam waist. However, SCAPE2b is normally used at lower magnifications. In this case, in-plane resolution (Y, Z) is a function of the system's alignment and pixel sampling density. The standard in-plane sampling density is ~ 1.39 x 1.15 µm (Y, Z) at a magnification of 4.65x. Out-of-plane resolution (X) remains 1.2 µm, dependent

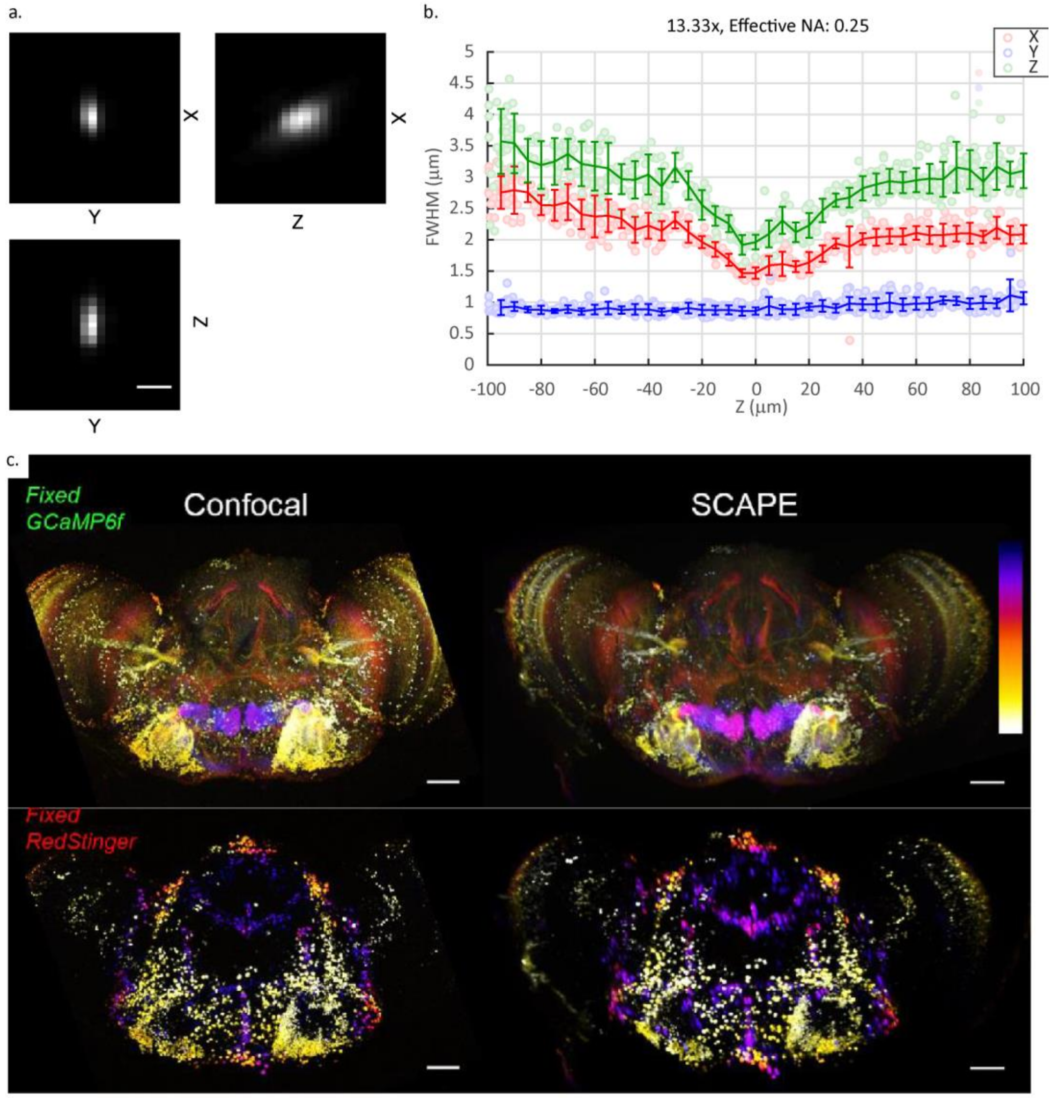

Figure 2.18: *Characterization of SCAPE2b resolution and image quality*
a. *Cross section through an image of a 200 nm bead imaged on SCAPE2b. Scale bar – 2 µm* ***b.*** *Resolution of SCAPE2b when imaging 200 nm beads along each of the 3 dimensions plotted as a function of depth in a non-scattering sample* ***c.*** *Image quality of SCAPE in comparison to confocal microscopy in an ex-vivo flat mount of a sparsely labeled adult Drosophila brain (UAS-GCaMP6f; UAS-RedSinger, Fru-Gal4). Colors represent depth into the sample encoded up to a range of 120 µm. Scale bar – 50 µm. The drosophila explanted brain was provided by Dr. Evan Schaffer and Neeli Mishra from the lab of Dr. Richard Axel. The dataset acquired and figure prepared by Dr. Wenze Li.*

on the properties of the sheet waist. At this lower magnification, the image quality remains comparable to that of confocal microscopy. **Figure 2.18**c shows a comparison of an explanted adult Drosophila brain in which only 2% of neurons were labeled (*UAS-GCaMP6f; UAS-RedSinger, Fru-Gal4*). An image was acquired on SCAPE and then on a Zeiss confocal microscope.

2nd Generation SCAPE Applications

Below, I present a few brief examples of high-speed volumetric imaging using SCAPE2b. The first example is in crawling Drosophila larvae which were originally imaged as a demonstration with SCAPE1.0. A comparison of functional imaging performance between successive generations of the system is presented to highlight the effects of the improvements to system design. The second example is in the nervous system of the zebrafish larvae which allows us to span the potential depth range of the system. Finally, I show the performance of SCAPE2b in a less optically transparent medium, the mouse brain.

Comparison of SCAPE Generations in Drosophila Larva

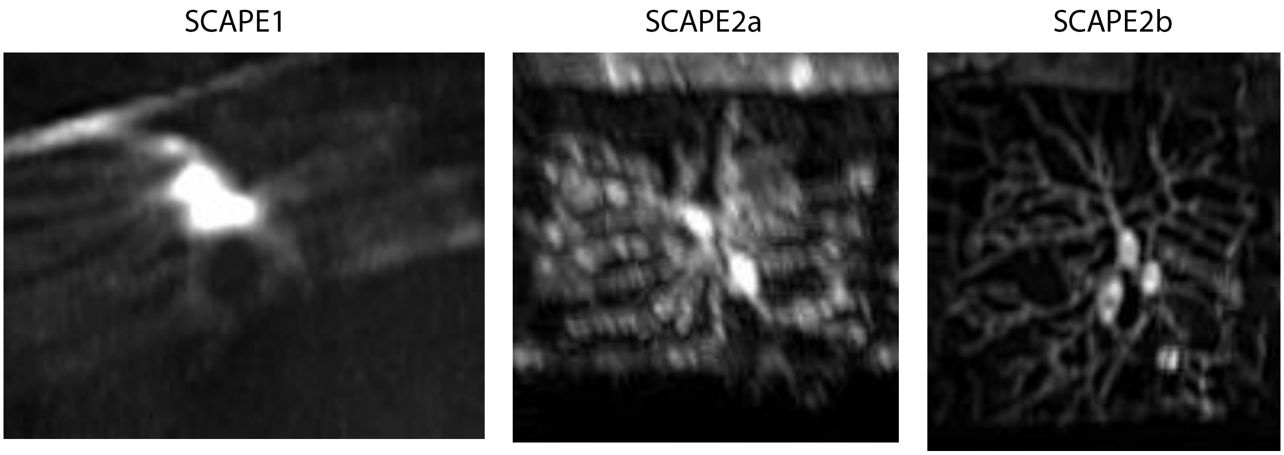

Figure 2.19: *Comparison of image quality between successive SCAPE generations*
Data shows an image of the soma and dendritic processes of vpda neurons in Drosophila larvae (221-Gal4, UAS-CD4tdGFP)

We presented results imaging the Drosophila larvae in (Bouchard, Voleti et al. 2015) in which it was possible to visualize the motion of neuronal soma within the larvae’s body wall during crawling behavior. Later work with SCAPE1 attempting to visualize dendritic structure along with soma position during crawling behavior was only able to visualize cell bodies. **Figure 2.19** shows that dendritic processes when imaged with SCAPE1 were far too dim and fine to be characterized properly. Imaging with SCAPE2a allowed us to clearly visualize dendritic processes extending from the soma for the first time, while improvements in design and alignment made to SCAPE2b allowed these processes to be clearly delineated with high resolution. Imaging with SCAPE2b also allowed clear visualization of nuclei within the soma themselves.

All data in the examples shown was acquired on larvae expressing GFP in vpda neurons in the drosophila body wall (*221-Gal4, UAS-CD4tdGFP*) at 10 volumes/sec. The camera imaged between 1000-2000 fps and the galvo step size was between 2-3 µm. The data has been gamma processed with a factor of 0.5 to improve contrast between the bright soma and the dim dendritic processes. The image was then unsharp-masked slightly to boost the contrast of the dendritic processes. The images are maximum intensity projections of the first 50-100 µm below the surface of the worm to exclude gut autofluorescence. The improved resolution, imaging speed and dual-color capabilities of SCAPE2b was used to characterize the calcium dynamics and dendritic folding patterns of every proprioceptive neuron in the Drosophila larva’s body wall (Vaadia, Li et al. 2018).

Imaging the Nervous System of the Larval *Dario rerio* (Zebrafish)

The zebrafish larva is a useful model organism in the field of neuroscience. It contains ~ 100,000 neurons distributed over a volume that can easily fit within the field of view of a microscope (Ahrens, Orger et al. 2013). Nearly the entire nervous system of the animal can remain optically transparent throughout the imaging period (4-9 days post fertilization) and is among the simplest vertebrate model organisms. Over the course of my graduate work, I have

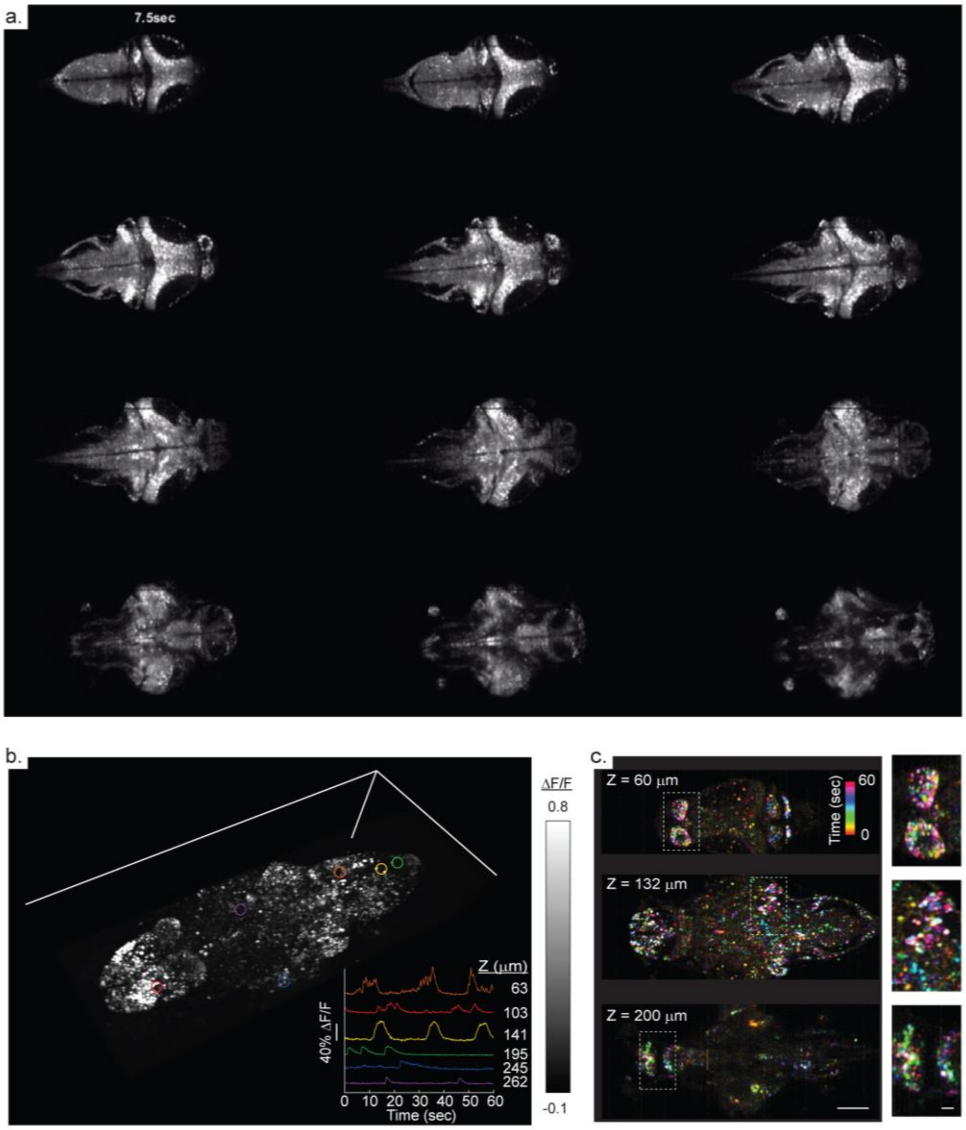

Figure 2.20: *High-speed imaging of zebrafish larva expressing panneuronal nuclear-localized GCaMP6f* ***a.*** *Multiple depth planes of a single volume acquired in 0.167 sec* ***b.*** *Volume rendering of a time-maximum intensity projection taken over all 360 time points over a 1 minute run. (Inset) Time series extracted from 6 neurons drawn from locations within the brain at 6 depth planes within the fish* ***c)*** *Time-encoded color projection of 3 depth planes showing spontaneous activity over a range of brain regions. Insets show ~2x close ups of indicated regions. Scale bars are 100 µm and 20 µm. HuC:H2B-GCaMP6f fish obtained from Janelia. Data acquired in collaboration with Dr. Jeremy Ullman and Dr. David Reutens from The University of Queensland, Australia. Figure adapted from (Hillman, Voleti et al. 2018)*

been fortunate enough to work with a variety of researchers who are studying the visual system, vestibular system, motor systems and more within this organism.

Figure 2.20a shows an example of high-speed SCAPE imaging of neural activity in zebrafish larva at 6 days post fertilization expressing GCaMP6f in the nuclei of all of its neurons.

Here, a field of view of 820x380x260 μm corresponding to 688x135x216 voxels was imaged at 6 volumes per second. More than 1 TB of data was acquired over the course of 40 minutes. This is a demonstration of the system's ability to perform high-speed, functional imaging at rates high enough to resolve neuronal activity. **Figure 2.20**b shows that the SNR was sufficient to extract diverse waveforms of calcium activity from cells distributed throughout the brain. **Figure 2.20**c is a color-encoded projection in which the colors indicate the time at which a specific voxel reached its highest signal level. The dense clusters in the habenula (top) or the forebrain (middle, bottom) show cells with wildly different coloration, further demonstrating how the system is capable of differentiating activity patterns from dense clusters of cells that are situated adjacent to one another. In comparison to conventional light sheet which have also been used to perform functional volumetric imaging in zebrafish larva (Ahrens, Orger et al. 2013), an oblique light sheet has the additional advantage of avoiding illumination of the eyes from the side, reducing ocular stimulation as well as providing access to deeper regions of the brain located behind the eyes.

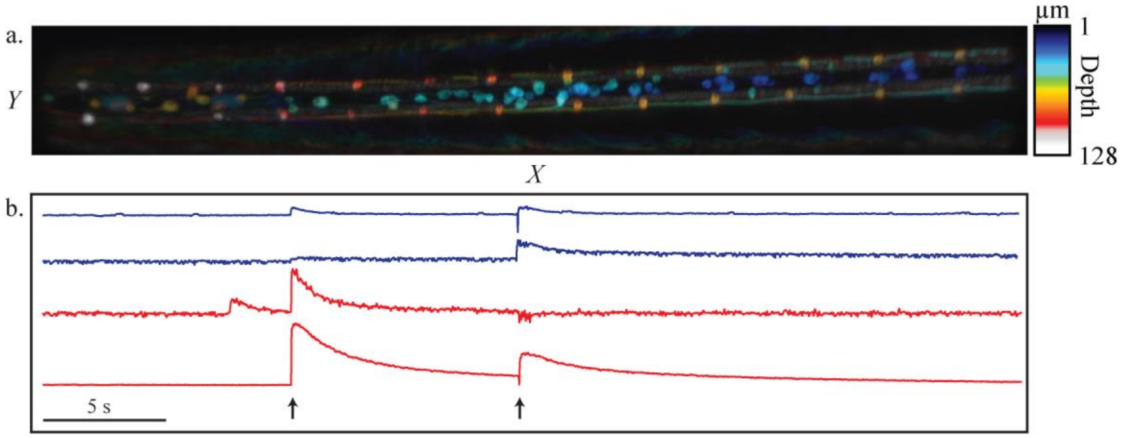

Figure 2.21: *SCAPE imaging of neurons in living zebrafish spine.*
a. *Depth encoded projection of transgenic zebrafish line labeling motor neurons and interneurons (Tg(213A:Gal4; UAS:GCaMP6F)). Interneurons labeled in blue/green and are found ~30 μm above the motor neurons labeled in red/orange. Entire volume was taken in 2 seconds. (Scale bars - 100 μm)* ***b.*** *Functional data taken from run acquired with volume rate of 50 Hz. Activity extracted from two motor neurons (red) and interneurons (blue) in response to electric stimuli indicated by arrows. Data acquired in collaboration with Mingyue Wu and Dr. Claire Wyart from Le Institut du Cerveau et de la Moelle Epinière, France.*

The larval zebrafish spine contains central pattern generators involved in locomotion that need to be imaged at higher volume rates at the cellular level to capture the relationship between behavior and neuronal firing. The spine itself contains a number of cell types residing in a tubular region over a millimeter in length. To permit imaging of this structure with SCAPE microscopy, larvae were embedded in 1% agarose at 3-4 days post fertilization as detailed in Appendix D. The rostral-caudal axis of the spine was precisely oriented along the Y axis in order to allow imaging of the entire spine in as small of an X range as possible. The variable slit controlling the light sheet's numerical aperture was fully opened in order to improve sectioning ability and narrow the depth of field to approximately 80 microns. The sample was also tilted so that the cells within the spinal cord occupied the minimum number of rows on the camera. The structural image in **Figure 2.21**a was filtered using total variation denoising in Fiji, and was gamma corrected with a factor of 0.5 to enhance contrast. With a sampling density of 0.5 microns in the X dimension, it is possible to visualize axonal tracts extending from single interneurons and motor neurons towards the brain. The functional data in **Figure 2.21**b was acquired by maximizing the camera's frame rate over a narrow ROI. A 785 x 80 pixel region on the camera (representing an in-plane field of view of 1084 x 91 µm) was acquired at 2605 fps. The galvo swept over a range of 101 µm with a camera frame being acquire every 1.95 µm. This allowed us to achieve a volume rate of 50 Hz and the lower sampling density nevertheless permitted visualization of all cell bodies. Responses from four neurons within the zebrafish spine are shown in Figure 3b, validating the system's ability to acquire high-fidelity calcium signals at high volume rates. High-speed imaging of this sort permits us to not only see calcium activity, but also potentially correct for motion artefacts and resolve timing differences of firing events between individual neurons.

Depth Penetration into the Mouse Brain

Larger, scattering samples such as the brain of a live mouse place different demands on the capabilities of the system. For SCAPE1, we characterized the depth penetration of the system using 488 nm excitation by imaging scattering phantoms with controlled scattering/absorption coefficients, as well as vasculature within the mouse brain (Bouchard, Voleti et al. 2015). In a comparison we performed between 2-photon microscopy and SCAPE1.0, we showed that small capillaries could be visualized in the mouse brain 150 µm below the surface of the cortex, with large diving vessels clearly visible beyond 200 µm. SCAPE2b has similar performance with respect to depth penetration both within the green (500-550 nm) and red (580-650) emission ranges.

To image cortical vasculature, the mouse was anesthetized with urethane and a transparent cranial window was placed above the somatosensory cortex as detailed in Appendix D. We imaged GFP in the endothelial walls of the vessels down to a depth of ~ 200 µm (**Figure 2.22**). It is also possible to image the vascular lumen via intravenous injections of fluorescent

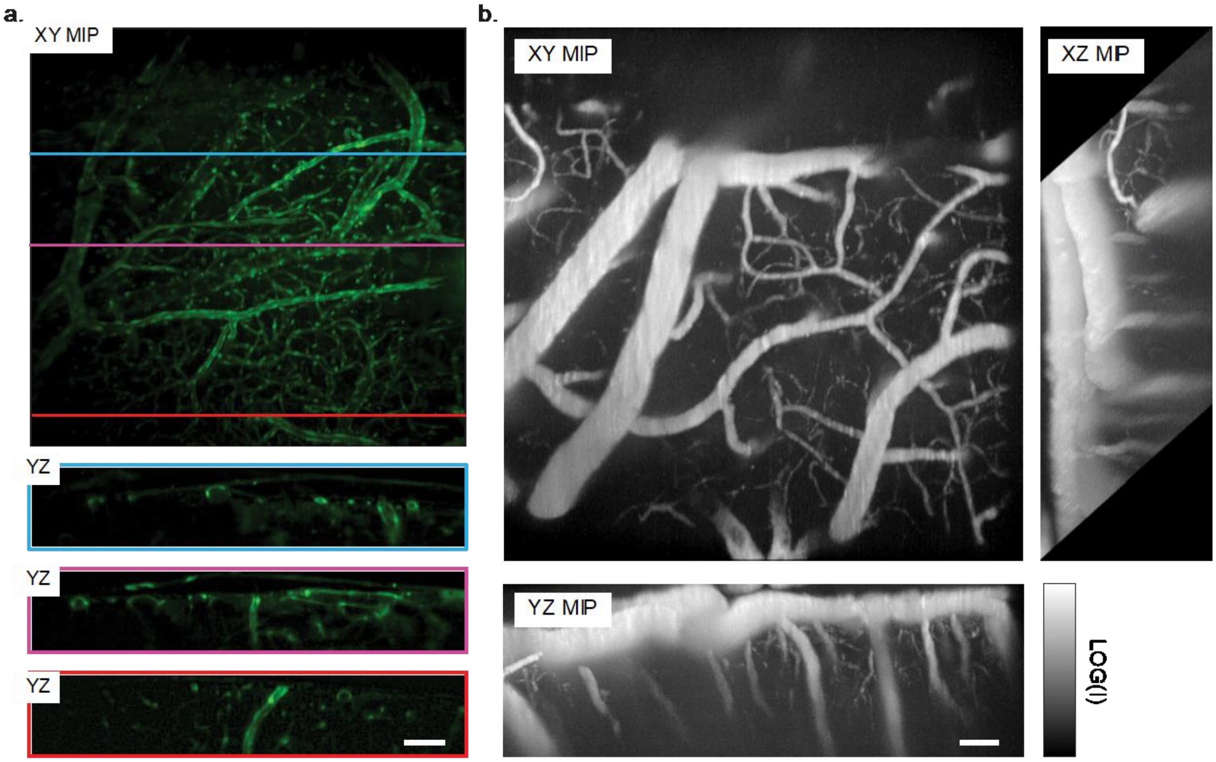

Figure 2.22: *SCAPE imaging of vasculature in the adult mouse brain*
a. *(Top) Maximum intensity projection in XY plane showing GFP in the endothelial cells of the cortical vessels of transgenic mice* (Rag1$^{\mathrm{tm1Mom}}$Tg(TIE2GFP) 287Sato/J). *Field of view is ~1 mm x 1 mm (Bottom) Cross-sectional YZ planes showing cortical vessels imaged up to 200 µm below the surface of the cortex. Raw data is shown after a gamma correction with a factor of 0.5 to compensate for attenuation at deeper layers of the brain. Scale bar – 100 µm* ***b*** *Maximum intensity projection along each of the 3 dimensions in which the intravascular lumen was labeled with Texas-Red dextran. Scale bar – 50 µm.*

dyes. **Figure 2.22**b shows maximum intensity projections of a single volume in which Texas-Red was injected into the cortical vasculature. Similar to GFP, the diving vessels can be visualized to a depth of ~ 220 µm. The data in **Figure 2.22**b was acquired at 10 volumes/sec in order to characterize vascular dilations occurring in 3D (not shown). The ability to use the image splitter to perform multi-channel imaging allows us to probe, for example, calcium activity in a variety of cellular compartments such as the endothelium, smooth muscle cells, neurons or glia simultaneously. In the Hillman lab, dual color imaging of the mouse brain has allowed simultaneous measurement of activity in these compartments and vascular dilation.

Chapter 3 – Biological Applications of SCAPE Microscopy

The ability to perform 3D imaging at volume rates matching - or even exceeding - the 2D frame rates of previous systems like point-scanning confocal and two-photon microscopy made SCAPE an attractive imaging choice for a number of research groups within and outside of Columbia University. Each group's application came with its own model organism, experimental preparation and research question that served to test the versatility of the system along various axes of its performance. The axes of performance explored herein are volumetric imaging speed, resolution, phototoxicity, field of view and adaptability to different experimental paradigms.

In this chapter, I first briefly lay out the system's various orientations to showcase its adaptability. Later subsections chronicle my work in each model system: zebrafish heart, Caenorhabditis elegans brain and cleared/uncleared tissue preparations. I describe the imaging challenges presented by each sample, and then summarize the capabilities of prior imaging systems that currently serve as the state of the art for that application. I detail any relevant modifications I made to SCAPE as well as how the sample was imaged, and finally present the results of my work.

Adaptability and Versatility

Benchtop microscopes are generally built to accommodate an upright or inverted configuration. Upright configurations image the sample from above, whereas inverted configurations image the sample from below. These systems are also attached to robust metallic frames that couple the sample or slide holders to the microscope body containing the optical trains necessary for imaging. As a result, labs are confined to only imaging the samples that are compatible with the microscope frame. For example, inverted setups might be favored in tissue culture settings that grow cells on glass-bottom petri-dishes. However, they won't be able to accommodate a zebrafish brain which is best imaged from the top in order to avoid aberrations caused by imaging through scattering tissues such as the blood vessels and the yolk sac. In vivo experiments in the mammalian brain also require top-down access in order to image the brain through a coverslip into a cranial window, however the zebrafish heart can only be imaged from the animal's ventral side so an inverted configuration is ideal if one is to avoid rotating the animal into an unnatural position.

Recently, more and more commercial entities are recognizing the value of such versatility. After all, the "bread-and-butter" experimental setup of a given lab might – over the course of an instrument's lifetime – change to outgrow all available space around a microscope body or require a different orientation between the sample and objective. Commercial systems such as Bruker's Ultima® and Thorlabs' Bergamo® II two-photon microscopes decouple the sample stage from the microscope itself, leaving more room for customization around the objective lens. These systems are geared to work alongside the electrophysiology, virtual reality or behavioral rigs that were discussed in the first chapter. Certain multi-photon systems (eg: Thorlabs Bergamo II and multi-photon Mesoscope) are even offering an option to articulate the objective lens around a set focal point in order to image through the cranial windows at the ideal angle.

Such versatility was a key consideration when I made design choices with SCAPE microscopy. SCAPE is built in a multi-tiered configuration in which the optical components sit on a breadboard that is independent of the vibration isolated table upon which the entire system rests. The breadboard is elevated using fixed-length pedestals to a height of 6 to 10 inches above the optical table which allows for ample space around the objective lens for auxiliary equipment pertinent to the experiment. See **Figure 3.1** for examples of various imaging configurations that SCAPE has been used for.

Upright Configuration

C. elegans
Zebrafish brain
Zebrafish spine
Mouse brain
Drosophila Larva
Drosophila adult brain
Retinal Flatmount

Side-facing Configuration

Imaging Plant Roots

Inverted Configuration

Crawling C. elegans
Zebrafish Heart
Drosophila Larva
Cleared Brain Tissue

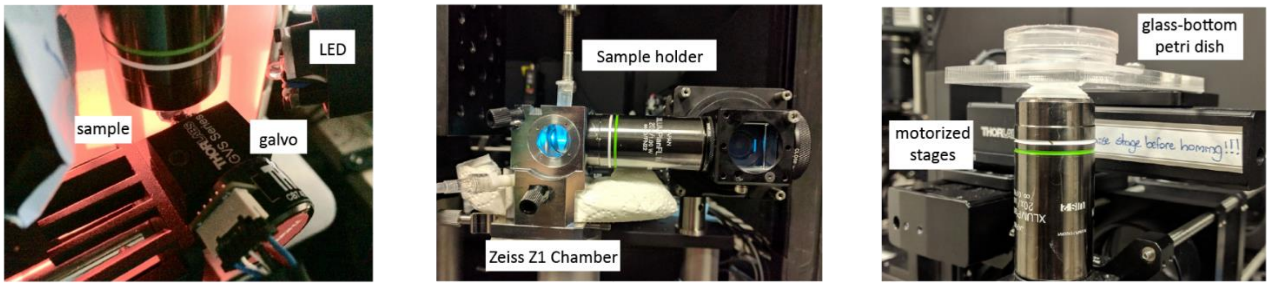

Top-down imaging of zebrafish larva on galvo with LED stimulation

Side-face imaging of vertically mounted plant root

Inverted imaging through a glass bottom petri dish

Figure 3.1*: Various sample preparations which require multiple configurations with respect to the primary objective lens (Left) Zebrafish imaged on a galvo-mirror with an LED stimulus presented from below (Middle) SCAPE coupled to the imaging chamber designed for the Zeiss Z.1 Light Sheet*

SCAPE's stationary objective lens can be oriented at a wide range of angles, from in-plane to the optical path (to image a horizontal plan) to any of 360 degree angles provided by a rotating 90 degree turning mirror. Most commonly, we use SCAPE in an upright or inverted configuration. We have also used the system in a horizontal configuration to image samples of plant root placed within a fluid-filled sample chamber (taken from the Zeiss Z1 microscope) used in conventional light sheet imaging geometries.

Imaging the Beating Heart of the Larval *Dario rerio* (Zebrafish) - Speed

The zebrafish heart is a popular model for studying cardiovascular development and regeneration. There are over a thousand mutations identified in hundreds of genes within the zebrafish (Nusslein-Volhard 2012), with dozens of mutants identified relating cardiac development alone (Staudt and Stainier 2012). Many of these genes - such as the *nkx2.5* – are also conserved in the human genome and speak to the clinical usefulness of zebrafish models (Bakkers 2011). A zebrafish embryo with disrupted circulatory flow can also survive up to 5 days post fertilization, making them ideal samples for studying circulatory and cardiac disorders that may disrupt proper blood flow and be terminal in other model organisms (Bakkers 2011, Gonzalez-Rosa, Burns et al. 2017).

Zebrafish embryos are also optically transparent and can be cultivated in large numbers within laboratory settings. They progress from a fertilized zygote to a basic embryo developing a linear cardiac tube capable of active peristalsis by 24 hours post fertilization (hpf). Differentiation between the atrium and ventricle occurs between 24-48 hpf, with the two chambers manifesting sequential contractions by 36 hpf (Glickman and Yelon 2002). By 72 hpf, valvular leaflets within the atrioventricular (AV) canal start to form, becoming fully attached to the cardiac trabeculae by 7 days post fertilization (dpf) (Staudt and Stainier 2012). As a result, early to late stages of cardiac development within a single animal can be studied at the cellular level over the course of a few days. These aspects of the zebrafish embryo encourage its use for rapid, high-throughput screening for drug discovery or phenotypic characterization of genetic mutants (Letamendia, Quevedo et al. 2012, Spomer, Pfriem et al. 2012, Kithcart and MacRae 2017).

From a practical imaging standpoint, embryonic hearts are small enough to entirely fit within the field of view of an optical microscope (< 500 x 500 x 500 µm) and are optically transparent allowing laser sources straightforward access to both cardiac chambers for fluorescence imaging. This optical access makes the zebrafish heart ideal for more detailed cellular-level studies relating long-term development (on the order of days) to short term behaviors (on the order of seconds) such as cardiac conduction and blood flow. However, the perpetual motion of the heart complicates high-speed volumetric imaging required for such studies, speaking to the need for imaging systems that are capable of handling this challenge.

Current Approaches and State of the Art

The zebrafish heart beats 2 to 4 times every second. While imaging at or near these rates can allow one to ascertain variations in heart rate as a function of mutation or drug response, such speeds are not sufficient to resolve the motion of individual cells. Previous work using particle image velocimetry based techniques suggest that red blood cells can reach speeds up to 3.5 mm/s in an 70 hpf embryo (Lee, Moghadam et al. 2013). Studies using light sheet microscopy show that cardiomyocytes within the beating heart can reach speeds up to 1 mm/s (Vermot, Fraser et al. 2008). Data quality in both of these cases will in large part be determined by the system's ability to deal with the resulting motion blur.

As an example, let us consider a camera acquiring at 100 fps performing 2D imaging of blood flow through the heart. For a particle traveling at 3.5 mm/sec, an acquisition time of 10 ms represents a transit distance of 35 µm, close to 4x the diameter of a red blood cell. At such high speeds, the red blood cell (RBC) would appear blurred precluding accurate assessment of cellular position and velocity. An acquisition time of 1 ms (1000 fps) would represent a transit distance of 3.5 µm, or 50% of the RBC's cellular diameter. Analogously, if one were performing 3D depth-sectioned imaging, one would need to ensure that all of the planes over the thickness of a single red blood cell are in similarly short duration. As a result, cellular level image of the beating zebrafish heart can require acquisition rates upwards of a hundred volumes per second. Optical gating techniques rely on the periodicity of the heart in order to achieve high volume rates and have been combined with many imaging modalities including confocal spinning disk microscopy, confocal line scanning microscopy, OCT, bright field microscopy (Taylor 2014). However, brightfield microscopy does not provide depth sectioning and OCT does not take advantage of fluorescence contrast. As described in previous sections, confocal spinning disk and confocal line scanning overexpose the sample to light during volumetric acquisitions causing extensive photobleaching. Due to its high single-plane imaging speeds (100's of Hz) and relatively low levels of phototoxicity, light sheet microscopy has become a useful tool in studying both the development and function of the zebrafish heart (Weber and Huisken 2015).

There are two main types of optical gating techniques using light sheet microscopy: prospective gating and retrospective gating:

Prospective gating approaches only trigger the acquisition of a z-plane at a pre-selected point within the cardiac phase. Here, a secondary input source – such as a brightfield channel – is required in addition to the primary light sheet microscope. This secondary input source is used to ascertain the cardiac phase and predict the time at which to trigger the acquisition. Volumetric imaging is achieved by acquiring a single camera frame at each z-plane, sequentially stepping through all of the depths within the sample (Taylor, Girkin et al. 2012). Because each z-plane requires a single heartbeat, the time needed to image an N-plane volume is at minimum equivalent to the duration of N heartbeats. Because all of the z-planes are acquired at a single point within the cardiac phase, prospective gating does not provide short-term information about the behavior of the heart (eg: motion of the cardiac wall or blood flow) and has primarily been used for longitudinal imaging studies over the course of hours/days (Taylor, Nelson et al. 2019).

In comparison, retrospective gating techniques do not require triggered acquisitions and illuminate a single plane within the heart for multiple heartbeats (1-2 sec = 2-4 heart beats). Volumetric imaging is performed by sequentially stepping the light sheet through each successive depth within the sample. The videos acquired at each z-plane are then temporally co-aligned and locked to the same cardiac phase, resulting in a 4D reconstruction with an "effective" volumetric imaging speed equivalent to the single-plane frame rates (Mahou, Vermot et al. 2014, Mickoleit, Schmid et al. 2014). Imaging a plane at 400 fps would theoretically result in a reconstructed volume rate of 400 volumes/sec. However, the actual time to acquire a single volume can be greater than a minute (1-2 seconds/plane * N planes), while the overall duration of a volumetric reconstruction is limited to the duration of a single plane acquisition (on the order of seconds). Furthermore, while retrospective gating techniques do provide information about the motion of cells or calcium conduction in the cardiac wall (Mickoleit, Schmid et al. 2014, Weber, Scherf et al. 2017), this method continues to rely on cardiac periodicity. As such, it is unsuited to the study of aperiodic behaviors such as arrhythmias or blood flow.

There have previously been demonstrations of high-speed light sheet microscopy in the zebrafish heart that do not rely on optical gating. SPIM systems that rapidly scan the sheet through the sample, and refocus the detection objective using electrically tunable lenses (ETL) have achieved imaging speeds up to 60 volumes/sec (Fahrbach, Voigt et al. 2013, Mickoleit, Schmid et al. 2014). Because conventional SPIM systems utilize separate orthogonal light paths for excitation and detection, this approach requires synchronization between the ETL and the galvanometric mirror used to scan the light sheet through the sample. The ETL is un-ideal for high-speed axial scanning for a number of reasons. The axial scan range of the lens decays exponentially as a function of driving frequency; an ETL used to axially scan the image plane through a 20x objective will scan over 240 µm when driven at 10 Hz but only 80 µm when driven at 100 Hz. ETL's also display unstable resonance when driven above certain frequencies, which preclude the usage of non-smooth waveforms as driving functions (eg: sawtooth). Finally, the usage of smooth sinusoidal driving frequencies means interplane spacing between adjacent depths will be non-uniform.

Modifying SCAPE to Image the Zebrafish Heart

Here, we utilize SCAPE microscopy to track individual red blood cells as they flow through the beating heart, as well as analyze cellular level calcium transients within the cardiac wall of the beating and paralyzed hearts. Like ETL-based SPIM systems, SCAPE is also a light sheet imaging technique that does not rely on optical gating. However, unlike ETL-based techniques, we do not need to synchronize two separate optical components in order to maintain the alignment between our light sheet and the detection plane; the confocal scanning and descanning paradigm does this automatically with a single mirror. And as mentioned previously, the galvo mirror can be driven at hundreds of Hz with sinusoidal waveforms with little loss in uniformity or scan range.

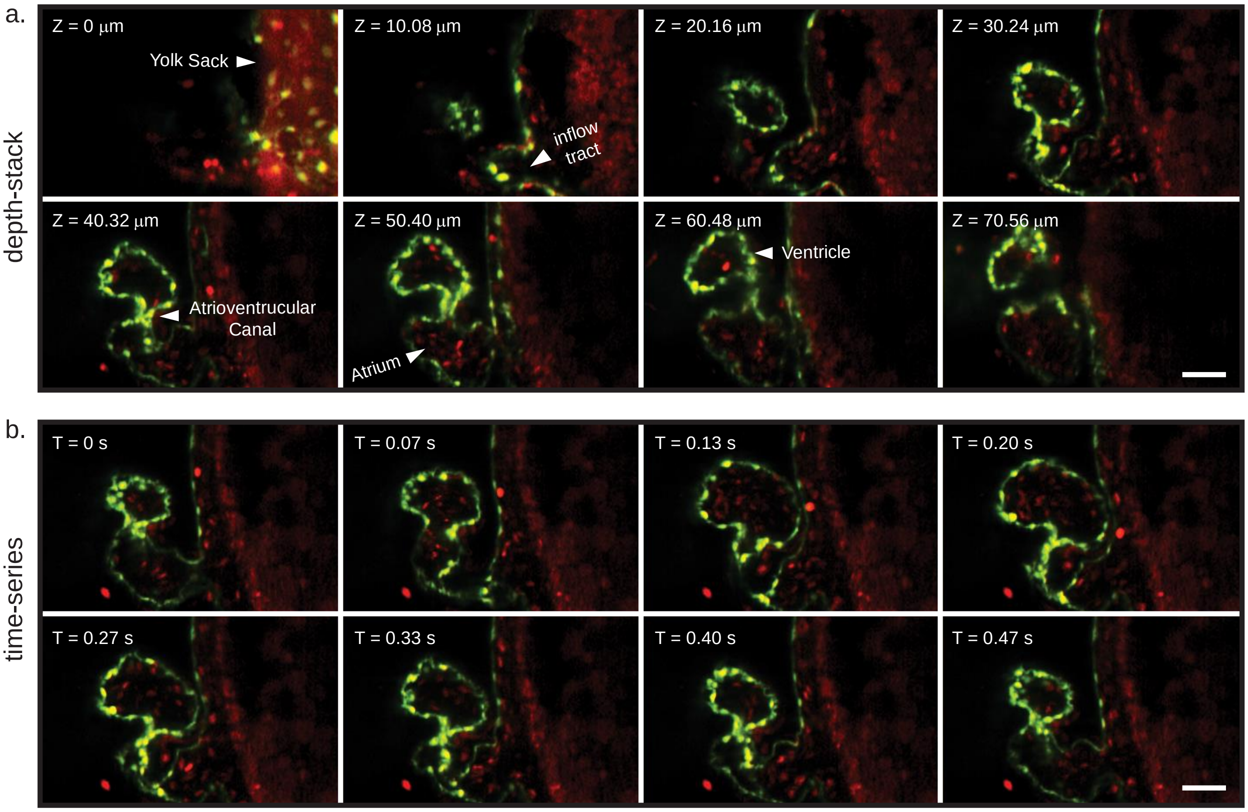

Figure 3.2: *Dual-color imaging of beating zebrafish heart using SCAPE2b at 15 volumes/sec*
a. *Depth stack of a single volume acquired in 0.066 sec* ***b.*** *Time series of a single depth plane 37 µm below the surface of the sample over the course of one heartbeat, starting with atrial contraction and ending at ventricular systole. Scale bar – 50 µm Images were acquired at 15 volumes/sec. Data acquired in collaboration with Caitlin Ford and Dr. Kimara Targoff at Columbia University.*

Without any modifications, SCAPE2b can perform 4D light sheet imaging at 10-70 volumes/sec over the entire zebrafish heart. To image blood flow within the heart, a ~72 dpf larva expressing GFP within the cytosol of cardiac myocytes and dsRed in the red blood cells (*Tg(flk1:EGFP)*^{s843}*; Tg(gata1:DsRed)*^{sd2}). The zebrafish embryos were mounted as described in Appendix D. Both fluorophores were excited with a 488 nm laser with multi-color emission achieved via the custom image splitter with a 560 LP dichroic, 525/45 nm bandpass emission filter for the green channel and 618/50 nm bandpass emission filter for the red channel. The region on the camera sensor (Andor Zyla 4.2) was cropped to a field of 1400x120 pixels or 1940x141 µm (Y, Z) in order to achieve frame rates of 1736 fps while still keeping the sample in the field of view. By stepping the light sheet along the x-dimension in 1.95 µm step

Sample / speed	**Camera FPS / Exposure Time**	**Field of View (x, y, z), μm**	**Sampling Density (x, y, z), μm**	**Number of Pixels (x, y, z)**	**Volume Rate (Hz)**	**Pixel Rate (Hz)**
Zebrafish atrium (Zyla)	2893 fps/ 0.48 ms	94 x 700 x 68	**4.7**x1.4x1.14	**20**x500x60	152.3 Hz	86.7 MHz
Zebrafish atrium (HICAM)	28885 fps/ 0.034 ms	94 x 700 x 68	**4.7**x1.4x1.14	**20**x500x60	1444 Hz	867 MHz
Zebrafish atrium (HICAM)	28885 fps/ 0.034 ms	94 x 700 x 68	**2.0**x1.4x1.14	**47**x500x60	614.6 Hz	867 MHz
C. elegans (Zyla)	1860 fps/ 0.5 ms	300 x 690 x 65	1.5x0.69x0.59	200x1000x110	9.3 Hz	119 MHz
C. elegans (HICAM)	9280 fps/ 0.11 ms	300 x 690 x 65	1.5x0.69x0.59	200x1000x110	46.4 Hz	1.02 GHz
Zebrafish spine (Zyla)	2605 fps /0.38 ms	101 x 1084 x 91	1.95x1.4x1.14	52x785x80	50.07 Hz	164 MHz
Zebrafish spine (HICAM)	20474 fps/ 0.048 ms	101 x 1084 x 91	1.95x1.4x1.14	52x785x80	393 Hz	1.29 GHz
Mouse cortex (Zyla)	2003 fps/ 0.5 ms	**404** x 833 x **103**	2.0x1.27x1.03	**202**x656x**100**	10 Hz	131 MHz
Mouse cortex (HICAM)	18308 fps/ 0.054 ms	**404** x 822 x **103**	2.0x1.27x1.03	**202**x648x**100**	90 Hz	1.19 GHz
Mouse cortex (HICAM)	9558 fps/ 0.1 ms	**808** x 822 x **206**	2.0x1.27x1.03	**404**x648x**200**	23.7 Hz	1.24 GHz

Table 1: *Comparison of imaging parameters between Andor Zyla and HICAM Fluo.*
Blue rows indicate actual values used on SCAPE3 for high-speed acquisitions using the Andor Zyla sCMOS camera on SCAPE2/3. Green rows indicated expected performance using the HICAM Fluo for almost identical camera acquisition ROI's. ROI's were altered slightly to maximize frame rate using the HICAM Fluo.

sizes over a range of 222 μm, we were able to image the entire beating zebrafish heart at 15 volumes/sec (**Figure 3.2**). The image quality is sufficient to visualize the ridges along the cardiac endothelium, as well as individual red blood cells within the atrium. By heavily sacrificing the field of view and sampling density, we were able to image subsections of the heart at higher volume rates. In comparison to optical gating techniques, SCAPE achieves 4D imaging in real time, i.e. the sample only needs to be illuminated for the duration of one cardiac cycle in order to image a single cardiac cycle.

However, the achievable volume rate is limited by the maximum achievable pixel rates of the camera. The various sCMOS sensors on the market (Andor Zyla, Hamamatsu Flash, PCO Flash), have maximum achievable pixel rates of ~417 Mpixels/sec. In comparison, CMOS cameras on the market are capable of exceeding this rate by an order of magnitude (eg: PCO.dimax HS4 can acquire a 2000x2000 ROI at 2277 fps for a pixel rate of 9.11 Gpixel/sec).

However, the short exposure times used at these frame rates can significantly degrade SNR. The HICAM Fluo is an ultrahigh speed CMOS camera coupled to an image intensifier capable of acquiring data over a 1280x1024 pixel ROI at 1000 fps resulting in a pixel rate of 1.3 Gpixels/sec. In **Table 1**, I show a brief comparison of expected improvements to speed, sampling density and field of view when using the HICAM Fluo. The theoretical values in Table 2 represent the best performance we can expect from the camera assuming a maintenance in laser powers and SNR.

Installation of the HICAM Fluo involved milling a mounting-plate compatible with the camera's inbuilt screw holes and then replacing the camera/tube-lens unit of a pre-aligned system. Because I had previously designed the camera telescope in a way so that the camera/tube-lens unit is easily removable, this switch did not affect the alignment of the rest of the system. The HICAM outputs a 10 µs TTL pulse at the start of each frame and is capable of accepting an external start trigger. These inputs were connected to an existing SCAPE system's DAQ board, replacing the FIRE and EXTERNAL START triggers that served the same function as for the Andor Zyla.

The microscope was placed in an inverted configuration and 72 hpf zebrafish larvae were prepared as described in Appendix D. A SCAPE2b system shown in **Figure 2.16**c was utilized with the following modifications. The central dichroic mirror of the system found adjacent to the galvo mirror was replaced to permit reflection of both 488 and 561 nm excitation, with transmission outside of these bands (*Semrock, Di01-R488/561-25x36*) For these experiments, the system's magnification and numerical aperture were adjusted to optimize sampling density (~6.21x, effective NA: 0.35). The camera telescope was configured with an Edmund Optics 20x/0.60 (O3), a 70 mm tube lens and HICAM Fluo. The image splitter within the camera telescope utilized two 560 nm long-pass filters *(Semrock, FF560-FDi01-25x36)*, a 525/45 band-pass filter for green emission *(Semrock, FF01-525/45-25)*, and a 618/50 band-pass filter for red emission *(Semrock, FF01-618/50-25)*. An aperture stop was placed in the excitation path between the second and third cylindrical lens (CL2, CL3) in order to crop the lateral extent of the field of view and allow the two color channels to be placed closer together on the camera chip.

Imaging Blood Flow in the Zebrafish Heart

Figure 3.3 shows results obtained in a zebrafish larvae (3-dpf) expressing GFP in the myocardium and dsRed in the red blood cells (*Tg(flk1:EGFP)*^{s843}*; Tg(gata1:DsRed)*^{sd2}) (Traver, Paw et al. 2003, Beis, Bartman et al. 2005). The power at the back aperture was measured as 1.1 mW at 488 nm (575 µW at the sample, calculated as transmission from the back aperture). The fish was restrained in 1.5-2% agarose and dual-color images were acquired. A region of 640 x 148 pixels on the camera sensor (representing an in-plane field of view of 684 x 127 µm and an in-plane sampling density of 1.07 x 0.86 µm along the Y and Z dimensions respectively) was acquired at 12,719 fps on the HICAM Fluo sensor. The galvo mirror was swept over a scan range of 271 µm and with a camera frame acquired every 1.41 µm. The motion of the cardiac wall as well as blood flow can be clearly visualized at these imaging speeds over the course of a 10 second acquisition.

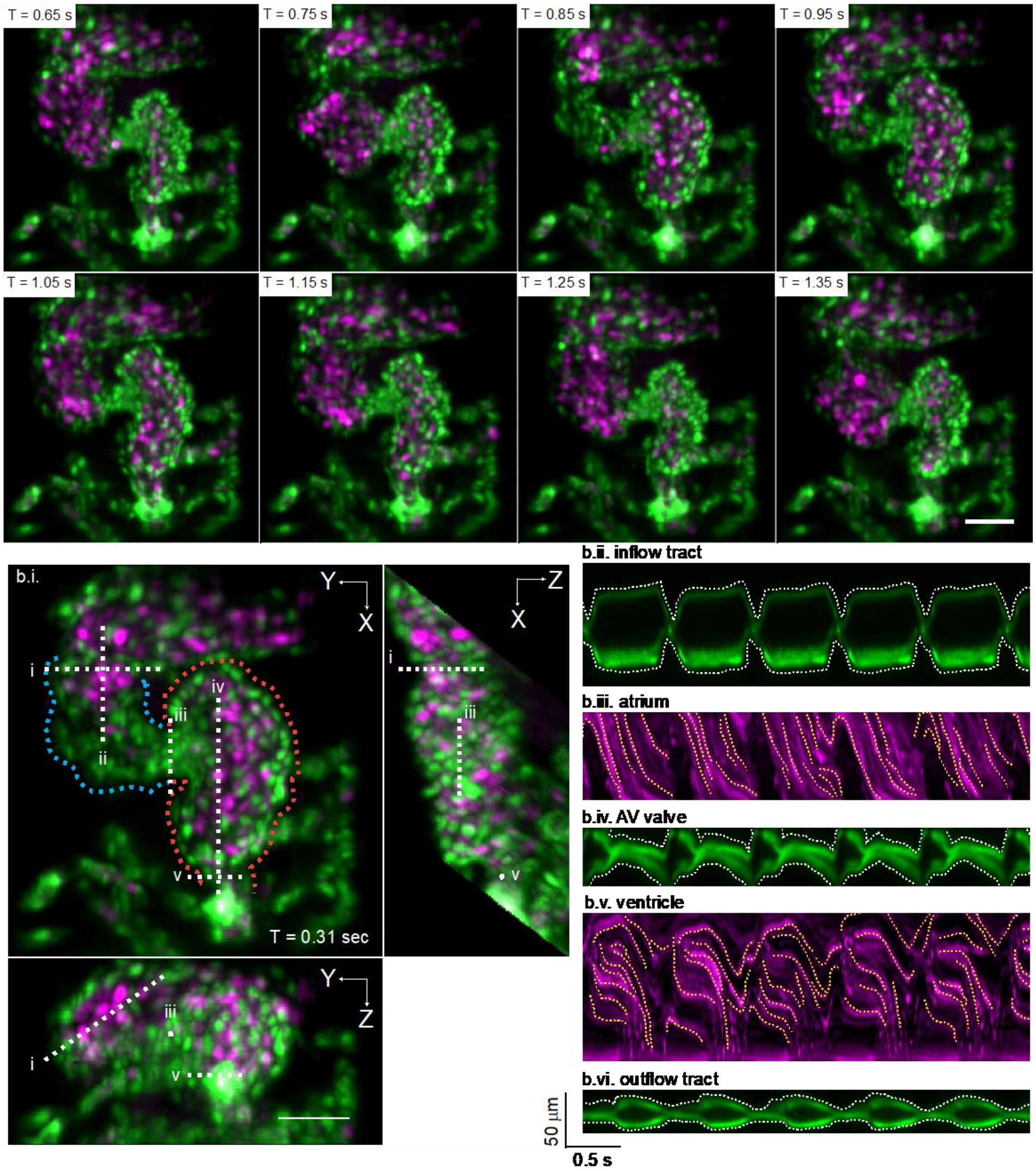

Figure 3.3: *Imaging blood flow in the zebrafish heart at 100 volumes/sec expressing GFP in the myocardium and dsRed in the red blood cells*

a. *Maximum intensity projections along the z-dimension showing 8 time points along a single heartbeat starting with atrial contraction, and ending at the atrial diastole. Each time point was acquired in 0.01 sec and every 10th time point is shown above.* ***b.i.*** *Maximum intensity projection of a single time point in the zebrafish heart acquired at 100 volumes/sec shows the heart at ventricular diastole (T = 0.31 sec). Outlines of the atrium and ventricle are shown in red and blue respectively* ***b.i-vi.*** *Kymographs taken along the white dashed lines shown in (a.i). The periodic opening and closing of the the green kymographs shows that data is truly axially resolved, and the yellow lines in the red kymographs indicate the tracks of red blood cells along the plane. Zebrafish were provided by Caitlin Ford and Dr. Kimara Targoff.*

Unlike optical gating techniques, the acquisition happened in real time, i.e. the sample only needs to be illuminated for the duration of one cardiac cycle in order to image a single cardiac cycle.

The two channels were registered to one another and the data was affine transformed into cartesian space. The principle components of every pixel along the time dimension was computed for each channel prior to reshaping (Schindelin, Arganda-Carreras et al. 2012)the camera frames into a 4D dataset. The top 4000 and 850 principle components were kept within the green and red channels respectively which served to remove spurious noise artefacts from the intensifier while keeping intact high-resolution structures such as the cells on the cardiac wall and single red blood cells. The data was up-sampled to have uniform pixel sizes (0.86 µm/pixel) and maximum intensity projections shown. After this data pre-processing, kymographs of the atrium and ventricle were taken. In the dsRed channel, the kymographs showcase trajectories of red blood cells in each of these chambers, and were taken over the collapsed top-down (XY) maximum intensity projections along each of the 2 lines indicated in **Figure 3.3**b (atrium: ii, ventricle: iv). The kymographs of the green channels showcase the dynamics of the inflow canal (i), atrioventricular canal (iii) and outflow tract (v) and were only taken across a single z-plane indicated in **Figure 3.3**b.

By adjusting the acquisition parameters slightly, we could achieve even higher volumetric imaging rates. By acquiring an ROI of 640 x 100 pixels on the camera chip, we achieved a camera frame rate of 18,308 fps. At this speed, we imaged a field of view of 197 x 292 x 78 µm (X, Y, Z) was acquired with a sampling density of 3.9 x 1.07 x 0.86 µm (X, Y, Z) at 321 volumes per second. After acquiring the data shown in **Figure 3.3**, I implemented a 561 nm laser in tandem with the

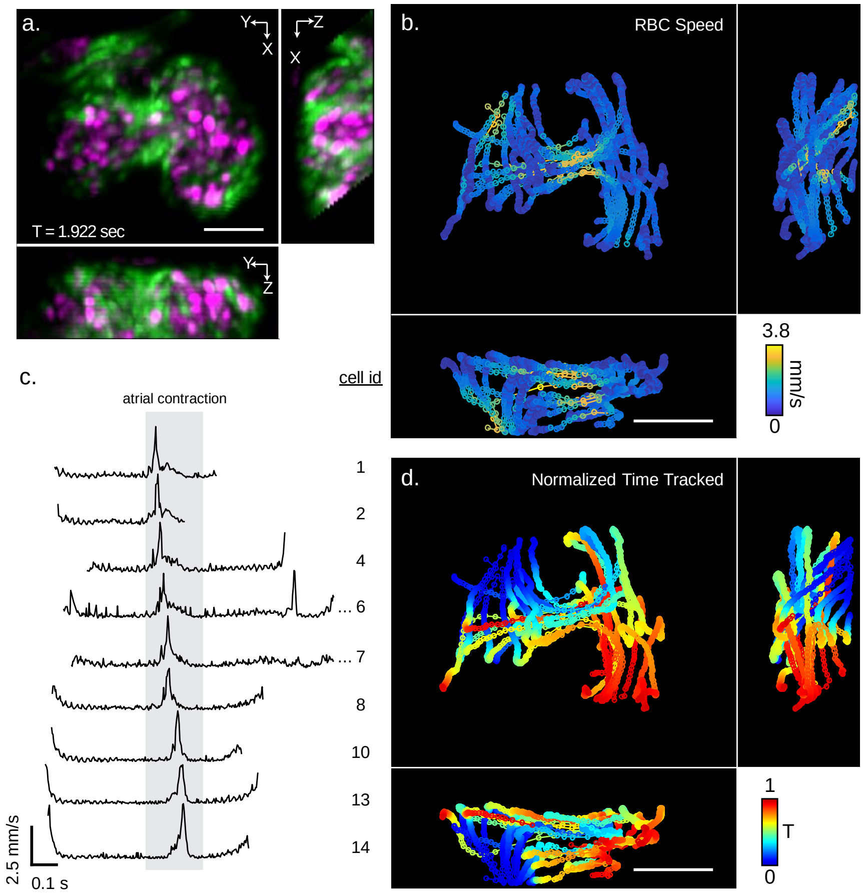

***Figure 3.4:** Imaging the zebrafish heart at 321 volumes/sec*
***a.** Maximum intensity projection of a single time points in the zebrafish heart acquired in 3.1 ms. **b.** Trajectories of 16 RBC's automatically tracked as they move through the heart. Colors encode trajectory of the RBC from the beginning (blue) to end (red) of the track normalized by the overall duration of the track **c.** Speed of selected RBC's as they pass through the atrium. Cell ID corresponds to to the plots of individual cellular trajectories on Figure S4 **d.** Same trajectories shown in (b.ii) color-coded as a function of speed. All scale bars are 50 µm*

488 nm to improve the excitation efficiency of the dsRed channel by 3.9x. The power at the back aperture was measured as 1.8 mW at 488 nm (941 µW at the sample) and 0.4 mW at 561 nm (201 µW at the sample). **Figure 3.4**a shows the maximum intensity projections of a single time point acquired at this speed. At these rates, travel of RBC's through high-speed flow areas such as the atrioventricular canal during atrial systole can be tracked using semi-automated techniques. Co-registered tiff stacks of the zebrafish heart imaged at 321 VPS were upsampled to have uniform pixel sizes (0.86 µm/pixel) and denoised as described above. The red channel was imported into Bitplane's Imaris and red blood cells tracked using the inbuilt particle tracking algorithm. 16 trajectories over 9 consecutive heart beats were manually inspected and shown

along each of the 3 dimensions. The tracks are color-coded as to reflect the duration of the time tracked (**Figure 3.4**b) and instantaneous speeds (**Figure 3.4**d) of cells traveling up to 3.8 mm/sec

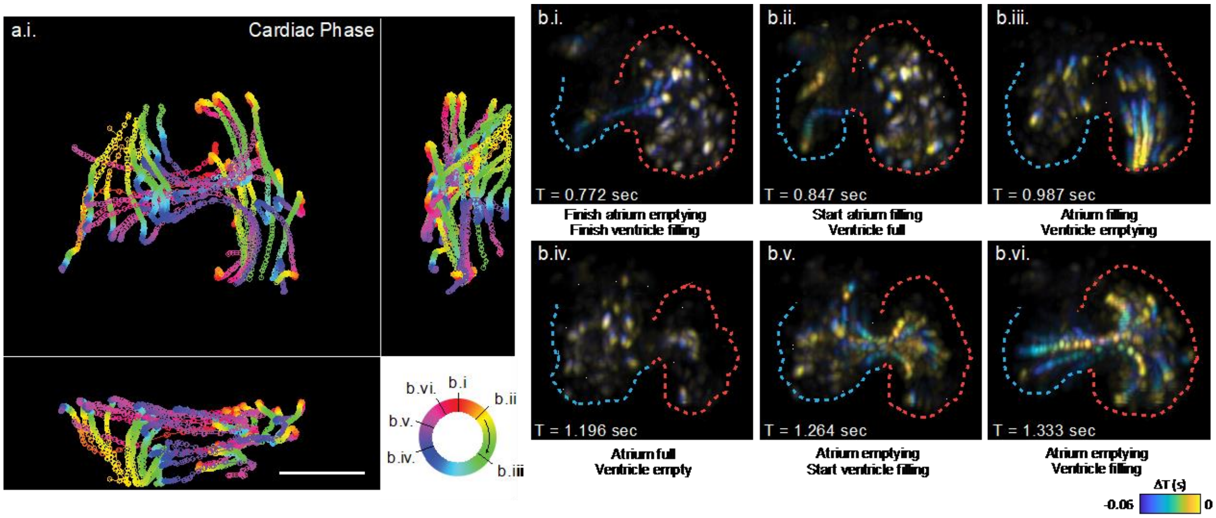

***Figure 3.5**: Zebrafish heart (321 volume/sec) encoded as a function of cardiac phase.*
The circular color-map represents the periodicity of the heartbeat and the montage on the right shows the behavior of the RBC's within the heart and an outline of the atrial (blue) and ventricular (red) cardiac wall at different phases of the cardiac contraction cycle. Scale bar – 50 µm

along each of the three dimensions. Speeds were calculated from the positional information. Semi-automatic tracking was attempted in the data set acquired at 100 volumes/sec however the tracking consistently failed in the high-velocity flow zones of the AV canal.

The cardiac phase of the heart was determined by taking the autocorrelation of the mean signal in the red channel. The trajectories of each red blood cell were co-aligned to one another using the cardiac phase. An illustration of the cardiac phase is shown in **Figure 3.5**a in which the tracks are encoded using a circular colormap to represent the behavior of the heart at a given point in the cell's trajectory. Red represents the end of atrial emptying and ventricular diastole, while green through blue represent ventricular systole and emptying combined with atrial refilling. **Figure 3.4**b shows the speed of a subset of RBC's in this co-aligned space in which peak velocities are achieved during transit through the atrioventricular canal. Note how different RBC's pass through the canal at different points during atrial contraction. The cellular ID's in

Figure 3.4b refer to the cellular ID's shown in **Figure 3.6** which shows a top-down projection of each trajectory individually after having been encoded for the amount of time that the RBC was tracked, cardiac phase and the speed of the cell.

These cells demonstrate a wide variety of behaviors apart from the typical transit through the AV canal. While the majority of cells simply enter the atrium, transition through the AV canal and then exit the ventricle in a single cardiac cycle. However, some cells (12 and 14) remain within the heart over 2-4 heartbeats while cell 2 re-enters the atrium after having entered the ventricle. Such patterns show case behavior that can be readily observed both at 100 and 321 volumes.

This demonstration showcases our ability to perform truly 3-D object tracking on objects moving at speeds upwards of 3.5 mm/sec in incredibly chaotic flow fields. By sacrificing field of view or sampling density in the scan direction, I have previously imaged the heart at rates upwards of 500 volumes/sec with the HICAM Fluo (data not shown). In the zebrafish heart, this increased speed significantly compromised sampling density. However, because the only truly mechanical impediment to imaging speed with SCAPE2b is the linerate of the galvo scanner, achieving rates at or above 1000 volumes/sec in specific circumstances is fully within the realm of possibility with this imaging system. The ability to perform particle tracking at such high rates could also be used for a number of non-biological tracking applications, as well as applications such as elastography or 3D mass-transport characterization.

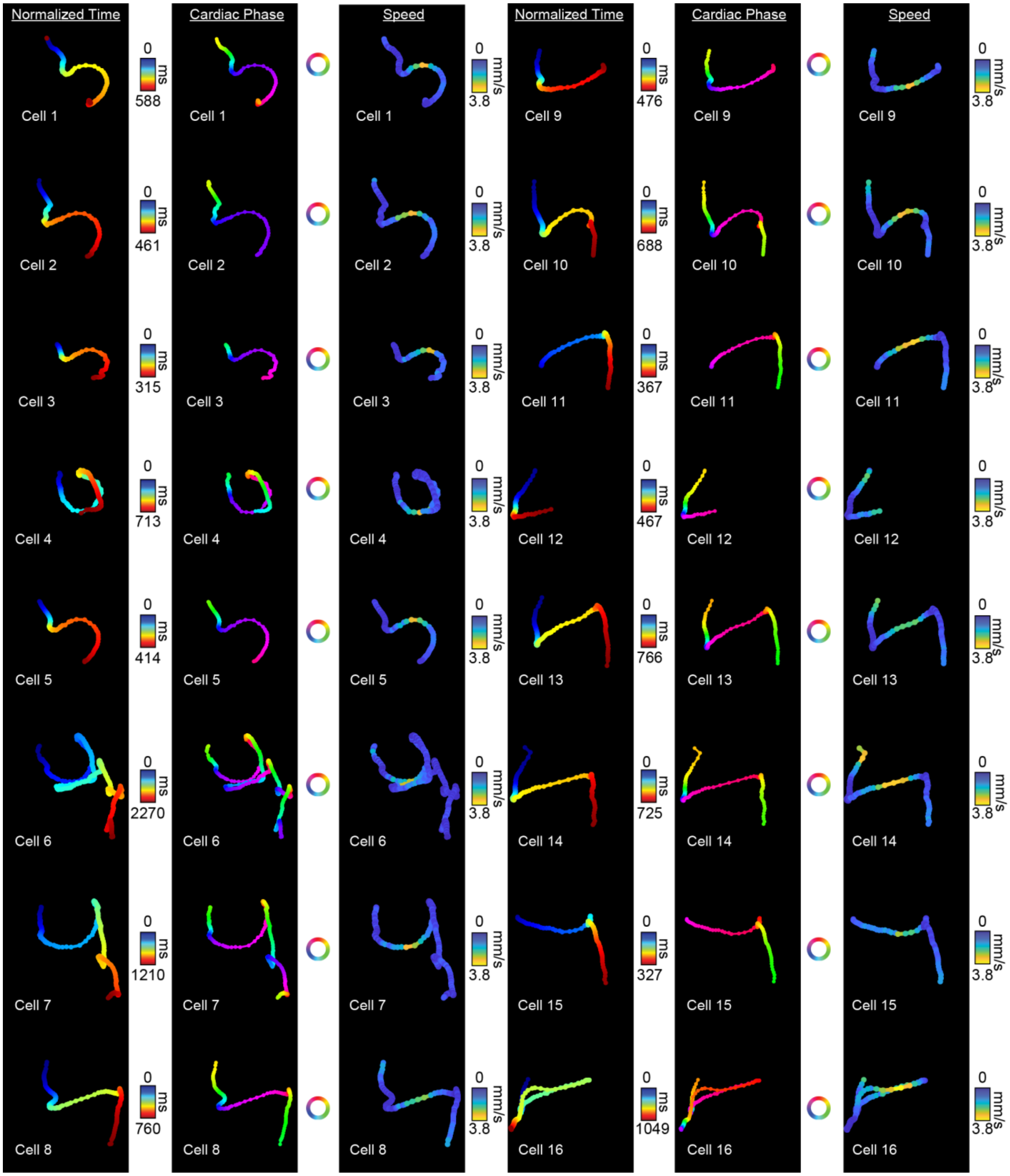

Figure 3.6: *Top-down (XY) projections of the trajectories of 16 red blood cells encoded as a function of normalized time tracked (left), cardiac phase (center) as explained by* ***Figure 3.5****, and speed.(right)*

Imaging Calcium Activity in the Zebrafish Heart

These high imaging speeds also allow us to analyze calcium dynamics in a beating zebrafish heart at the single cell level. A 3-dpf zebrafish larva expressing dsRed within the cardiomyocyte nuclei and GCaMP in the myocardial cytosol (*Tg(myl7:GCaMP)*^{s878}*; Tg(-5.1myl7:nDsRed2)*^{f2}) was mounted as described in Appendix D (Mably, Burns et al. 2003, Arnaout, Ferrer et al. 2007). This will allow us to track the motion of cells within the cardiac wall as well as extract calcium signals from within them. Both the atrium and ventricle are positioned to be in frame any given time and the sheet is swept from the inflow valve to the bulbous arteriosus.

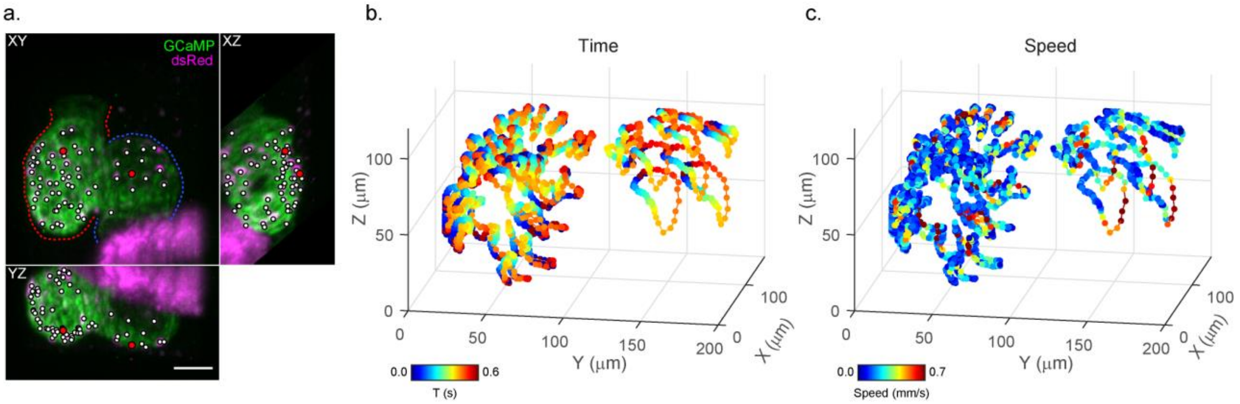

Figure 3.7: *Imaging calcium dynamics in the beating zebrafish heart at 100 volumes/sec*
a. *Maximum intensity projections along each dimension of a single time point of the zebrafish heart acquired in 0.01 sec expressing cytosolic GCaMP and nuclear localized dsRed in the myocardium. The atrium is outlined in blue and the ventricle is outlined in red. White dots indicate the positions of 67 tracked cells and the two red dots indicate ventricular and atrial cell analyzed in* ***Figure 3.8****. Scale bar – 50 µm* ***b.*** *Trajectories within the beating heart in which the colors encode the time at which the cellular nuclei were in that particular position* ***c.*** *Same trajectories shown in (b) but colors encode speed of the heart. Zebrafish were provided by Caitlin Ford and Dr. Kimara Targoff. Tracking the cellular trajectories in both the beating and anesthetized heart was performed by Dr. Chentao Wen and Dr. Kotaro Kimura*

We imaged a region of 640 x 180 pixels on the camera sensor (representing an in-plane field of view of 684 x 155 µm and an in-plane sampling density of 1.07 x 0.86 µm along the Y and Z dimensions respectively) at 10,568 fps. The galvo swept the sheet through a scan range of ~ 180 µm taking a camera frame every 2.09 µm. The volume was acquired at 100 volumes/sec and imaged with both 488 nm and 561 nm excitation. The power at the back aperture was measured as 1.5 mW at 488 nm (785 µW at the sample) and 1.6 mW at 561 nm (837 µW at the sample). A 5 second scan was acquired on the beating heart.

A subset of cardiac nuclei in both the atrium and ventricle were tracked using a deep-learning, U-net based cell segmentation algorithm (Wen, Miura et al. 2018). This subset was manually inspected for tracking errors and 67 myocytic nuclei within the beating heart were selected for further analysis. GCaMP and nDsRed2 signals from each cell were extracted using these cell locations using an 10x10x10 µm square region of interest from each of the color channels. These signals were then corrected for photobleaching by dividing them by a linear curve fit to the log of their time courses. The signals were then moving average filtered with a cut-off frequency of 2.02 Hz to eliminate further artefacts due to motion. The $\Delta F/F_0$ signals for each channel were calculated in which F_0 was calculated as the bottom 10% of the signal throughout the time course with ΔF calculated as the signal’s deviation from this baseline.

Figure 3.7a shows the maximum intensity projections of a single time point acquired in 0.01 seconds within the beating heart along each of the 3 dimensions, with the markers indicating the location of each tracked cell at that time point. **Figure 3.7**b shows the 3D tracks over a 0.6 second range (60 time point) wherein the colors encode the tracking duration, while the colors in **Figure 3.7**c encode the speed of each cell in the beating heart. By combining the HICAM Fluo with SCAPE’s unique scanning and de-scanning paradigm, we are able to track nuclei and extract calcium dynamics from cells traveling upwards of 0.7 mm/s without resorting to optical gated approaches.

Figure 3.8a.i-iv shows the trajectory of the atrial cell highlighted in **Figure 3.7**a in 3D space. As before, the colors indicate time tracked and speed (**Figure 3.8**a.i-ii). I have also encoded the trajectories’ colors to normalized GCaMP and normalized ratio values of those particular cells.

The trajectories are encoded to *normalized* GCaMP and ratio values to ease visualization due to inter-cellular variability in $\Delta F/F_0$ and $\Delta R/R_0$ values. **Figure 3.8**a.i shows time encoded over 60 time points, whereas the trajectories for the full 5 seconds of tracking is shown for the rest of the metrics (**Figure 3.8**a.ii-iv), allowing us to observe the expected periodicity of the heartbeat represented in both the cellular velocity traces as well as calcium dynamics. **Figure 3.8**b.i-iv shows the same information encoded for the ventricular cell highlighted in **Figure 3.7**a.

Note how the cellular calcium dynamics between the atrium and ventricle are different. The GCaMP peak within the atrial cell occurs after the high-velocity portion of the trajectory, however we can see that the intracellular calcium actually begins rising at approximately the same time as the cell's speed starts to increase (**Figure 3.8**a.ii-iii). In comparison, the ventricular GCaMP precedes the high-velocity portion of the trajectory. From a biological perspective, these results are expected. In the previous section describing blood flow measurements, we note that the highest RBC speeds were achieved by red blood cells transiting through the atrioventricular canal during atrial systole. This would require the rapid contraction of the atrium (an active, calcium dependent process) in concert with the rapid expansion of the ventricle (a passive calcium independent process). This would then be followed by a slower ventricular contraction which would result in an active increase in intracellular calcium within the ventricle's cardiac wall.

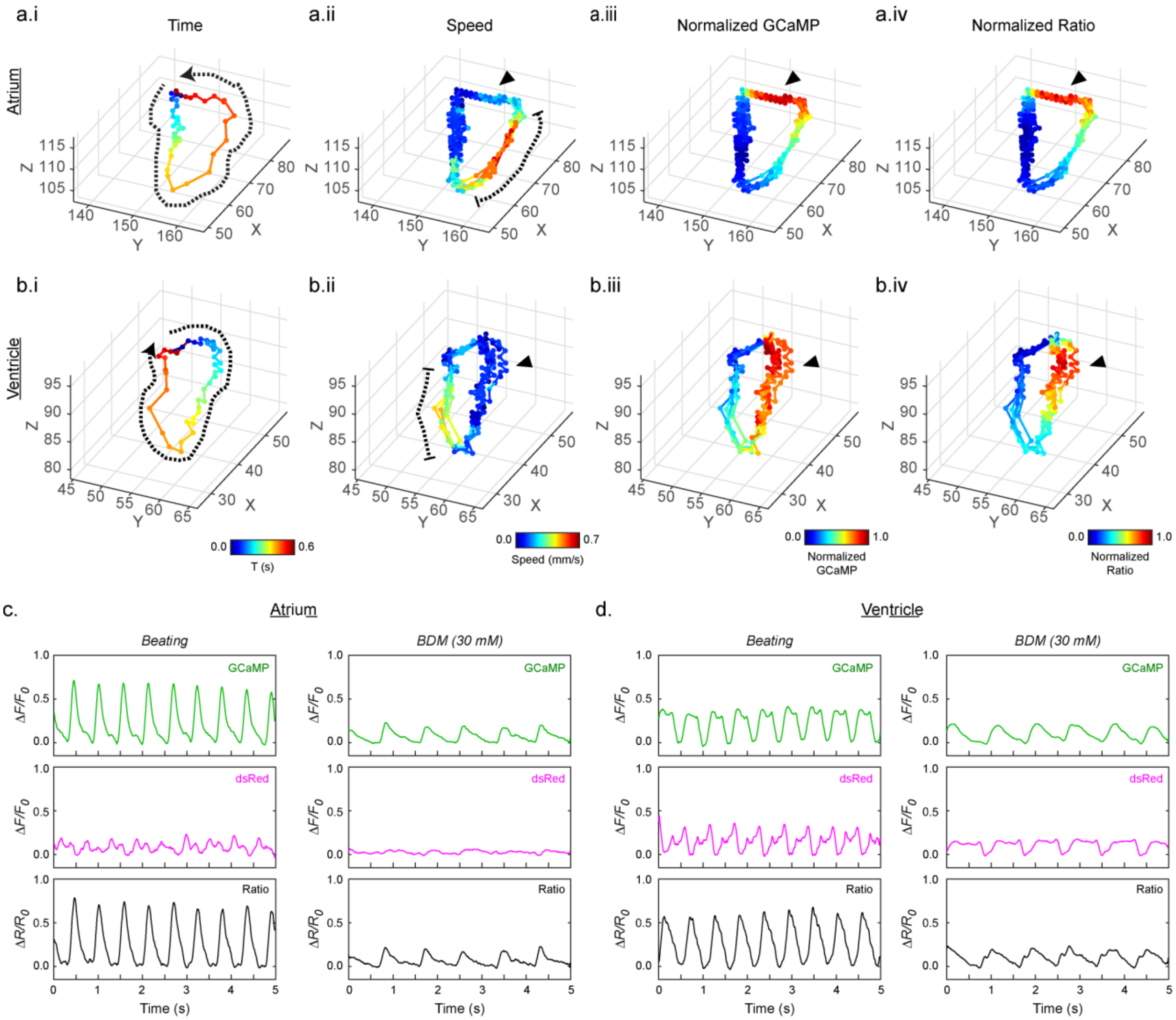

Figure 3.8: *Analysis of calcium dynamics in a single atrial and ventricular cell*
a. *Trajectory of atrial cell encoded for i. time tracked, ii. speed, iii. normalized GCaMP and iv. normalized ratio for a cell within the atrium of the zebrafish heart* ***b.*** *Trajectory of ventricular cell encoded for the same parameters in* ***(a)***. ***(a.i)*** *and* ***(b.i)*** *plot the trajectory over 0.6 seconds or 60 time points.* ***(a.ii-iv)*** *and* ***(b.ii-iv)*** *plot the trajectories over the full 5 seconds (500 time points). The black circular arrow shown in* ***(a.i)*** *and* ***(b.i)*** *indicates the cells' direction of travel. The segment highlighted in* ***(a.ii)*** *and* ***(b.ii)*** *indicate parts of the cellular trajectory in which the cell is traveling at its highest speeds. The black triangles in* ***(a.ii-iv)*** *and* ***(b.ii-iv)*** *indicate the portion of the trajectory with the cell has its highest GCaMP/ratio signal* ***c.*** *GCaMP, nDsRed2 and ratio-ed signals of the atrial cell shown in* ***(a)*** *during normal beating and after the addition of 30 mM of BDM expressed* ***d.*** *GCaMP, nDsRed2 and ratio-ed signals of the ventricular cell shown in* ***(b)*** *during normal beating and after the addition of 30 mM of BDM*

However, one caveat to this approach is that our measurements in the atrial or ventricular cells might simply be due to the chambers' contraction which would result in an increased concentration of the GCaMP fluorophore within the region of interest. This could in principle cause our GCaMP measurements to increase, mimicking the waveform produced by an actual

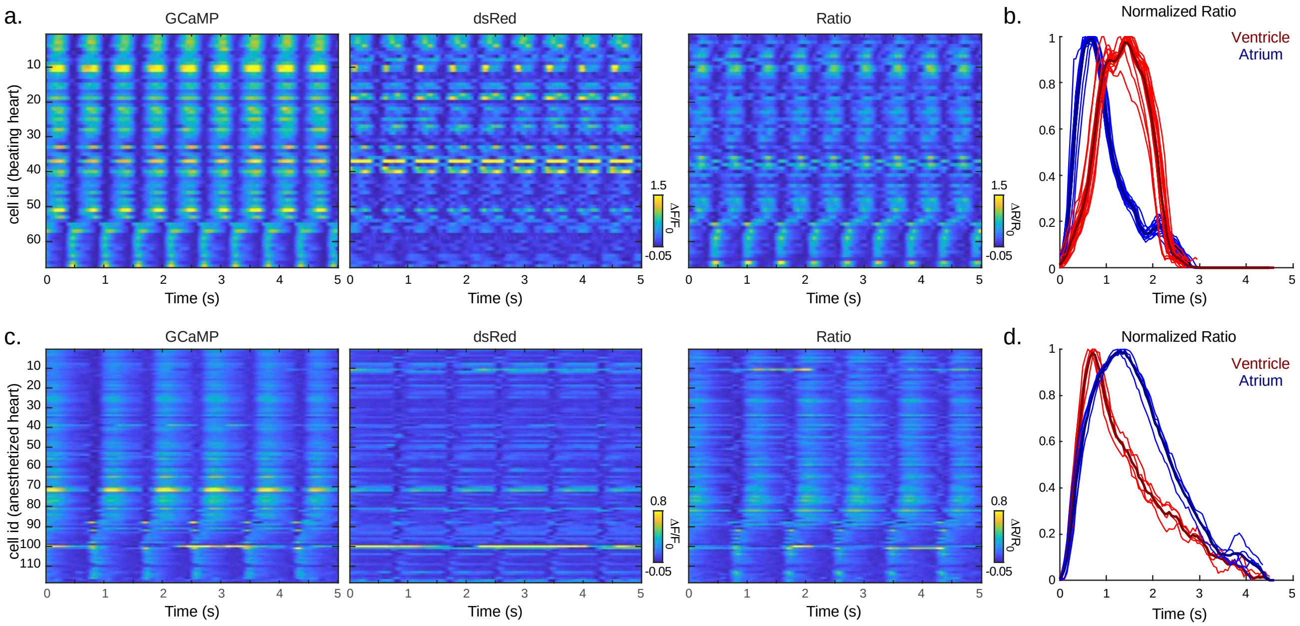

Figure 3.9: *Comparison between calcium dynamics of beating and anesthetized zebrafish heart* ***a.*** *GCaMP, dsRed and ratio of all 67 tracked cells in the beating heart* ***b.*** *Normalized ratio of cells in atrium and ventricle of the beating heart averaged over multiple heart beats* ***c.*** *GCaMP, dsRed and ratio of all 118 tracked cells in the anesthetized heart* ***d.*** *Normalized ratio of cells in atrium and ventricle of the anesthetized heart averaged over multiple heart beats*

intracellular calcium increase. Because nDsRed2 is a static fluorophore that does not respond to intracellular processes, increases in the nDsRed2 signal should purely be due to variations in sample motion and tracking. To correct for this confound, we ratio-ed our GCaMP signals to our nDsRed2 signals noting that the location of the GCaMP peaks within the trajectories before and after ratio-ing are similar to one another (**Figure 3.8**a.iv and **Figure 3.8**b.iv). $\Delta R/R_0$ is calculated similarly to $\Delta F/F_0$ in which the baseline is established with the bottom 10% of the R signal. We also present results on the same animal acquired with the same imaging parameters 10 minutes after the application of a 30 mM solution of fish water containing 2,3-Butanedione monoxime ≥ 98% (BDM) (*Sigma-Aldrich, B0753*). BDM is a myosin inhibitor (Ostap 2002) which has been shown to reduce the cardiac rates in zebrafish hearts by ~ 31% (De Luca, Zaccaria et al. 2014) and interfere with electro-mechanical coupling of the heart, facilitating the detection of calcium transients within the wall while paralyzing its motion (Kirchmaier, Poon et al. 2012). However, these calcium transients are far slower and of lower fluorescence intensity than when the heart was beating (**Figure 3.8**c-d).

Figure 3.9a shows the GCaMP, nDsRed2 and ratio-ed signals of all 67 tracked cells in the beating heart and 118 tracked cells in the paralyzed heart. Note how there are also substantial increases to the nDsRed2signals in some cells that may not have been due to motion, and therefore did not vary smoothly with respect to GCaMP (see nDsRed2 in **Figure 3.9**a). I hypothesize that this effect might be due to the differences in fluorophore localization. GCaMP localized to the cyotosol whereas DsRed2 only localized to the nucleus. Differences between the effects of compression on cytosolic fluorescence as opposed to nuclear fluorescence could explain this variation. Variations in the nDsRed2 signals are far smoother after the application of BDM, resulting in cleaner ratioed signals (see ratio in **Figure 3.9**c). By taking the auto-correlation of the GCaMP signal for each cell, the average GCaMP fluctuations over ~ 10 heartbeats for each cell in the beating heart and ~ 5 heartbeats for each cell in the anesthetized heart were found. **Figure 3.9**b and **Figure 3.9**d shows the time courses averaged over heartbeats for every tracked cell in each chamber in the beating and anesthetized heart respectively.

This demonstration showcases our ability to perform calcium signal extraction and analysis from cells moving at high speeds, as well as our ability to probe the effects of pharmacological agents on complex biological systems.

Imaging the Nervous System of the *Caenorhabditis Elegans* (Nematode) - Resolution

Since Sydney Brenner’s initial work in the 1970’s, the C. elegans has become a commonly used model organism in neuroscience for a number of reasons (Goldstein 2016). A single animal can produce up to 1000 progeny which grow en masse on petri dishes. They reach adulthood within 3 days and can also be frozen for storage without killing the animal, making them easy and inexpensive to cultivate. C. elegans contain ~1000 somatic cells of which 302 are neurons and 56 are glia arranged in distributed ganglia throughout the body. Even with this relative anatomical simplicity, the C. elegans exhibits and has been used to study a wide variety of behaviors such as locomotion (Gjorgjieva, Biron et al. 2014) and chemosensation (Bargmann 2006, Hart and Chao 2010). The C. Elegans neuronal connectome is well-established (White, Southgate et al. 1986), providing a framework for sophisticated modeling and interpretation of real-time observations. Furthermore, the amenability of the animal to genetic analysis and targeted mutation has also allowed it to become a model to study the development of its well characterized and incredibly diverse nervous system (Hobert 2010).

From a practical perspective, the adult worm is ~ 1 mm in length and 50 µm in diameter remaining optically transparent throughout its entire life cycle – an incredibly useful feature for fluorescence microscopy (Corsi 2006). The scale of its nervous system provides the opportunity to visualize the activity patterns of every neuron in a behaving animal with optical microscopy, leveraging genetically-encoded fluorescent reporters of neural activity such as GCaMP. Because one of the original intents of developing SCAPE was to study neuronal activity in large volumes of tissue, most applications of SCAPE had previously only demanded single-cell resolution over large fields of view. Cells within organisms of interest (larval zebrafish, drosophila, mouse olfactory epithelia) were on the order of 3-5 µm in size and occupied 9-16 voxels at a time. Other samples such as the apical dendrites of layer 5 neurons or blood vessels within the mouse cortex were large, extended structures with clearly defined syncytia. Caenorhabditis elegans (C. Elegans), in comparison, contains neurons on the order of 1-2 µm demanding higher resolution than the standard SCAPE2b design. Furthermore, while neuronal firing can occur on the orders of seconds (Kato, Kaplan et al. 2015), the animal is capable of moving at speeds upwards of 0.25 mm/s (Nguyen, Shipley et al. 2016) and exhibiting a range of behaviors that can occur at sub-second time scales presenting completely different imaging requirements when imaging immobilized vs freely crawling animals.

State of the Art in Imaging the C. elegans Nervous System

A number of technologies have previously addressed the challenge of high-speed, volumetric imaging of the C. elegans nervous system. These include spinning disk confocal microscopy, wide-field temporally focused microscopy, light-field microscopy, and conventional light-sheet microscopy variants.

Spinning disk confocal microscopy is the current gold standard for imaging the nervous system of the crawling C. elegans (Nguyen, Shipley et al. 2016, Nguyen, Linder et al. 2017). These systems use high-magnification, high-NA objective lenses (~40x/1.3NA) that are rapidly piezo-scanned (~3 Hz sine wave) in order to perform simultaneous dual-color (green and red) imaging. The lateral (XY) field of view is ~ 150 x 150 µm with pixel sizes of 0.32 µm. The animal is imaged at ~200 fps onto a high-speed sCMOS camera and the volume rate is ~ 6 volumes/sec, corresponding to the forward and backwards strokes of the 3 Hz sine wave. The piezo is translated through a 50 µm travel range resulting in an ~ 1.5 µm step size between individual z-planes. However, because frames are acquired during the non-linear portions of the sinusoidal wave, the distance between individual z-planes is not always constant. As discussed previously, confocal microscopy suffers from excessive photobleaching concerns due to the fact that every z-plane acquired within the volume involves re-exposure of the entire volume to illumination.

Wide-field temporal focusing microscopy is a multi-photon illumination technique (Schrodel, Prevedel et al. 2013). In comparison to regular two-photon point scanning which spatially focuses the laser beam in order to create a tight spot of high photon density, temporal focusing adds a variable delay to the spectral components of high-frequency pulsed lasers such that these spectral components only overlap at the focal plane of the objective lens. This creates a disk with 60 µm diameter and 1.2 µm thickness of two-photon excitation within the sample that provides optical sectioning between different z-planes. Because multi-photon excitation using temporal focusing is an inherently light starved process, the photons comprising the spectrally widened pulse only have a single plane with which to interact with the fluorophores in question. The achievable fields of view are therefore limited by the available laser power and authors note that maximum achievable disk size with the described implementation was only ~200 µm. In this demonstration, imaging was also performed at 200 fps (~4-6 volumes/sec) by axially driving the sample stage in 2 µm increments with a triangular waveform for a maximum acquisition time of 4 minutes. Because of the travel time required for the stage to move from one plane to the next, the exposure time of the sample at each z-plane is only ~2.5ms, corresponding to a higher frame rate of 400 fps.

Light field microscopy has also been previously used to provide single-shot imaging of panneuronal calcium activity in immobilized and moving C. elegans (Prevedel, Yoon et al. 2014). Because the volume rates of light-field microscopes are equivalent to camera frame rates, these systems were able to capture the crawling C. elegans at 50 Hz and reconstruct volumes from individual frames over a lateral field of view of 350 x 350 µm. However, the system was unable to provide the in-plane resolutions necessary for single-cell discrimination over the entire axial range of the animal. The reported lateral resolution of the system was 1.5 µm at the focal plane of the objective, and 3 µm when 25 µm away from the focal plane, while the reported axial resolution of the system was 2.6 µm. Authors provide an alternative configuration using an ultra-high magnification/NA objective lens (100x/1.4NA) which can provide 0.25 µm lateral resolution and 1 µm axial resolution over a 150 µm field of view. Recent work has demonstrated sub-micron resolution light field microscopy in live cells (Li, Guo et al. 2018) however fields of view are limited to below 100x100 µm laterally and below 3 µm axially. Finally, as previously noted, volume reconstruction is a computationally intensive process with authors reporting a 1000 time point reconstruction taking ~ 12 hours after hardware parallelizing.

Finally, conventional light sheet microscopes which use separate, orthogonally aligned illumination and detection telescopes have previously been applied to study the nervous system of the C. elegans (Ardiel, Kumar et al. 2017). These studies were performed on an inverted SPIM system to study the development of neuro-muscular control within the C. elegans embryo. Calcium imaging in neurons was performed at 1.4 volumes/sec and within the musculature at 5 volumes/sec, acquiring at 200-400 fps and axially translating the sheet over a range of ~ 40 µm. Axial scanning was performed by galvo-scanning the light sheet and tracking the sheet's motion with a piezo stage. The inertial constraints of this approach place an upper limit to total achievable volume rate. Total acquisition times for a single volume were less than 4 minutes.

Development and System Modifications for C. elegans Imaging

Bearing these previous approaches in mind the goal for my work with C. elegans was to find some modifications to the existing SCAPE2b layout that can achieve a number performance metrics. In order to image the entire body of freely crawling animals, the volumetric speed of the system had to scale beyond the standard 5-6 Hz volume rates typically used to image immobilized animals. This requirement was relatively straightforward as SCAPE does not rely on slow-moving piezo-scanners in order to acquire the multiple cross sections in a volume. The achievable field of view of the system needed to be large enough to comfortably fit the entire (or a large portion) of the animal's body for acquisition in a single time point (i.e. without stitching). The resolution over this field of view needed to be sufficient to resolve single cells (i.e. sub- or near- micron resolution). The system needed to display low levels of phototoxicity in order to facilitate imaging within this delicate organism for over 4 minutes, matching the acquisition times demonstrated by previous methods.

The interface between the second and third objective lens, as illustrated in **Figure 2.12**, is the main source of light loss within the system. The overall light collection efficiency is influenced by the numerical apertures of the each of the three objectives, as well as the angle of the light sheet within the sample. The highest resolution and best light collection efficiency are achieved when the conjugate image is at a large angle relative to the optical axis of O2.

Because we need to have isotropic magnification from the sample to the conjugate image, which is equivalent to creating a shallow light sheet within the sample. This implies that using high-NA lenses as the primary objective (O1) is the most straightforward solution to improving system performance. Indeed, this is the strategy adopted by the developers of oblique plane microscopy who have previously used either a 60x/1.2NA water immersed lens or a 60x/1.35NA oil immersed lens as the primary objective to image sub-cellular structures such as the trabeculae of cardiomyocytes (Dunsby 2008, Kumar, Wilding et al. 2011, Sikkel, Kumar et al. 2016). I have constructed a version of SCAPE that uses an Olympus 63x/1.3NA silicone oil immersion lens (data not shown) however this system predictably sacrificed a significant portion of its field of view (< 500 x 500 µm). Therefore, we decided that we would like to keep the Olympus 20x/1.0NA (or a lens with similar magnification) as the primary objective (O1).

Objective 2	Objective 3	System Magnification	Predicted Numerical Aperture
Mitutoyo 50x/0.75NA	Nikon 10x/0.45 NA	2.3x -13.3x	(SCAPE3) 0.24
Mitutoyo 50x/0.75NA	Nikon 20x/0.75NA	4.7x -26.6x	0.48
Mitutoyo 50x/0.75NA	Nikon 40x/0.95NA	9.3x – 53.2x	0.72
Nikon 20x/0.75NA	Mitutoyo 50x/0.75NA	11.6-66.5	0.48
Nikon 20x/0.75NA	Edm. Opt. 20x/0.60NA	26.66x	0.35

Table 2: *Predicted performance of various combinations of Objective 2 and Objective 3*

The Mitutoyo 50x/0.75NA lens was chosen as O2 because it was optomechanically compatible with each of the lenses seen in the Objective 3 column while preserving the angular collection efficiency of the primary objective lens (O1, Olympus 20x/1.0NA).

While the simplest solution would be to switch the third camera objective (O3) to a higher-NA objective lens, finding high-NA objective lenses that are optomechanically compatible with one another was a challenge. I found a number of promising lens pairs that could potentially be used to implement scalable magnification (see Table 2) in which the third objective lens was placed on a motorized objective lens switcher. When used in combination with tube lenses ranging from 35 mm to 200 mm, such a system should theoretically be able to provide magnifications ranging from ~2-66x.

In an effort to improve the numerical aperture and effective collection efficiency as much as possible, I first built systems which used the Mitutoyo 50x/0.75NA lens as the second objective lens (creating the conjugate image of the light sheet). This lens has a working distance of 5.2 mm and would therefore be optomechanically compatible with a lens with an NA as high as 0.95, thereby boosting the effective numerical aperture of the system to ~ 0.72. The telescopes between O1 and O2 were altered so that the magnification between the sample and the conjugate image plane was isotropic in the lateral and axial magnification ($M_L = n1/n2 = 1.33$). I found, however, that usage of the Mitutoyo 50x/0.75NA lens as the second objective lens introduces significant spherical aberrations that cause an extended point spread function at all depths (see **Figure 3.10**). This aberration can be reduced by occluding parts of the back aperture of the

Mitutoyo 50x/0.75, however doing so decreases the light collection efficiency of the system by a factor of ~ 50%.

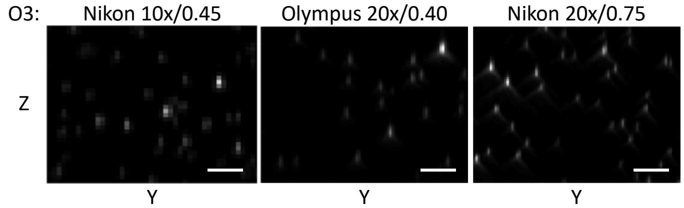

Figure 3.10: *Comparison of system aberrations in SCAPE4 with different objective lenses as O3.*
Image shown is from the "camera" plane. Note the emergence of coma with a higher system magnification (Olympus 20x/0.40) while preserving the numerical aperture of O3. The coma is worsened when switching O3 with a higher numerical aperture. Scale bar – 10 µm.

I hypothesize that the aberration might stem from a number of factors. Recall that we need to map the back pupil of the first objective lens (Olympus 20x/1.0NA) onto the back pupil of the second objective lens (Mitutoyo 50x/0.75NA). The first factor comes from issues in aligning the scan and de-scan telescopes. High-magnification objectives have smaller back pupil diameters than low-magnification objectives with the same numerical aperture, and a lateral misalignment cause significantly larger disruptions to the angle of the light rays that create conjugate image plane. Axial misalignments of the high-magnification objective lenses can similarly cause more depth-dependent inhomogeneity than that of low-magnification objective lenses. In short, the alignment tolerances are far stricter. SCAPE2b has thus far used a coupled cage-mounted system. Here, all of the lenses in the scan telescope, or all of the lenses in the detection systems were all co-aligned along the same rail. This precluded the need for independent alignment of each lens to its neighbors and significantly simplified alignment. Establishing independent optomechanical control of each lens component might have allowed us to achieve tighter alignment tolerances, but would also hinder the ease of system dissemination and adoption further downstream. Furthermore, in comparison to previous oblique plane illumination systems using high magnification objective lenses (Dunsby 2008, Kumar, Wilding et al. 2011, Sikkel, Kumar et al. 2016, Yang, Wang et al. 2018), this implementation uses a far steeper sheet angle in which the camera telescope is mounted far more obliquely than these authors' previous work.

Regardless, the first attempt at imaging the C. elegans used a Mitutoyo 50x/0.75NA and Olympus 20x/0.40NA lens as the second and third objective lens respectively. The magnification of the entire system was set 9.3x. Because C. elegans can grow to 30-40 µm in thickness, they are ideally suited to imaging with a high-NA sheet. The entirety of an approximately 1mm long, sparsely-labeled C. elegans was immobilized and imaged (**Figure 3.11**ab). The raw data was gamma corrected with a factor of 0.5 was taken to improve the dynamic range between neurons and processes for improved visualization. The images were also sharpened to improve visualization of the processes.

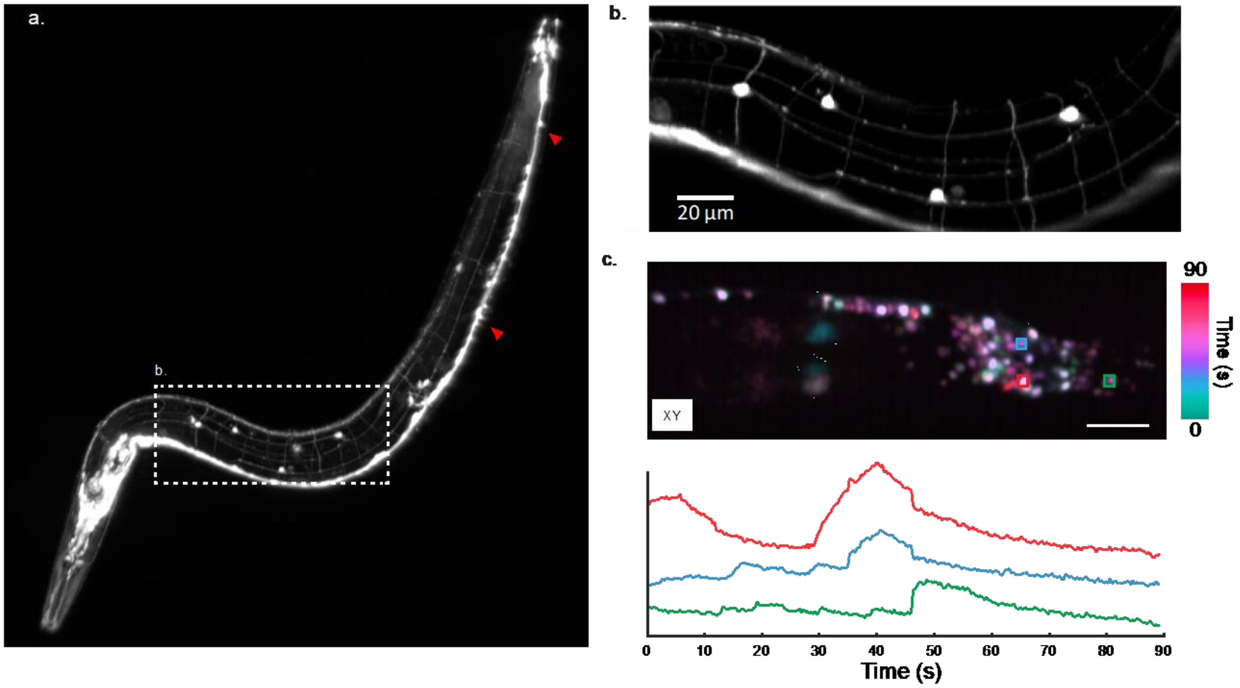

Figure 3.11: *Early results in the C. elegans with SCAPE*
a. *XY- maximum intensity projection of entire animal acquired in under 10 seconds. Red arrows indicate regions of blurring due to spherical aberrations* ***b.*** *XY- maximum intensity projection of region indicated in (a). Strain: nid-1(ur41) V; edIs20 X – GFP.* ***c.*** *Imaging C. elegans expressing panneuronal, nuclear-localized GCaMP6s using a modified SCAPE system. (Top) Top down maximum intensity projection of the nerve bundle. A maximum time-projection of stack was then color-coded and shown above. (Bottom) Time courses from three regions of interest corresponding to individual neurons within the nerve bundle. Scale bar – 10 µm. C. Elegans strain provided by Danielle Cosio in the laboratory of Dr. Ed Boyden.*

In the neural cluster at the head of the sample, the neurons are so densely clustered that panneuronal imaging typically requires a nuclear-localized marker in order to discriminate between individual neurons (Schrodel, Prevedel et al. 2013, Prevedel, Yoon et al. 2014). Imaging of even smaller samples as well as potentially sub-cellular structures requires higher magnification and resolution than could be achieved with the existing SCAPE2b design.

I continued to explore a number of lens combinations, illumination schema and telescope designs for SCAPE4 in order to achieve the requisite magnifications, numerical apertures and resolutions. By using the Nikon 20x/0.75NA lens and the Mitutoyo 50x/0.75NA lens are the second and third objective lens of the system respectively, I built a system nearly identical to SCAPE2b but with double its theoretical numerical aperture (NA_{eff} = 0.48, see Table 2) and a magnification of 23.4x. The sample is embedded in agarose as described in Appendix D. The sample was immobilized and imaging performed solely in the dense nerve cord at the sample's head. A region of 1190x199 pixels (corresponding to an in-plane field of view of 333 x 43 µm) was acquired over a scan range of 98.4 µm with a frame acquired every 0.92 µm. The total volumetric imaging speed was at 2.98 volumes/sec. The data was smoothed with a Gaussian filter with a kernel size of ~0.5 µm and the top-down maximum intensity projection shown (**Figure 3.11**c), wherein the color encodes the time point at which a particular voxel was at its maximum intensity A number of spontaneous events in the individual neuronal nuclei can be clearly visualized. Unfortunately, opto-mechanical limitations arising from the physical bulk of the Nikon 20x/0.75NA precludes an implementation in which the Nikon 40x/0.95NA lens can be used as O3.

In order to perform imaging of the immobilized C. elegans brain, the final layout of the system is as follows. I added a 561 nm laser for more efficient excitation of red fluorophores and a field stop was placed between the second and third cylindrical lenses (CL2, 3) in order to crop the field of view down to the width of the C. elegans head. As mentioned previously, this would serve to reduce the lateral extent of each of the two-color channels on the camera chip, allowing us to place them closer together on the camera chip and minimize the data written to disk. The camera telescope was altered to have a magnification of 26.66x and effective numerical aperture of ~0.35. This was done by switching the objective lens to an Edmund Optics 20x/0.60NA and replacing the 70 mm camera tube lens with a 200 mm lens (Thorlabs, TTL200). By using a 20x/0.60NA lens as the objective on our camera telescope, simple changes to the tube lens can allow us to achieve magnifications equivalent to that of SCAPE2b (4.65x) while providing access to SCAPE's full field of view along the y- dimension (~ 1 mm). In comparison, using the 50x/0.75 would preclude access to a field of view greater than ~ 500 µm, and would require a 14 mm tube lens with a high numerical aperture in order to achieve standard SCAPE2b magnification.

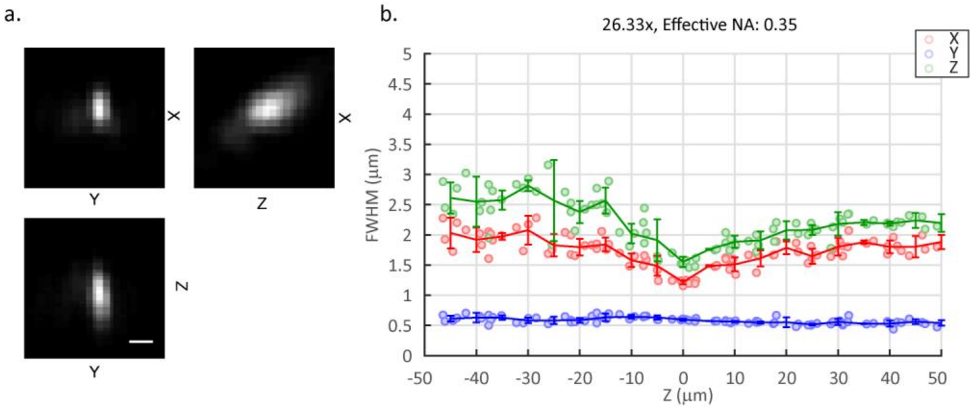

Figure 3.12: *Resolution of SCAPE system built for C. elegans*
a. *Cross section through an image of a 200 nm bead imaged. Scale bar – 1 µm* ***b.*** *Resolution when imaging 200 nm beads along each of the 3 dimensions plotted as a function of depth in a non-scattering sample*

This resulted in an overall system resolution of 0.6 and 1.5 µm in the Y and Z directions respectively. The resolution along the sheet dimension remains ~ 1.2 µm at the focal plane. We find this is sufficient to achieve single cell resolution in the dense nerve bundle at the head of the

C. elegans. The camera used to image the immobilized worm was an Andor Zyla 4.2+, while the camera used to image the crawling worm was the HICAM Fluo.

Final Layout and Results

Whole brain imaging of immobilized C. elegans

For whole-brain neuronal imaging, the animal expressed nuclear-localized, panneuronal GCaMP6s and tagRFP (*AML32 – wtfls5[rab-3p::NLS::GCaMP6s +rab-3p::NLS:tagRFP]*) in order to facilitate ratiometric determination of calcium signals during sample motion. Because GCaMP6 has a low background signal, the static red fluorophore also served as a marker for cellular position by which to define the region of interest. Using the layout of SCAPE just described, a young adult C. elegans was chosen.

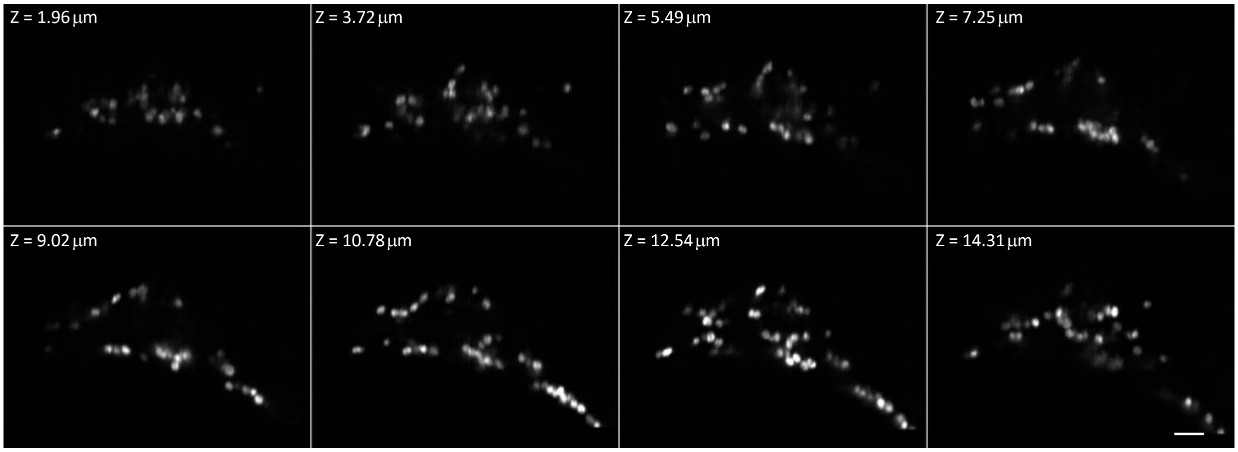

Figure 3.13: *Single volume of C. elegans expressing nuclear localized panneuronal tag-RFP. Data shown was acquired at 6 volumes/sec and is the average of 25 time points. Every 9th z-plane is shown over the thickness of the animal. Scale bar is 10 µm.*

Simultaneous dual color acquisition enabled simultaneous imaging of static RFP and functional GCaMP6s with dual illumination at 488 and 561 nm. Imaging was performed at 5.96 volumes/sec for 10 minutes. The power at the back aperture was measured as 0.13 mW at 488 nm (66.9 µW at the sample) and 0.13 mW at 561 nm (72.7 µW at the sample). A field of view of 1900 x 162 pixels (corresponding to an in-plane field of view of 456 x 32 µm) was acquired on an Andor Zyla 4.2+ at 477 fps. After registering both the GCaMP and tagRFP channels with one another and cropping the data to solely include the region containing the worm's head, the in-plane field of view decreased to 103x31.4 µm. While the camera is capable of

acquiring faster over a larger field of view, we intentionally increased the exposure time to improve SNR, decrease the data analysis load and decrease laser power on the sample. The galvo was swept over a range of 59.3 µm with a frame taken every 0.75 µm. These parameters were selected to match the imaging rates duration of published whole-brain C. elegans imaging studies using confocal spinning-disk microscopy (Nguyen, Shipley et al. 2016) while exceeding the sampling densities in each of the three dimensions (typical SDC: 0.32 x 0.32 x 1.5 µm/pixel v/s SCAPE: 0.75 x 0.24 x 0.19 µm/pixel x-y-z). Resolution and sampling density were sufficient to resolve individual neurons within the head of the animal in the tag-RFP channel (**Figure 3.13**).

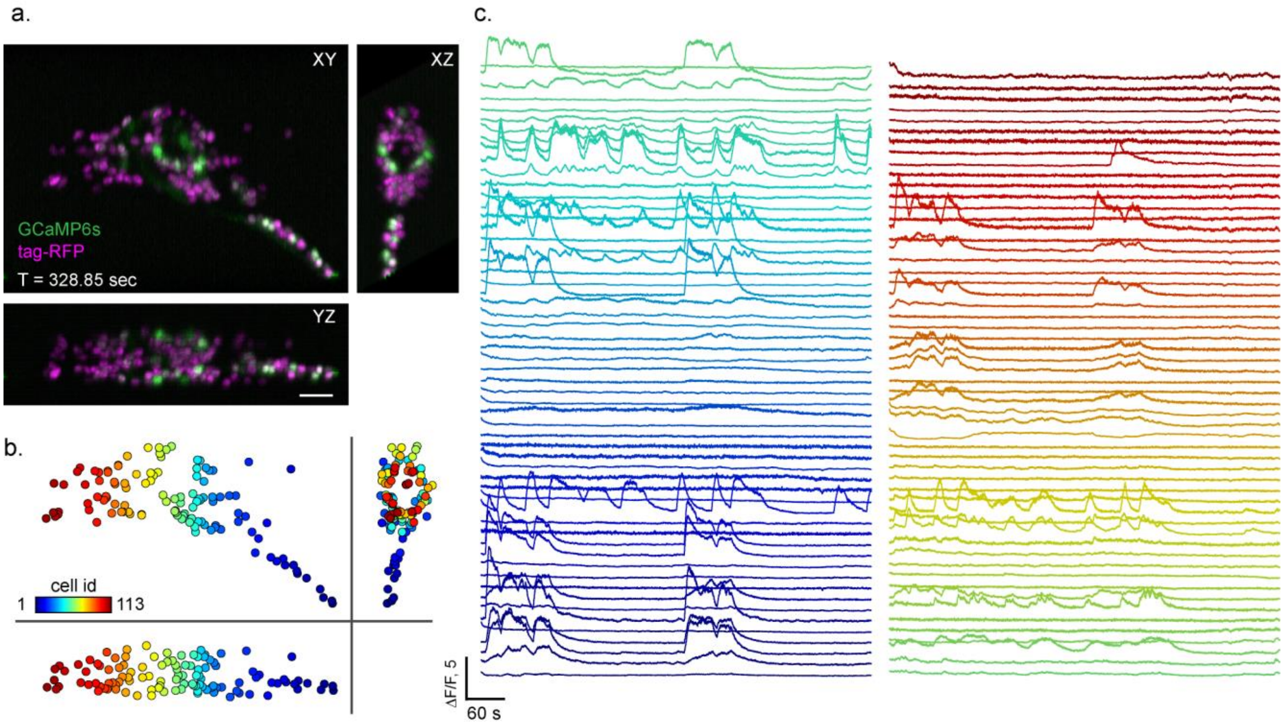

Figure 3.14: *Extracting calcium dynamics from C. Elegans expressing NLS-GCaMP6s/tagRFP (AML32)*
a. Top-down and side-facing maximum intensity projection of a single time point acquired at 5.96 volumes/sec of an immobilized C. elegans. Scale bar – 10 µm ***b****. 113 neurons were identified and encoded along the rostral-caudal axis, with their extracted time-courses shown on the right.*

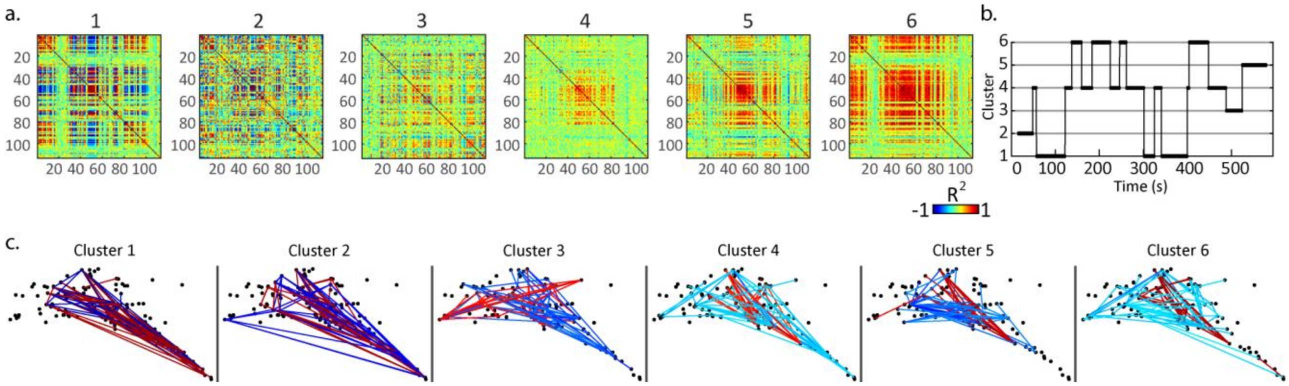

Figure 3.15: *Functional correlative analysis of neuronal firing in C. elegans*
a. *6 cluster medians representing the most common states of correlated activity between 113 cells shown in **Figure 3.14**b **b.** Time course showing the brain switching between the most dominant cluster over the course of a 10 minute run **c.** Graph showing the connections between cells of 50 highest and lowest correlations*

The two color channels were registered to one another and the data was affine transformed into Cartesian space. The data was up-sampled using cubic interpolation to have uniform pixel sizes (0.20 µm/pixel). **Figure 3.14**a shows a maximum intensity projection of a single time point from this dataset. The red channel was exported to a 16-bit tiff format and cell identification was performed using the TrackPy particle-tracking algorithm (Allan, Caswell et al. 2018). Because the tracking was only used to compensate for a slowly occurring sample drift over a 10-minute period, mean-intensity projections of every 25 time points (~4.2 sec) provided sufficient temporal resolution for cell identification while improving the SNR of each cell for better cell tracking. Cell locations between these time points were then interpolated onto the rest of the dataset. 113 tracks corresponding to individual cells were found over the 10 second run (**Figure 3.14**b). A 1.2x1.2x1.2 µm^2 region of interest surrounding the ROI was used to extract the signal from both the green (GCaMP6s) and magenta (tag-RFP) channels of each cell. Owing to the minimal fluctuations in RFP (after photobleaching compensation) GCaMP signals were not ratiometrically corrected, but were converted to ΔF/F using the average of the lowest 20 values of baseline GCaMP fluorescence within the last 200 seconds of acquisition as each cell's baseline (**Figure 3.14**c).

Similar to data analysis techniques used to characterize dynamic functional connectivity in the fMRI literature, I used sliding window correlation coupled with k-means clustering analysis to characterize dynamic changes in correlated activity (Allen, Damaraju et al. 2014). The pairwise correlation matrices were calculated over the 10 minute acquisition using a rectangular window of 180 time points (~30.2 s) that slid in steps of 1 time point, resulting in a 3D matrix of correlation matrices (C: 113x113xT where C_t: 113x113). Commonly occurring structures within this correlation matrices were found using k-means clustering (with 6 clusters) upon the sequence of correlation matrices. The k-means algorithm was run for 500 iterations using randomly initialized seeds and an L1-norm as the distance metric. The outputs of these 500 iterations were re-run through k-means and the medians of the 6 resulting clusters are shown in **Figure 3.15**a. The 6 clusters show a range of connectivity patterns from strong anti-correlations (Clusters 1, 2) to predominantly correlated activity between all 113 neurons (Clusters 4, 5, 6). The dominant cluster at any given time point was found by calculating the distance between each of the cluster medians and the windowed correlation graph at that time (C_t). The cluster median with the minimum distance was classified as the dominant cluster at that time (**Figure 3.15**b). Network graphs shown in **Figure 3.15**c depict connections between the cells with the 50 most correlated, and 50 most anti-correlated activity traces for a specific cluster. The color of each line represents the R^2 of the correlation as indicated in the color bar.

Photobleaching Comparison

To further validate the strengths SCAPE2b configuration for *C. elegans* imaging, a photobleaching comparison was performed between the SCAPE2 system and a spinning disk confocal microscope (Nikon Eclipse Ti2 with CSU-W1, 50 µm pinholes). Young adult worms expressing panneuronal, nuclear-localized GCaMP6s and tagRFP (AML70: wtfls5[rab-

3p::NLS::GCaMP6s + rab-3p::NLS::tagRFP]) were repeatedly volume-scanned with both systems. Only photobleaching of the static red fluorophore was analyzed within this study. Living worms were pre-screened for similar levels of brightness on SCAPE2. Worms in which the top 1% of all voxels within the red channel different by less than 5% were determined to have brightness levels similar enough for further comparisons. Worms of similar brightness were transferred to each respective system and thousands of volumes were subsequently acquired, with the field of view centering upon the dense nerve ganglia within the animal's head. Laser powers on each system were adjusted such that the average signal in the top 1% of all pixels were found to differ by less than 5% at the start of the run. Imaging parameters for SCAPE2 were matched to be as close to that of a commercial available spinning disk confocal microscope.

	Confocal Spinning disk	**SCAPE 2.0**
Integration time per frame	5 ms	5 ms
On-camera pixel size	0.32x0.32 µm (X, Y)	0.36x0.29 µm (Y, Z)
Camera QE, read noise	95%, 1.6 e^- (median)	92%, 1.2 e^- (median)
Camera Background	98.5 +/- 3.2 counts	104 +/- 2.95 counts
Inter-plane step-size	1.5 µm (z-planes)	1.5 µm (x-planes)
z-planes per volume	35	40
z-range	50 µm	60 µm
Excitation wavelength	561 nm	561 nm
Emission wavelength	605/50 nm	618/50 nm
Effective NA	0.75	0.35
Actual volume rate	0.44 VPS (owing to piezo speed)	4.75 VPS (200 fps, no overhead)

Table 3: *Imaging parameters for comparative photobleaching measurements*

The data acquired on both systems was then cropped to have nearly identical numbers of voxels. The data was background subtracted and the average signal from the top 1% of both datasets was plotted as a function of the number of volumes acquired. Fluorescence signal from the confocal spinning disk microscope and SCAPE microscopy degraded by 68% and 6% respectively within the first 2660 volumes. SCAPE microscopy was also able to acquire this time series over an order of magnitude faster than the confocal spinning disk microscope used within the study owing to the fact that volume acquisitions on the latter were performed by moving the sample with piezo-stages. An exponential fit of the SCAPE photobleaching curve indicated that the sample would experience a 50% reduction in tagRFP signal after the collection of ~28370 volumes (approximately 1-2 hours of imaging at 4-6 volumes/sec).

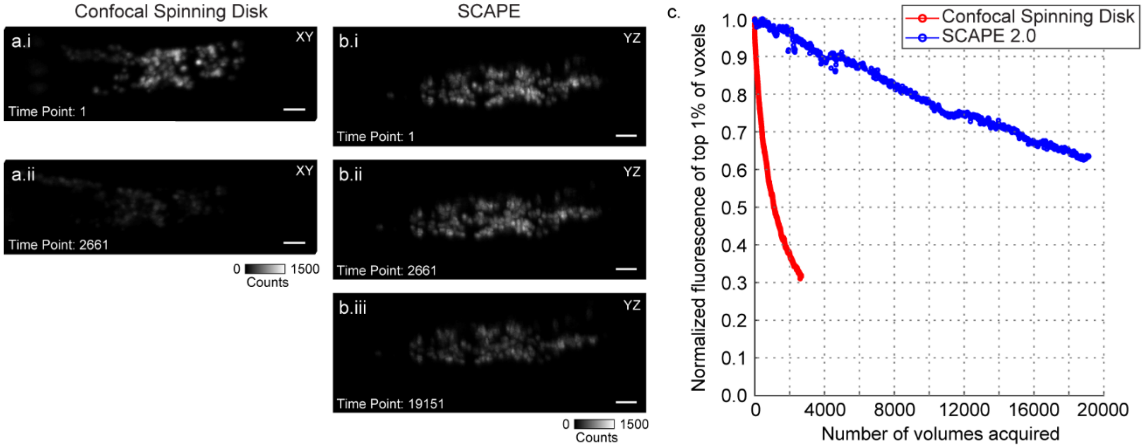

Figure 3.16: *Comparing photobleaching of live C. elegans between confocal spinning disk and SCAPE 2.0.* ***a(i)*** *Top-down (X-Y) MIP of the first volume, and* ***a(ii)*** *the 2,661*st *volume acquired sequentially on a living C. elegans worm using a confocal spinning disk microscope (RFP only at 561 nm excitation). After 2,661 volumes, the spinning disk worm is heavily photobleached.* ***b(i)*** *Side-facing (Y-Z) MIP of the first volume,* ***b(ii)*** *the 2,661th volume and* ***b(iii)*** *the 19,151th volume acquired on a living C. elegans worm using SCAPE 2.0 (RFP only with 561 nm excitation). The 2,661*th *volume acquired on SCAPE shows minimal photobleaching compared to the first volume, with only modest photobleaching after nearly 20,000 volumes. Scale bars 10 µm for both systems.* ***c.*** *Normalized mean fluorescence of the top 1 percentile of pixels plotted as a function of the number of volumes acquired.*

Whole body imaging of crawling C. elegans

In order to image the entire body of the C. elegans, I re-installed the HICAM Fluo into the camera telescope, keeping the Edmund Optics 20x/0.60 NA objective lens and a 200 mm tube lens on the camera telescope. In this configuration, the field of view in Y is limited by the number of columns on the camera sensor and not the actual lateral extent of the laser excitation. A field of view of 1280 x 127 pixels (corresponding to an in-plane field of view of 474 x 40.6 µm) was imaged at 6900 fps. In order to facilitate dual-color imaging, the field stop between the

2nd and 3rd cylindrical lens was closed down to limit the lateral extent of the sheet to 50% of the columns

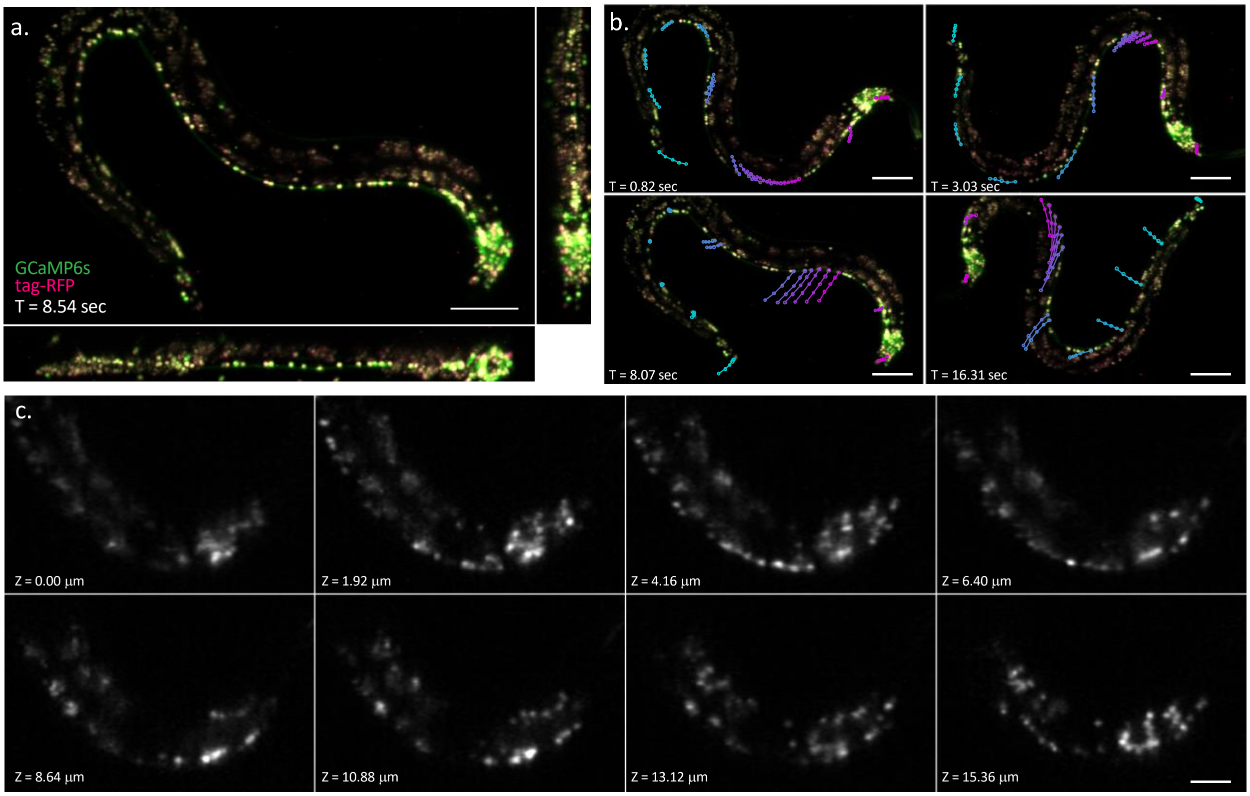

Figure 3.17: *Dual color imaging of the entire crawling C. elegans at 25.7 volumes/sec expressing NLS-GCaMP6s/tagRFP* ***a.*** *Maximum intensity projections across the 3 dimensions (X, Y, Z) for a single time point acquired in 0.039 s* ***b.*** *Top-down maximum intensity projections of 4 time points acquired in 0.039 s showing manually tracked neurons with traces spanning a 0.194 sec temporal window* ***c.*** *Close-up of the head of the C. elegans at 1 time point showing a montage of different z-planes within the image. Scale bars in (a, b) are 50 µm. Scale bar in (c) is 20 µm. Manual tracking of the cells shown in (b) was performed by Srinidhi Bharadwaj.*

on the camera chip. Each of the color channels therefore took up a field of view of 229 x 40.6 µm within the camera frame. This high frame rate was needed in order to simultaneously scan over a large range along the X-dimension (374 µm), while maintaining a high sampling density in X (1.42 µm). The animal was imaged at 25.7 volumes/sec using both the 488 nm and 561 nm lasers (**Figure 3.17**a).

The laser power at the back aperture was calculated as 18.3 mW at 488 nm (9.57 mW at the sample) and 8.65 mW at 561 nm (4.52 mW at the sample). While this may seem high in comparison to other measurements, recall that when scanning over a range of 374 µm at 25.74 volumes/sec, the sheet will be moving at a rate of ~9.63 mm/s. At this rate, a sheet with a width of 1.2 µm will only dwell on a single location for 125 µs, depositing ~1.19 µJ (488 nm) and 0.565 µJ (488 nm) of power with each volume. Given 25.74 volumes per second acquired, the average power on a given plane is actually 29.9 µW (488 nm) and 13.1 µW (561 nm).

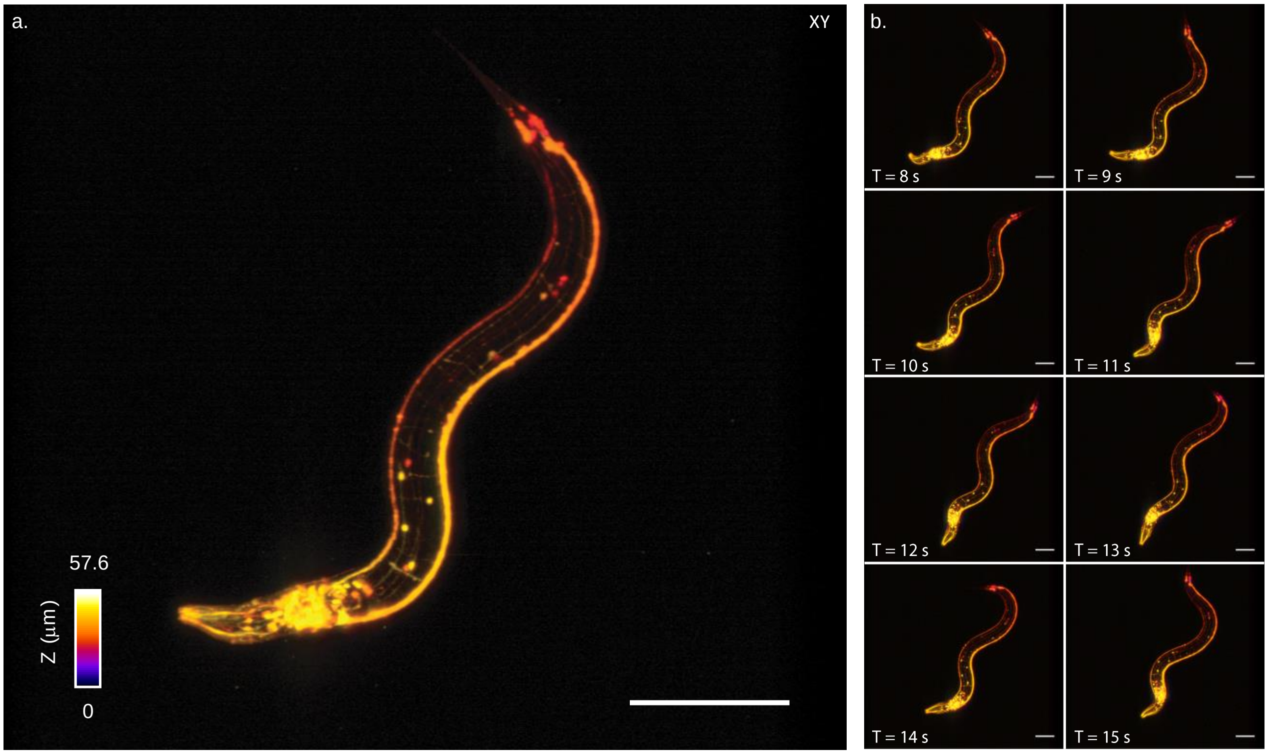

Figure 3.18: *Single color imaging of the entire crawling C. elegans at 10 volumes/sec (IM324: edls20[F25B3.3::GFP+rol-6(su1006)])*
a. *A single time point acquired in 0.1 seconds in which color encodes depth into the sample. The field of view is 525 x 465 x 60 µm*
b. *Montage showing time points acquired every 1 second in which standard crawling via sinusoidal undulation can be seen. Scale bar - 100 µm*

A subset of the neurons were manually tracked throughout the field of view and are shown in **Figure 3.17**b for various time points, illustrating that cells can be distinguished and exhibit minimal motion induced blur with SCAPE's acquisition scheme over a large enough field of view.

The field of view in the y direction was only limited due to the usage of the image splitter. It is important to note that if two HICAM Fluo cameras were configured in a primary/secondary configuration with each acquiring a single channel, it would be entirely possible to double the achievable field of view in this dimension without significant loss in imaging speed. **Figure 3.18**a shows the image of a worm expressing panneuronal GFP (*IM324: edls20[F25B3.3::GFP+rol-6(su1006)]*) imaged with the HICAM Fluo at 10 volumes/sec. Similar to the worm in **Figure 3.17**, the worm was mounted on top of a pad of 10% agarose in a manually engraved channel and imaged through a coverslip. A region of 1280 x 180 pixels (corresponding to an in-plane field of view of 465 x 60 µm) was imaged on the camera at 5600 fps. This allows us to scan the galvo over a range of 500 µm with a camera frame acquired every 0.9 µm.

The laser power at the back aperture 3.75 mW at 488 nm (1.91 mW at the sample). When accounting for the sheet's speed through the sample (5 mm/s) and average dwell time of the sheet at any given point (240 µs) and the width of the sheet (1.2 µm), the amount of laser power deposited at the sample for each volume is actually 0.458 µJ. At 10 volumes/sec, the laser power at any given scan plane within the sample is actually 4.58 µW.

Structural Imaging with SCAPE Microscopy

Methods such as CLARITY, CUBIC and expansion microscopy have introduced the potential for large-scale interrogation of structure and connectivity in diverse tissues . However, imaging these samples in-toto with near isotropic sampling density and sufficient resolution is made complicated by the same bottlenecks that have impeded functional volumetric imaging in living organisms. While light sheet illumination is becoming standard for imaging large samples, systems that rely on side-faced illumination such as ultramicroscopy (Dodt, Leischner et al.

2007, Saghafi, Becker et al. 2010, Saghafi, Becker et al. 2013, Dodt, Saghafi et al. 2015) and COLM (Tomer, Ye et al. 2014, Tomer and Deisseroth 2015) require sample mounting procedures that preclude high-speed imaging of moving or behaving samples. Such systems are also unsuitable for structural imaging in mounted, sliced or fixed samples. Inverted SPIM setups which image the sample from the top down can also be configured with objective lens combinations that are optimized for large field of view structural imaging (Kumar, Wu et al. 2014, Migliori, Datta et al. 2017). However, these architectures may face challenges when imaging tissues treated with organic solvents and immersion media that can destroy the coatings on expensive objective lens components. Open-top SPIM type set-ups have shown promise for imaging planar samples with moving stages at greater than 5 mm deep into the sample (Glaser, Reder et al. 2017, Glaser, Reder et al. 2019). These systems separate the optics from potentially destructive clearing agents with coverglass or other thin transparent composites, using specialized optical components to compensate for aberrations stemming from the resulting index of refraction mismatches. Interestingly, SCAPE's ability to switch from an inverted to upright configuration can allow it make use of both of these benefits. When imaging samples with aqueous media such as those used for expansion microscopy (n = 1.33), an upright configuration can allow the objective lens to simply dip into the immersion medium. For more corrosive substances, an inverted configuration can be used imaging the sample through a glass bottom petri dish while keeping the objective lens safe from harm. This inverted configuration is how the cleared brain presented later in this section was imaged.

Here, we show that in addition to the functional imaging applications previously described, SCAPE can also be used for high-throughput scanning of intact and cleared tissue. The same SCAPE2b configuration shown in **Figure 2.12**c can be utilized for high-throughput depth-resolved imaging of complex structures. In order to acquire the comparatively larger fields of view necessary to image these intact samples, we dwell the galvo mirror at a single position and scan the sample through a stationary sheet by utilizing a motorized stage. This was the volume acquisition paradigm used in the original demonstration of oblique plane microscopy (OPM) (Dunsby 2008). The numerical aperture of the sheet is adjusted to account for the thickness of the sample and the camera magnification is selected to provide the desired y-z sample density. The sample is then translated through the sheet using a motorized stage while running the camera at high frame rates. With these types of scans, the sampling density along the x-dimension is dictated by the camera frame rate and the stage scanning speed (e.g. 1mm/s speed at 1000 fps provides 1um sample density).

Imaging the Cleared Brain

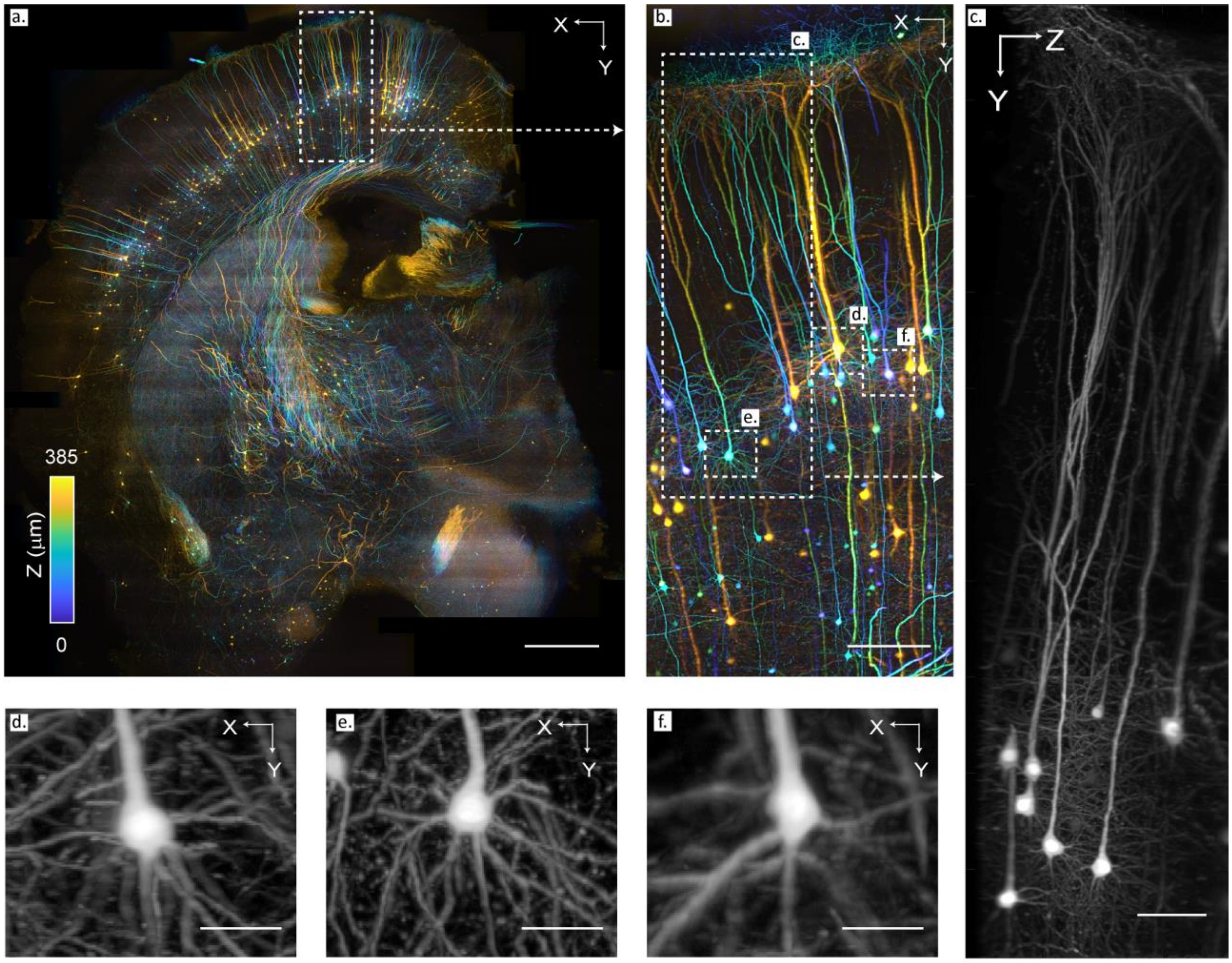

Z: 0 - 120 µm Z: 139 - 236 µm Z: 289 - 385 µm

Figure 3.19: *Imaging the cleared brain (Thy1-YFP) on SCAPE2b*
a. *Top-down view of a coronal hemi-section of a mCUBIC-cleared brain acquired using stage-scanning volume acquisition and reconstructed via pairwise stitching algorithms. The colors encode depth into the sample through a z-range of 385 µm. The data was gamma corrected with a factor of 0.5 prior to encoding to enhance contrast between cell bodies and dendrites. Scale bar- 1mm* ***b.*** *A close-up of region outlined in (a). Scale bar – 250 µm* ***c.*** *YZ maximum intensity projection taken along the X direction of the region highlighted in (b). Scale bar – 100 µm* ***.d-f.*** *XY maximum intensity projections of regions indicated in (b) over the depth specified below figures shows ability to clearly visualize dendritic processes throughout the full ~ 400 µm thick section. This dataset was acquired on an OPM-style stage-scanning variant of SCAPE2b built by Kripa Patel who acquired the data and stitched together the larger dataset using methods described below.*

The cleared brain was placed on top of a glass-bottom petri dish and imaged from below in an inverted configuration. The system was built to the exact specifications of SCAPE2b, using 488 nm excitation and a 500 LP emission filter onto an Andor Zyla 4.2+. Each camera frame acquired an 800 x 400 pixel ROI (covering a field of view of approximately 1096 x 460 µm) at

520 fps. In “stage-scanning mode”, the stage was translated continuously along the x-direction over a range of 3.5-9 mm for each scan with an image acquired on the camera at 1 µm intervals. The effective magnification of the system in this case is ~4.66x providing a 1.0 x 1.37 x 1.14 µm (X, Y, Z) sampling density. The stage was then translated along the Y-dimension before starting the subsequent scan with a 50% overlap between adjacent scans. The system acquired 18 scans to cover the entire area of the cleared brain hemi-section (~8.5 x 9.5 x 0.46 mm field of view) with a cumulative imaging time of ~ 3.83 minutes discounting stage re-settling time. Image stitching of the cleared brain hemi-section was performed using the Grid Stitching plugin in Fiji (Preibisch, Saalfeld et al. 2009, Schindelin, Arganda-Carreras et al. 2012). Overlap was set to about 500um in the y dimension. Strips were stitched 2 or 3 at a time to ensure proper overlap, and fused using linear blending.

This demonstration shows that large sections of cleared tissue can be rapidly imaged over arbitrarily large fields of view. At this magnification, it becomes possible to trace individual dendritic processes and axonal projections hundreds of microns from the soma body (**Figure 3.19**). In sparser samples, projections from intracortical regions can also be theoretically segmented, skeletonized and used for further quantitative analysis.

In order to explore the degree of detail accessible to the SCAPE2b system, we further increased the magnification to zoom in on individual dendritic processes. The lenses in the camera telescope were replaced with a Mitutoyo 50x/0.75NA objective lens and a 200 mm tube lens, resulting in a system magnification of 66.5x. An ROI of 1990 x 600 pixels (corresponding to a 194.5 x 47.1 um in plane field of view) was acquired on the Andor Zyla at 9.7 fps. In this instance, the size of the camera chip (i.e. the number of columns) played the role of the field stop and limited the field of view along the Y-dimension. The galvo was

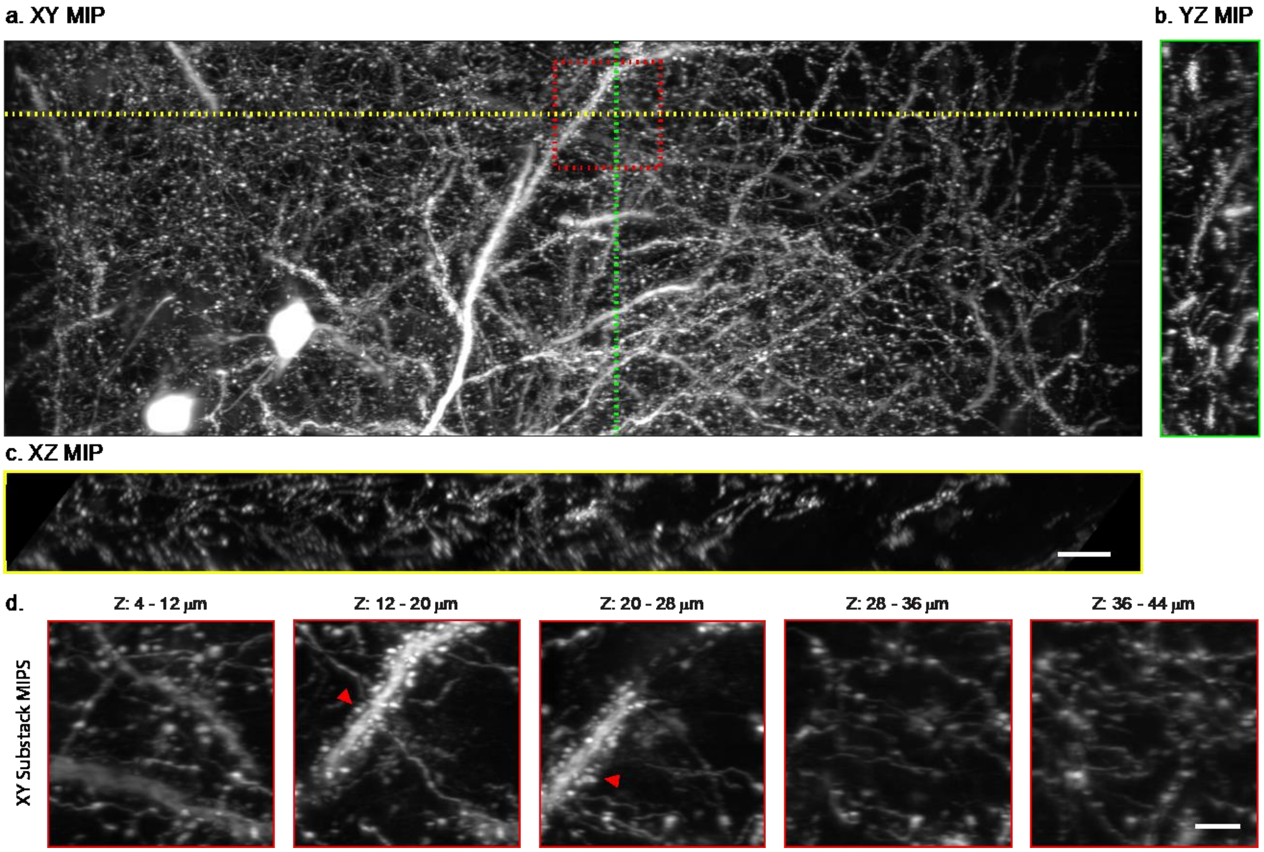

***Figure 3.20**: High-magnification (66.5x) imaging dendritic spines in cleared brain tissue*
a.** XY maximum intensity projection of entire 500 x 187 x 47 µm volume of cleared brain tissue b. YZ maximum intensity projection of a +/- 5 µm substack centered along the green line shown in (a)* ***b. *XZ maximum intensity projection of a +/- 5 µm substack centered along the yellow line shown in (a). Scale bar is 50 µm and is shared for (a, b, c)* ***d.*** *Zoomed in XY maximum intensity projection of the red square shown in (a) over the indicated depth ranges. Scale bar – 10 µm. The color-scale for all data shown in this figure is shown with a gamma correction of 0.5 to improve contrast between the larger dendritic stalks and lower intensity finer processes.*

swept over a range of 500 µm with a camera frame acquired every 0.5 µm. The volume took 100 sec to acquire.

At this magnification, it is not only possible to see dendritic processes, but also dendritic spines spanning the 50 µm depth range of the acquisition (red arrows in **Figure 3.20**d). Furthermore, we can see small intracellular structures within the neuronal soma as well. The image was intentionally acquired at 100 fps so as to not bleach the sample. Were the camera acquiring at the maximum frame rate, the entire volume could be ~4 sec. At this magnification and imaging rate, the entire hemi-section shown in **Figure 3.19** would be acquired at this magnification in ~ 9 hours at the level of resolution required to see dendritic spines and would consume ~ 19.4 TB of storage space.

Imaging in the Retinal Flatmount

Two modes of volume acquisition were showcased using the retinal flat-mount preparation: galvo scanning and stage scanning. In both instances, the sample was imaged using 488 nm excitation and a 500 LP emission filter onto an Andor Zyla 4.2+. The retinal flatmount was mounted on a glass slide with the photoreceptor layer face-down, and imaged through a glass coverslip. The mouse retina expressed a virally injected Alexa-488 enhanced GFP that was injected into the vitreous of the eye under isoflurane (AAV2-CAG-ChR2-GFP-NA1.6). The virus has been shown to express primarily in Aii amacrine and retinal ganglion cells (Wu, Ivanova et al. 2011).

In “stage-scanning mode”, the stage was translated continuously along the x-direction over a range of 4.5 mm and sample imaged at 250 fps, with an image acquired on the camera at 1 µm intervals. Each camera frame covered a field of view of approximately 860 x 250 µm within the YZ plane, sampled at 1.37 and 1.14 µm along the Y and Z dimensions respectively. The stage was then translated along the Y-dimension before starting the subsequent scan with a 25% overlap between adjacent scans. The system acquired 7 scans to cover the entire area of the retinal flat-mount (~4.75 x 4.35 x 0.32 mm field of view) with a cumulative imaging time of

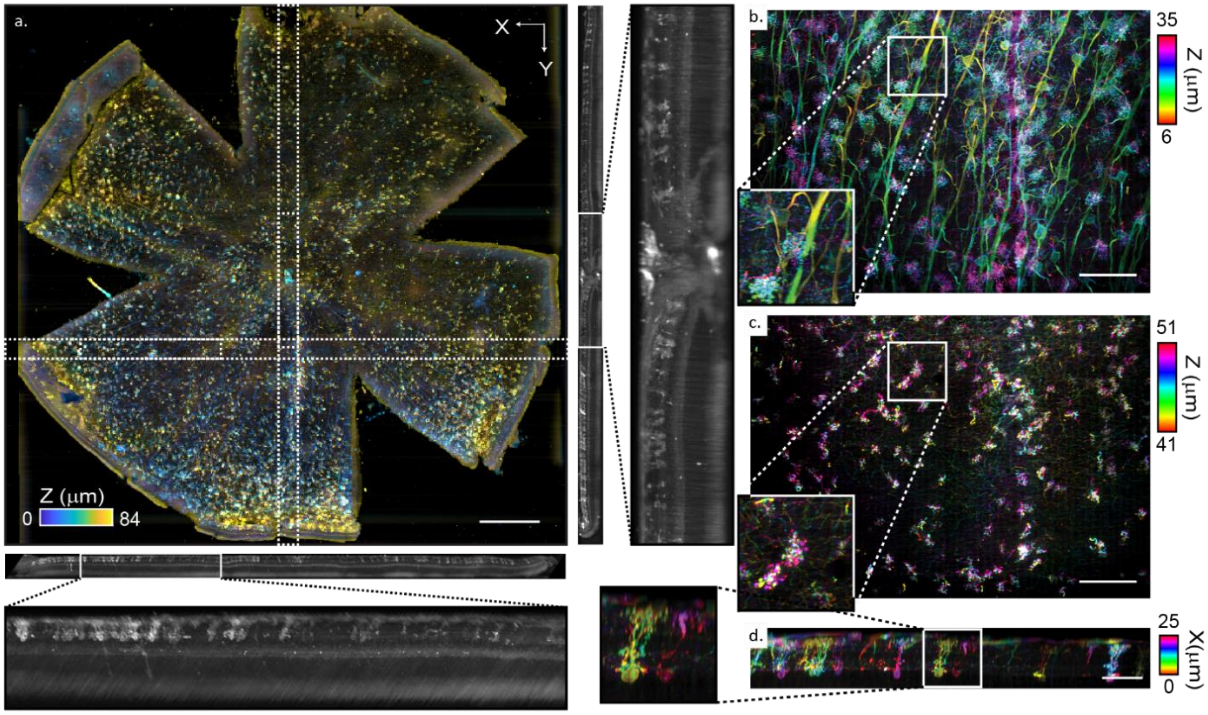

***Figure 3.21**: Structural imaging of explanted mouse retinal flatmount*
(Left) Top-down view of a stitched retinal flatmount acquired via stage-scanning in which colors encode depth into sample through 84 µm. Side-views show projections along the X and Y dimensions of regions indicated over the full 235 µm thickness of the sample. Scale bar -500 µm ***b,c.*** *High-magnification top-down (XY) view of retinal flatmount in which colors encode depth over the specified range (top and middle image). Scale bar – 100 µm* ***d.*** *A maximum intensity projection from the side (YZ) was taken over a 25 µm scan range, in which the color encodes the location of the structures within the sub-scan. The full extent of the bipolar cells can be visualized extending apical tufts into the ganglionic cell layer. Scale bar - 50 µm. (b. and d.) are shown with a gamma correction of 0.5 whereas (c.) is shown with a gamma correction of 0.25 to enhance the contrast between the brightly fluorescent soma and dim dendritic processes. Insets are magnified by 2x. The sample was provided by Brent Young and Ning Tian for providing the retinal flat mounted sample. The large field of view retinal flatmount image shown in (a) was acquired on an OPM-style stage-scanning variant of the SCAPE2b design built by Kripa Patel who acquired the data and stitched together the dataset using methods described below.*

~2.1 minutes discounting stage re-settling time. In total, 7 strips, each with a field of view of [X,Y,Z] = 4500 x 680 x 275 pixels, were stitched together with about 25% overlap in the y dimension.

Image stitching of the entire retinal flatmount was performed using the BigStitcher plugin in Fiji (Schindelin, Arganda-Carreras et al. 2012, Hörl, Rojas Rusak et al. 2018). In BigStitcher, tiles were loaded as multi-resolution HDF5 files and initially positioned with the "arrange tiles in grid" option. The default settings for the stitching wizard were used to find the correct stitching parameters and the final stitched image was fused through linear blending. The data shown in

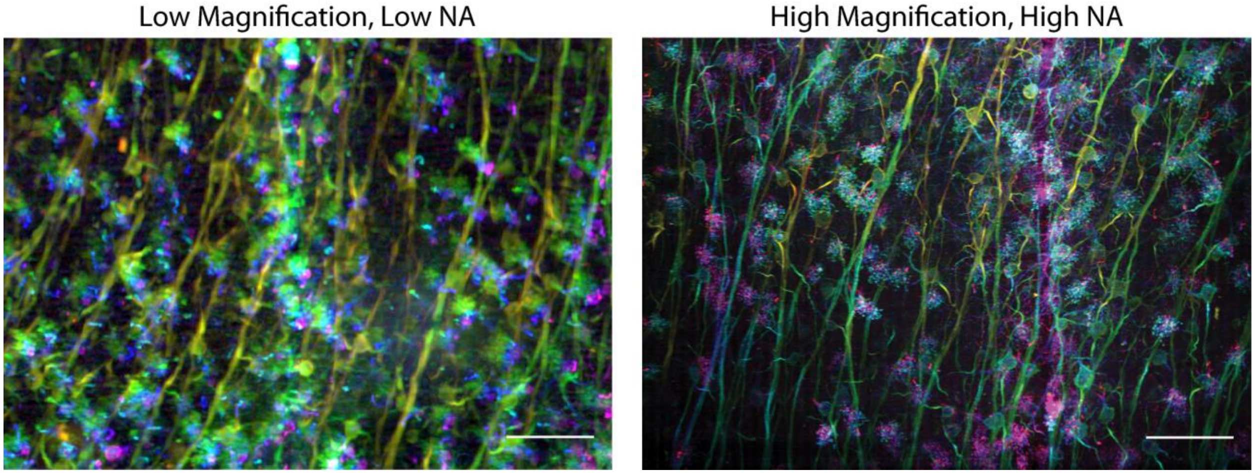

Low Magnification, Low NA

High Magnification, High NA

Figure 3.22: *Comparison of the retinal flat-mount imaged at high-mag, high-NA (26.6x, 0.35NA) and low-mag, low-NA (4.66x, 0.25NA). The top-down (XY) view is show as a depth-projection of the top ~30 µm of the sample. Retinal ganglion cells, as well as their axonal projections can be clearly visualized in both views. Scale bar – 100 µm*

was cropped in the z-dimension to remove blank space above and below the sample (**Figure 3.21**a). The effective magnification of the system in this case is ~4.66x.

In "galvo-scanning mode", a volume of ~ 400x700x100 µm was acquired at high magnification (~26.66x) with the same configuration used to image the immobilized C. elegans and the oblique sheet was swept through using the sample using the galvo mirror. The sampling density of the higher-magnification volume was 0.24 x 0.24 x 0.2 µm (X, Y, Z). The volume was acquired in 81 seconds due to low sample fluorescence and dense sampling along the scan direction (0.24 µm/pixel). Apical tufts from Amacrine Aii cells can be seen extending into the ganglionic cell layer of the retina **Figure 3.21**b-d) and fine dendritic structure across the inner and outer nuclear layers can be also be visualized (**Figure 3.21**c). **Figure 3.22** shows a comparison between the image quality of high and low magnification imaging on SCAPE. While the latter can definitely be used for a range of applications such as cell identification and tracking, higher magnification implementations can be useful for the tracing of fine processes.

Alternative Illumination Scheme

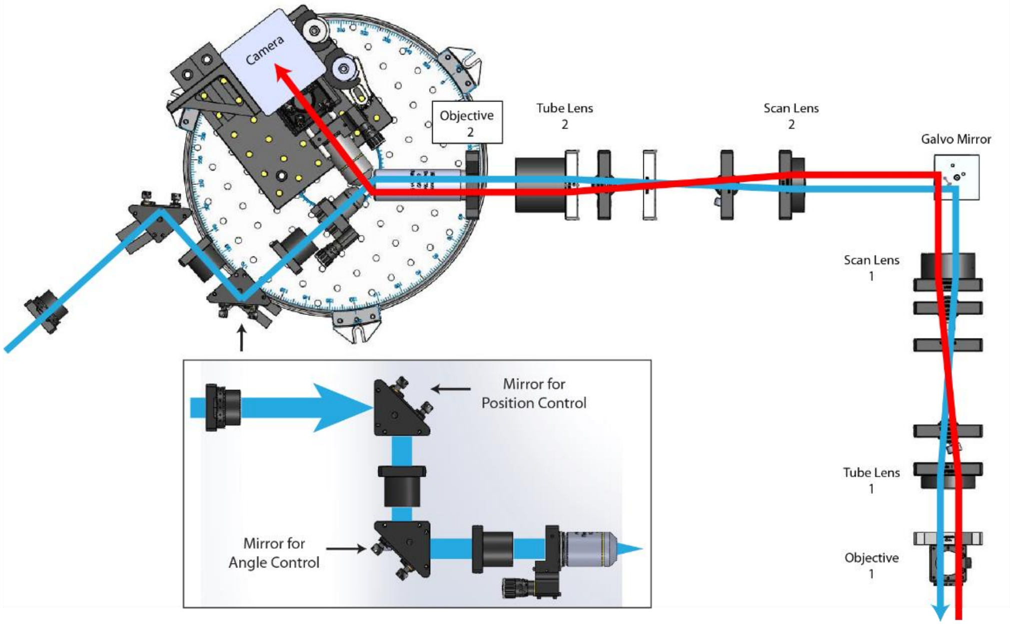

Figure 3.23: *Schematic of alternative illumination scheme for SCAPE microscopy (Inset) Zoomed in schematic of laser launch. Blue lines are illumination lines and red lines represent pathway of fluorescence.*

SCAPE2b relies on a dichroic mirror placed before the galvo mirror to separate the excitation from the detection path – similar to a confocal microscope – which means that the addition of multiple laser lines would require replacing the central dichroic mirror. Because the conjugate image space between O2 and O3 should perfectly map to the sample, it is possible to introduce the sheet into the system via the second objective lens placed in this space. While a previous group has implemented such a laser launch to perform sheet-based excitation in oblique plane microscopy, their implementation utilized a piezo-scanner to perform volumetric imaging which limited their achievable depth range to ~ 80 µm (Kumar, Wilding et al. 2011, Sikkel, Kumar et al. 2016). Their scan range would similarly have been ~ 100 µm. By using galvo-based scanning, we are able to achieve a scanned field of view equivalent to what is accessible by the scan telescope. For our system using an Olympus 20x/1.0NA lens, this field of view would be ~ 800 µm.

See **Figure 3.23** for a schematic of a launch-based system. I designed a custom laser-launch using Solidworks to implement this alternative illumination scheme. The optics were chosen to create an approximately 600 µm long sheet with variable sheet thickness. Mirrors positioned at planes conjugate to the object and back focal plane of the launch objective lens afford control of the sheet’s direction of travel and position respectively. The launch is oriented at 90˚ with respect to the camera telescope. With a lack of the dichroic, the camera telescope only needs to replace its emission filter to accommodate different excitation wavelengths. This setup was used to acquire the C. elegans image shown in **Figure 3.11**a.

Chapter 4 – Conclusion

This work has detailed the development of swept, confocally aligned planar excitation microscopy from a first-generation prototype to a stable workhorse system that is being increasingly used by the research community. Over the past seven years, I’ve worked with scientists from over 20 different labs from all areas of biological research, hosting them in our facilities as well as building temporary systems at imaging courses around the world. In this text, I’ve presented my theoretical work in modeling the system, the current system’s capabilities, and results from those applications that I have focused on most closely. Future work on SCAPE will involve technical advances with respect to system design, exploration of untapped application spaces, and the implementation of increasingly sophisticated data acquisition and analysis pipelines

The simplest improvements to system performance come from the availability of better hardware. Commercially available objective lenses are continuously improving, with longer working distances and higher numerical apertures. This will eventually push the achievable resolutions and light collection efficiencies of SCAPE closer to that of high-NA spinning disk or point-scanning confocal microscopes. Over the course of the past seven years alone, the availability of better camera sensor technology has allowed us to increase imaging speed of our own system by over an order of magnitude while still maintaining sufficient SNR to resolve biological structures with single cell resolution. Improvements to laser technology over the past few years have already fueled development of SCAPE systems utilizing near-infrared or multi-photon excitation, which will be capable of penetrating deeper into scattering tissue such as the mouse brain (Galwaduge, Yu et al. 2016, Yu, galwaduge et al. 2017, Yu, Galwaduge et al. 2018).

While the system described has used a single water-immersed, low-magnification objective lens at the interface between the system and sample, a range of other configurations following the basic principles outlined in Chapter 2 are also possible. For example, I have previously built a system which uses dry objective lenses at the sample obviating the need for sample immersion (ideal for in toto imaging of behaving land-dwelling organisms). I have also built a prototype of a system that substitutes the objective lenses with achromats in order to access fields of view on the order of 0.5 – 1 cm. Development of miniaturized and handheld systems based on swept, oblique plane geometries are currently underway (Patel, Voleti et al. 2017). Alternative configurations for swept, oblique plane microscopes with similar geometries to SCAPE have already demonstrated the ability to perform sub-cellular resolution over relatively small fields of view, as well as the ability to perform single-protein tracking using single-molecule localization techniques (Yang, Wang et al. 2018).

Furthermore, we can incorporate a host of features to SCAPE that have already made their way into the standard light sheet microscopy community. For example, high-speed axial scanning of the light sheet can improve sheet uniformity over a significantly larger depth of field than if we were to purely use Gaussian beams (Dean, Roudot et al. 2015), while adding structured illumination patterns to the sheet will allow us to image high spatial frequency features in samples that are beyond the resolution limits of the current system (Keller, Schmidt et al. 2010, Gao, Shao et al. 2012, Chen, Legant et al. 2014). Adaptive optics implementations on the excitation or detection pathways can further help improve the system’s resilience to sample aberrations.

From an applications perspective, the capabilities of SCAPE are attractive for a number of model systems. In addition to the numerous model organisms showcased within this text, SCAPE has been used to image the volvox, hydra, Platynereis dumerilii, and Arabidopsis thaliana at various conferences over the years. Each of these organisms has an active community of researchers who could benefit from the versatile, high-speed, 3D imaging capabilities of SCAPE. Similarly, rapid 3D imaging of human tissues can be useful in a range of clinical settings; for example, the system could serve as a more comprehensive alternative to 2D histology in a pathology lab or provide the ability to visualize subcellular structures in-vivo and in real-time to aid in faster diagnoses. In previous chapters, I've provided an example of 3D blood flow tracking in the zebrafish heart. More generally, 3D particle tracking can be used to characterize microflows in a variety of industrial/microfluidic applications, or characterize biomechanical properties in 3D anisotropic substances. The range of possibilities in the last seven years has grown, and shall continue to grow.

Finally, the increasing complexity and scope of this work would doubtless require the development of robust image acquisition and analysis pipelines catered to each application. Currently, our approach towards imaging a given sample requires us to optimize the system acquisition parameters, acquire our data, and process the results as three discrete steps – each of which require significant, direct user intervention. Previous work in the light sheet community has already shown that system optimization and acquisition can occur both simultaneously and autonomously (Royer, Lemon et al. 2016). Another study performing online analysis to target neuronal laser ablation in tandem with 3D functional imaging in zebrafish also shows the benefits of closed-loop imaging and analysis (Vladimirov, Wang et al. 2018). All of the applications that I’ve presented in this work could benefit from robust pipelines that are capable of online cell tracking, registration, signal extraction, visualization and statistical inference.

References

These references apply for Chapters 1-4. Appendices A-E contain no references and Appendix F which is a standalone work in its own right, and contains its own bibliography.

1. Ahrens, M. B., M. B. Orger, D. N. Robson, J. M. Li and P. J. Keller (2013). "Whole-brain functional imaging at cellular resolution using light-sheet microscopy." Nat Methods **10**(5): 413-420.
2. Ahrens, M. B., M. B. Orger, D. N. Robson, J. M. Li and P. J. Keller (2013). "Whole-brain functional imaging at cellular resolution using light-sheet microscopy." Nat Methods **10**(5): 413-420.
3. Allan, D. B., T. Caswell, N. C. Keim and C. M. van der Wel. (2018, 2018, April 21). "trackpy: Trackpy v0.4.1 (Version v0.4.1." from http://doi.org/10.5281/zenodo.1226458.
4. Allen, E. A., E. Damaraju, S. M. Plis, E. B. Erhardt, T. Eichele and V. D. Calhoun (2014). "Tracking whole-brain connectivity dynamics in the resting state." Cereb Cortex **24**(3): 663-676.
5. Ardiel, E. L., A. Kumar, J. Marbach, R. Christensen, R. Gupta, W. Duncan, J. S. Daniels, N. Stuurman, D. Colon-Ramos and H. Shroff (2017). "Visualizing Calcium Flux in Freely Moving Nematode Embryos." Biophys J **112**(9): 1975-1983.
6. Arnaout, R., T. Ferrer, J. Huisken, K. Spitzer, D. Y. Stainier, M. Tristani-Firouzi and N. C. Chi (2007). "Zebrafish model for human long QT syndrome." Proc Natl Acad Sci U S A **104**(27): 11316-11321.
7. Bakkers, J. (2011). "Zebrafish as a model to study cardiac development and human cardiac disease." Cardiovasc Res **91**(2): 279-288.
8. Bargmann, C. I. (2006). "Chemosensation in C. elegans." WormBook: 1-29.
9. Beis, D., T. Bartman, S. W. Jin, I. C. Scott, L. A. D'Amico, E. A. Ober, H. Verkade, J. Frantsve, H. A. Field, A. Wehman, H. Baier, A. Tallafuss, L. Bally-Cuif, J. N. Chen, D. Y. Stainier and B. Jungblut (2005). "Genetic and cellular analyses of zebrafish atrioventricular cushion and valve development." Development **132**(18): 4193-4204.
10. Berezin, M. Y. and S. Achilefu (2010). "Fluorescence lifetime measurements and biological imaging." Chem Rev **110**(5): 2641-2684.
11. Bilan, D. S. and V. V. Belousov (2016). "Genetically encoded probes for NAD(+)/NADH monitoring." Free Radic Biol Med **100**: 32-42.
12. Born, M. and E. Wolf (1970). Principles of Optics: Electromagnetic Theory of Propagation, Interference and Diffraction of Light, Pergamon Press.
13. Botcherby, E. J., R. Juškaitis, M. J. Booth and T. Wilson (2007). "Aberration-free optical refocusing in high numerical aperture microscopy." Optics Letters **32**(14): 2007-2009.
14. Botcherby, E. J., R. Juškaitis, M. J. Booth and T. Wilson (2008). "An optical technique for remote focusing in microscopy." Optics Communications **281**(4): 880-887.

15. Bouchard, M. B. (2014). 2D and 3D high-speed multispectral optical imaging systems for in-vivo biomedical research. Ph.D., Columbia University.

16. Bouchard, M. B., V. Voleti, C. S. Mendes, C. Lacefield, W. B. Grueber, R. S. Mann, R. M. Bruno and E. M. C. Hillman (2015). "Swept confocally-aligned planar excitation (SCAPE) microscopy for high speed volumetric imaging of behaving organisms." Nature photonics **9**(2): 113-119.

17. Bouchard, M. B., V. Voleti, C. S. Mendes, C. Lacefield, W. B. Grueber, R. S. Mann, R. M. Bruno and E. M. C. Hillman (2015). "Swept confocally-aligned planar excitation (SCAPE) microscopy for high speed volumetric imaging of behaving organisms." Nature photonics **9**: 113-119.

18. Broxton, M., L. Grosenick, S. Yang, N. Cohen, A. Andalman, K. Deisseroth and M. Levoy (2013). "Wave optics theory and 3-D deconvolution for the light field microscope." Opt Express **21**(21): 25418-25439.

19. Burgess, S. a., M. B. Bouchard, B. Yuan and E. M. C. Hillman (2008). "Simultaneous multiwavelength laminar optical tomography." Optics letters **33**(22): 2710-2712.

20. Chandler, D. E. and R. W. Roberson (2009). Bioimaging : current concepts in light and electron microscopy. Sudbury, Mass., Jones and Bartlett Publishers.

21. Chen, B.-c., W. R. Legant, K. Wang, L. Shao, D. E. Milkie, M. W. Davidson, C. Janetopoulos, X. S. Wu, J. A. H. Iii, Z. Liu, B. P. English, Y. Mimori-kiyosue, D. P. Romero, A. T. Ritter, J. Lippincott-schwartz, L. Fritz-laylin, R. D. Mullins, D. M. Mitchell, J. N. Bembenek, A.-c. Reymann, R. Böhme, S. W. Grill, J. T. Wang, G. Seydoux, U. S. Tulu, D. P. Kiehart, E. Betzig, W. Michael, C. Janetopoulos, X. S. Wu, J. A. H. Iii, Z. Liu, P. Brian, Y. Mimori-kiyosue, D. P. Romero, A. T. Ritter, J. Lippincott, L. Fritz-laylin, R. D. Mullins, D. M. Mitchell, N. Joshua, A.-c. Reymann, R. Böhme, S. W. Grill, J. T. Wang, G. Seydoux, U. S. Tulu, D. P. Kiehart and E. Betzig (2014). "Lattice light-sheet microscopy: Imaging molecules to embryos at high spatiotemporal resolution." Science **346**(6208): 1257998-1257998.

22. Chen, Q., J. Cichon, W. Wang, L. Qiu, S.-J. R. Lee, N. R. Campbell, N. Destefino, M. J. Goard, Z. Fu, R. Yasuda, L. L. Looger, B. R. Arenkiel, W.-B. Gan and G. Feng (2012). "Imaging neural activity using Thy1-GCaMP transgenic mice." Neuron **76**(2): 297-308.

23. Chen, T. W., T. J. Wardill, Y. Sun, S. R. Pulver, S. L. Renninger, A. Baohan, E. R. Schreiter, R. A. Kerr, M. B. Orger, V. Jayaraman, L. L. Looger, K. Svoboda and D. S. Kim (2013). "Ultrasensitive fluorescent proteins for imaging neuronal activity." Nature **499**(7458): 295-300.

24. Cheng, A., J. T. Goncalves, P. Golshani, K. Arisaka and C. Portera-Cailliau (2011). "Simultaneous two-photon calcium imaging at different depths with spatiotemporal multiplexing." Nat Methods **8**(2): 139-142.

25. Cong, L., Z. Wang, Y. Chai, W. Hang, C. Shang, W. Yang, L. Bai, J. Du, K. Wang and Q. Wen (2017). "Rapid whole brain imaging of neural activity in freely behaving larval zebrafish (Danio rerio)." Elife **6**.

26. Corbett, A. D., R. A. B. Burton, G. Bub, P. S. Salter, S. Tuohy, M. J. Booth and T. Wilson (2014). "Quantifying distortions in two-photon remote focussing microscope images using a volumetric calibration specimen." Frontiers in Physiology **5**(OCT): 1-9.

27. Corsi, A. K. (2006). "A biochemist's guide to Caenorhabditis elegans." Anal Biochem **359**(1): 1-17.

28. Cranfill, P. J., B. R. Sell, M. A. Baird, J. R. Allen, Z. Lavagnino, H. M. de Gruiter, G. J. Kremers, M. W. Davidson, A. Ustione and D. W. Piston (2016). "Quantitative assessment of fluorescent proteins." Nat Methods **13**(7): 557-562.

29. De Luca, E., G. M. Zaccaria, M. Hadhoud, G. Rizzo, R. Ponzini, U. Morbiducci and M. M. Santoro (2014). "ZebraBeat: a flexible platform for the analysis of the cardiac rate in zebrafish embryos." Scientific Reports **4**(1).

30. Dean, K. M., P. Roudot, E. S. Welf, G. Danuser and R. Fiolka (2015). "Deconvolution-free Subcellular Imaging with Axially Swept Light Sheet Microscopy." Biophys J **108**(12): 2807-2815.

31. Dodt, H.-U., U. Leischner, A. Schierloh, N. Jährling, C. P. Mauch, K. Deininger, J. M. Deussing, M. Eder, W. Zieglgänsberger and K. Becker (2007). "Ultramicroscopy: three-dimensional visualization of neuronal networks in the whole mouse brain." Nature methods **4**(4): 331-336.

32. Dodt, H.-U., S. Saghafi, K. Becker, N. Jährling, C. Hahn, M. Pende, M. Wanis and A. Niendorf (2015). "Ultramicroscopy: development and outlook." Neurophotonics **2**(4): 041407-041407.

33. Dunsby, C. (2008). "Optically sectioned imaging by oblique plane microscopy." Optics express **16**(25): 20306-20316.

34. Dunsby, C. (2008). "Optically sectioned imaging by oblique plane microscopy." Optics express **16**: 20306-20316.

35. Dwyer, P. J., C. A. DiMarzio and M. Rajadhyaksha (2007). "Confocal theta line-scanning microscope for imaging human tissues." Appl Opt **46**(10): 1843-1851.

36. Dwyer, P. J., C. a. DiMarzio and M. Rajadhyaksha (2007). "Confocal theta line-scanning microscope for imaging human tissues." Applied optics **46**(10): 1843-1851.

37. Dwyer, P. J., C. A. DiMarzio, J. M. Zavislan, W. J. Fox and M. Rajadhyaksha (2006). "Confocal reflectance theta line scanning microscope for imaging human skin in vivo." Opt Lett **31**(7): 942-944.

38. Dwyer, P. J., C. a. DiMarzio, J. M. Zavislan, W. J. Fox and M. Rajadhyaksha (2006). "Confocal reflectance theta line scanning microscope for imaging human skin in vivo." Optics letters **31**(7): 942-944.

39. Fahrbach, F. O., F. F. Voigt, B. Schmid, F. Helmchen and J. Huisken (2013). "Rapid 3D light-sheet microscopy with a tunable lens." Opt Express **21**(18): 21010-21026.

40. Galwaduge, P. T., H. Yu, K. B. Patel, V. Voleti, M. Shaik and E. M. C. Hillman (2016). Towards Two-Photon Swept Confocally Aligned Planar Excitation Microscopy (2P-SCAPE). Biomedical Optics 2016, Fort Lauderdale, Florida, Optical Society of America.

41. Gao, L., L. Shao, C. D. Higgins, J. S. Poulton, M. Peifer, M. W. Davidson, X. Wu, B. Goldstein and E. Betzig (2012). "Noninvasive imaging beyond the diffraction limit of 3D dynamics in thickly fluorescent specimens." Cell **151**(6): 1370-1385.

42. Gjorgjieva, J., D. Biron and G. Haspel (2014). "Neurobiology of Caenorhabditis elegans Locomotion: Where Do We Stand?" Bioscience **64**(6): 476-486.

43. Glaser, A. K., N. P. Reder, Y. Chen, E. F. McCarty, C. Yin, L. Wei, Y. Wang, L. D. True and J. T. C. Liu (2017). "Light-sheet microscopy for slide-free non-destructive pathology of large clinical specimens." Nature Biomedical Engineering **1**(June): s41551-41017.

44. Glaser, A. K., N. P. Reder, Y. Chen, C. Yin, L. Wei, S. Kang, L. A. Barner, W. Xie, E. F. McCarty, C. Mao, A. R. Halpern, C. R. Stoltzfus, J. S. Daniels, M. Y. Gerner, P. R. Nicovich, J. C. Vaughan, L. D. True and J. T. C. Liu (2019). "Multi-immersion open-top light-sheet microscope for high-throughput imaging of cleared tissues." bioRxiv.

45. Glickman, N. S. and D. Yelon (2002). "Cardiac development in zebrafish: coordination of form and function." Semin Cell Dev Biol **13**(6): 507-513.

46. Goldstein, B. (2016). "Sydney Brenner on the Genetics of Caenorhabditis elegans." Genetics **204**(1): 1-2.

47. Gonzalez-Rosa, J. M., C. E. Burns and C. G. Burns (2017). "Zebrafish heart regeneration: 15 years of discoveries." Regeneration (Oxf) **4**(3): 105-123.

48. Grewe, B. F., D. Langer, H. Kasper, B. M. Kampa and F. Helmchen (2010). "High-speed in vivo calcium imaging reveals neuronal network activity with near-millisecond precision." Nature methods **7**(5): 399-405.

49. Grewe, B. F., D. Langer, H. Kasper, B. M. Kampa and F. Helmchen (2010). "High-speed in vivo calcium imaging reveals neuronal network activity with near-millisecond precision." Nat Methods **7**(5): 399-405.

50. Grosberg, L. E., A. J. Radosevich, S. Asfaha, T. C. Wang and E. M. Hillman (2011). "Spectral characterization and unmixing of intrinsic contrast in intact normal and diseased gastric tissues using hyperspectral two-photon microscopy." PLoS One **6**(5): e19925.

51. Hart, A. C. and M. Y. Chao (2010). From Odors to Behaviors in Caenorhabditis elegans. The Neurobiology of Olfaction. A. Menini. Boca Raton (FL).

52. Hillman, E. M. C., D. a. Boas, A. M. Dale and A. K. Dunn (2004). "Laminar optical tomography: demonstration of millimeter-scale depth-resolved imaging in turbid media." Optics letters **29**(14): 1650-1652.

53. Hillman, E. M. C., V. Voleti, K. B. Patel, W. Li, P. T. Galwaduge and H. Yu (2018). "High-speed 3D imaging of cellular activity in the brain: The advantages of axially-extended beams and light sheets." Current Opinion in Neurobiology.

54. Hobert, O. (2010). "Neurogenesis in the nematode Caenorhabditis elegans." WormBook: 1-24.

55. Holekamp, T. F., D. Turaga and T. E. Holy (2008). "Fast Three-Dimensional Fluorescence Imaging of Activity in Neural Populations by Objective-Coupled Planar Illumination Microscopy." Neuron **57**: 661-672.

56. Hörl, D., F. Rojas Rusak, F. Preusser, P. Tillberg, N. Randel, R. K. Chhetri, A. Cardona, P. J. Keller, H. Harz, H. Leonhardt, M. Treier and S. Preibisch (2018). "BigStitcher: Reconstructing high-resolution image datasets of cleared and expanded samples." bioRxiv: 343954.

57. Hu, H., Y. Wei, D. Wang, N. Su, X. Chen, Y. Zhao, G. Liu and Y. Yang (2018). "Glucose monitoring in living cells with single fluorescent protein-based sensors." RSC Advances **8**(5): 2485-2489.

58. Huisken, J. and D. Y. Stainier (2009). "Selective plane illumination microscopy techniques in developmental biology." Development **136**(12): 1963-1975.

59. Huisken, J., J. Swoger, F. Del Bene, J. Wittbrodt and E. H. Stelzer (2004). "Optical sectioning deep inside live embryos by selective plane illumination microscopy." Science **305**(5686): 1007-1009.

60. Ji, N., J. Freeman and S. L. Smith (2016). "Technologies for imaging neural activity in large volumes." Nature Neuroscience **19**(3): 1154-1164.

61. Kasahara, T. H. (2002). Microscope Objective Lens. U. S. P. Office. United States of America, Olympus Optical Co., Ltd.**:** 22.

62. Kato, S., H. S. Kaplan, T. Schrodel, S. Skora, T. H. Lindsay, E. Yemini, S. Lockery and M. Zimmer (2015). "Global brain dynamics embed the motor command sequence of Caenorhabditis elegans." Cell **163**(3): 656-669.

63. Keller, P. J., A. D. Schmidt, A. Santella, K. Khairy, Z. Bao, J. Wittbrodt and E. H. K. Stelzer (2010). "Fast , high-contrast imaging of animal development with scanned light sheet – based structured- illumination microscopy." Nature Publishing Group **7**(8): 637-642.

64. Keller, P. J., A. D. Schmidt, J. Wittbrodt and E. H. Stelzer (2008). "Reconstruction of zebrafish early embryonic development by scanned light sheet microscopy." Science **322**(5904): 1065-1069.

65. Kirchmaier, B. C., K. L. Poon, T. Schwerte, J. Huisken, C. Winkler, B. Jungblut, D. Y. Stainier and T. Brand (2012). "The Popeye domain containing 2 (popdc2) gene in zebrafish is required for heart and skeletal muscle development." Dev Biol **363**(2): 438-450.

66. Kithcart, A. and C. A. MacRae (2017). "Using Zebrafish for High-Throughput Screening of Novel Cardiovascular Drugs." JACC Basic Transl Sci **2**(1): 1-12.

67. Kumar, A., Y. Wu, R. Christensen, P. Chandris, W. Gandler, E. McCreedy, A. Bokinsky, D. A. Colón-Ramos, Z. Bao, M. McAuliffe, G. Rondeau and H. Shroff (2014). "Dual-view plane illumination microscopy for rapid and spatially isotropic imaging." Nature Protocols **9**(11): 2555-2573.

68. Kumar, S., D. Wilding, M. B. Sikkel, A. R. Lyon, K. T. MacLeod and C. Dunsby (2011). "High-speed 2D and 3D fluorescence microscopy of cardiac myocytes." Optics Express **19**: 13839-13847.

69. Kumar, S., D. Wilding, M. B. Sikkel, A. R. Lyon, K. T. MacLeod and C. Dunsby (2011). "High-speed 2D and 3D fluorescence microscopy of cardiac myocytes." Optics Express **19**(15): 13839-13847.

70. Lee, J., M. E. Moghadam, E. Kung, H. Cao, T. Beebe, Y. Miller, B. L. Roman, C. L. Lien, N. C. Chi, A. L. Marsden and T. K. Hsiai (2013). "Moving domain computational fluid dynamics to interface with an embryonic model of cardiac morphogenesis." PLoS One **8**(8): e72924.

71. Lemon, W. C., S. R. Pulver, B. Hockendorf, K. McDole, K. Branson, J. Freeman and P. J. Keller (2015). "Whole-central nervous system functional imaging in larval Drosophila." Nat Commun **6**: 7924.

72. Letamendia, A., C. Quevedo, I. Ibarbia, J. M. Virto, O. Holgado, M. Diez, J. C. Izpisua Belmonte and C. Callol-Massot (2012). "Development and validation of an automated high-throughput system for zebrafish in vivo screenings." PLoS One **7**(5): e36690.

73. Li, H., C. Guo, D. Kim-Holzapfel, W. Li, Y. Altshuller, B. Schroeder, W. Liu, Y. Meng, J. French, K.-I. Takamaru, M. Frohman and S. Jia (2018). "Fast, volumetric live-cell imaging using high resolution light-field microscopy." BioArxiv.

74. Lu, R., W. Sun, Y. Liang, A. Kerlin, J. Bierfeld, J. D. Seelig, D. E. Wilson, B. Scholl, B. Mohar, M. Tanimoto, M. Koyama, D. Fitzpatrick, M. B. Orger and N. Ji (2017). "Video-rate volumetric functional imaging of the brain at synaptic resolution." Nat Neurosci **20**(4): 620-628.

75. Mably, J. D., C. G. Burns, J.-N. Chen, M. C. Fishman and M.-A. P. K. Mohideen (2003). "heart of glass Regulates the Concentric Growth of the Heart in Zebrafish." Current Biology **13**(24): 2138-2147.

76. Mahou, P., J. Vermot, E. Beaurepaire and W. Supatto (2014). "Multicolor two-photon light-sheet microscopy." Nature Methods **11**(6): 600-601.

77. Mamontova, A. V., I. D. Solovyev, A. P. Savitsky, C. Shakhov Acapital Em, K. A. Lukyanov and A. M. Bogdanov (2018). "Bright GFP with subnanosecond fluorescence lifetime." Sci Rep **8**(1): 13224.

78. Martynov, V. I., A. A. Pakhomov, I. E. Deyev and A. G. Petrenko (2018). "Genetically encoded fluorescent indicators for live cell pH imaging." Biochim Biophys Acta Gen Subj **1862**(12): 2924-2939.

79. Maxwell, J. C. (1858). "On the General Laws of Optical Instruments." Quarterly Journal of Pure and Applied Mathematics **2**: 232-246.

80. Mickoleit, M., B. Schmid, M. Weber, F. O. Fahrbach, S. Hombach, S. Reischauer and J. Huisken (2014). "High-resolution reconstruction of the beating zebrafish heart." Nature Methods **11**(July): 919-924.

81. Migliori, B., M. S. Datta, M. C. Apak and R. Tomer (2017). "Light Sheet Theta Microscopy for High-resolution Quantitative Imaging of Large Biological Systems." bioRxiv: 119289-119289.

82. Nadella, K. M., H. Ros, C. Baragli, V. A. Griffiths, G. Konstantinou, T. Koimtzis, G. J. Evans, P. A. Kirkby and R. A. Silver (2016). "Random-access scanning microscopy for 3D imaging in awake behaving animals." Nat Methods **13**(12): 1001-1004.

83. Negrean, A. and H. D. Mansvelder (2014). "Optimal lens design and use in laser-scanning microscopy." Biomedical optics express **5**(5): 1588-1609.

84. Nguyen, J. P., A. N. Linder, G. S. Plummer, J. W. Shaevitz and A. M. Leifer (2017). "Automatically tracking neurons in a moving and deforming brain." PLoS Comput Biol **13**(5): e1005517.

85. Nguyen, J. P., F. B. Shipley, A. N. Linder, G. S. Plummer, M. Liu, S. U. Setru, J. W. Shaevitz and A. M. Leifer (2016). "Whole-brain calcium imaging with cellular resolution in freely behaving Caenorhabditis elegans." Proc Natl Acad Sci U S A **113**(8): E1074-1081.

86. Nusslein-Volhard, C. (2012). "The zebrafish issue of Development." Development **139**(22): 4099-4103.

87. Ostap, E. M. (2002). "2,3-Butanedione monoxime (BDM) as a myosin inhibitor." Journal of Muscle Research and Cell Motility **23**(4): 305-308.

88. Patel, K., V. Voleti, H. T. Zhao, C. Perez-campos and E. M. C. Hillman (2017). "Developing SCAPE Microscopy for Real-time , 3D Cellular Imaging at the Point-of-Care." **2017**: 3-5.

89. Pawley, J. B. (1995). Handbook of Confocal Microscopy. New York, Springer Science.

90. Preibisch, S., S. Saalfeld and P. Tomancak (2009). "Globally optimal stitching of tiled 3D microscopic image acquisitions." Bioinformatics **25**(11): 1463-1465.

91. Prevedel, R., Y.-G. Yoon, M. Hoffmann, N. Pak, G. Wetzstein, S. Kato, T. Schrödel, R. Raskar, M. Zimmer, E. S. Boyden and A. Vaziri (2014). "Simultaneous whole-animal 3D imaging of neuronal activity using light-field microscopy." Nature Methods **11**(7): 727-730.

92. Prevedel, R., Y. G. Yoon, M. Hoffmann, N. Pak, G. Wetzstein, S. Kato, T. Schrodel, R. Raskar, M. Zimmer, E. S. Boyden and A. Vaziri (2014). "Simultaneous whole-animal 3D imaging of neuronal activity using light-field microscopy." Nat Methods **11**(7): 727-730.

93. Radosevich, A. J., M. B. Bouchard, S. A. Burgess, B. R. Chen and E. M. Hillman (2008). "Hyperspectral in vivo two photon microscopy of intirnsic contrast." Optics Letters.

94. Robie, A. A., K. M. Seagraves, S. E. Egnor and K. Branson (2017). "Machine vision methods for analyzing social interactions." J Exp Biol **220**(Pt 1): 25-34.

95. Rodriguez, E. A., R. E. Campbell, J. Y. Lin, M. Z. Lin, A. Miyawaki, A. E. Palmer, X. Shu, J. Zhang and R. Y. Tsien (2017). "The Growing and Glowing Toolbox of Fluorescent and Photoactive Proteins." Trends Biochem Sci **42**(2): 111-129.

96. Royer, L. A., W. C. Lemon, R. K. Chhetri, Y. Wan, M. Coleman, E. W. Myers and P. J. Keller (2016). "Adaptive light-sheet microscopy for long-term, high-resolution imaging in living organisms." Nat Biotechnol **34**(12): 1267-1278.

97. Saghafi, S., K. Becker, C. Hahn and H.-U. Dodt (2013). "3D-ultramicroscopy utilizing aspheric optics." Journal of biophotonics **9**: 1-9.

98. Saghafi, S., K. Becker, N. Jährling, M. Richter, E. R. Kramer and H. U. Dodt (2010). "Image enhancement in ultramicroscopy by improved laser light sheets." Journal of Biophotonics **3**(10-11): 686-695.

99. Schindelin, J., I. Arganda-Carreras, E. Frise, V. Kaynig, M. Longair, T. Pietzsch, S. Preibisch, C. Rueden, S. Saalfeld, B. Schmid, J. Y. Tinevez, D. J. White, V. Hartenstein, K. Eliceiri, P. Tomancak and A. Cardona (2012). "Fiji: an open-source platform for biological-image analysis." Nat Methods **9**(7): 676-682.

100. Schmied, C. and P. Tomancak (2016). "Sample Preparation and Mounting of Drosophila Embryos for Multiview Light Sheet Microscopy." Methods Mol Biol **1478**: 189-202.

101. Schrodel, T., R. Prevedel, K. Aumayr, M. Zimmer and A. Vaziri (2013). "Brain-wide 3D imaging of neuronal activity in Caenorhabditis elegans with sculpted light." Nat Methods **10**(10): 1013-1020.

102. Siedentopf, H. and R. Zsigmondy (1902). "Uber Sichtbarmachung und Größenbestimmung ultramikoskopischer Teilchen, mit besonderer Anwendung auf Goldrubingläser." Annalen der Physik **315**(1): 1-39.

103. Sikkel, M. B., S. Kumar, V. Maioli, C. Rowlands, F. Gordon, S. E. Harding, A. R. Lyon, K. T. Macleod and C. Dunsby (2016). "High speed sCMOS-based oblique plane microscopy applied to the study of calcium dynamics in cardiac myocytes." Journal of Biophotonics **323**: 3-6.

104. Sikkel, M. B., S. Kumar, V. Maioli, C. Rowlands, F. Gordon, S. E. Harding, A. R. Lyon, K. T. Macleod and C. Dunsby (2016). "High speed sCMOS-based oblique plane microscopy applied to the study of calcium dynamics in cardiac myocytes." Journal of Biophotonics **323**(3): 3-6.

105. Song, A., A. S. Charles, S. A. Koay, J. L. Gauthier, S. Y. Thiberge, J. W. Pillow and D. W. Tank (2017). "Volumetric two-photon imaging of neurons using stereoscopy (vTwINS)." Nat Methods **14**(4): 420-426.

106. Spomer, W., A. Pfriem, R. Alshut, S. Just and C. Pylatiuk (2012). "High-throughput screening of zebrafish embryos using automated heart detection and imaging." J Lab Autom **17**(6): 435-442.

107. Staudt, D. and D. Stainier (2012). "Uncovering the molecular and cellular mechanisms of heart development using the zebrafish." Annu Rev Genet **46**: 397-418.

108. Tallini, Y. N., J. F. Brekke, B. Shui, R. Doran, S. M. Hwang, J. Nakai, G. Salama, S. S. Segal and M. I. Kotlikoff (2007). "Propagated endothelial Ca2+ waves and arteriolar dilation in vivo: measurements in Cx40BAC GCaMP2 transgenic mice." Circ Res **101**(12): 1300-1309.

109. Tallini, Y. N., M. Ohkura, B. R. Choi, G. Ji, K. Imoto, R. Doran, J. Lee, P. Plan, J. Wilson, H. B. Xin, A. Sanbe, J. Gulick, J. Mathai, J. Robbins, G. Salama, J. Nakai and M. I. Kotlikoff (2006). "Imaging cellular signals in the heart in vivo: Cardiac expression of the high-signal Ca2+ indicator GCaMP2." Proc Natl Acad Sci U S A **103**(12): 4753-4758.

110. Taylor, J. M. (2014). "Optically gated beating-heart imaging." Front Physiol **5**: 481.

111. Taylor, J. M., J. M. Girkin and G. M. Love (2012). "High-resolution 3D optical microscopy inside the beating zebrafish heart using prospective gating." Biomedical Optics Express **3**(12).

112. Taylor, J. M., C. J. Nelson, F. A. Bruton, A. K. Baghbadrani, C. Buckley, C. S. Tucker, J. J. Mullins and M. A. Denvir (2019). "Hybrid optical gating for long-term 3D time-lapse imaging of the beating embryonic zebrafish heart." BioArxiv.

113. Thouvenin, O. and C. Wyart (2017). "Tracking microscopy enables whole-brain imaging in freely moving zebrafish." Nat Methods **14**(11): 1041-1042.

114. Tomer, R. and K. Deisseroth (2015). "Rapid High-resolution Brain Mapping with CLARITY Optimized Light Sheet Microscopy (COLM)." Microscopy and Microanalysis **21**(S3): 717-718.

115. Tomer, R., K. Khairy and P. J. Keller (2011). "Shedding light on the system: studying embryonic development with light sheet microscopy." Curr Opin Genet Dev **21**(5): 558-565.

116. Tomer, R., L. Ye, B. Hsueh and K. Deisseroth (2014). "Advanced CLARITY for rapid and high-resolution imaging of intact tissues." Nat Protoc **9**(7): 1682-1697.

117. Traver, D., B. H. Paw, K. D. Poss, W. T. Penberthy, S. Lin and L. I. Zon (2003). "Transplantation and in vivo imaging of multilineage engraftment in zebrafish bloodless mutants." Nat Immunol **4**(12): 1238-1246.

118. Tsai, P. S., N. Nishimura, E. J. Yoder, E. M. Dolnick, A. G. White and D. Kleinfeld (2002). Principles, Design and Construction of a Two-Photon Laser Scanning Microscope for In Vitro and In Vivo Brain Imaging. In Vivo Optical Imaging of Brain Function. R. D. Frostig. Boca Raton, CRC Press LLC. **1:** 113-171.

119. Vaadia, R., W. Li, V. Voleti, A. Singhania, E. M. C. Hillman and W. B. Grueber (2018). "Characterization of proprioceptive system dynamics in behaving Drosophila larvae using high-speed volumetric microscopy." BioArxiv.

120. Vermot, J., S. E. Fraser and M. Liebling (2008). "Fast fluorescence microscopy for imaging the dynamics of embryonic development." HFSP J **2**(3): 143-155.

121. Vladimirov, N., C. Wang, B. Hockendorf, A. Pujala, M. Tanimoto, Y. Mu, C. T. Yang, J. D. Wittenbach, J. Freeman, S. Preibisch, M. Koyama, P. J. Keller and M. B. Ahrens (2018). "Brain-wide circuit interrogation at the cellular level guided by online analysis of neuronal function." Nat Methods **15**(12): 1117-1125.

122. Voie, A. H., D. H. Burns and F. A. Spelman (1993). "Orthogonal-plane fluorescence optical sectioning: three-dimensional imaging of macroscopic biological specimens." J Microsc **170**(Pt 3): 229-236.

123. Wang, H., M. Jing and Y. Li (2018). "Lighting up the brain: genetically encoded fluorescent sensors for imaging neurotransmitters and neuromodulators." Curr Opin Neurobiol **50**: 171-178.

124. Watson, B. O., V. Nikolenko and R. Yuste (2009). "Two-photon imaging with diffractive optical elements." Front Neural Circuits **3**(6): 1-6.

125. Weber, M. and J. Huisken (2015). "In vivo imaging of cardiac development and function in zebrafish using light sheet microscopy." Swiss Med Wkly **145**: w14227.

126. Weber, M., N. Scherf, P. Kohl and J. Huisken (2017). "Cell-accurate optical mapping across the entire developing heart." 1-23.

127. Wen, C., T. Miura, Y. Fujie, T. Teramoto, T. Ishihara and K. D. Kimura (2018). "Deep-learning-based flexible pipeline for segmenting and tracking in 3D image time series for whole brain imaging." BioArxiv.

128. White, J. G., E. Southgate, J. N. Thomson and S. Brenner (1986). "The structure of the nervous system of the nematode Caenorhabditis elegans." Philos Trans R Soc Lond B Biol Sci **314**(1165): 1-340.

129. Wu, C., E. Ivanova, J. Cui, Q. Lu and Z. H. Pan (2011). "Action potential generation at an axon initial segment-like process in the axonless retinal AII amacrine cell." J Neurosci **31**(41): 14654-14659.

130. Xu, Y., P. Zou and A. E. Cohen (2017). "Voltage imaging with genetically encoded indicators." Curr Opin Chem Biol **39**: 1-10.

131. Yang, B., Y. Wang, S. Feng, V. Pessino, N. Stuurman and B. Huang (2018). "High Numerical Aperture Epi-illumination Selective Plane Illumination Microscopy." bioRxiv.

132. Yu, H., P. T. galwaduge, V. Voleti, K. Patel, W. Li, M. A. Shaik and E. M. Hillman (2017). Two-photon Swept Confocally Aligned Planar Excitation Microscopy (2P-SCAPE). Optics in the Life Sciences Congress, San Diego, California, Optical Society of America.

133. Yu, H., P. T. Galwaduge, V. Voleti, K. B. Patel, M. A. Shaik, W. Li and E. M. C. Hillman (2018). Combining Near-infrared Excitation with Swept Confocally-aligned Planar Excitation (SCAPE) Microscopy for Fast, Volumetric Imaging in Mouse Brain. Biophotonics Congress: Biomedical Optics Congress 2018 (Microscopy/Translational/Brain/OTS), Hollywood, Florida, Optical Society of America.

Appendix A. Calibration Protocol

Lateral Calibration (y)

The sample used here is a glass slide embedded with fluorescent beads of multiple sizes (*Spherotech, FPS-M57-6*). The Spherotech slide is also ideal because the beads are all embedded in a single depth plane.

Take an HR scan with a 0.5 µm sampling density. Translate the bead in the lateral dimension (y) using a stage by a known distance ($\Delta y_{distance}$, typically 0.001'' or 25.4 µm) and take another scan. Repeat 10 times.

Make Tiff stacks of each scan using the SCAPE Read GUI. Place all of the Tiff stacks into a single directory and open them as a hypervolume (X, Y, Z, Scan Number) in Fiji. Take the XY-MIP (X, Y, Scan Number) and track the XY position of a single bead through multiple scans. The average displacement per step in the lateral dimension is found in pixels (Δy_{pixels}).

$$Lateral\ Calibration\ Factor = \frac{\Delta y_{distance}}{\Delta y_{pixels}}$$

If a plot of these values yields a line that is not linear, check your measurements and calculations. If the system is indeed found to have a non-linear calibration, the system may be generated a distorted image along the y direction (this is not common in our systems).

Scan Calibration (x)

The same Spherotech slide used in the Lateral Calibration section is used here. Take a scan with the SCAPE system using sufficiently large voltage range applied to the galvo, $X_{FOV\text{-}volt}$, and large number of steps, $X_{totalSteps}$, acquired on the camera over this range. The sampling density should be fine enough that multiple images are acquired per bead. In SCAPE, each scan consists of a finite number of galvo steps, $X_{totalSteps}$, over the scan direction. One of these steps is reserved as a "fly-back step" in which the galvo returns to its starting position at the start of the scan. The step size in "volts" applied to the galvo between sequential camera frames is therefore calculated as:

$$V_{X_{stepSize}} = \frac{V_{X_{FOV}}}{\mathrm{X}_{totalSteps}-2}$$

with units of volts per pixel, where $V_{X\ FOV}$ is the voltage range corresponding to the full x-range field of view.

Move the sample in the scan dimension (x) using a stage by a known distance ($\Delta X_{distance}$, typically 0.001'' or 25.4 µm), and take another scan. Repeat 10 times.

Make Tiff stacks of each scan using the SCAPE Read GUI. Place all of the Tiff stacks into a single directory and open them as a hypervolume (X, Y, Z, Scan Number) in Fiji. Take the XY-MIP (X, Y, Scan Number) and track the XY position of a single bead through multiple scans. The average displacement in the scan dimension is found in pixels (Δx_{pixels}). The scan calibration factor (i.e. microns/volt) is found by using the equation below:

$$Scan\ Calibration\ Factor = \frac{\Delta \mathrm{x}_{distance}}{\Delta \mathrm{x}_{pixels} * V_{X_{stepSize}}}$$

Be sure to use the correct value of $V_{X_{stepSize}}$ for the scan pattern used during acquisition of the calibration measurements.

If a plot of these values yields a line that is not linear, check your measurements and calculations. If the system is indeed found to have a non-linear calibration, the system may be generated a distorted image along the x direction (this is not common in our systems). If pronounced, you may wish to center the galvo position on the most linear part of the field of view (e.g. add a galvo offset from 0).

Depth Calibration (z)

The sample used is a 3D phantom is made using a sparse distribution of 1 µm beads embedded in 1-2% agar gel. It is important to use small beads to prevent localization errors later in this protocol.

Take an HR scan with a 0.5 µm sampling density. Translate the bead in the depth dimension (z) using a stage by a known distance ($\Delta z_{distance}$, typically 0.001'' or 25.4 µm) and take another scan. Repeat 5-10 times.

Make Tiff stacks of each scan using the SCAPE Read GUI. Place all of the Tiff stacks into a single directory and open them as a hypervolume (X, Y, Z, Scan Number) in Fiji. Take the YZ-MIP (Y, Z, Scan Number) and track the YZ position of a single bead through multiple scans. The average displacement per step in the lateral dimension is found in pixels (Δz_{pixels}).

$$Depth\ Calibration\ Factor = \frac{\Delta z_{distance}}{\Delta z_{pixels}}$$

If a plot of these values yields a line that is not linear, check your measurements and calculations. If the system is indeed found to have a non-linear calibration, the system may be generated a distorted image along the z direction.

Sheet Angle

The dataset acquired to perform a depth calibration can similarly be used to calculate the system's sheet angle within the sample.

Instead of taking the YZ MIP of the hyperstack, take the XZ MIP and collapse each scan number (X, Z). Track the position of pairs of beads from one depth to another. The difference in their heights, Z, and scan position, X, can be used to find the angular position of the sheet within the sample. Because the

Notes

The lateral calibration factor detailed above is given in units of microns/pixel and should not change unless the magnification of the object onto the camera is altered by replacing optical components within the system. The depth calibration is similarly stable in our systems and given by microns/pixel, but can be altered if the angle of the light sheet is altered by adjusting the position of the sheet forming beam on the back aperture of the primary objective lens.

The scan calibration factor is given in units of micron/volt. This parameter will not change unless the scan telescope optics are changed (i.e. the scan lens, tube lens and objective lens), or the galvo system is altered or changed such that 1 volt no longer produces the same angular scan. However, the scan field of view and sampling density are imaging parameters that are deliberately changed during imaging to afford different x-direction fields of view, sample densities and volumetric imaging speeds. To calculate pixel size of a given data set in the scan dimension, multiply the scan calibration factor acquired above by $V_{X_{stepSize}}$ (volts per pixel) for the given scan pattern used to yield calibration in terms of microns per x-pixel.

This entire procedure can be fully automated by incorporating a sufficiently high-precision motorized stage and automated bead detection. Alternatively, using a fluorescent sample of sufficiently high enough resolution with a known structure along all 3 dimensions (eg. Argolite fluorescence calibration slides) can also be used to provide information about the system’s sampling density along each of the 3 dimensions.

Appendix B. Performance metrics

Light Throughput

Excitation

Laser power is measured at 4 locations within the system using the Thorlabs power meter set to the wavelength of the laser in use (this will generally be 488 nm). Switch off the room lights. Note that the beam must hit the sensor at normal incidence for the most accurate reading.

1. **Between the laser and the filter wheel:** This will allow you to record any discrepancy between the SCAPE GUI's laser power input and the actual laser power.
    a. Note that normal incidence in this case would actually reflect the beam back into the resonator cavity *which is dangerous and can damage the laser. DO NOT DO THIS*. Introduce the sensor into the beam path at an angle and slowly rotate the sensor so that it approaches *but does not reach* normal incidence. Be mindful of where the reflected beam is at all times.
2. **After the filter wheel:** This will allow you to turn down the laser power and use normal incidence. I generally set the filter wheel at 1% transmission and measure the power on the sensor between the 2 steering mirrors immediately after the filter wheel.
3. **At the back aperture of the primary objective lens:** This will give you a relative measure of light transmission through the majority of optical components within your system.
    a. Unscrew the primary objective lens along with the objective lens adapter from the flip mirror cube. Remove the flip mirror from its mount so that the beam passes through the cube and exits out of the SM1 threaded hole. If there is a slit in the system, open it

completely. Place the sensor flat against the surface of the mirror cube and translate it against this surface in order to capture the beam completely with the sensor.

4. **Under the primary objective lens, at the sample:** This will give you a metric of light throughput through the primary objective lens.
    - **a.** Reinsert the flip mirror into the cube, and screw the primary objective lens back into the light path. Place the sensor underneath the objective lens without any water and tilt the objective lens until the maximum power reading is achieved. I've found that on SCAPE3 and the Axel system, this reading is ~45% of the power measured at the back aperture.
5. **(Optional) Steps 3+4 with a pinhole:** If you are attempting to compare two systems, you might get slightly results for the 3rd and 4th steps on your two systems. The sensitivity to alignment of the powell lens and clipping at various apertures in the cylindrical lens train can affect *overall* light transmission from the filter wheel to the back aperture. This step will provide more information about the distribution of laser light at a specific point along the sheet.
    - **a.** Place an SM2 alignment target (LCPA1) at the image plane between the scan and tube lens in the **scan** telescope. The hole at the center of the target will serve as a field stop.
    - **b.** Unscrew the primary objective and adapter from the flip mirror mount. Remove the flip mirror from this mount and place the sensor in the same location as in Step 3.
    - **c.** Move the galvo slowly until the sheet is centered on the target and the maximum signal on the sensor is achieved. This signal represents the amount of laser light at the

back aperture of your objective lens that serves to illuminate the center of your FOV in the Y-dimension.

   - **d.** Reinsert the flip mirror into the cube and screw the primary objective lens back into the light path. Place the sensor underneath the objective lens without any water and tilt the objective lens until max power reading is achieved. This reading as a fraction of the reading taken in Step 5c should be similar to what is achieved in Steps 3 and 4 (~45% on SCAPE3 and Axel SCAPE)
   - **e.** If you take this measurement over the entire scan range of your FOV, this measurement will give you the fall-off in excitation throughput over your scan range.

Detection

This step provides a metric of the system’s collection efficiency independent of the amount of the amount of laser light used for fluorescence.

1. Place a self-illuminating sample under the primary objective lens, cover with DI water and bring it into focus on the camera. One can use a tritium keychain (B06X1BPBN4, Amazon) for this purpose.

2. Place an SM2 alignment target at the image plane between the scan (S2) and tube (T2) lens in the **descan** telescope.

3. Set the exposure time to 1 second, center the galvo, turn off the room lights AND the monitor. The tritium sample is very dim so excess light will throw off your measurement. The hole at the center of the SM2 target will serve as a field stop. In a well aligned system, this hole will be vertically centered on the camera chip and will be visible when the room lights are on. When the lights are off, the light from the tritium vial will glow through the hole.

4. Acquire 30 frames, average them and find the average signal within the hole. The value should be ~ 1200-1400 counts on the sCMOS detector for SCAPE3 and SCAPE3 replicas.

If you scan the galvo mirror while leaving the laser off, you can measure the system's fall-off in detection throughput (independent of laser excitation) at the center of the YZ field of view as a function of X.

Field of View

To assess the accessible field of view, take an HR scan of a flat, homogenous sample (2 μm sampling density, 2000 μm FOV). Fluorescent tape, a field of fluorescent dye underneath a coverslip (FITC, Texas Red) or fluorescent plastic slides are all suitable choices for samples. Note that when using dyes, it is important to stay away from the sample's boundaries, bubbles and other reflective features that may be present. Reflection of laser illumination at these interfaces will artificially inflate the signal generated in that region.

Maximum/Mean intensity projections along the scan (x) and lateral (y) dimensions can be normalized and used to assess the FWHM field of view of the system along these two dimensions.

Identifying Distortions (XZ and YZ)

In order to quantify aberrations in both planes, take the data necessary to acquire a depth calibration as specified in 0. Track the position of the same bead across multiple depths. Repeat for multiple beads. The distance between beads should not change as a function of depths along each dimension. If the distance between beads chances along the X dimension as a function of depth, this may indicate that the angle of the sheet is varying as a function of the galvo scan and one should check the mapping of the galvo onto the back focal plane of O1. If the distance between beads changes along the Y dimension, this may indicate improper mapping of the pupil planes of O1 and O2 onto one another.

Resolution

Images of sub-diffraction limit sized fluorescent microspheres (200 nm, F8811, Life Technologies, 515 nm emission) embedded in 1-2% low-melting point agarose hydrogel are used to characterize resolution over the field of view. Sonicate the fluorescent microsphere solution prior to making the phantom to avoid measurement errors due to clumping. A three-dimensional phantom is created by gluing a standard aluminum washer to an acrylic or glass slide. The hole within the washer is then filled with agar bead solution and immediately covered with either a glass coverslip or a sheet of FEP. The edges of the washer are then sealed using dental acrylic and then protected from drying using water-proof nail polish. This phantom can last up to several weeks without degrading in quality. Alternatively, because SCAPE can image from an inverted configuration, agar containing the 200 nm beads can be placed into a glass bottom petri dish and imaged through the cover glass from below.

Image the beads at the desired magnification on SCAPE using a small step size (<0.2 µm) in the scan dimension. Affine transform the data and use Fiji’s 3D objects counter in order to find the centroid locations of all beads within the sample. Use these centroids to extract volumetric ROI’s surrounding the sample. This type of analysis permits analysis of individual beads as well as bulk bead analysis to quantify how resolution varies as a function of FOV.

Appendix C. Alignment Strategy

This procedure is a general alignment strategy for building SCAPE2b. It grew out of the techniques I had developed while aligning SCAPE2a, and refined to take into account the slightly different degrees of freedom and optical components found in SCAPE2b. For a more in-depth instructions about how to build the latest versions of SCAPE microscopy, please contact the Hillman laboratory.

Alignment Tools

We strategically place cage-mounted targets (CPA1, CPA2, LCPA1; Thorlabs) at various locations within our optical telescopes to assist with alignment. We have also developed a custom acrylic components modeled on these hanging targets to denote the offset at which the laser needs to impinge upon the back aperture of the primary objective lens (O1), henceforth referred to as the "offset alignment target." We use cage plates (LCP01, Thorlabs) and cage plate stops (ERCPS, Thorlabs) to mark the location of the image planes conjugate to the focal planes of O1 and O2.

A custom, adjustable fiber launch was also created using a single-mode fiber, a collimator, a 650 nm visual fault locator and two turning mirrors. This fiber launch provided a small, easily adjustable laser source for alignment.

Fluorescent samples such as microspheres embedded in glass slides (FPS-5057-UR5, Spherotech), fluorescent plastic tape (B0088HTD0A, Amazon), and stained convallaria root samples (As-812z, MSMedia) were all used as phantoms at various stages of alignment.

Basic SCAPE Alignment

Prior to alignment, I created a detailed optical model of the system’s lens layout (carefully editing the distances between successive lenses and telescopes) using Optalix-PRO, and then imported this model into Solidworks. The appropriate optomechanics (i.e. lens tubes, cage plates, etc) were placed around the appropriate lenses within the Solidworks model. The scan telescope, detection telescope, excitation optics were all separate sub-assemblies in Solidworks, and are assembled independently as individual modules prior to placement on an optical breadboard. The excitation optics consist of a beam-shaping telescope (i.e. the Powell lens and the first cylindrical lens), as well as the sliding mirror mount (consisting of the second cylindrical lens, a turning mirror and a variable aperture slit). Each telescope consists of cage plates that are collectively responsible for holding lenses, denoting the locations of crucial focal planes, and supporting mounting posts that secure the telescope to the table. Mounting posts for the scan, de-scan and beam-shaping telescope are mounted directly into the appropriate screw-holes of the optical breadboard. The sliding mirror mount also screws directly into the table. Distances between the cage plates are crucial to ensuring proper alignment of individual lenses within each telescope, as well as proper alignment of the telescopes relative to one another. These distances are set with calipers. The locations of each free-standing component of the system (mirrors, filter wheels, lasers, galvo mirror, and camera telescope) are all roughly placed on the table in the locations indicated within the Solidworks model.

One can think of SCAPE as being aligned in three steps. The first is proper alignment of the detection pathway, i.e. the optical path from the object to the camera. The second is alignment of the excitation pathway, i.e. the optical path from the laser into the object. And third is a fine alignment of the camera telescope for optimal image quality.

When performing the first step, adequate care must be taken to map the pupils of the primary and secondary objective lens (O1, O2) onto one another. Assuming proper assembly and mounting of the individual scan and detection telescopes, the two telescopes will be positioned orthogonally on the breadboard. Their respective optical axes will intersect at a point coincident with the front focal planes of their respective scan lenses (S1, S2). The galvo mirror's reflective face must be carefully positioned at this point and its angle adjusted so that a ray traveling along the optical axis of the scan telescope will pass through the optical axis of the detection telescope. This can be achieved by using the custom fiber launch to align a laser into the scan telescope, (passing through O1, T1 and S1 in that order), reflecting off of the galvo mirror, passing through the dichroic mirror and through the detection telescope (S2, T2 and O2 in that order). We always hand-aligned the galvo mirror mount, however a relatively inexpensive XY stage and rotation mount could offer more precise control if one chooses. At this point, the angle of the galvo mirror should remain fixed at this "center" position.

To verify alignment, place an alignment target at the focal plane of the detection telescope (between S2 and T2). The focal plane of the detection telescope will be relayed onto the focal plane of the second objective lens (O2). Roughly position the camera telescope to bring this relayed image into focus. Commercially available alignment targets (LCPA1, Thorlabs) have a pinhole and vertical/horizontal lines that can be used as references for the axes of the optical system. The camera on the camera telescope is oriented such that the vertical/horizontal lines are coincident with the horizontal/vertical axes of the camera sensor respectively. The position of the camera telescope is altered to center the image of the alignment target's pinhole on the camera sensor. Once this step is completed, move the alignment target to the focal plane in the scan telescope (between S1 and T1) without adjusting/altering the positioning of the galvo mirror. If the optical axes are parallel to one another, the image of the alignment target's pinhole should not move on the camera.

The second step will align the laser beam from its source into the object. If multiple laser sources are used, the positioning of the dichroic mirrors and beam-combiners should be adjusted so that the laser sources are co-aligned when entering the beam-shaping telescope. The laser beam is aligned centrally through the beam-shaping optics (i.e. the powell/cylindrical lens telescope) and then aligned centrally into the sliding mirror mount. The mirror within the sliding mirror mount is adjusted so that the beam is traveling centrally through the third cylindrical lens. The rotation of the powell and cylindrical lenses are adjusted relative to one another so that beam magnification and focusing occurs solely in the vertical direction. We find the need to place a layer of thin tape around each cylindrical lens to ensure centration within the lens tube. The beam should be elliptical and collimated between the second and third objective lens. The third cylindrical lens focuses the laser beam onto the galvo mirror into a thin horizontal line. The alignment target is alternately hung at the focal plane of the scan telescope (between S1 and T1), and at some arbitrary location between T1 and O1. If the beam passes centrally through the target at the focal plane, this is an indication that the ***direction*** of light travel is parallel to the optical axis of the telescope. If the beam passes centrally through the target between T1 and O1, this is an indication that the ***location*** of the beam on the galvo mirror lies along the optical axis of the scan telescope. The translation stage and mirrors on the sliding mirror mount are used to adjust the direction and location of the beam within the scan telescope. The axial position of the second cylindrical lens used to focus the laser beam onto the galvo mirror. If the beam is not horizontal, the rotation of the Powell and cylindrical lenses are adjusted. After these steps are completed, the laser excitation will create a light sheet focused at the focal plane of the primary objective lens, O1, i.e. within the sample. The light sheet will be propagating parallel to the optical axis of the scan telescope. The translation stage of the sliding mirror mount is used to maintain the beam's ***direction*** of travel, while offsetting the location of the beam on the back aperture (or focal plane) of the primary objective lens. This step creates SCAPE's angled light sheet within the sample.

The final step is the fine alignment of the camera telescope. A 3D structured sample (for example, a multi-layered fluorescent tape phantom or the convallaria fluorescent slide) is placed underneath the primary objective and its depth adjusted to be coincident to the focal plane of the lens. The dichroic mirrors used for dual-color imaging in the camera telescope are removed, and the system is placed in "bypass mode." The alignment targets can be intermittently placed at the focal plane of either the scan or detection telescope to serve as a field stop for the center of the system's field of view. The position of the camera telescope should be adjusted such that the alignment target's pinhole is imaged onto the middle row/column (horizontal/vertical respectively) of camera sensor. Objects at the focal plane of the primary objective lens will map onto this middle row. Objects above and below the focal plane of the primary objective will map above and below this middle row respectively. The fine focus knob of the camera telescope's objective lens (O3) should be adjusted to achieve best focus. If the camera telescope cannot bring objects above and below the focal plane into focus simultaneously, the angle of the camera telescope relative to the optical axis of the detection telescope must be adjusted. Bright samples with large structures, such as the multi-layer tape phantom, can be used to roughly adjust the angle and position of the camera telescope. Once a course alignment has been completed, one can also use a 3D suspension of fluorescent microspheres embedded in agar to optimize performance. Once the camera telescope is appropriately aligned, the dichroic mirrors are placed back into the image splitter. The mirrors on the image splitter to perform a fine centration of both color channels on the camera chip (the convallaria slide might be better suited to this step as it is brightly fluorescent over a broad spectral range). The mirrors within the image splitter are then used to horizontally offset the two channels onto the right and left side of the camera chip. To preserve the camera frame-rate, the channels should remain vertically centered on the chip.

Appendix D. Sample Mounting/Preparation Procedures

This section provides a brief description of standard mounting procedures for the samples presented within this text. A far more comprehensive accounting of each procedure is found in the thesis work of Dr. Wenze Li. Note that each experiment will also contain equipment in addition to what is described here (cameras, electrodes, behavioral rigs) that are vital to that particular use case. These additional components will be described within the text as each use-case is explored.

Mouse Cortex

For non-awake imaging experiments, the animals are anesthetized with 1.5 mg/kg urethane administered intraperitoneally, accompanied with 0.5 mg/kg Glycopyrrolate prior to the implantation of a transparent cranial window. For animals undergoing awake imaging, animals are anesthetized with isoflurane for the duration of the surgery and then imaged after a period of recovery approved by Columbia University's IACUC.

During the surgery, the animal's core body temperature is monitored and maintained at 36.5° +/- 0.5° using a homeothermic temperature controller (FHC 40-90-8D). The head is secured in a stereotactic frame, its scalp retracted and the skull immediately above the region of interest removed. The dura mater directly below the skull is also removed. A glass coverslip is placed above the exposed region and then cemented in place to the surrounding skull using dental acrylic. A custom-designed acrylic or aluminum head-plate is also glued to the skull with cyanoacrylate.

The animal is head-fixed onto a rigid platform underneath the objective lens to minimize motion during imaging. All experiments imaging the rodent cortex are performed with the system in an upright configuration with the objective lens pointing down at the sample.

Zebrafish Larval Brain

Zebrafish were kept at 28°C and handled according to protocols approved by Columbia University IACUC. A fluorescence dissection scope is used to check whether the animal is expressing the fluorophore of interest. Data shown in this text were acquired on samples imaged between 6-9 days post fertilization.

The nervous system of the zebrafish is more easily accessible from the dorsal side of the animal and is therefore generally imaged from above with the microscope in an upright configuration. The sample is mounted in ~1% low melting point agarose within a glass-bottom petri dish and then covered with a glass slide which serves to flatten the surface of the agarose drop. The petri-dish is then filled with system water from the zebrafish facility's water system to prevent the agarose from drying, with the optional addition of anti-fungal solutions.

Zebrafish Larval Heart

Zebrafish were kept at 28°C and handled according to protocols approved by Columbia University IACUC. A fluorescence dissection scope is used to check whether the animal is expressing the fluorophore of interest. Depending on the age of the sample, the zebrafish needs to be de-chorionated prior to mounting which can be accomplished through a dissection scope and a pair of fine metal tweezers. We image the zebrafish heart between 20-96 hours post fertilization (hpf). Data presented in this text was acquired on samples at 72 hpf.

The zebrafish heart is imaged from below with the microscope in an inverted configuration from below because the heart is found adjacent to the yolk sac on the ventral side of the animal. Zebrafish larva were embedded in a drop of 1-1.5% low gelling point agarose and mounted with their ventral side down on a glass-bottom petri dish. The angle of the rostral-caudal axis was gently adjusted with a fine plastic pipette tip so that the animal faces nose-down, facilitating better access to the heart. The glass bottom dish is filled with fish water obtained to prevent drying of the sample during imaging. Anti-fungal solutions can be diluted into the system water if necessary.

Drosophila Larva

A standard fluorescence dissection scope is used to identify larva at the correct developmental timepoint with appropriate fluorescence expression. Larvae at early stages of development (L1) can be approximately 1 mm in length and fit within the field of view of standard. Larva immediately before the pupa stage (L3) can be 2-3 times that size. Larva can be imaged in either an upright or inverted configuration depending on the features of interest. For example, neurons on the ventral surface of the body wall as well as within the ventral nerve chord are better imaged in the inverted configuration whereas neurons on the dorsal side are better imaged in an upright configuration.

The animal is gently lifted out of its native environment and cleaned with a gentle solution of PBS. For inverted imaging, the animal is placed on a glass-bottom petri dish and covered with a layer of low melting point agarose. This prevents the sample from floating away within the immersion media while still allowing it to freely crawl on the petri dish. Animals imaged upright are placed on a glass slide. A micro-channel is made using multiple layers of FEP plastic and placed on a glass slide. The larva is inserted into the channel to encourage its direction in a particular direction and a glass coverslip is placed atop the larva. The layers of FEP act as a spacer which prevents the coverslip from crushing the sample and restricting its motion.

C. Elegans

As the C. Elegans is such a thin, non-scattering sample, either upright or inverted imaging geometries are capable of allowing one to visualize the entire animal. A standard fluorescence dissection scope is used to select for samples of the right size and expression. The sample is then embedded in 2% low-melting point agarose and coverslip placed upon it, which should be sufficient for immobilization. A low-dose paralytic can also be dropped on top of the agar if immobilization is crucial to imaging. For immobilized imaging, the y-axis of the system which corresponds to the length of the sheet is aligned to the rostral caudal axis of the animal in order to fit the animal into the smallest field of view along the scan range.

Appendix E. Optical Layouts of SCAPE Generations

		SCAPE 1	SCAPE 2a	SCAPE 2b	Alterations for Chapter 3			
Scan Telescope	**Objective 1, O1**	Olympus 20x/1.0NA W	Olympus 20x/1.0NA W	Olympus 20x/1.0NA W	Identical to SCAPE2b			
	Tube 1, T1	50 mm, 1’’ diameter	150 mm, 2’’ diameter	150 mm, 2’’ diameter				
	Scan 1, S1	100 mm, 1’’ diameter	75 mm, 2’’ diameter	75 mm plossl, 2’’ diameter				
Detection Telescope	**Scan 2, S2**	50 mm, 1’’ diameter	60 mm, 1’’ diameter	60 mm, 1’’ diameter	60 mm, 1’’ diameter			
	Tube 2, T2	100 mm, 2’’ diameter	100 mm, 2’’ diameter	100 mm, 2’’ diameter	100 mm plossl, 2’’ diameter			
	Objective 2, O2	Olympus 20x/0.75 NA dry	Nikon 20x/0.75NA dry	Nikon 20x/0.75NA dry	Nikon 20x/0.75NA dry			
Camera Telescope	**Objective 3, O3**	Olympus 10x/0.30 NA dry	Nikon 10x/0.45 NA dry	Nikon 10x/0.45 NA dry	EO 20x/0.60 NA dry	EO 20x/0.60 NA dry	EO 20x/0.60 NA dry	Mitutoyo 50x/0.75 NA dry
	Tube 3, T3	75 mm, 1’’ diameter	75 mm, 1’’ diameter	Morell, 70 mm tube	70 mm	200 mm	200 mm	200 mm
	Camera	Andor Zyla 5.5	Andor Zyla 4.2	Andor Zyla 4.2+	HICAM Fluo	Andor Zyla	HICAM Fluo	Zyla
Excitation Telescope	**Laser**	Melles Griot, (488 nm, 30 mW)	Melles Griot, (488 nm, 50 mW)	Coherent Obis (488 nm, 150 mW)	Coherent Obis (488 nm, 150 mW) Cobolt DPL (561 nm, 100 mW)			
	CL1 (orientation)	50 mm CL (vertical)	20 mm CL (vertical)	30° Powell Lens (vertical)	Identical to SCAPE 2b			
	CL2 (orientation)	250 mm CL (vertical)	250 mm CL (vertical)	50 mm CL(vertical)				
	CL3 (orientation)	50 mm CL (vertical)	100 mm CL (horizontal)	75 mm CL(vertical)				
	CL4 (orientation)	100 mm CL (horizontal)	50 mm CL (horizontal)					
	CL5 (orientation)	50 mm CL (horizontal)	75 mm CL (vertical)					
	Extra			Variable Slit				

Table 4: *Optical layouts of successive SCAPE generations*

Appendix F. Select Publications and Presentations

1. **Voleti V**, Li W, Patel KB, … Hillman EMC. (2019) "Real-time volumetric microscopy of in-vivo dynamics and large-scale samples with SCAPE 2.0." (Accepted to Nature Methods, In Press)
2. **Voleti V**, & Hillman EMC. (2017) "Single Objective Light Sheet Microscopy." Light Sheet Microscopy. Book Chapter. (Submitted, In press)
3. Bouchard MB, **Voleti V**, . . . Hillman, EMC. "Swept confocally-aligned planar excitation (SCAPE) microscopy for high speed volumetric imaging of behaving organisms." *Nature photonics*, (2015) *9:* 113-119.
4. Hillman EMC, **Voleti V**, . . . Galwaduge, PT. "High-speed 3D imaging of cellular activity in the brain: The advantages of axially-extended beams and light sheets." *Current Opinion in Neurobiology*, (2018) 50: 190-200.
4. Hillman EMC, **Voleti V**, Li Wenze, Yu H. "Light-Sheet Microscopy in Neuroscience." *Annual Reviews in Neuroscience*, (2019) 42: 295-313.
5. Vaadia R*, Li W*, **Voleti V**, … Hillman, EMC, Grueber WB. "Characterization of the proprioceptive system dynamics in behaving Drosophila larvae using high-speed volumetric microscopy." *Current Biology*, (2019). 29(6): 935-944. * co-authors
6. Li, L*, Li, W*, **Voleti, V**, Hillman, EMC, Firestein, SJ, (2019). "Evidence for widespread inhibition in peripheral olfactory coding" (In Preparation) *co-authors
7. Nguyen HD, Ullmann JFP, McLachlan GJ, **Voleti V,** Li W, **Hillman EMC,** Reutens DC, Janke A, "Whole-volume clustering of time series data from zebrafish brain calcium images via mixture modeling". *Stat Anal Data Min: The ASA Data Sci Journal*, (2018). 11:5–16.

Conference Presentations

1. **V. Voleti,** M.B. Bouchard, C. Lacefield, R.M. Bruno, E.M.C. Hillman. *High-speed 3D in-vivo imaging of neuronal populations during laser scanning intersecting plane tomography* . At the Society for Neuroscience Annual Meeting, November 2013; San Diego, CA. paper 289.11/NNN12. **(Poster presentation)**
3. **V. Voleti,** M. B. Bouchard, and E. M. Hillman, "Design of a Second Generation Laser Scanning Intersecting Plane Tomography (LSIPT) System," in *Biomedical Optics 2014*, OSA Technical Digest (online) (Optical Society of America, 2014), paper BS2B.5. **(Conference Talk)**
4. **V. Voleti,** M.B. Bouchard, C.S. Mendes, C. Lacefield, W.B. Grueber, R.S. Mann, R.M. Bruno, E.M.C. Hillman. *High-sped, volumetric imaging of behaving organisms using swept*

oblique light sheet (solis) microscopy. At the Society for Neuroscience Annual Meeting, November 2014; Washington D.C. paper 850.13/UU76. **(Poster presentation)**

5. **V. Voleti,** M. B. Bouchard, C. Lacefield, R. M. Bruno, and E. M. Hillman, "Fast, Volumetric Imaging of In Vivo Brains with Swept Confocally Aligned Planar Excitation (SCAPE) Microscopy," in *Optics in the Life Sciences*, OSA Technical Digest (online) (Optical Society of America, 2015), paper BrM2B.3. **(Conference Talk)**
6. **V. Voleti,** W. Li, M. Greaney, C. O. Lacefield, D. Schoppik, R. Bruno, and E. M. Hillman, "SCAPE microscopy for high-speed volumetric functional imaging of the awake, behaving brain," in *Biomedical Optics 2016*, OSA Technical Digest (online) (Optical Society of America, 2016), paper BTu2D.3. **(Conference Talk)**
7. **V. Voleti,** W. Li, M. A. Shaik, M. Wu, C. P. Campos, C. Wyart, and E. M. Hillman, "Imaging the nervous system at different spatiotemporal scales with SCAPE microscopy," in *Optics in the Life Sciences Congress*, OSA Technical Digest (online) (Optical Society of America, 2017), paper BrS2B.3. **(Conference Talk)**
8. **V. Voleti,** W. Li, R. Vaadia, E. Schaffer, N. Mishra, K. Patel, M. Shaik, W. Grueber, E.M.C. Hillman. *A second generation SCAPE system for fast, 3D imaging of neural activity*. Society of General Physiologists, The Optical Revolution in Physiology: From Membrane to Brain, September 2017; MBL Woods Hole, MA. **(Poster presentation)**

Patents

International Patent Application (PCT/US2017/034984), "SCAPE microscopy with Phase Modulating Element and Image Reconstruction" (filing date May 30, 2017) (Elizabeth M.C. Hillman and **Venkatakaushik Voleti**, applicants)

Appendix G. Overview of Single-Objective Light Sheet Microscopy Systems

---

The following is a reproduction of a chapter on single-objective light sheet microscopy systems provided as a reference for the reader authored by myself and Dr. Hillman in 2017

Single objective light sheet microscopes represent an alternative approach to the 2 or more orthogonal objective-lens geometries used in conventional light sheet systems. These single-objective approaches can provide the benefits of sheet-based illumination while accommodating a different range of sample geometries, including intact tissues and freely moving organisms, while also facilitating high-speed volumetric imaging. This chapter reviews the different single-objective light sheet configurations demonstrated to date and details their unique system requirements, features, trade-offs and applications.

Introduction: Why Use Single Objective Systems?

Conventional light sheet microscopes (LSMs) consist of two orthogonally aligned optical trains: one which generates a sheet of laser light within the sample, and another which images fluorescence generated by this sheet onto a detector. A 3D light-sheet image is then formed by physically translating the sample through the co-aligned light sheet, or by translating the sheet through the sample and tracking its motion with the detection telescope. Key benefits of light-sheet include parallel imaging of the entire plane with little extraneous excitation light leading to much lower levels of phototoxicity and higher relative imaging speeds that point-scanning confocal microscopy, in addition to relatively simple and inexpensive instrumentation. However, the orthogonality requirement of conventional LSMs means that sample geometries are generally restricted, often requiring embedding or specialized sample mounting procedures to enable proper illumination, immersion and repositioning of the sample.

As a result, early applications of light sheet microscopy focused on small, cylindrical samples that could be mounted and positioned within the constraints of an orthogonal objective imaging geometry. For example, *Drosophila* embryos, zebrafish larvae and small cleared samples could be embedded in small cylinders of agar for positioning between 2 or more orthogonal lenses [1,2]. In these studies, LSM was used to capture 3D microscopic structure, or physical migration of cells during embryogenesis over the course of hours or days. Such developmental studies were able to tolerate slow volumetric imaging speeds, sample constraint and rotation and translation, while system improvements focused on optimization for the isotropic, high resolution critical to enabling segmentation and tracking of developing cells and structures [3–5]. Nevertheless, as the benefits of light sheet imaging methods have been more broadly recognized, a diverse range of samples that require a less constrained imaging geometry have emerged that could benefit from the phototoxicity and speed advantages of light-sheet imaging. These include samples that would usually be imaged on a standard confocal, two-photon or epi-fluorescence microscope including cell cultures in multi-well plates, samples within perfusion chambers requiring environmental control or application of drugs, dyes or insertion of electrodes, samples requiring behavioral monitoring, tracking stages, tiling or other lateral scanning and intact, living samples such as the mouse brain or even human tissue for clinical microscopy.

A number of innovative approaches have been developed over the past decade to address the challenge of imaging intact or unmounted samples. iSPIM and its multi-view variant, diSPIM, mount the illumination and detection paths on an inverted frame, with the light sheet entering the sample at 45 degrees, providing top-down access to samples [6,7]. Similarly, open-top SPIM systems image the sample from below through a glass window [8,9]. However, as with conventional LSMs, these geometries remain constrained by the availability of suitable objective lenses, which are generally designed to balance NA, working distance, immersion media, physical bulk and shape for standard upright or inverted imaging. All orthogonal LSM geometries require selection of at least two compatible objective lenses that can be physically positioned to co-align the light sheet and detection plane and provide clearance for sample placement and maneuvering. The current list of well-corrected, compatible objectives lens *pairs* that provide adequate access to the sample is quite limited, with few offering both high NA, compatible immersion and sufficient working distance to enable imaging of large or intact samples.

Another approach is to add light-sheet generating modules to commercial high-NA epi-fluorescence microscopy frames. These modules sit at the sample and provide horizontal sheet illumination co-aligned to the microscope's detection plane [10,11], but again face sample mounting, sample size and refractive index mismatch constraints. Additional approaches to improving sample positioning have redirected the illumination path to alter the required angle between the two objectives, for example Bayesian light sheet, which mounts the sample on a refracting prism to bend the incident sheet. Pi-SPIM and O-SPIM tilt the excitation beam emerging from an illumination objective below the sample to enable co-alignment of the illumination plane with an oblique detection objective above [12,13]. 'Reflected light sheet' methods mount two offset objectives above and below the sample and use reflective components such as prism-mirrors or AFM cantilevers to flip the light sheet horizontally to illuminate the sample in the focal plane of the detection objective [14,15]. The Leica TCS SP8 DLS system achieves a similar geometry using an inverted confocal microscope as a light source, with a collar on an opposing upright detection objective that holds two mirror elements to form a light sheet at its focal plane. Rather than using a standard excitation objective lens, objective-coupled planar illumination (OCPI) microscopy attaches a custom-designed, low-numerical aperture optic to the detection objective to introduce the light sheet into the sample [16–18].. A similar miniaturized configuration has been demonstrated that uses a composite prism-mirror and gradient index (GRIN) lens [19]. In both cases, the light sheet created aligns with the objective's focal plane while leaving space under the detection lens to introduce the sample. Volumetric imaging of intact samples is then achieved via rigidly coupled translation of the excitation and detection components.

Although all of the methods described above have aimed to address the physical constraints of standard orthogonal LSM geometries, all introduce related sample mounting complexities, limiting sample size and diversity, and require careful, often independent coordination of excitation and emission light paths, limiting volumetric imaging speeds.

Single objective light sheet microscopes, as defined here, utilize only a single lens at the sample that provides both the illuminating light sheet, and detects the resulting fluorescence. As a result, single-objective light-sheet methods have an imaging geometry similar to a standard confocal or epi-fluorescence microscopes and can be used to image intact, planar or a diverse range of samples, often without the need for physical mounting or immobilization. An additional benefit delivered by some single-objective light sheet embodiments is improved volumetric imaging speed, achieved via coordinated sheet scanning and descanning without the need for physical translation of objective lenses or the sample. Below, we review a range of different single objective light sheet configurations, starting with their general form and considerations for their excitation and detection paths. We then review the ways in which each method accomplishes volumetric imaging. Design parameters that affect the performance of these systems are then summarized, including tradeoffs and constraints compared to conventional LSMs. Finally, we provide examples of the types of experiments to which single-objective light sheet systems have been applied.

Optical Configurations and Design Considerations for Single-Objective Light-Sheet.

Optical Layouts

As with conventional LSMs, single-objective implementations must co-align the light sheet to an image plane conjugate to the detector to achieve good optical sectioning. The key challenge, therefore, becomes finding a way to introduce a sheet into the sample using only a single objective lens that also serves to create an image of the sheet. Broadly, there have been two approaches to accomplish this goal: The first approach is to aim the excitation beam at an ancillary optical component such as a small prism-mirror adjacent to the sample to create a horizontal light sheet that is co-aligned with the standard focal plane of the primary objective lens within the sample. The second is to introduce the light sheet non-orthogonally into the sample (e.g. obliquely from the objective’s edge) and co-align the detector to the generated oblique plane.

Horizontal-Sheet Single-Objective Systems

Galland et al. and Meddens et al. both reported ‘horizontal sheet’ single-objective systems in which the same objective lens is used to generate the sheet at the sample and detect the emitted fluorescence [16,20,21] (**Figure G.1**a). These systems use custom-fabricated sample holders with 45° reflective surfaces that redirect a laser beam/sheet initially propagating parallel to the objective’s optical axis into the lens’ focal plane. This approach has been implemented with both high and low numerical aperture objective lenses [21]. Notably, the ability to use high magnification, low working distance objectives allows high-resolution imaging of organelles of single cells, as well as use in conjunction with single-molecule localization techniques such as PALM and STORM with lower levels of background than conventional wide-field epi-illumination (example shown below in **Figure G.5**). Galland et al., also demonstrated multi-view imaging of a Drosophila embryo embedded within a rotating capillary tube alongside a millimeter sized mirror. Nevertheless, the need to position one or more suitable reflective components at the sample constrains sample selection, requires special sample mounting (preventing most imaging of intact samples) and introduces sample-dependent alignment challenges and scanning complexities as discussed further below.

Oblique and Axial-Illumination Single-Objective Systems

Oblique illumination single-objective light sheet systems do not use reflective components at the sample, instead forming a non-horizontal sheet entering the tissue at an angle. As such, oblique illumination systems typically do not require specialized sample mounting procedures and can permit greater versatility in terms of experimental design. In oblique configurations, different depths within the sample are illuminated simultaneously, with one dimension of the light sheet encoding an oblique depth section (x-z), and the other encoding the lateral direction (y) (**Figure G.1**b). A key component of such systems is then the need to rotate and map this oblique plane at the sample onto the focal plane of a camera to generate a light-sheet condition and thus achieve optical sectioning. This approach was first implemented as Oblique plane microscopy (OPM), in which an oblique light sheet was generated at the sample through a high NA objective lens, while the image of the sheet was relayed back through the same objective and rotated via an intermediate image plane between two obliquely aligned objective lenses onto a camera. Volumetric images in OPM are formed either by translating the sample laterally (along x) through the oblique sheet, or by adjusting the light sheet's axial position using remote focusing principles as detailed further below (**Figure G.1**c) [22–24]. Axial-plane optical microscopy (APOM) extends OPM to the case of the light sheet being exactly vertical, parallel to the optical axis. Here, 90 degree image rotation is achieved using a mirror at the intermediate image plane (**Figure G.1**e) [25]. Volumetric images are formed via lateral sample translation. In swept confocally-aligned planar excitation (SCAPE) microscopy, an oblique light sheet is formed at the sample, but an intermediate galvanometer mirror is used to sweep this light sheet across the sample along x, while de-scanning returning light to a stationary intermediate oblique plane which is then rotated and mapped onto a fast camera (**Figure G.1**d) [26]. Volumetric imaging is then achieved by acquiring images while the galvanometer mirror is scanned, permitting very high speed imaging without sample or objective lens motion.

A.1.1.1 HILO and VAEM Single-Objective Methods

We note that another microscopy method that uses oblique planar illumination is highly inclined and laminated sheet (HILO) (also called variable angle epifluorescence, VAEM) [27,28] (**Figure**

G.1f). HILO represents an extension of TIRF microscopy, tilting illumination so that a plane of light enters the sample (e.g. a single cell), providing sensitivity to structures within the cell, rather than the cell's membrane via a TIRF evanescent wave. Such illumination has been used in conjunction with single-molecule localization techniques, providing lower background and photodamage than conventional epi-fluorescence imaging. However, it is important to note that HILO and VAEM do not to co-align the detector plane to the angle of the illumination plane. The plane itself is also not a Gaussian light sheet, but a collimated plane on the order of 7-30 microns thick. This lack of alignment between the inclined illumination plane and standard detection plane limits the field of view, since contrast is only optimal in the region where the light sheet intersects with the objective lens's focal plane. As such, these methods are not strictly single-objective light sheet methods, since they are not utilizing a light sheet to provide optical sectioning per se.

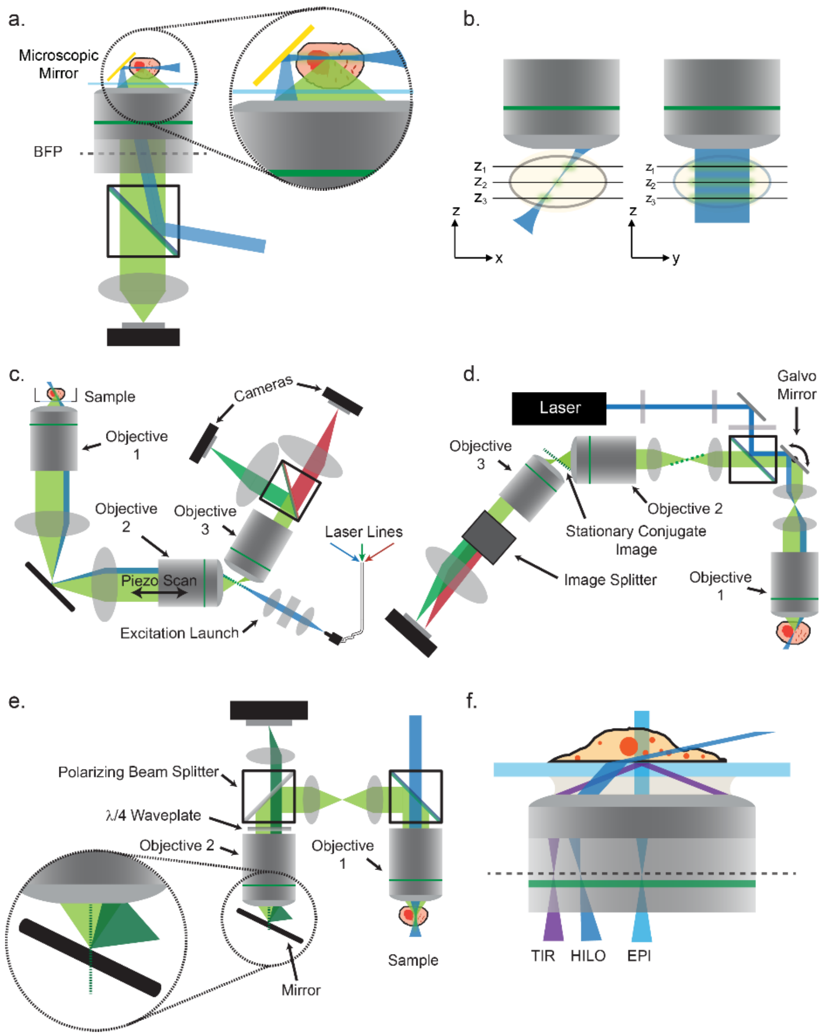

Figure G.1. *Single-objective light sheet microscopy configurations.*
a) *Micro-mirror based light sheet microscopy. Inset is a close-up of the reflective surface next to the sample* ***b)*** *Sample geometry for angled illumination* ***c)*** *Oblique plane microscopy (OPM) d) Swept confocally aligned planar excitation (SCAPE) microscopy* ***e)*** *Axial plane optical microscopy (APOM). Inset shows light exiting (light green) and re-entering (dark green) the objective lens after reflection by an angled mirror* ***f)*** *Highly inclined laminated optical sheet (HILO) microscopy*

A.1.2 Excitation Side: Light sheet Formation and Parameters

To break down the different aspects of single objective light sheet approaches, we will focus first on excitation-side light sheet formation. The field of view and sectioning capabilities of all light sheet systems are highly dependent on the properties of the illuminating light sheet. In comparison to conventional LSMs that create the sheet using a dedicated low NA illumination objective, single-objective techniques do so by under-filling their high NA primary objective lenses.

The properties of a simple Gaussian light sheet (or beam) generated at the sample are governed by the width, position, angle, convergence and focal plane of the light entering the back aperture of the objective lens, as depicted in (**Figure G.2**a-e). As with conventional light sheet approaches, the light sheet itself can be formed via a range of methods including using a cylindrical lens to focus one axis of the beam at the back focal plane (**Figure G.2**b), or by scanning a pencil-beam in one dimension using a galvanometer mirror imaged to the objective’s back focal plane (**Figure G.2**c). In this case, larger scan angles or higher convergence angles at the back focal plane will produce a light sheet with a longer lateral sheet width (y) at the sample (**Figure G.2**b).

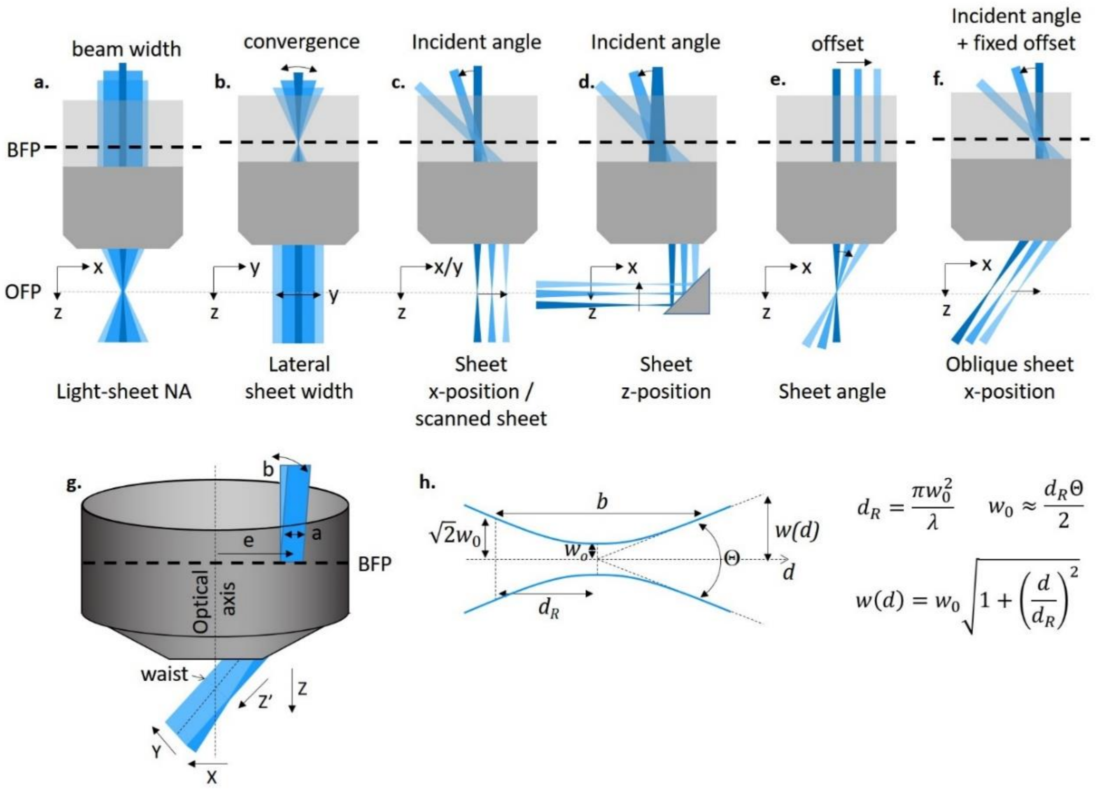

Figure G.2. *Parameters governing the shape, angle and position of a light sheet using a high NA objective lens.* ***a)*** *The width of the beam at the back aperture defines the numerical aperture (NA) of the light sheet and thus the sheet's waist thickness in the sample* ***b)*** *The convergence of the beam at the back aperture determines the light sheet's lateral width at the sample.* ***c)*** *The angle of the input beam defines the offset of the sheet focus in the sample along x/y.* ***d)*** *A reflective surface converts lateral scanning to axial scanning.* ***e)*** *The offset of the input beam along x defines the angle of the sheet in the sample.* ***f)*** *Changing the angle of an offset incoming beam causes an oblique sheet to sweep along x.* ***g)*** *Defining the geometry of oblique illumination single objective light sheet methods such as OPM and SCAPE.* ***h)*** *Basic Gaussian beam properties that apply to simple light sheets. Note direction d can be either axial, lateral or oblique in single objective light sheet methods.*

A.1.2.1 Excitation Configurations for Horizontal-Sheet Single-Objective Systems

In horizontal-sheet based single-objective light sheet systems (Figure G.1a), the illumination beam enters the objective's back aperture at an angle, but intersects with the center of the lens' back focal plane at an angle (**Figure G.2**d). In the orthogonal dimension, the beam is focused at the back focal plane. As a result, a light sheet is formed that enters the sample chamber parallel to the optical axis at the edge of the field of view where it can be reflected by a 45° mirrored element, projecting the beam to align with the objective's horizontal front focal plane. Varying the beam's input angle at the back focal plane causes the light sheet to translate axially after reflection from the 45 degree mirror (**Figure G.2**d). However, it should be noted that this beam scanning alone will not maintain alignment between the objective's focal plane and the light sheet plane. Similarly, axial translation of the objective lens alone will only change the location of the objective's focal plane in the sample, and not the absolute axial position of the light sheet (although the light sheet's beam waist position will shift laterally). Thus, as described further below, formation of volumetric images in this configuration requires a complex combination of scanning, axial translation and defocus to maintain the light sheet imaging condition throughout a volume.

A.1.2.1 Excitation Configurations for Oblique-Sheet Single-Objective Systems

In oblique illumination single-objective systems, a simple light sheet can be formed by an illumination beam entering the objective lens parallel to the optical axis but offset towards the edge of the back aperture (**Figure G.2**e-g). In the orthogonal dimension, this beam is brought to a focus at the back focal plane, with the convergence of this focus dictating the lateral width (along y) of the light sheet at the sample. This configuration creates an angled light sheet within the sample whose waist intersects the objective focal plane of the primary objective in the center of the field of view (**Figure G.2**g). In SCAPE microscopy, the excitation sheet is then swept along the x-direction at the sample by adjusting the angle of incidence of the beam at the back focal plane shown in **Figure G.2**f. The lateral field of view along x is thus governed by the scanning range and objective lens field of view. In systems that rely on lateral translation to sample along the x-direction (e.g. some OPM configurations and APOM), single-objective techniques offer the opportunity to achieve efficient multi-depth imaging over very large x-direction ranges. For all systems, field of view along the y-direction is governed by the lateral width of the sheet and the objective's field of view along the sheet's y-direction, although aperturing may reduce this range at the camera.

A.1.2.2 Beam-Waist Considerations for Oblique v/s Horizontal Sheet Configurations

This geometry highlights an important distinction between oblique illumination light sheet systems and horizontal-sheet / conventional LSMs where the sheet is co-aligned to the focal plane of the detection objective lens. In horizontal sheet systems, the Rayleigh range d_R (**Figure G.2**h) dictates the lateral field of view (x) over which the sample is imaged with a desired axial resolution – with axial sectioning (along z) and contrast degrading at the edges of the field of view. Systems typically incorporate optical components such as mechanical slits [20] or variable beam expanders [21] to tune the light sheet NA for given applications, extending the Rayleigh range in exchange for sectioning ability in larger organisms, or diminishing it for smaller samples (**Figure G.2**a). However, in oblique illumination systems, the light sheet's beam waist influences depth-range (z) rather than lateral range (x), while sheet divergence above and below the beam waist will degrade resolution and optical sectioning in the x-direction.

Having the Rayleigh range influence axial rather than lateral range can be an advantage for oblique illumination systems which typically aim to image the upper layers of intact samples – in an analogous way to standard confocal or two-photon systems. As with these point-scanning techniques, the achievable imaging depth depends upon the scattering and attenuation properties of the sample – which limit the ability of the excitation beam to form a tight focus (or a well-formed sheet) and for emission light to be minimally scattered on its way out of the sample (for confocal). In most living samples, this depth range is typically 100-400 microns, a range over which a Gaussian beam can have a waist thickness between 2 and 5 microns. The numerical aperture of the excitation sheet can thus be adjusted to provide optimal x-direction sectioning over the desired depth range of the sample being imaged, e.g. improved sectioning resolution can be achieved in a thin, 50 micron thick C-elegans worm compared to a larger sample with longer axial extent where in turn, high-resolution spatial sampling may be less necessary.

A.1.2.3 Advanced Methods for Excitation Sheet Formation

A wide range of approaches to condition, pattern or improve the excitation light sheet can feasibly be implemented for single-objective light sheet systems, just as they have been applied to conventional LSMs. For example, while the discussion above focuses on formation of sheets with Gaussian properties, alternative approaches could include using Bessel or Airy beams that can maintain their beam profiles over longer depth ranges than Gaussian beams – albeit at the expense of decreased sectioning as a result of higher contributions from side-lobes [29,30]. Structured illumination schemes, or methods such as optical lock-in detection which take advantage of photo-switching dynamics in optical probes can similarly provide access to super-resolution imaging in combination with PALM and STORM [4,31–33]. Light sheet conditioning, such as with adaptive optics could be particularly important in single-objective systems which are typically using partial pupils of lenses and are thus susceptible to aberrations such as field curvatures.

A.1.3 Detection Optics – Image Formation and Rotation

A.1.3.1 Detection-Side Optics for Horizontal-Sheet Systems

Single-objective light sheet techniques that co-align the light sheet to the primary objective lens' focal plane within the sample, e.g. using prism mirrors at the sample, do not need specialized detection optics: A dichroic filter would typically be used to separate excitation light, and the image corresponding to the objective’s focal plane would be mapped to a camera via an emission filter. However, an important distinction compared to multi-objective conventional LSMs is that these single-objective approaches can feasibly accommodate a wider range of objective lenses (e.g. higher NA, shorter working distance or unusual immersion requirements) since they do not face the same physical constraints of accommodating an orthogonal excitation objective at the sample. Combined with sample holder designs that permit redirection of the light sheet, these single-objective systems have thus been applied to very high resolution light sheet imaging, leveraging the power of higher NA detection optics [20,34]. As mentioned above, despite using an obliquely aligned illumination plane, HILO also uses direct imaging of the objective’s focal plane through the primary objective such that the field of view corresponds to the intersection of the oblique illuminated plane and the objective’s standard focal plane.

A.1.3.2 Detection-Side Strategies for Single-Objective Oblique and Axial Light-Sheet Systems

In comparison, oblique-illumination single objective light sheet systems (e.g. OPM, SCAPE and APOM) require specialized detection strategies to create a rotated focal plane such that a focused image of the oblique light sheet in the sample maps onto the face of a detector array such as a camera. Image rotation methods demonstrated to date have all leveraged the “perfect 3D imaging” principle described originally by Maxwell in 1856 [35]. Although it is often assumed that an objective lens can only form an image of an object at its focal plane, the premise of this imaging condition is that a 3D distribution of points in object space can be mapped into a conjugate image space without astigmatism, curvature or distortion by an optical system, given that the system satisfies the following condition:

$$M = \frac{n_0}{n_i}$$

Equation 1

where M is the magnification of the system from object to image space, n_o is the refractive index of the immersion medium in object space and n_i is the refractive index of the medium in image space.

This principle has been elegantly exploited by Botcherby et al for ‘remote focusing’ applications using well-corrected objective lenses [36]. By mapping the back pupil planes of a first and second objective onto one another, the two lenses effectively function as an encoder and decoder such that a focused spot in the 3D field of view of one lens (e.g. in the sample) yields a wavefront at the back pupil that can be mapped via a telescope to the back pupil of the other objective lens and refocused to a spot in the other objective’s 3D field of view (e.g. at an intermediate image plane – see **Figure G.3**a for the relative geometry of this mapping). Reference [37] provides a detailed analysis of the relationship between image quality, field of view and objective lens properties when using this technique. This concept has been used to permit remote axial repositioning of a confocal or two-photon excitation spot without requiring movement of the primary objective lens at the sample, as well as remote scanning of detection planes at the intermediate image plane [36,38–40]

OPM first leveraged this “perfect, 3D imaging” principle for oblique illumination light sheet microscopy, recognizing that an oblique sheet of laser light within the sample would thus generate an oblique plane of fluorescence in the conjugate image space of a second objective lens. A third objective lens could then be focused onto this conjugate image to map an image of the oblique sheet onto a camera sensor (**Figure G.3**b). SCAPE microscopy utilizes a similar approach to re-map and rotate the detection image plane to correspond to the location of the oblique light sheet at the sample. However, SCAPE also incorporates the additional use of a galvanometric mirror that both scans the excitation sheet laterally at the sample (along x), and de-scans the returning light to maintain a stationary intermediate oblique image plane. This intermediate image then corresponds to a moving oblique focal plane which is continuously aligned with the moving oblique light sheet at the sample (as detailed further below). As noted above, an implementation of OPM has also been demonstrated that further leverages the perfect 3D imaging condition by introducing the excitation light sheet into the second objective at the intermediate oblique image plane, mapping this 3D excitation plane to the sample (**Figure G.1**c) [23,24,41].

One alternative to using a 3rd objective at the intermediate image plane is to place an oblique mirror at this position and map light back through the 2nd objective lens, as utilized in APOM [39]. The mirror serves to rotate the detection plane such that a tube lens behind the second objective focuses the rotated image onto a camera (**Figure G.3**c). This approach is generally equivalent to the 2-objective image rotation method described above (**Figure G.3**b), for the case where the two objective lenses are identical. In APOM, this “remote tilting” technique requires an ultra-high NA primary objective lens (e.g. 100x/1.4 Oil) to enable 90 degree rotation such that the camera plane is aligned with an axial sheet of laser illumination within the sample. Details on the theoretical limitations of remote tilting are detailed in [42]. Although mirror-based rotation can be easier to fine tune in practice, one important constraint is the light necessarily lost owing to the need for beam splitters to first direct light into the second objective, and then allow reflected light to reach a camera telescope. This limitation reduces detected light by at least a factor of two even with the use of a polarizing beam splitter and waveplate [25,39].

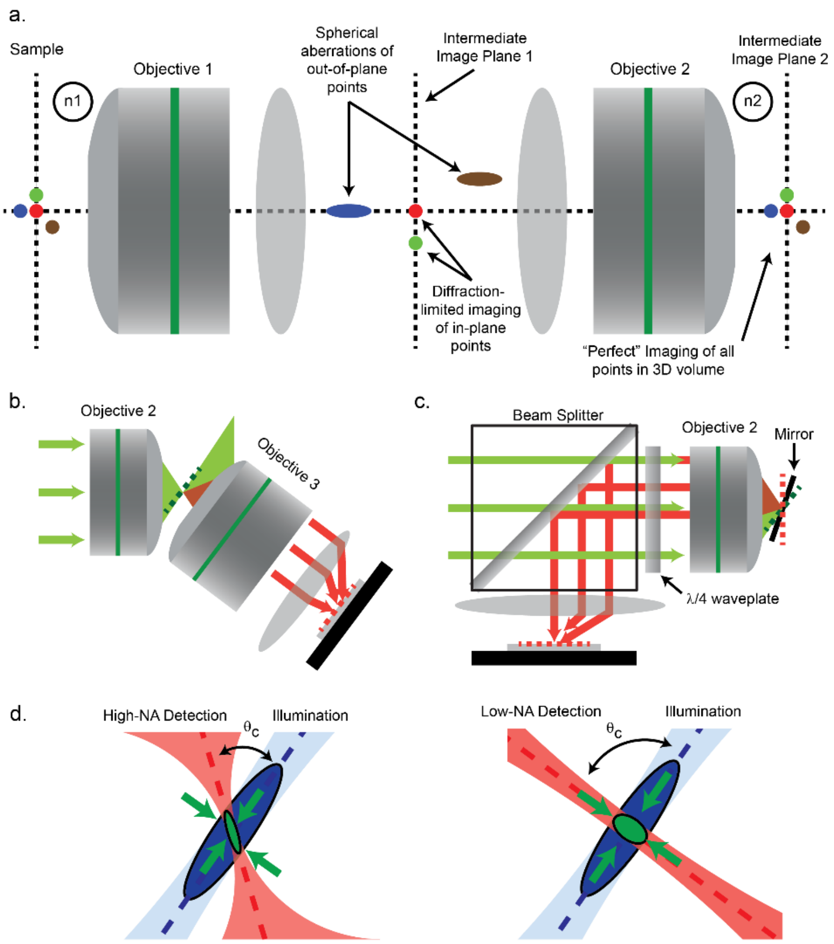

Figure G.3. Methods for image rotation of oblique planes
a) A perfect, 3D imaging system as proposed by [36]. Traditional imaging systems place a sensor at the first intermediate image plane. Using a second telescope consisting of an additional tube and objective lens allows one to satisfy the condition specified in Equation 1, and map a 3D set of points perfectly into a conjugate image space **b)** OPM and SCAPE microscopy use direct imaging of the oblique plane with a third objective lens. Light that reaches the detector is shown in red. **c)** APOM uses a mirror at the conjugate image plane to effectively rotate the oblique image (green) onto the focal plane of the second objective lens. Light from the rotated plane, and the plane itself, is shown in red. The mirror is placed at ½ of the angle of the oblique plane with respect to the focal plane. In APOM, this oblique plane and mirror are 90° and 45° respectively from the focal plane of Objective 2 **d)** Effects on system resolution of the detection collection angle (red), the light sheet (blue) and their relative crossing angle (θ_c).

A.1.3.3 Camera Field of View Considerations for Oblique and Axial Sheet Systems

Oblique and axial-illumination single objective systems all generate y-z' projections of the sample at the camera, rather than capturing the more conventional x-y plane. The lateral field of view (y, corresponding to the length of the light sheet) can be over 1 mm at 20x, and is only limited by the objective's field of view. However, z' corresponds to oblique depth (= z in APOM), which in most samples will be limited by both light scattering and the Rayleigh range of the light sheet. As a result, camera images in these systems are usually wider along y than z'. By enabling read-out modes of cameras that utilize fewer rows than columns, it becomes possible to achieve much higher frame rates than conventional LSMs that would typically acquire a square region of interest covering x-y. For example, modern sCMOS cameras can read 100 rows (corresponding to 100 depths along z') and 2000 columns (corresponding to pixels along y) at over 2000 frames per second. Additionally, in SCAPE a spectral image splitter within the detection path after the 3rd objective lens enables two spectrally-separated images to be positioned side by side on the camera, providing dual-color imaging without increasing the number of rows needed, and thus without compromising imaging speed compared to single-color imaging. An important consequence of Equation 1 is that, for most immersion medium combinations, meeting this condition means that the overall magnification of the system between the first and second objective lenses must be close to 1. Therefore, the camera light path must incorporate appropriate magnification to map the intermediate image onto the camera to provide the desired sample density at the specimen in relation to pixels on the camera chip.

A.1.3.1 Image Rotation Light-Collection and NA Trade-Offs

The need to re-image the oblique intermediate image plane (either directly or via remote-tilting) places constraints on detection collection NA as depicted in **Figure G.3**b-c. In the simplest case, one can consider aligning a 3rd objective lens with the intermediate oblique image plane, which for a 45 degree image rotation will capture < 50% of the cone of fluorescence light from the 2nd objective. Although maximizing this collection efficiency should yield the highest resolution and signal to noise, there are two important considerations. First, the solid angle of light entering the 3rd objective corresponds to the fraction of the primary objective's pupil, and thus the detection cone intersecting with the oblique light sheet at the sample (**Figure G.3**d). A smaller cone of light collected, the higher the effective crossing angle between the light sheet and the detection cone θ_c (**Figure G.3Error! Reference source not found.**d). Thus, although decreasing the fraction of light collected will reduce signal and in-plane resolution, these effects weigh against potential improvements in sectioning and point-spread function isotropy arising from the higher crossing-angle – in the case where $\theta_c = 90$ degrees, the geometry of the oblique-illumination system will approach that of a conventional LSM with modest detection NA. It should also be considered that single-objective, oblique illumination systems are compatible with applications that currently utilize point-scanning and spinning disk confocal – systems which provide far poorer performance in terms of signal to noise relative to phototoxicity, even accounting for detection-side loses in single-objective light-sheet systems [43]. Nevertheless, improving the efficiency of image rotation in oblique-illumination single-objective light sheet systems is an important aspect of system design that could yield further improvements in resolution and detection throughput.

A.1.4 Scanning Approaches for Volumetric Imaging

The sections above describe the two basic elements required in single-objective systems for forming an excitation light sheet at the sample and focusing an array detector such as a camera to be co-aligned with this sheet. The remaining distinctions between the single-objective light sheet techniques described to date are in the way in which they generate a volumetric image.

A.1.4.1 Volumetric Image Formation in Horizontal-Sheet Single-Objective Systems

The horizontal-sheet based systems described above use custom sample holders wherein miniature reflectors convert the lateral position of the beam exiting the objective lens into a beam at a constant axial depth within the sample (**Figure G.2**d). However, the axial motion of the light sheet must also be coupled to axial translation of the objective lens to maintain a co-aligned light sheet imaging condition. In systems demonstrated to date, a galvanometric mirror has been used to scan the beam on the back focal plane of the objective lens, providing axial displacement of the sheet, while piezo-scanning of the objective lens is used to maintain focus on the sheet. Additionally, axial movement of the objective or sample also changes the location of the beam waist along x with respect to the optical axis. This effect can be compensated for with an electrically tunable lens placed within the excitation path to adjust the divergence of the sheet-forming beam and thus shift the beam-waist position during scanning [21]. Although complex, it is interesting to note that varying the location of the beam waist dynamically can also be leveraged to enable improved sectioning and contrast via stitching of multiple overlapping images acquired with a higher NA light sheet [44,45]. Where the light sheet is formed from a scanning beam, a secondary scanning galvanometric mirror co-aligned to the back focal plane of the primary objective lens is used [21].

It should be noted that approaches such as objective-coupled planar imaging (OCPI) and the Leica TCS SP8 DLS system that rigidly mount excitation optics or reflective elements to the detection objective, do not require such complex coordination of light sheet and detection planes. In this case, volumetric imaging is achieved either via sample translation or movement of the detection objective itself. However, specialized sample holders and optics would likely be required to adapt these approaches to high NA, low working distance objective lenses for applications such as single-molecule localization experiments.

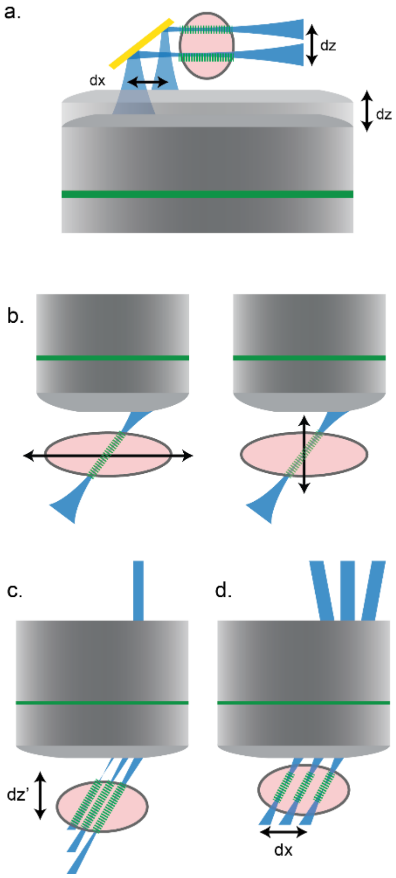

Figure G.4: *Comparison of different sheet-scanning paradigms for 3D imaging using single-objective light sheet geometries* ***a)*** *Horizontal-sheet systems convert lateral (dx) translation of the sheet into axial (dz) displacement within the sample. The sheet is kept in focus with the objective's focal plane by piezo-scanning the primary objective lens* ***b)*** *Laterally or axially displacing the sample through a static sheet is the simplest way of acquiring multiple planes within the volume.* ***c)*** *OPM combines remote focusing techniques with piezo-scanning of the second objective (See* ***Figure G.1****c) to axially displace the sheet within the sample* ***d)*** *SCAPE microscopy uses galvo-based confocal scanning and de-scanning in order to sweep the sheet laterally through the sample (See* ***Figure G.1****d).*

A.1.4.2 Volumetric Image Formation using Stage-Scanning

Stage scanning is a simple approach to volumetric imaging for most single-objective light sheet methods and can utilize standard motorized x-y or z stages to hold samples (**Figure G.4**b). As the stage translates the sample through a stationary, co-aligned light sheet and detection plane, images can be acquired at each position and then stacked to form a volume. The sample can be scanned either axially or laterally, depending on the light sheet orientation, with OPM's oblique sheet permitting the use of both modes, and APOM scanning laterally when used with an axial light sheet [22,25,41]. Systems that use stage scanning will generally provide the most uniform imaging parameters over the scan, but resolution and contrast will decrease with distance from the light sheet's beam waist if a Gaussian beam is used. When stage scanning, the speed of volumetric acquisition is determined by the maximum velocity and stability of the stage, as well as the maximum camera frame rate. For lateral scanning, the field of view can be as large as the travel range of the stage scanner (e.g. >200 mm) and can therefore accommodate a wide range of samples (**Figure G.5**). However, the use of physical sample translation is typically slow, or can be disruptive to the sample for repeated volumetric imaging at high speeds.

A.1.4.3 Volumetric Scanning in Oblique-Illumination Systems

An alternative approach to axially scanning the primary objective, implemented within OPM, is to further leverage remote focusing principles detailed in section A.1.3.2 [37] and piezo-scan the second objective lens at the intermediate image plane, while also using the second objective lens as the light sheet launch as shown in **Figure G.1**c. The effect of this scanning is that both the light sheet and detection plane stay co-aligned in conjugate image space, but move axially relative to the primary objective's focal plane at the sample (**Figure G.4**c). Although the volumetric field of view produced is rhomboid and fairly small, this approach achieves volumetric imaging at the sample without requiring any relative motion of the sample or primary objective [23,24].

SCAPE microscopy takes an alternative approach to volumetric image formation by incorporating a galvanometer mirror into the optical path to sweep the light sheet laterally across the sample (across x) – achieving a similar effect to laterally translating the sample through the oblique sheet but without requiring relative movement of the primary objective lens or sample (**Figure G.4**d). SCAPE further takes advantage of scanning and descanning principles used in confocal microscopy such that the galvanometer mirror causing the light sheet to sweep across the sample also redirects fluorescent light returning from the sample. As a result, the intermediate oblique image plane (already mapped from the sample plane via 'perfect 3D imaging') remains stationary, yet remains focused on the light sheet, irrespective of the light sheet's lateral position within the sample. A camera aligned via a 3rd objective lens, focused on the intermediate oblique imaging plane formed by the second objective then acquires images corresponding to oblique y-z' planes within the sample. These images can be simply stacked to form a volumetric image of the sample, yielding x-y lateral fields of up to 1 mm x 1 mm when using a 20x primary objective lens. The single-axis galvanometer mirror is the only moving part in SCAPE microscopy, and moves at the volumetric imaging rate (e.g. 20 lines per second for 20 volume-per second imaging). Camera read-out speeds exceeding 2,000 frames per second can be achieved using 100 rows (corresponding to 100 z-depths) enabling 2000 x 200 x 100 (y-x-z) voxel volumetric imaging at 10 VPS. In this way, SCAPE achieves very high speed volumetric imaging without requiring motion of the objective lens or specialized mounting or positioning of the sample.

A.1.5 Factors and Trade-Offs Affecting Imaging Performance

A.1.5.1 Factors Affecting Penetration Depth:

All light-sheet methods are limited in penetration depth by the scattering properties of the sample, which in turn depend upon the excitation and emission wavelengths used. Shorter excitation wavelengths will generally scatter more, affecting the quality and intensity of the light sheet with increasing distance along its propagation direction, while fluorescence emission light will face scattering and thus blurring on its way out of the tissue. Scattered excitation light can also add to background signal, reducing optical sectioning and contrast at deeper layers. In conventional LSM methods, these effects are sometimes addressed in small, discrete samples using multi-view systems that stitch together images acquired with illumination impinging from different sides of the sample.

Although multi-view approaches are feasible for single-objective light-sheet configurations, for example following the concept of Di-SPIM [7], single-objective techniques are not generally used to image deeper into samples than the limit of scattering and attenuation. However, it is interesting to note that oblique illumination single-objective light sheet methods have the advantage of being able to image very scattering samples, even if they are only able to map the surface topography or just below the samples' surface – something that cannot be readily achieved using standard orthogonal light-sheet configurations. This feature again highlights the utility of single-objective light-sheet methods for applications more similar to those of point-scanning and spinning disk confocal. Nevertheless, improvements in penetration and resolution at depth in scattering tissues already applied to standard light sheet methods could be applied to single-objective methods including the use of multi-angle illumination, structured illumination, adaptive optics, Bessel/Airy beams, longer (less scattering) wavelengths and two-photon implementations [4,46–51]

A.1.5.2 Factors Affecting Field of View, Resolution Homogeneity and Isotropy:

As with all light sheet methods, the resolution of single-objective systems is not uniform, nor isotropic across the 3D field of view, even in non-scattering samples. The limitations on horizontal-sheet systems are similar to conventional light sheet geometries, with trade-offs between a longer x-direction field of view and the level of axial sectioning in z.

In oblique and axial-illumination geometries using stage scanning, the sheet's waist affects the usable axial range, rather than the x-direction range, trading off depth of field with sectioning in the x-direction. X-direction sectioning can be almost isotropic in samples requiring a relatively narrow depth of field (e.g. 50 microns), whereas axial ranges up to around 400 microns can also be achieved with relatively uniform x-direction sectioning along this axial range. In stage scanning systems, sampling density in x is dictated by the speed of the translation stage relative to the image acquisition rate. An advantage of this configuration over horizontal sheet systems is that large-area scanning can be achieved with fewer stitching artefacts along x and y, since acquisition along x can be continuous, and resolution parameters should remain constant for a given axial depth. The single-objective geometry provides a further advantage over rotated dual-objective light sheet systems, such as Di-SPIM and inverted SPIM whose physical geometries can obstruct scanning of large samples and which face more significant challenges for retaining immersion media.

SCAPE microscopy and certain implementations of OPM can also achieve volumetric imaging by optically scanning the light sheet, without relative motion of the sample or primary objective lens. In SCAPE, the x-direction field of view this thus governed by the scan range of the galvanometer system following the same conditions as a confocal microscope. At 20x, a sample area of 1 mm x 1 mm (x-y) can be achieved with relatively uniform resolution across this extent. OPM has been implemented with a remotely-actuated axial scan of the oblique sheet, generating a smaller effective 3D field of view. However, in both cases, these scanning configurations will yield less uniform resolution and isotropy across the entire volume compared to stage-scanning, but in turn can provide much higher volumetric imaging speeds in intact samples. As with conventional LSMs, these implementations can similarly be implemented for large-area scanning via stitching of adjacent volumes.

A.1.5.3 Comparing Single-Objective Light-Sheet Methods to Confocal Microscopy:

The single-objective light sheet geometry provides an imaging configuration similar to a conventional confocal or two-photon microscope. These point-scanning systems are widely used to image living biological samples, but are limited in their ability to capture volumetric data at high speeds owing to both the limitations on point-scanning speeds achievable, and the level of phototoxicity seen with repeated imaging.

Although current implementations of oblique and axial-illumination single-objective light sheet systems may offer slightly lower diffraction-limited resolution compared to conventional point-scanning or spinning disk confocal, they can deliver significantly faster acquisition speeds with much lower photobleaching and phototoxicity, while having equivalent abilities to stage-scan over large samples, or image intact, complex living samples at rapid volumetric imaging speeds.

The lower phototoxicity in light sheet systems is the result of at least three factors: 1) Illumination of only the tissue being imaged, and not tissue either side of the focal plane, 2) The increased interaction probability of photons that are exciting fluorescence along their propagation direction, enabling the use of less illumination light per fluorescent interaction and 3) The significantly increased integration time available in light sheet imaging, equal to the frame rate rather than the pixel-rate of imaging, e.g. for a 400 x 400 pixel plane, this effect provides 160,000 times longer for light to be collected in parallel by pixels on a camera compared to point-scanning for the same volume rate. Thus, although a plane of illumination light is required rather than a diffraction limited spot, substantially less overall illumination of the tissue to achieve equivalent signal to noise. Experimentally observed advantages in terms of both signal to noise and photobleaching in samples expressing fluorescent proteins are consistent with a supralinear relationship recently reported, which demonstrates that equivalent energy delivered as longer integration at lower powers results in significantly less photobleaching than higher powers for shorter durations [43,52]. Consequently, single-objective light sheet methods may provide a compelling alternative to confocal microscopy for a wide range of biomedical applications.

A.1.6 Image Processing, Display, Analysis

The simplest form of light-sheet image reconstruction is to stack acquired planes to form a volumetric image. However, multi-view light sheet systems typically require more substantial data processing to register and merge multiple images from different illumination angles, compensating for depth-dependent light sheet degradation. More complex algorithms to apply deconvolution and computational image reconstructions can provide much improved, and even isotropic resolution, though these approaches also require substantial computation pipelines and resources as they scale to ever larger data sets [53,54].

Most single-objective light sheet systems demonstrated to date do not utilize multiple views, instead prioritizing volumetric imaging speed and sample diversity. In this case, volumetric images can be generated most simply by stacking sequentially acquired planes, although this approach must account for the orientation of the sheet within the sample: Most SCAPE scan patterns, and stage-translation imaging in OPM result in images acquired at a constant incidence angle. Each camera-row acquired will then represent an x-y plane, but with each shifted laterally in x with increasing depth. The illumination sheet angle can either be calculated from system parameters, inferred from imaging data or determined from calibration measurements acquired on a 3D structured fluorescent phantom. Volumetric images can thus be corrected into Cartesian space by shifting each x-y plane along x to account for the oblique sheet angle. System aberrations or misalignments may also cause the relative size of voxels in x-y and z to be non-uniform, an effect that can be quantified and / or corrected via calibration measurements.

Although this post-processing is required for quantitative image analysis or visualization of depth-projections, for simple data review, this transform isn't strictly necessary, a feature important for review of very rapidly acquired and thus very large datasets during the course of an in-vivo experiment. The minimal processing requirements for single-objective light sheet imaging are a major advantage over emerging high-speed 3D imaging methods such as light-field imaging, a method that requires significant computational image reconstruction to render a 3D image from raw data that cannot otherwise be rapidly visualized [55,56].

Once volumes have been formed, standard image analysis techniques can be used to process or analyze data. For example, deconvolution can sharpen images, but may need to take into account spatially varying point-spread-functions within the 3D field of view. Intensity scaling can also be used to compensate for depth-dependent attenuation, especially in more scattering tissues such as the mouse brain. If images are acquired sufficiently quickly (as in SCAPE and most OPM implementations) it is not necessary to register sequential frames to account for sample motion – in fact images of the 4D dynamics of moving samples can be acquired.

Fast volumetric imaging methods such as SCAPE also present new opportunities to quantify imaging features such as cellular activity from fluorescent calcium indicators. Extracting such signals can require volumetric image registration of 4D tracking of cells and extraction of intensity signals over time. Multi-color imaging can be performed by using an image-splitter or multiple cameras [26,41] enabling ratiometric analysis as well as co-imaging of a static marker for tracking and correction to compensate for motion and position-dependent intensity dynamics.

Applications

Super-Resolution Imaging with Single-Objective Light Sheet Geometries

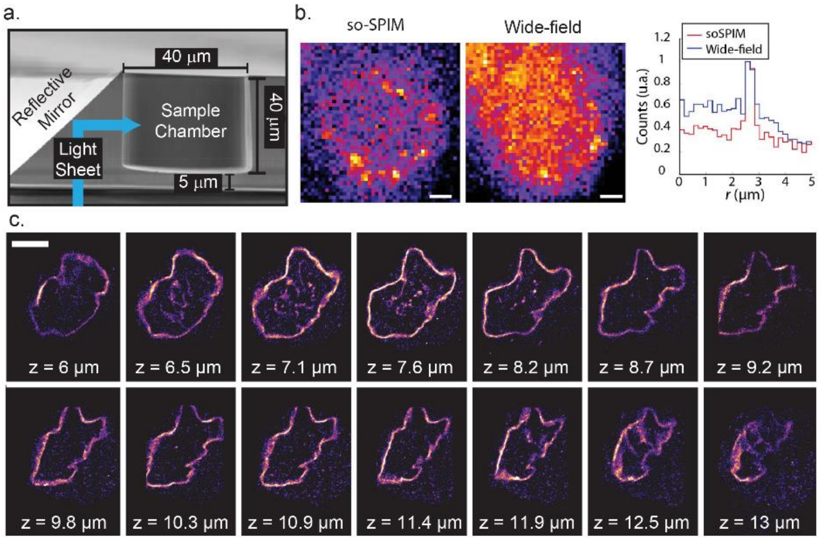

Figure G.5: *Super-resolution imaging with horizontal-sheet single-objective light-sheet microscopy*
a) *Example of a custom-fabricated sample holder tailored to imaging single/multi-cellular samples which places a miniaturized reflective surface adjacent to a micro-well. The sample is imaged from below in an inverted configuration* ***b)*** *Example of one of the 4000 frames acquired during a STORM sequence acquisition on the nucleus membrane protein Lamin-B1 labeled with Alexa Fluor 647 dyes in a suspended S180 cell. The image on the left was acquired with light sheet illumination ($w_o = 1.5$ µm) while the image on the right was acquired using widefield illumination. Graph shows a cross-section through "two single-molecule events acquired with [light-sheet] illumination (red line) and widefield illumination (blue line)", Scalebar, 1 µm c) Axial cross-sections of 3D STORM super-resolution images taken with so-SPIM. Lamin-B1 in suspended S180 cells labeled with photoactivatable dye FLIP 565. Scalebar, 5µm. Adapted by permission from Macmillan Publishers Ltd: Nature Methods, Galland et al., 2017.*

There are a number of ways to excite fluorescence for single-molecule, super-resolution imaging, including epi-illumination, total internal reflectance illumination, HILO and structured illumination. Illumination with a highly inclined oblique plane, as used in HILO, can provide a 7x improvement in signal-to-background in comparison to widefield illumination [27] and has been utilized in combination with PALM and STORM for subcellular imaging [27,57–59].

Using a horizontal-sheet single-objective light sheet approach for single-cell imaging affords a similar reduction in out-of-focus fluorescence while enabling deeper and more flexible imaging than HILO [60]. Custom sample chambers (**Figure G.5**a) must be tailored to the dimensions of individual samples, as well as the specifications of the primary objective lens. **Figure G.5** shows an example result from Galland et al [21] where and inverted horizontal-sheet single objective light sheet system was used to perform volumetric STORM imaging on a suspended S180 cell (**Figure G.5**c). **Figure G.5**b demonstrates how light-sheet illumination provides improved sectioning and reduced background compared to wide-field illumination.

Although this example shows horizontal-sheet single-objective light sheet applied to imaging a single cell, a large range of samples can be imaged via fabrication of sample chambers that are tailored to specific experiments. Demonstrations have included microfluidic applications in [20] as well as larger-scale *Drosophila* embryos.

Large FOV, High-Throughput Imaging with Oblique Light-Sheet Systems

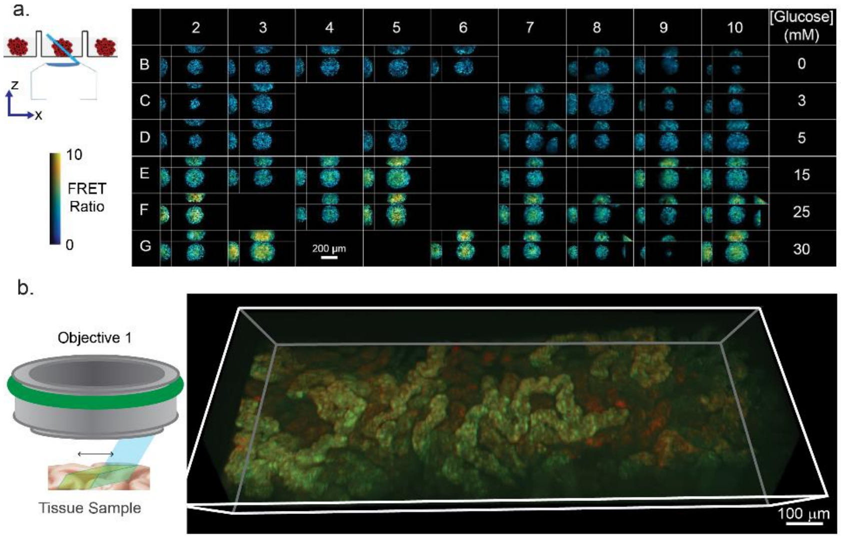

Figure G.6: *Large field of view imaging with oblique illumination light sheet systems*
a) *OPM experimental setup for imaging spheroids embedded in multi-well plates. Images show Demonstration of ssOPM plate-reading capability on 42 wells for culture media with varying glucose concentration. Glucose concentration in the culture medium increases down the plate as indicated on the right hand side. For each well, an x-z (top), y-z (left) and x-y (bottom right) slice is shown. The false color scale indicates FRET ratio and brightness indicates intensity of sensitized emission. Reproduced with permission from Maioli et al. 2016.* ***b)*** *SCAPE imaging of fresh-tissue biopsies. Red and green autofluorescence in a 1.2 mm stitched 3D view of kidney tubules acquired with SCAPE microscopy in 5 sec at 10 vol/sec. Figure reproduced with permission from Patel et al. 2017. Scale bar: 100 µm*

The desire to bring light-sheet imaging benefits to common biological samples such as tissue slices and cell cultures on microscope slides, in multi-well plates and in microfluidic channels has driven the development of a number of rotated 2-objective light sheet systems that permit top-down or bottom-up light-sheet imaging [8,9,16]. However, the two-objective configuration of these systems introduces complexities in scanning, coverglass aberrations and difficulties in maintaining immersion media for the long-working distance objectives required. In comparison, oblique illumination single-objective light sheet systems such as OPM, APOM and SCAPE microscopy can provide significant benefits for depth-resolved imaging of planar samples or intact tissues of large lateral extent.

Figure G.6a shows an example of dual-color OPM with stage-scanning applied to imaging a FRET-based glucose sensor in cultured spheroids[41]. These images were acquired on an OPM system that had been integrated onto a commercially-available, inverted microscope frame (Olympus IX71) using a water-dipped objective lens (Olympus 60x/1.2NA). A spheroid within each of 42 wells of a 96-well plate was imaged with an overall acquisition time of 9 minutes for 42 separate fields of view. This example demonstrates OPM's ability to compensate for both well-to-well variations in focal distance and the curved surface of the spheroids themselves.

Figure G.6b shows an example of large-scale data acquired on fresh, unstained mouse kidney using SCAPE microscopy. Here, the image was formed by stitching a sequence of volumes acquired at 10 volumes per second as the tissue was translated across the field of view by hand. This volume-stitching approach differs from using carefully controlled linear translation to generate volumetric data and is possible because at 10 volumes/second, consecutive volumes have enough overlapping spatial features to permit 3D stitching [61]. This freedom from needing a motorized stage can potentially be translated to handheld implementations for clinical use.

In both of these examples, the depth of field imaged was sufficient to capture the required features of the sample. As noted above, the depth of field in single-objective oblique light sheet systems can be adjusted by changing the numerical aperture of the light sheet, trading off axial range for x-direction optical resolution. However, in tissues or samples with low scattering levels (such as cleared tissues [62]), oblique light-sheet imaging over a deeper axial range can also be achieved by simply moving the beam waist more deeply into the sample. In the case of SCAPE, imaging can be achieved using a 2 mm working distance 20x, 1.0 NA objective lens, affording a significant depth-range that can be accessed via imaging of successive depth planes using a modest NA beam (e.g. each layer covering a 300 micron range with good diffraction-limited resolution). The speed advantage offered by light-sheet methods combined with stage scanning could offer significantly faster imaging of large samples than with conventional confocal point scanning microscopy. Single-objective oblique and axial light-sheet methods are further compatible with serial microtome-type imaging schemes, where superficial layers can be successively removed from the block-face permitting very high-speed volumetric imaging of large cleared samples with minimal tissue distortion.

The use of a single objective lens in oblique-illumination systems could also facilitate integration of these systems onto conventional microscope frames [21–24,41]. In addition to simplifying sample placement and preparation, use of a conventional frame can allow users to easily switch between light sheet illumination and other microscopy techniques.

High-Speed Functional Imaging of Brain Activity using SCAPE

In neuroscience research it is desirable to be able to capture the dynamic activity of many neurons within the brain at high speeds. Calcium sensitive dyes, and more recently calcium-sensitive fluorescent proteins can provide an optical read-out of cellular-level neural activity, with the field generating an ever increasing palette of indicators of different colors with sensitivity to different functional parameters and applications reaching beyond neuroscience. The currently favored method to image calcium indicators in the brain is point-scanning two-photon microscopy, which can provide high resolution imaging over 500 microns into the intact brain. However, efforts to increase volumetric imaging speeds have reached a limit for point-scanning, for example if a 200 μm^3 volume is sampled at 10 Hz with a 1μm sampling density, the image system's pixelwise sample rate must be 80 MHz. This rate is equal to the pulse-rate of standard Ti:Sapphire lasers used for two-photon microscopy such that imaging would need to be achieved with only one laser pulse per pixel, in turn meaning that images could not be acquired any faster than this rate [16,63]. Moreover, to achieve this volumetric imaging speed, a galvanometer scanner capable of 400 kHz line-scan rates would be required.

Oblique light sheet microscopy is not bound by the same constraints as point-scanning microscopy. In the case of SCAPE microscopy, to image at 10 volumes per second, its galvanometer scans at only 10 lines per second. The pixel-rate of the camera being used limits the pixel-wise bandwidth of the system, which with modern sCMOS can be at least 540 MHz. Since each planar image is acquired in parallel, the frame rate of the camera in the case above would be only 2 kHz, whereas each pixel would have 0.5 ms to integrate sufficient signal (compared to a single laser pulse). Combined with SCAPE's efficient use of scanning and descanning rather than translation of the objective lens, these features mean that the volumetric imaging speed of SCAPE is currently only limited by available camera frame-rates and the quantum yield / photobleaching sensitivity of available fluorophores. Moreover, large field of view and single, stationary objective lens used in SCAPE makes it possible to image samples more usually imaged using confocal and two-photon microscopy, including the intact mouse brain, or delicate small organisms such as zebrafish, fruit-flies and C. Elegans in configurations incorporating features such as behavioral monitoring and stimulation.

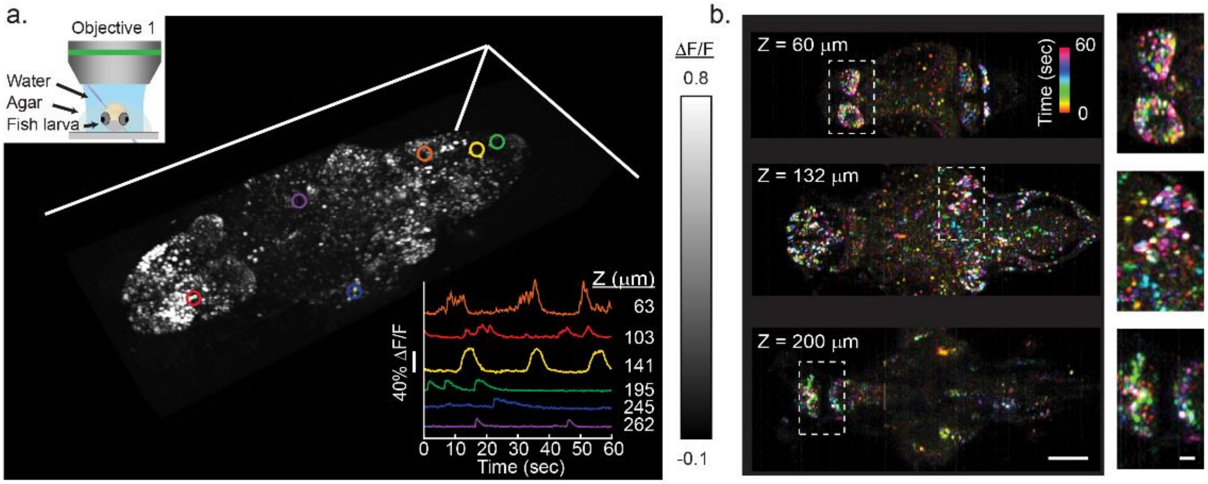

Figure G.7: *SCAPE imaging of spontaneous activity in the whole brain of larval zebrafish*
Data acquired at 6 vol/sec, FOV ~ 820x380x260 μm ***a)*** *Volume rendering of maximum intensity projection taken over all 360 time points over a 1 minute run. (Inset) Time series extracted from 6 neurons drawn from locations within the brain at 6 depth planes within the fish* ***b)*** *Time-encoded color projection of 3 depth planes showing spontaneous activity over a range of brain regions. Insets show ~2x close ups of indicated regions. Scale bars are 100 μm and 20 μm.*

Figure G.7 shows an example of high-speed SCAPE imaging of neural activity in a 6 days past fertilization zebrafish larva expressing the calcium-sensitive fluorophore GCaMP in the nuclei of its neurons. Here, a field of view of 820x380x260 μm corresponding to 688x135x216 voxels was imaged at 6 volumes per second continuously for a period of 40 minutes. Images were acquired with a 488 nm excitation continuous wave laser. The zebrafish was mounted in a drop of 1-2% agarose and imaged from above. In this configuration in which oblique illumination has the additional advantage of avoiding illumination of the eyes from the side, as used in conventional light sheet systems, reducing ocular stimulation as well as providing access to deeper regions of the brain located behind the absorbing eyes.

This example demonstrates high-speed SCAPE imaging in a larval zebrafish that has relatively low levels of light scattering. SCAPE has also been applied to imaging the intact mouse brain, as shown in Bouchard et al using single-photon 488 nm excitation. In this case, scattering limited penetration depth, such that fine features such as capillaries could be resolved down to a depth of 150-200 µm, while only larger structures could be visualized beyond 300 µm. Development of red-shifted fluorophores as well as two-photon implementations of SCAPE could provide new access to high-speed volumetric imaging that is currently beyond the reach of point-scanning two-photon.

Conclusion

Although many new variations on standard light sheet geometries have been developed in the past decade, single-objective light sheet systems possess some unique qualities, both in terms of their design considerations and in the range of applications they can be applied to. Here, we described 'horizontal-sheet' configurations that require sample holders with integrated reflective surfaces to position the light sheet, as well as axial and oblique illumination light sheet systems that can be used to image intact samples over a wide range of length scales. We highlighted the way in which oblique light sheet approaches such as OPM and SCAPE can achieve very high speed volumetric imaging speeds, while also providing light sheet advantages including low photodamage and high signal to noise. We note that these methods thus present a promising alternative to point scanning or spinning disk confocal microscopy for a wide range of biomedical applications including high-speed neuroimaging.

Since single-objective light sheet microscopes are still a relatively small subset of all sheet-based imaging techniques, there are many potential avenues for future development that remain unexplored. From a technology development standpoint, we anticipate that the resolution and light collection efficiencies of existing systems will scale with the availability of high-quality or custom-designed objective lenses, while acquisition speeds will improve alongside advances in camera technology. Many developments that have improved the resolution, isotropy and overall image quality of conventional LSM's also have the potential to be implemented for single-objective configurations. These include, but are not limited to, the implementation of structured illumination (Bessel, Bessel array, Lattice), real-time corrections for system/sample induced aberrations, multi-angle illumination to eliminate shadowing artefacts and multi-view acquisition/fusion to improve isotropy and resolution. Penetration depth of the sheet into tissue can be improved by moving into longer wavelength single-photon and multi-photon excitation regimes. Similarly, the optimization of red-shifted fluorescent indicators should lessen the blurring effects of scattered emission photons as they make their way out of the sample. Combining sheet-based illumination with other imaging modalities is also made easier when incorporation of these features only needs to design around a single objective lens. For example, Zhang et al. combined an oblique beam-scanning setup with optical coherence tomography to achieve simultaneous reflectance and fluorescence imaging in 3D.

Single-objective approaches also offer new freedom in terms of experimental design owing to the available space around the sample for equipment such as behavioral rigs, monitoring systems, perfusion systems and electrophysiology. While the examples provided in this chapter have focused primarily on research applications in the life sciences, further potential exists for the application of single-objective methods to areas such as clinical imaging, industrial and process engineering applications.

In summary, single-objective light sheet methods are an emerging branch of light-sheet microscopy delivering the benefits of light-sheet imaging to a diverse range of new applications, while providing new capabilities such as high-speed imaging that are a valuable complement to the already rich value of conventional light sheet imaging geometries.

Acknowledgments

Dr. Matthew Bouchard made significant contributions to the initial development of SCAPE microscopy. Kripa Patel acquired and processed the data shown in Figure 5b. Drs Jeremy Ullmann and David Reutens provided seizure zebrafish expertise, with fish provided by Dr. Misha Ahrens at Janelia Farm. We gratefully acknowledge funding from the following sources for this work: NIH (NINDS) 5U01NS094296 (BRAIN), R21NS053684, R01 NS076628 and R01NS063226 (Hillman), NSF CAREER 0954796 (Hillman), NSF IGERT 0801530 (Voleti), MURI, W911NF-12-1-0594, The Human Frontier Science Program (Hillman/Cauli) and the Wallace H. Coulter Foundation and The Kavli Foundation (Hillman).

Financial conflict of interest:

SCAPE IP is licensed to Leica Microsystems for commercial development.

References:

1. Huisken, J., Swoger, J., Bene, F. Del, Wittbrodt, J., and Stelzer, E.H.K. (2004) Optical Sectioning Deep Inside Live Embryos by Selective Plane Illumination Microscopy. *Science (80-.).*, **305** (1007), 1007–1009.

2. Krzic, U., Gunther, S., Saunders, T.E., Streichan, S.J., and Hufnagel, L. (2012) Multiview Microscope for Rapid in toto Imaging. *Nat. Methods*, (juNe), 1–7.

3. Keller, P.J., Schmidt, A.D., Wittbrodt, J., and Stelzer, E.H.K. (2008) Reconstruction of Zebrafish Early Light Sheet Microscopy. *Science (80-.).*, **322** (14), 1065–1070.

4. Keller, P.J., Schmidt, A.D., Santella, A., Khairy, K., Bao, Z., Wittbrodt, J., and Stelzer, E.H.K. (2010) Fast , high-contrast imaging of animal development with scanned light sheet – based structured- illumination microscopy. *Nat. Publ. Gr.*, **7** (8), 637–642.

5. Tomer, R., Khairy, K., Amat, F., and Keller, P.J. (2012) Quantitative high-speed imaging of entire developing embryos with simultaneous multiview light-sheet microscopy. *Nat. Methods*, **9** (7), 755–63.

6. Wu, Y., Ghitani, A., Christensen, R., Santella, A., Du, Z., Rondeau, G., Bao, Z., Colón-Ramos, D., and Shroff, H. (2011) Inverted selective plane illumination microscopy (iSPIM) enables coupled cell identity lineaging and neurodevelopmental imaging in Caenorhabditis elegans. *Proc. Natl. Acad. Sci. U. S. A.*, **108** (1), 17708–17713.

7. Kumar, A., Wu, Y., Christensen, R., Chandris, P., Gandler, W., McCreedy, E., Bokinsky, A., Colón-Ramos, D.A., Bao, Z., McAuliffe, M., Rondeau, G., and Shroff, H. (2014) Dual-view plane illumination microscopy for rapid and spatially isotropic imaging. *Nat. Protoc.*, **9** (11), 2555–2573.

8. McGorty, R., Liu, H., Kamiyama, D., Dong, Z., Guo, S., and Huang, B. (2015) Open-top selective plane illumination microscope for conventionally mounted specimens. *Opt.*

Express, **23** (12), 16142–53.

9. Glaser, A.K., Reder, N.P., Chen, Y., McCarty, E.F., Yin, C., Wei, L., Wang, Y., True, L.D., and Liu, J.T.C. (2017) Light-sheet microscopy for slide-free non-destructive pathology of large clinical specimens. *Nat. Biomed. Eng.*, **1** (June), s41551-17.

10. Guan, Z., Lee, J., Jiang, H., Dong, S., Jen, N., Hsiai, T., Ho, C.-M., and Fei, P. (2016) Compact plane illumination plugin device to enable light sheet fluorescence imaging of multi-cellular organisms on an inverted wide-field microscope. *Biomed. Opt. Express*, **7** (1), 194.

11. Paiè, P., Bragheri, F., Bassi, A., and Osellame, R. (2016) Selective plane illumination microscopy on a chip. *Lab Chip*, **16**, 1556–1560.

12. Theer, P., Dragneva, D., and Knop, M. (2016) piSPIM: high NA high resolution isotropic light-sheet imaging in cell culture dishes. *Sci Rep*, **6** (September), 32880.

13. Daniels, J., Zemek, J., and Rondeau, G. (2016) Innovations in ASI Light Sheet Microscopes : The Oblique SPIM. *Proc. Am. Soc. Cell Biol. Meet.*, 97.

14. Gebhardt, J.C.M., Suter, D.M., Roy, R., Zhao, Z.W., Chapman, A.R., Basu, S., Maniatis, T., and Xie, X.S. (2013) Single-molecule imaging of transcription factor binding to DNA in live mammalian cells. *Nat. Methods*, **10** (5), 421–426.

15. Greiss, F., Deligiannaki, M., Jung, C., Gaul, U., and Braun, D. (2016) Single-Molecule Imaging in Living Drosophila Embryos with Reflected Light-Sheet Microscopy. *Biophys. J.*, **110** (4), 939–946.

16. Holekamp, T.F., Turaga, D., and Holy, T.E. (2008) Fast Three-Dimensional Fluorescence Imaging of Activity in Neural Populations by Objective-Coupled Planar Illumination Microscopy. *Neuron*, **57** (5), 661–672.

17. Turaga, D., and Holy, T.E. (2008) Miniaturization and defocus correction for objective-coupled planar illumination microscopy. *Opt. Lett.*, **33** (20), 2302–4.

18. Turaga, D., and Holy, T.E. (2012) Organization of Vomeronasal Sensory Coding Revealed by Fast Volumetric Calcium Imaging. *J. Neurosci.*, **32** (5), 1612–1621.

19. Engelbrecht, C.J., Voigt, F., and Helmchen, F. (2010) Miniaturized selective plane illumination microscopy for high-contrast in vivo fluorescence imaging. *Opt. Lett.*, **35** (9), 1413–5.

20. Meddens, M.B.M., Liu, S., Finnegan, P.S., Edwards, T.L., James, C.D., and Lidke, K.A. (2016) Single objective light-sheet microscopy for high-speed whole-cell 3D super-resolution. *Biomed. Opt. Express*, **7** (6), 2219–2236.

21. Galland, R., Grenci, G., Aravind, A., Viasnoff, V., Studer, V., and Sibarita, J.-B. (2015) 3D high- and super-resolution imaging using single-objective SPIM - Supplement. *Nat. Methods*, **12** (August 2014), 1–13.

22. Dunsby, C. (2008) Optically sectioned imaging by oblique plane microscopy. *Opt. Express*, **16** (25), 20306–16.

23. Kumar, S., Wilding, D., Sikkel, M.B., Lyon, A.R., MacLeod, K.T., and Dunsby, C. (2011) High-speed 2D and 3D fluorescence microscopy of cardiac myocytes. *Opt. Express*, **19** (15), 13839–13847.

24. Sikkel, M.B., Kumar, S., Maioli, V., Rowlands, C., Gordon, F., Harding, S.E., Lyon, A.R., Macleod, K.T., and Dunsby, C. (2016) High speed sCMOS-based oblique plane microscopy applied to the study of calcium dynamics in cardiac myocytes. *J. Biophotonics*, **323** (3), 3–6.

25. Li, T., Ota, S., Kim, J., Wong, Z.J., Wang, Y., Yin, X., and Zhang, X. (2014) Axial Plane Optical Microscopy. *Sci. Rep.*, **4**, 1–6.

26. Bouchard, M.B., Voleti, V., Mendes, C.S., Lacefield, C., Grueber, W.B., Mann, R.S., Bruno, R.M., and Hillman, E.M.C. (2015) Swept confocally-aligned planar excitation (SCAPE) microscopy for high speed volumetric imaging of behaving organisms. *Nat. Photonics*, **9** (2), 113–119.

27. Tokunaga, M., Imamoto, N., and Sakata-Sogawa, K. (2008) Highly inclined thin illumination enables clear single-molecule imaging in cells. *Nat. Methods*, **5** (3), 159–161.

28. Konopka, C.A., and Bednarek, S.Y. (2008) Variable-angle epifluorescence microscopy: A new way to look at protein dynamics in the plant cell cortex. *Plant J.*, **53** (1), 186–196.

29. Planchon, T.A.T., Gao, L., Milkie, D.E. DE, Davidson, M.W., Galbraith, J.A., and Catherine, G. (2011) Rapid three-dimensional isotropic imaging of living cells using Bessel beam plane illumination. *Nat. …*, **8** (5), 417–523.

30. Vettenburg, T., Bustin, N., and Harvey, A.R. (2010) Fidelity optimization for aberration-tolerant hybrid imaging systems. *Opt. Express*, **18** (9), 9220–9228.

31. Gao, L., Shao, L., Chen, B.-C., and Betzig, E. (2014) 3D live fluorescence imaging of cellular dynamics using Bessel beam plane illumination microscopy. *Nat. Protoc.*, **9** (5), 1083–1101.

32. Chen, B., Legant, W.R., Wang, K., Shao, L., Milkie, D.E., Davidson, M.W., Janetopoulos, C., Wu, X.S., Iii, J.A.H., Liu, Z., English, B.P., Mimori-kiyosue, Y., Romero, D.P., Ritter, A.T., Lippincott-schwartz, J., Fritz-laylin, L., Mullins, R.D., Mitchell, D.M., Bembenek, J.N.,

Reymann, A., Böhme, R., Grill, S.W., Wang, J.T., Seydoux, G., Tulu, U.S., Kiehart, D.P., Betzig, E., Michael, W., Janetopoulos, C., Wu, X.S., Iii, J.A.H., Liu, Z., Brian, P., Mimori-kiyosue, Y., Romero, D.P., Ritter, A.T., Lippincott-, J., Fritz-laylin, L., Mullins, R.D., Mitchell, D.M., Joshua, N., Reymann, A., Böhme, R., Grill, S.W., Wang, J.T., Seydoux, G., Tulu, U.S., Kiehart, D.P., and Betzig, E. (2014) Lattice light-sheet microscopy: Imaging molecules to embryos at high spatiotemporal resolution. *Science (80-.).*, **346** (6208), 1257998.

33. Vettenburg, T., Corral, A., Rodríguez-Pulido, A., Flors, C., and Ripoll, J. (2017) Photoswitching-Enabled Contrast Enhancement in Light Sheet Fluorescence Microscopy. *ACS Photonics*, **4** (3), 424–428.

34. Singh, A.P., Galland, R., Finch-Edmondson, M.L., Grenci, G., Sibarita, J.B., Studer, V., Viasnoff, V., and Saunders, T.E. (2017) 3D Protein Dynamics in the Cell Nucleus. *Biophys. J.*, **112** (1), 133–142.

35. Maxwell, J.C. (1858) On the General Laws of Optical Instruments. *Q. J. Pure Appl. Math.*, **2**, 232–246.

36. Botcherby, E.J., Juškaitis, R., Booth, M.J., and Wilson, T. (2007) Aberration-free optical refocusing in high numerical aperture microscopy. *Opt. Lett.*, **32** (14), 2007–2009.

37. Botcherby, E.J., Juškaitis, R., Booth, M.J., and Wilson, T. (2008) An optical technique for remote focusing in microscopy. *Opt. Commun.*, **281** (4), 880–887.

38. Curran, A., Tuohy, S., Aarts, D.G.A.L., Booth, M.J., Wilson, T., and Dullens, R.P.A. (2014) Decoupled and simultaneous three-dimensional imaging and optical manipulation through a single objective. *Optica*, **1** (4), 223.

39. Anselmi, F., Ventalon, C., Begue, A., Ogden, D., and Emiliani, V. (2011) Three-dimensional imaging and photostimulation by remote-focusing and holographic light patterning. *Proc. Natl. Acad. Sci.*, **108** (49), 19504–19509.

40. Sofroniew, N.J., Flickinger, D., King, J., and Svoboda, K. (2016) A large field of view two-photon mesoscope with subcellular resolution for in vivo imaging. *Elife*, **5** (JUN2016), 1–20.

41. Maioli, V., Chennell, G., Sparks, H., Lana, T., Kumar, S., Carling, D., Sardini, A., and Dunsby, C. (2016) Time-lapse 3-D measurements of a glucose biosensor in multicellular spheroids by light sheet fluorescence microscopy in commercial 96-well plates. *Sci. Rep.*, **6** (1), 37777.

42. Kim, J., Li, T., Wang, Y., and Zhang, X. (2014) Vectorial point spread function and optical transfer function in oblique plane imaging. *Opt. Express*, **22** (9), 11140–11151.

43. Hillman, E.M.C., Patel, K., Voleti, V., Li, W., and Yu, H. (2017) High-speed 3D imaging of cellular activity in the brain : The advantages of axially-extended beams and light sheets. *Curr. Opin. Neurobiol.*

44. Fu, Q., Martin, B.L., Matus, D.Q., and Gao, L. (2016) Imaging multicellular specimens with real-time optimized tiling light-sheet selective plane illumination microscopy. *Nat. Commun.*, **7** (11088), 1–10.

45. Gao, L. (2015) Optimization of the excitation light sheet in selective plane illumination microscopy. *Biomed. Opt. Express*, **6** (3), 881–890.

46. Huisken, J., and Stainier, D.Y.R. (2007) Even fluorescence excitation by multidirectional selective plane illumination microscopy (mSPIM). *Opt. Lett.*, **32** (17), 2608–2610.

47. Truong, T. V, Supatto, W., Koos, D.S., Choi, J.M., and Fraser, S.E. (2011) Deep and fast live imaging with two-photon scanned light-sheet microscopy. *Nat. Methods*, **8** (9), 757–60.

48. Piksarv, P., Marti, D., Le, T., Unterhuber, A., Forbes, L.H., Andrews, M.R., Stingl, A., Drexler, W., Andersen, P.E., and Dholakia, K. (2017) Integrated single- and two-photon light sheet microscopy using accelerating beams. *Sci. Rep.*, **7** (1), 1435.

49. Mertz, J., and Kim, J. (2010) Scanning light-sheet microscopy in the whole mouse brain with HiLo background rejection. *J. Biomed. Opt.*, **15** (1), 16027.

50. Lavagnino, Z., Sancataldo, G., d'Amora, M., Follert, P., De Pietri Tonelli, D., Diaspro, A., and Cella Zanacchi, F. (2016) 4D (x-y-z-t) imaging of thick biological samples by means of Two-Photon inverted Selective Plane Illumination Microscopy (2PE-iSPIM). *Sci. Rep.*, **6** (1), 23923.

51. Zhao, M., Zhang, H., Li, Y., Ashok, A., Liang, R., Zhou, W., and Peng, L. (2014) Cellular imaging of deep organ using two-photon Bessel light-sheet nonlinear structured illumination microscopy. *Biomed. Opt. Express*, **5** (5), 1296–1308.

52. Cranfill, P.J., Sell, B.R., Baird, M.A., Allen, J.R., Lavagnino, Z., de Gruiter, H.M., Kremers, G.-J., Davidson, M.W., Ustione, A., and Piston, D.W. (2016) Quantitative assessment of fluorescent proteins. *Nat. Methods*, **13** (7), 557–562.

53. Preibisch, S., Amat, F., Stamataki, E., Sarov, M., Singer, R.H., Myers, E., and Tomancak, P. (2014) Efficient Bayesian-based multiview deconvolution. *Nat. Methods*, **11** (6), 645–648.

54. Schmid, B., and Huisken, J. (2015) Real-time multi-view deconvolution. *Bioinformatics*, **31** (20), 3398–3400.

55. Prevedel, R., Yoon, Y.-G., Hoffmann, M., Pak, N., Wetzstein, G., Kato, S., Schrödel, T., Raskar, R., Zimmer, M., Boyden, E.S., and Vaziri, A. (2014) Simultaneous whole-animal 3D

imaging of neuronal activity using light-field microscopy. *Nat. Methods*, **11** (7), 727–730.

56. Nöbauer, T., Skocek, O., Pernía-Andrade, A.J., Weilguny, L., Traub, F.M., Molodtsov, M.I., and Vaziri, A. (2017) Video rate volumetric Ca2+ imaging across cortex using seeded iterative demixing (SID) microscopy. *Nat. Methods*, **14** (8), 811–818.

57. Asakawa, H., Yang, H.-J., Yamamoto, T.G., Ohtsuki, C., Chikashige, Y., Sakata-Sogawa, K., Tokunaga, M., Iwamoto, M., Hiraoka, Y., and Haraguchi, T. (2014) Characterization of nuclear pore complex components in fission yeast Schizosaccharomyces pombe. *Nucleus*, **5** (2), 149–162.

58. Ito, Y., Sakata-Sogawa, K., and Tokunaga, M. (2017) Multi-color single-molecule tracking and subtrajectory analysis for quantification of spatiotemporal dynamics and kinetics upon T cell activation. *Sci. Rep.*, **7** (1), 6994.

59. Mönkemöller, V., Øie, C., Hübner, W., Huser, T., and McCourt, P. (2015) Multimodal super-resolution optical microscopy visualizes the close connection between membrane and the cytoskeleton in liver sinusoidal endothelial cell fenestrations. *Sci. Rep.*, **5** (October), 16279.

60. Hu, Y.S., Zimmerley, M., Li, Y., Watters, R., and Cang, H. (2014) Single-molecule super-resolution light-sheet microscopy. *ChemPhysChem*, **15** (4), 577–586.

61. Patel, K., Voleti, V., Zhao, H.T., Perez-campos, C., and Hillman, E.M.C. (2017) Developing SCAPE Microscopy for Real-time , 3D Cellular Imaging at the Point-of-Care. **2017**, 3–5.

62. Richardson, D.S., and Lichtman, J.W. (2015) Clarifying Tissue Clearing. *Cell*, **162** (2), 246–257.

63. Pawley, J.B. (1995) *Handbook of Biological Confocal Microscopy*, Springer Science, New York.